

DEVELOPMENT OF A NOVEL SELF-CENTERING CONCENTRICALLY BRACED STEEL FRAME SYSTEM

by

Gerard J. O'Reilly

A thesis submitted in fulfilment of the requirements
for the degree of
Master of Engineering Science

Committee in charge:

Supervisor: Dr. Jamie Goggins

External Examiner: Prof. Brian Broderick

Internal Examiner: Prof. Padraig O'Donoghue

Department of Civil Engineering
College of Engineering & Informatics
National University of Ireland, Galway
Galway
Ireland

August, 2013

Abstract

Resistance to seismic loading in steel structures is often provided by the use of concentrically braced frames (CBFs), which are designed to undergo numerous cycles of inelastic deformation through the tensile yielding and inelastic global buckling of its bracing members. This inelastic behaviour leads to the possibility that structures designed according to current codified approaches are likely to have residual deformations after a major seismic event, meaning the structure may have not collapsed, but large permanent deformations exist in the structure. These residual deformations represent a major problem as they can often render a structure unusable, or cause significant delays such that the down-time associated with rectifying these residual deformations incur significant economic losses.

The aim of this thesis is to develop and test a novel CBF system in order to eliminate the occurrence of these residual deformations following major seismic events. This is done by combining the existing CBF system with a post-tensioning arrangement to give a self-centering CBF (SC-CBF). This post-tensioning arrangement consists of a series of strands running parallel to the beam members and between the beam flanges to be anchored at the exterior columns of the frame. This arrangement provides a recentering system for the frame which ensures the self-centering behaviour of the novel system.

The mechanics of the SC-CBF are developed and the general behaviour is described. An experimental test setup is then designed to investigate a variety of SC-CBFs under quasi-static cyclic loading. This testing, conducted using the strong floor and reaction frame in the structures laboratory at the Engineering Building in NUI Galway, demonstrates both the self-centering nature of the SC-CBF, and also the added energy dissipation provided by the brace members. Using the results of the nine experimental tests carried out, a numerical model is developed and verified using OpenSees. The model is initially developed based on previous research in the modelling of CBFs and self-centering systems, and is then developed further for the specific arrangement of the SC-CBF. The model is validated using the results of the tests carried out, where both physical testing and numerical modelling are shown to be in good agreement. Finally, the development of the SC-CBF into a performance-based design (PBD) framework is presented briefly. This outlines how the definition of the seismic hazard for a given site can be defined, together with the selection of suitable ground motions, to accurately represent the hazard levels associated with that specific site. The definition of performance goals for each level of seismic hazard is discussed, where these goals correspond to the expected damage state for each of the hazard levels considered. The design methods that can use the definition of seismic hazard for a given site, and produce a SC-CBF design that achieves the performance goals outlined for the structure are then reviewed.

The outcome of this research is the proposal of a novel SC-CBF system to be used in seismically active regions. The mechanical properties of this SC-CBF have been identified theoretically and compared to both experimental test results and numerical modelling simulation, which both validates the concept of the frame and also validates the ability of the numerical model to capture the behaviour of the SC-CBF. In light of this, a methodology is proposed which integrates the design of such a system into a PBD framework such that SC-CBF's can be designed to incorporate different design goals corresponding to different seismic events of various return period.

Acknowledgements

There are many people that I owe much gratitude to for their help in completing this thesis. Firstly, I would like to express my immense gratitude to Dr. Jamie Goggins for his support and guidance during the course of this research. His advice and endless encouragement have been key to the completion of this research. He has helped better me as a researcher, and also as a person, and for this, I am forever grateful.

To Prof. Steve Mahin for giving me the opportunity to study at the University of California, Berkeley and the PEER Center for a year of this research project. His vast experience and expert advice and knowledge in earthquake engineering have been key during the early development stages of this research, and also shaped the scope for the project as a whole. My time in California was an amazing experience and for this, I am very grateful.

To all my friends at NUI Galway who have always provided many laughs and great memories down through the years. From the lads in Block R, to the many new friends at our new office, there was never a dull day around the office. A special thanks is owed to Jack English and Kevin Flynn for the many chats and coffee breaks during those hard times and late evenings which were always very welcome and most intuitive.

I have been very privileged to have been able to travel many parts of the world over the course of this research and meet many great friends from every corner of the earth. Among these people are:

All of the people at the Rose School in Italy who made my visits there in 2011 most worthwhile and enlightening. A special thanks is owed to Dave Welch for the many insightful discussions on a variety of topics that helped better this research, and of course a special thanks to Caterina Manieri.

Tracy Becker, Andrea Calabrese, Ken Ogorzalek, Frank McKenna, Vesna Terzic, Matt Schoettler and all those who made going to work at the Richmond Field Station every day a delight. Also, thanks to Charles James at the EERC Library for his help in locating many papers and documents, and of course the great chats that went along with those! A special thanks is owed to Prof. James Kelly, for not only allowing me take his class at Cal, but also his great company every day at the RFS.

Of course a big thanks is owed to all of my family, I have been very much an absentee brother/son over the past 3 years. To my sister, Paula, my brothers, Aidan, Conor and David, and above all to my parents Gerry and Maura for their support in every step of my education to date.

The scholarship provided by the Irish Research Council which funded this research is gratefully acknowledged. The funding provided by the International Office at NUI Galway and the University of California Education Abroad Program which permitted my exchange at UC Berkeley is also gratefully acknowledged.

Table of Contents

Abstract	iii
Acknowledgements	v
Table of Contents	vii
Declaration	xi
List of Figures	xii
List of Tables	xvii
Nomenclature	xviii
1 Introduction	1
1.1 Overview of Project	1
1.2 Introduction to Earthquake Engineering	1
1.2.1 Response of Structures to Earthquakes	1
1.2.2 Seismic Design of Structures	3
1.3 Scope and Objectives of Current Research	4
1.4 Organisation of Thesis	4
2 Literature Review	7
2.1 Introduction	7
2.2 Performance of CBFs in Past Earthquakes	7
2.3 Concentrically Braced Frames	9
2.3.1 Introduction	9
2.3.2 Frame Response Parameters	9
2.3.3 Brace Response Parameters	15
2.4 Post-Earthquake Residual Deformation	20
2.4.1 Introduction	20
2.4.2 Post-Earthquake Performance Assessment	21
2.4.3 Performance-Based Design	22
2.4.4 Factors Governing Residual Displacement	24
2.4.5 Seismic Design Considerations	26
2.5 Self-Centering Systems	28
2.5.1 Self-Centering Mechanism	28
2.5.2 Self-Centering Steel Systems	29
2.6 Summary	34

3 Mechanics of Self-Centering Concentrically Braced Frame	35
3.1 Introduction	35
3.2 SC-CBF Arrangement	36
3.3 SC-CBF Hysteretic Properties	38
3.3.1 Brace Response	38
3.3.2 Frame Response	40
3.3.3 Connection Response	40
3.4 Parametric Study	43
3.5 Summary	44
4 Experimental Setup and Design	47
4.1 Introduction	47
4.2 Overview of the Test Frame	47
4.2.1 Layout of the Frame	47
4.2.2 Base Connection of the Frame	49
4.2.3 Testing Sequence	49
4.3 Design of Test Frame	51
4.3.1 Beams and Columns	51
4.3.2 Beam Shear Connection	51
4.3.3 Beam Flange Reinforcement	52
4.3.4 Panel Zone Reinforcement	52
4.3.5 PT Strands and Anchorage	52
4.4 Specimens	53
4.4.1 Braces	53
4.4.2 Gusset Plates	53
4.5 Coupon Specimen Design	54
4.6 Loading Protocol	55
4.6.1 Coupon Testing	55
4.6.2 Test Specimens	55
4.7 Instrumentation	56
4.8 Summary	60
5 Experimental Results and Observations	61
5.1 Introduction	61
5.2 Coupon Specimen Testing	61
5.2.1 Test Setup	61
5.2.2 Specimen Results	62
5.3 Specimen Testing	65
5.3.1 Overview	65
5.3.2 Specimen B0	66
5.3.3 Specimen B1A	68
5.3.4 Specimen B2A	72
5.3.5 Specimen B2B	73
5.3.6 Specimen B1B	75
5.3.7 Specimen B3A	78
5.3.8 Specimen B4A	82
5.3.9 Specimen B3B	85
5.3.10 Specimen B4B	88
5.4 Summary of Test Results	90
5.5 Sources of Error	94

5.6	Summary	96
6	Numerical Modelling of a SC-CBF	99
6.1	Introduction	99
6.2	Braced Frame Modelling	99
6.2.1	Braces	99
6.2.2	Gusset Plate Connection	101
6.2.3	Low Cycle Fatigue Modelling	102
6.3	PT Connection Modelling	103
6.4	Proposed SC-CBF Model	105
6.4.1	Response of a PT Frame	107
6.4.2	Response of a SC-CBF	108
6.5	Validation of Proposed Model	109
6.5.1	Overview	109
6.5.2	Modelling of SC-CBF Test Frame	109
6.5.3	Model and Test Results Comparisons	110
6.6	Modelling of SC-CBF for Dynamic Analysis	120
6.7	Summary	124
7	Towards a Performance-Based Design Approach for SC-CBFs	125
7.1	Introduction	125
7.2	Previous Efforts and Suggested Improvements	125
7.3	Seismic Hazard Analysis	126
7.3.1	Introduction	126
7.3.2	Typical Code Approach	126
7.3.3	Uniform Hazard Approach	128
7.3.4	Impacts on Ground Motion Selection	131
7.4	Performance Limit States	132
7.5	Design Methodologies	134
7.5.1	Introduction	134
7.5.2	Force-Based Design as per Eurocode 8	134
7.5.3	Direct Displacement-Based Design	136
7.5.4	Summary of Design Methodologies	142
7.6	Summary	143
8	Conclusions and Future Work	145
8.1	Summary	145
8.1.1	Chapter 2: Literature Review	145
8.1.2	Chapter 3: Mechanics of Self-Centering Concentrically Braced Frame	145
8.1.3	Chapter 4: Experimental Setup and Design	146
8.1.4	Chapter 5: Experimental Results and Observations	146
8.1.5	Chapter 6: Numerical Modelling of a SC-CBF	147
8.1.6	Chapter 7: Towards a Performance-Based Design Approach for SC-CBFs	147
8.2	Conclusions	148
8.3	Future Work	149
References		151

A Test Frame Design Calculations	163
A.1 Beams and Columns	163
A.2 Pinned/Roller Connections	164
A.2.1 Welds	165
A.2.2 Pin Shear	165
A.2.3 Plate Yield	166
A.2.4 Bolts	166
A.3 Beam Shear Connection	166
A.3.1 Bolts	166
A.3.2 Welds	166
A.3.3 Net section	167
A.3.4 Moment on weld	167
A.4 Beam Flange Reinforcement	167
A.5 Panel Zone Reinforcement	167
B SC-CBF Test Setup Drawings	169
C Brace and Gusset Plate Details	173
D Coupon Specimen Drawings and Mill Certificates	177
E Coupon Specimen Results	187
F Strain Gauge Test Data	193

Declaration

This thesis or any part thereof, has not been, or is not currently being submitted for any degree at any other university.



A handwritten signature in black ink, appearing to read "Gerard J. O'Reilly". The signature is fluid and cursive, with a horizontal line underneath it. To the right of the line, the name "Gerard J. O'Reilly" is printed in a smaller, sans-serif font.

The work reported herein is as a result of my own investigations, except where acknowledged and referenced.



A handwritten signature in black ink, appearing to read "Gerard J. O'Reilly". The signature is fluid and cursive, with a horizontal line underneath it. To the right of the line, the name "Gerard J. O'Reilly" is printed in a smaller, sans-serif font.

List of Figures

1.1	Idealised SDOF system.	2
1.2	Construction of a response spectrum from an earthquake motion.	3
2.1	Steel frame building systems given in EC8.	8
2.2	Local slenderness parameters of various cross-sections [20].	13
2.3	Progression of brace failure through local buckling [90].	13
2.4	Displacement ductility, μ_Δ , versus global member slenderness, $\bar{\lambda}$ (Adapted from Nip et al. [90]).	14
2.5	Illustration of the 30° concept (Adapted from Lai [79]).	14
2.6	Yield line clearance approaches for out-of-plane buckling (Adapted from Lai [79]).	16
2.7	Typical load displacement response of a RHS brace member [59].	18
2.8	Normalised compressive strength versus slenderness prediction equations at ductility level of 5.0 [2, 59, 88, 120, 134].	19
2.9	Typical bilinear hysteresis model.	20
2.10	Interstorey drift measured from a CBF subjected to El-Centro earthquake record (PGA=2.0g) [56].	21
2.11	Relationship between earthquake design level and performance levels [109].	22
2.12	Building performance levels [89].	23
2.13	Performance domain based on residual deformations approach and Vision 2000 approach [30].	24
2.14	Influence of post-yield stiffness on residual displacements (Not to scale, adapted from Kawashima et al. [74]).	25
2.15	Comparison of hysteresis rules in residual displacement response spectra [30].	26
2.16	BRBF with and without secondary MRF [97].	27
2.17	PRESSS frame rocking system (Adapted from [99]).	29
2.18	Composition of a flag-shaped hysteretic loop.	29
2.19	Paramount building in San Francisco [115].	30
2.20	Comparison of the connection details prior to the 1994 Northridge earthquake (L) and the developed self centering system (R) for MRF's [100].	30
2.21	(a) Schematic of rocking frame (b) elastic response (c) rigid-body rotation (Adapted from Roke et al. [104]).	31
2.22	Mechanical configuration of SC-FDB [140].	32
2.23	Illustration of self-centering mechanism of SC-FDB [141].	32
2.24	Elevation of (a) SC-SPSW, (b) post-tensioning at beam-column connection, (c) post-tensioned connection after gap opening [38].	33
2.25	SCED brace composition (Adapted from [33]).	33
3.1	Schematic of proposed Self-Centering Concentrically Braced Frame (SC-CBF).	36
3.2	Hysteresis of proposed Self-Centering Concentrically Braced Frame (SC-CBF).	37

3.3	Displacement Δ applied to the roof of a CBF.	39
3.4	Beam-column rocking connection.	41
3.5	Spring model of system expansion (Adapted from Christopoulos [29]).	42
3.6	Sensitivity of response parameters to design parameters.	44
4.1	Front elevation (top) and general layout (bottom) of test frame.	48
4.2	Roller connection at outer columns of test frame.	49
4.3	Typical connection of brace gusset plate to beam-column connection [79].	50
4.4	Beam-only gusset plate connection presented in Berman and Bruneau [10].	50
4.5	PT anchorage system used in test frame.	53
4.6	Waveform of the ECCS loading protocol as per ECCS [42].	56
4.7	Layout of the test frame instrumentation.	57
4.8	Final test frame setup in the lab at NUI Galway prior to testing.	60
5.1	Instron 8500 Digital Control Test Machine.	62
5.2	Example stress-strain plot for coupon C2D1.	63
5.3	Fractured coupon specimens.	64
5.4	LVDT instrumentation on upper beam-column connection.	65
5.5	B0 test results.	67
5.6	Single loop of B1A specimen at 1.2% interstorey drift.	69
5.7	B1A test results.	70
5.8	Buckling out of plane of the B1A specimens.	71
5.9	Displaced profile of the B1A specimens after testing.	72
5.10	B2A test results.	74
5.11	B2B test results.	76
5.12	Gap opening of upper beam bottom flange during B2B testing.	77
5.13	Necking of RHS brace during B2B testing.	77
5.14	B1B test results.	79
5.15	B3A test results.	81
5.16	Local buckling in the B3A RHS brace.	82
5.17	Fractured B3A RHS brace.	83
5.18	B4A test results.	84
5.19	B4A local buckling of braces.	85
5.20	B4A specimens after testing.	85
5.21	Displaced profile of the B4A specimens after testing.	86
5.22	B3B test results.	87
5.23	B3B fractured braces.	88
5.24	B3B OOP displacements after testing	89
5.25	B4B test results.	91
5.26	B4B local buckling of braces.	92
5.27	B4B specimens after testing.	92
5.28	B4B OOP displacements after testing.	92
5.29	Energy dissipation to 1.5% drift versus normalised slenderness.	95
5.30	Percentage difference of PT forces for each test.	95
5.31	Percentage difference of brace OOP displacements for each test.	95
5.32	Percentage difference of k_r^θ for each test.	96
6.1	Illustration of the composition of the brace member model.	100
6.2	Proposed gusset plate connection model by Hsiao et al. [66].	102

6.3	Rotational spring model for PTED connection sub-assembly (Adapted from Christopoulos [29]).	104
6.4	Spring model accounting for beam depth (Adapted from Christopoulos [29]).	105
6.5	Proposed spring model connection used for SC-CBF arrangement.	105
6.6	Base shear versus interstorey drift for the SC-CBF with PT elements only.	107
6.7	Base shear versus interstorey drift for the SC-CBF.	109
6.8	Test frame model used for SC-CBF model validation.	110
6.9	B0 test and model comparison.	111
6.10	B1A test and model comparison.	113
6.11	B2A test and model comparison.	114
6.12	B2B test and model comparison.	115
6.13	B1B test and model comparison.	117
6.14	B3A test and model comparison.	118
6.15	B4A test and model comparison.	119
6.16	B3B test and model comparison.	121
6.17	B4B test and model comparison.	122
7.1	Eurocode 8 design spectrum.	127
7.2	Disaggregation plot produced from USGS [128] for the 10% in 50 year hazard level at 1 second for the PEER benchmark site described in Haselton et al. [63].	129
7.3	Uniform hazard spectra for the PEER benchmark site.	131
7.4	Illustration of positive and negative ϵ with respect to the target spectrum (Adapted from Baker and Cornell [7]).	132
7.5	Fundamentals of Direct Displacement-Based Design (DDBD).	137
7.6	Comparison of estimated EVD versus measured shake table values (Adapted from Salawdeh [105]).	141
F.1	Brace strain gauge locations.	194
F.2	B1A LHS Brace Strains v Time.	195
F.3	B1A RHS Brace Strains v Time.	195
F.4	B2A LHS Brace Strains v Time.	195
F.5	B2A RHS Brace Strains v Time.	196
F.6	B2B LHS Brace Strains v Time.	196
F.7	B2B RHS Brace Strains v Time.	196
F.8	B1B LHS Brace Strains v Time.	197
F.9	B1B RHS Brace Strains v Time.	197
F.10	B3A LHS Brace Strains v Time.	197
F.11	B3A RHS Brace Strains v Time.	198
F.12	B4A LHS Brace Strains v Time.	198
F.13	B4A RHS Brace Strains v Time.	198
F.14	B3B LHS Brace Strains v Time.	199
F.15	B3B RHS Brace Strains v Time.	199
F.16	B4B LHS Brace Strains v Time.	199
F.17	B4B RHS Brace Strains v Time.	200
F.18	B1A LHS Brace Strains v Drift.	201
F.19	B1A RHS Brace Strains v Drift.	201
F.20	B2B LHS Brace Strains v Drift.	202
F.21	B2B RHS Brace Strains v Drift.	202
F.22	B1B LHS Brace Strains v Drift.	203
F.23	B1B RHS Brace Strains v Drift.	203

F.24 B3A LHS Brace Strains v Drift.	204
F.25 B3A RHS Brace Strains v Drift.	204
F.26 B4A LHS Brace Strains v Drift.	205
F.27 B4A RHS Brace Strains v Drift.	205
F.28 B3B LHS Brace Strains v Drift.	206
F.29 B3B RHS Brace Strains v Drift.	206
F.30 B4B LHS Brace Strains v Drift.	207
F.31 B4B RHS Brace Strains v Drift.	207

List of Tables

4.1	Details of braces to be tested.	51
4.2	Brace details.	53
4.3	Details of coupons cut from each brace section.	55
4.4	Test frame instrumentation details.	58
5.1	Summary of test results for all coupons.	63
5.2	Summary of test specimens.	65
5.3	Summary of test results.	93
7.1	Disaggregation results for the 50%, 10% and 2% in 50 years hazard levels for the PEER benchmark site.	130
7.2	PBD response ordinate limits.	133
7.3	PBD member limits.	134
A.1	Beam member sizing details for test frame.	164
A.2	Column member sizing details for test frame.	165
C.1	Brace details.	174
C.2	Gusset plate design checks.	175
E.1	Test results for C1 coupons.	188
E.2	Test results for C2 coupons.	189
E.3	Test results for C3 coupons.	190
E.4	Test results for C4 coupons.	191

Nomenclature

α	Hilber, Hughes Taylor integrator parameter
α	Ratio of compressive to tensile strength
β	Newmark integrator parameter
χ	Compressive reduction factor for relevant buckling mode, as per Eurocode 3
\ddot{v}_g	Ground acceleration
\ddot{v}	Relative acceleration of an idealised SDOF
Δ	Displacement
δ	Displacement profile shape
δ_b	Axial shortening of beam
Δ_g	Total lateral expansion of frame
Δ'_g	Gap opening at each connection
Δ_r	Residual lateral displacement
Δ_y	Yield lateral displacement
Δ_a	Axial displacement of a brace
Δ_{max}	Maximum lateral displacement
Δ_{OOP}	OOP displacement of a brace
$\Delta_{r,max}$	Max residual lateral displacement
\dot{v}	Relative velocity of an idealised SDOF
ϵ	Material constant, as per EC3
ϵ	Number of standard deviation a logarithm of an observed ground motion is away from the mean expected value for a given period
ϵ	Strain
ϵ_0	Yield strain for a virgin piece of material
η	Utilisation ratio
Γ	Participation factor

γ	Newmark integrator parameter
γ_{ov}	Overstrength factor
κ	EVD adjustment factor depending on which stiffness is adopted
λ	Coefficient for κ depending on what hysteresis model is used
λ	Mass correction factor as per EC8
λ	Slenderness, as per EC3
λ_1	Squash load of the brace
μ	Ductility
μ	Mean
μ_f	Fracture ductility
μ_Δ	Displacement ductility
ω	Circular natural frequency
ω	Ratio of storey shear resisted by PT system
$\bar{\lambda}$	Normalised slenderness, as per EC3
Φ	Mode shape
σ	Standard deviation
σ	Stress
θ	Interstorey drift
θ_c	Connection rotation
θ_d	Design interstorey drift
v	Normalised compressive strength
ξ_{cbf}	EVD of a CBF
ξ_{el}	Elastic damping
ξ_{evd}	Equivalent viscous damping
ξ_{hyst}	Hysteretic damping
A	Percentage elongation of coupon at fracture
A_b	Beam cross-sectional area
A_c	Column cross-sectional area
A_{br}	Brace cross-d framesectional area
B	Bay width
b	Bilinear factor

b	Brace width
b_f	Coupon specimen final width
b_h	Beam height
c	Critical width for local buckling, as per EC3
c	Damping in an idealised SDOF
$c/t\epsilon$	Width to thickness ratio
c_h	Column height
C_t	Coefficient to estimate T_1 using EC8
E	Young's modulus
E_d	Energy dissipated
F	Force
f_y	Nominal yield stress
F_{ED}	Design force
F_{RD}	Resisting force
$f_{y,max}$	Actual value of f_y to be used in EC8
g	Acceleration due to gravity
H	Storey height
h	Brace height
h_i	Arbitrary storey height
i	Radius of gyration
I_b	Beam second moment of area
I_c	Column second moment of area
K	Stiffness
k	Effective length reduction factor
k	Stiffness of an idealised SDOF
K_1	Initial lateral stiffness of braced frame
K_2	Initial lateral stiffness of PT frame
K_3	Post decompression stiffness of PT frame
k_b	Beam axial stiffness
k_c	Column flexural stiffness
K_e	Effective stiffness

k_r^θ	Rotational stiffness of connection after decompression
k_{pt}	PT element axial stiffness
L	Brace length
M	Magnitude
M	Mass matrix
m	Mass
m	Sensitivity of total strain amplitude to the logarithm of number of cycles to failure during low cycle fatiguing
M_c	Decompression moment
m_e	Effective mass
M_{ED}	Design bending moment
M_{RD}	Bending moment capacity
n	Number of fibers around brace perimeter
N_{ED}	Design axial force
N_{RD}	Axial force capacity
p	Number of integration points per element
P_T	Axial force in PT strands
P_{T0}	Initial force in the PT strands
Q	Maximum possible residual lateral deformation ratio
q	Force modification factor
R	Displacement amplification factor
R	Rupture distance
R_ξ	EC8 spectral damping adjustment factor
S	EC8 soil type factor
S_0	Original cross section area of coupon
S_u	Ultimate cross section area of coupon
Sa	Pseudo-spectral acceleration
Sd	Spectral displacement
Sv	Pseudo-spectral velocity
T	Period of vibration
T_1	First mode period of vibration
T_e	Effective period

t_f	Coupon specimen final thickness
u	Absolute displacement of an idealised SDOF
v	Relative displacement of an idealised SDOF
V_b	Base shear
v_g	Ground displacement
V_{ED}	Design shear force
V_{RD}	Shear force capacity
Z	Coupon specimen cross section area reduction
z_i	Elevation of an arbitrary storey
BRB	Buckling restrained brace
BRBF	Buckling restrained braced frame
CBF	Concentrically braced frame
CFW	Continuous fillet weld
COV	Coefficient of variation
DDBD	Direct displacement-based design
EBF	Eccentrically braced frame
EC3	Eurocode 3
EC8	Eurocode 8
ED	Energy dissipation
EVD	Equivalent viscous damping
FBD	Force based design
FOS	Factor of safety
LBBF	Lower beam bottom flange
LBTF	Lower beam top flange
LHS	Left hand side
LVDT	Linear variable differential transformer
MDOF	Multi degree of freedom
MRF	Moment resisting frame
NLTH	Nonlinear time history
OOP	Out of plane
OpenSees	Open System for Earthquake Engineering Simulation

PBD	Performance based design
PGA	Peak ground acceleration
PRESSS	Precast Seismic Structural Systems
PSHA	Probabilistic seismic hazard assessment
PT	Post-tensioning
RCM	Reverse Cuthill-McKee
RDDI	Residual deformation damage index
RHS	Right hand side
RHS	Rolled hollow section
SC-CBF	Self-centering concentrically braced frame
SC-FDB	Self-centering friction damping brace
SC-SPSW	Self-centering steel plate shear wall
SCED	Self-centering energy dissipating
SDOF	Single degree of freedom
SHS	Square hollow section
UBBF	Upper beam bottom flange
UBTF	Upper beam top flange
UHS	Uniform hazard spectrum

Chapter 1

Introduction

1.1 Overview of Project

The development of concentrically braced frames (CBFs) for seismic design has been the focus of much research over the past few decades. While more details about the behaviour of these frames emerge, there is still one area that is lacking in terms of performance of the structure as a whole. Many seismic design codes seek to limit the amount of interstorey drift or displacements of a structure in an attempt to minimise damage to the structure. However, no explicit consideration is given to the state of the structure after an earthquake has occurred. This is very critical in terms of re-occupancy of the building, monetary losses after an earthquake and the speed to which the necessary repairs and modifications can be made to the structure in order to return to normal after an event.

This has led to the development of systems that seek to minimise these residual deformations that remain, and to provide a more resilient structure. This research aims to develop the current method of designing and detailing of CBFs into a system that will still provide the same lateral load capacity, but will minimise the residual displacements of the structure leading to a superior, more resilient type of CBF system. It is envisaged that using this type of configuration will lead to more resilient structures that will need very little attention following large seismic events apart from necessary checks and replacing damaged dissipative brace members. This results in structures that can be reoccupied almost immediately post earthquake, and leads to minimal monetary losses associated with downtime.

1.2 Introduction to Earthquake Engineering

1.2.1 Response of Structures to Earthquakes

Using the sum of inertial, elastic and damping forces for the single degree of freedom (SDOF) structure shown in Figure 1.1, which has mass m , stiffness k , damping c and relative roof displacement $v(t)$, and applying equilibrium to the system that is subject to an earthquake ground acceleration of $\ddot{v}_g(t)$, the following expression is obtained for the SDOF system:

$$m\ddot{v}(t) + cv(t) + kv(t) = -m\ddot{v}_g(t) \quad (1.1)$$

This is an idealised representation of a single storey in a structure where m is the mass of the floor and the stiffness, k , is the lateral stiffness provided by the structural system, such as columns or braces. The damping in the system, c , is a natural phenomenon that occurs in every

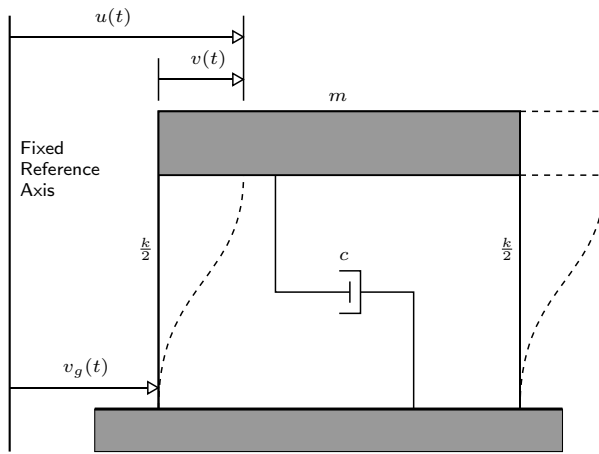


Figure 1.1: Idealised SDOF system.

dynamic system. The damping associated with this problem consists of the damping provided by the system itself, such as frictional energy dissipation of the non-structural components that can include partition walls, cladding, etc. Typical values for the damping associated with certain building types can be found in Chopra [27], where it is seen that steel structures are typically assigned a value of 3% of critical damping.

For a given earthquake excitation, the response of the system shown in Figure 1.1 can be computed over the duration of the input. This response of a system to a general dynamic loading, such as an earthquake, can be solved using one of two approaches outlined in Clough and Penzien [39]:

- Superposition methods
- Step-by-step methods

Superposition methods, such as Duhamel's integral, are solved by dividing the input loading into a series of finite pulses of loading and the response of the system to the entire loading is obtained by superimposing the solution of each of these pulses onto each other to give the complete response over time. The step-by-step methods, such as the widely used Newmark's β -method, is where the response of the system is solved by considering the loading as a series of steps and the solution is obtained by solving the system at each step based on the initial conditions at the beginning of the step. This is more suited to the nonlinear analysis of structures as it avoids the use of superposition as with the other approach to the problem. Using this approach of finding the response of an idealised SDOF to a given earthquake excitation and varying the natural period T , given by:

$$T = 2\pi \sqrt{\frac{m}{k}} \quad (1.2)$$

the response of the structure can be found for each value of T . Combining the maximum response for each period into a plot against period gives what is termed the response spectrum. This means that for a given record, the maximum response of a structure of certain period can be found by entering the x-axis and reading off the value on the y-axis. This is illustrated in Figure 1.2, where the response ordinate being plotted is relative displacement ($v(t)$), where this is termed the spectral displacement, S_d . This can be converted to a pseudo-spectral velocity,

Sv , and acceleration, Sa , through the relation given by:

$$\omega^2 Sd = \omega Sv = Sa \quad (1.3)$$

where ω is the circular natural frequency.

1.2.2 Seismic Design of Structures

There are currently two main methods of designing structures to resist seismic loading. These are termed “force-based design” and “displacement-based design”, where the principal difference is the driving metric in the design method are forces and displacements, respectively. These are both outlined in detail in Section 7.5 and, hence, just the general principle of designing for seismic loading is discussed here.

Eurocode 8 [18] represents the seismic hazard at a particular location in the form of a spectral acceleration spectrum which is expected to represent the type of earthquake spectrum generated from the method shown in Figure 1.2. The first mode of the structure is first estimated as it cannot be calculated until the actual structure has been sized, where after the first design, the actual period is calculated and the process repeated. The spectral acceleration at that period can be read from the elastic design spectrum and the equivalent lateral force is estimated by multiplying the spectral acceleration by its mass and dividing by a force modification factor. This force modification factor is intended to force the structure to undergo a degree of inelastic behaviour and, thus, dissipate the input earthquake energy in a safe and controlled manner. The total lateral force is then distributed along the height of the building using the equivalent lateral force method, and from basic structural analysis using these forces, the design forces in the members that need to be sized to can be determined.

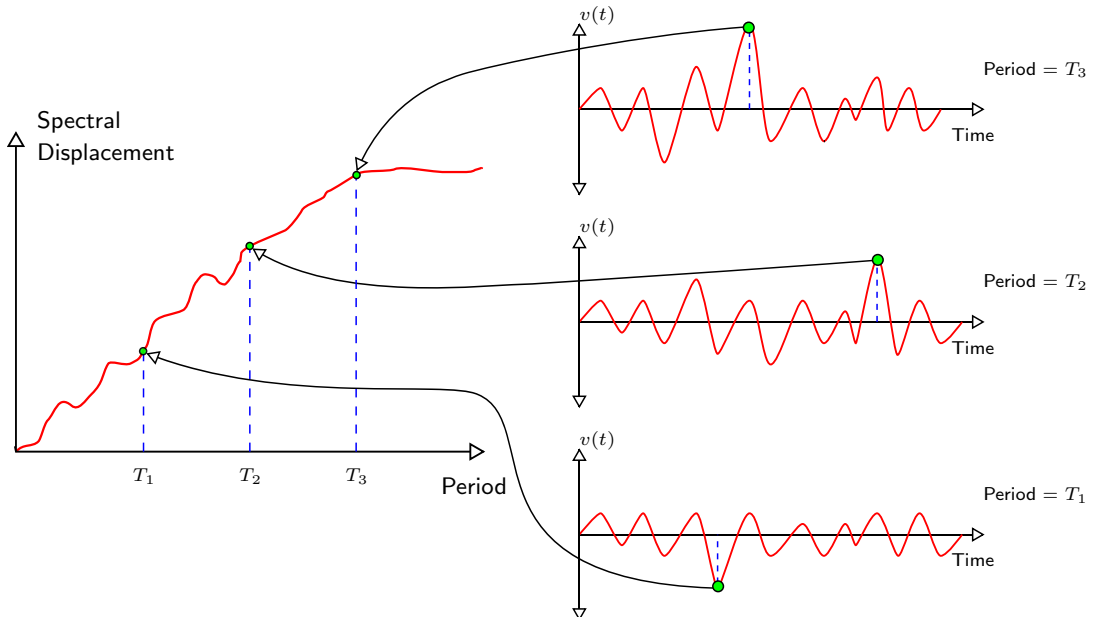


Figure 1.2: Construction of a response spectrum from an earthquake motion.

The intended locations of inelastic behaviour are then designed to the design force, and the other locations that are not intended to undergo any inelastic deformation are sized by applying

CHAPTER 1. INTRODUCTION

overstrength factors to the expected demand forces to ensure that the elements in non-dissipative energy zones remain elastic. This is to ensure that the intended locations of energy dissipation occurs in elements which can dissipate energy in a safe and controlled manner, while also maintaining the structural integrity of the building. This is termed capacity design and an example of this is in moment resisting frames where the columns are designed to remain elastic to ensure the beams are the members dissipating the energy and the structural integrity is maintained through the column members.

Most structural systems in earthquake engineering use this concept of specifying the locations of intended damage in a structure, where each system differs by using a different mechanism. For example, the moment resisting frame previously mentioned uses the flexural yielding in the beams as the energy dissipating mechanism, while concentrically braced frames (CBFs), which is the structural system focused on in this thesis, use the axial yielding and buckling of diagonal brace members as the dissipating mechanism.

1.3 Scope and Objectives of Current Research

The principal goal of this research is to develop the current conventional CBF system utilised in buildings into one that will self-center after experiencing earthquakes of various magnitudes. This is to be achieved by combining existing methods of self-centering structures with the conventional arrangement of a CBF to give a dual system of a CBF and self-centering system. This system is expected to exhibit a hysteretic behaviour that will ensure it returns to its original position following an earthquake.

Thus, the objectives of this research are as follows:

- Develop the conventional CBF system into a novel system that will self-center following severe cyclic loading. This is to be achieved by combining the CBF system with a self-centering mechanism developed and tested by previous researchers for other structural systems.
- Develop analytical expressions that describe the hysteretic behaviour of the self-centering concentrically braced frame (SC-CBF) system.
- Design and detail an experimental test setup to validate the SC-CBF concept by performing a number of cyclic tests on a range of brace specimens.
- Develop a numerical model that can be used to accurately capture the behaviour and characteristics of the SC-CBF.
- Validate this numerical model using the experimental tests carried out on the brace specimens.
- Develop a procedure that can be used to design SC-CBFs within a simplified performance-based design framework, and validate the concept by assessing the performance using the numerical model developed with a series of ground motion sets.

1.4 Organisation of Thesis

The development and testing of the SC-CBF is organised into the following chapters:

- Chapter 2 presents a literature review into the past performance of steel systems during earthquakes and goes on to discuss the behaviour of CBFs in particular. The area of post-earthquake residual deformations and the development of self-centering systems in earthquake engineering over the past two decades is then discussed.
- Chapter 3 then presents the principal concept being developed in this thesis. The details of the frame's composition are first presented followed by the derivation of analytical expressions that describe its hysteretic behaviour.
- Chapter 4 discusses the design and detailing of an experimental test setup for the SC-CBF concept. This consists of the test frame layout and the specimens that are to be tested. The loading protocol for the test frame is also presented along with the instrumentation layout for the frame.
- Chapter 5 presents the test results from the test specimens and the coupon specimens tested in the previous chapter. Test results along with a brief discussion are presented for each test.
- Chapter 6 develops a numerical model for the tested SC-CBF by combining the existing modelling parameters for both the self-centering frame and the CBF. This model is then validated using the experimental testing detailed in the previous two chapters for use in future studies on the SC-CBF.
- Chapter 7 proposes a performance-based design framework for which the SC-CBF can be designed within. This involves using a series of seismic hazard levels and performance goals for each level to be designed to. The SC-CBF can then be evaluated using the previously validated numerical for a series of structural arrangements.
- Chapter 8 summarises and presents the principal findings from this work along with recommendations for future work.

CHAPTER 1. INTRODUCTION

Chapter 2

Literature Review

2.1 Introduction

A comprehensive review into the various topics associated with this research is presented herein. Since this research is focused on the development of a new steel system for seismic design, a review into the performance of steel systems in past earthquakes is presented to highlight past deficiencies. This leads to the discussion of the response of concentrically braced frames (CBFs) under seismic loading, where the various parameters that effect the performance of these CBFs is examined at both a global, frame geometry level and a frame bracing level, where past experimental research investigations into braced frame behaviour are presented.

Since one of the principal aims of this research is to minimise the residual deformations that occur in bracing members after inelastic behaviour, a review into current research in this area is presented along with some considerations to minimise residual deformation. Another way of counteracting residual deformations in structures from a structural behaviour point of view is by the use of self-centering structural elements. The development of a self-centering system for conventional CBFs is the main focus of this research as currently, no such system exists that does not involve building rocking behaviour and some other energy dissipating mechanism. However, numerous systems for CBFs and self-centering of other structural systems have been tested and developed by many researchers and, hence, a review into these methods is presented.

2.2 Performance of CBFs in Past Earthquakes

There are many types of steel structure systems that can be used to resist seismic excitation Eurocode 8 [18] defines several different arrangements that can be used. These include systems such as moment resisting frames (MRFs), concentrically braced frames (CBFs) and eccentrically braced frames (EBFs), all of which are shown in Figure 2.1. What distinguishes each, apart from the geometrical arrangement, is the method of energy dissipation in the system. For the CBFs (Figure 2.1(a)), the principal method of energy dissipation is through axial yielding in tension and compressive buckling of the diagonal bracing elements, whereas for MRFs (2.1(b)), the dissipative zones are the plastic hinges formed in the beams at the beam-column connection. On the other hand, the dissipative mechanism for EBFs is through the yielding of the shear link in the beams. This report focuses primarily on CBFs and will now look at the development of CBFs into a seismic resisting system and the past performance of CBFs in major earthquakes around the world.

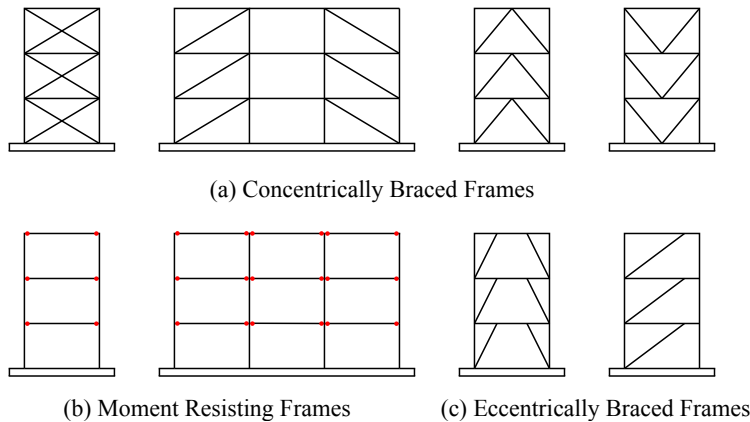


Figure 2.1: Steel frame building systems given in EC8.

CBF's were initially developed for resisting wind loading in the linear-elastic range of response, and in the early 1960's, rules for the seismic design were beginning to be formed for CBF. Khatib et al. [75] reported that up until the 1970's, the developments in the seismic response of braced frames had progressed slowly, but the expansion of offshore structures in seismic areas had stimulated investigations into the behaviour of these frames. While these investigations were being conducted, there was evidence gathering that braced frames had sustained significant damage during major earthquakes, such as the 1978 earthquake in Japan [117] and the Mexican earthquake of 1985 [5]. MRFs were widely regarded as being very effective in absorbing the demands of an earthquake, but when these frames were used in high rise structures, they tended to develop large inter-storey drifts that exceeded code prescribed limits. This stimulated the use of CBFs in these high rise structures to increase the building's stiffness, and hence reduce the interstorey drifts [68].

Uriz and Mahin [127] provide a review into the performance of CBFs in earthquakes during the period 1978 to 1995. These include the 1978 Miyagi-ken Oki earthquake in Japan, the 1985 Michoacan earthquake in Mexico, the 1994 earthquake in Northridge, California and the 1995 earthquake in Hyogo-ken Nanbu in Japan. Uriz and Mahin [127] note how there are several recurring problems in the typical detailing and proportioning of CBFs. A common occurrence in the review provided was the out-of-plane buckling of the bracing members, which in turn caused severe damage to cladding, partitions and other non-structural elements. This problem was also noted by Tremblay et al. [122] for the Northridge earthquake in 1994, where this out-of-plane buckling can cause permanent torsion in the beam elements of the steel frame. It was noted that this problem of out-of-plane buckling of bracing members was accentuated by the fact that most designers favoured out-of-plane buckling rather than in-plane buckling. It was suggested that damage to non-structural elements may be avoided if sufficient space is provided alongside these brace members to allow for this out-of-plane displacement to occur, or by selecting members that will buckle in-plane before they buckle out-of-plane [122, 121].

Another issue reported by Uriz and Mahin [127] on the performance of CBFs was the sizing of bracing members. For example, EC8 [18] imposes limits on the normalised slenderness ($\bar{\lambda}$) for brace elements, and specifies that must be between a value of 1.3 and 2.0 for X-bracing and less than 2.0 for diagonal braces. The limited number of brace sizes that are permitted in design results in similar braces being used in consecutive floors of a building. This then leads to concentration in damage of the lowest storey in which the same braces are used.

Although some of these problems in performance of CBFs in past earthquakes appear to be only minor detailing and code specified restraints, there is an additional problem that is associated with the inelastic response of steel structures. This is the residual deformations that occur during the inelastic response of the brace members. These residual deformations are well documented and will be discussed individually in Section 2.4, as they play an important part in the scope of this research.

2.3 Concentrically Braced Frames

2.3.1 Introduction

As seen in Figure 2.1, there are many different types of CBF that can be used in seismic design, with each one have a different response to earthquake excitation to another. In addition to the difference in arrangement of these frames, the composition of the braces in the frame plays an equally significant role in the response of the frame as a whole. The purpose of this section is to review the various parameters that dictate the performance at a global frame level, and also at the local brace properties level. At the global frame level, these include:

- Cross-sections types.
- Brace slenderness.
- Gusset plates.

Similarly, at a local brace property level, these will include:

- Material type and forming.
- Overstrength.
- Post-buckling compressive strength degradation.
- Fracture life.

2.3.2 Frame Response Parameters

Cross-Sections

There are a number of different types of steel cross-sections that can be used in CBFs. These include square, rectangular and circular tubular sections, angular sections, I-sections and many more built-up types of cross sections. This section will discuss some of the work previously done on all of the various available cross-sections for CBFs along with advantages and disadvantages of each of these.

Khatib et al. [75] provides a short review into various cross-sections and reports the finding of various studies [11, 55, 71, 129]. These studies all agree that the major controlling parameter of the cross-sections performance is the overall slenderness of the brace. A study by Ghanaat [55] investigated the performance of rods, pipes and double angles braces. The study concludes that double angle sand pipes performed well in terms of energy dissipation, especially if the slenderness of the member is low. The rods were deemed undesirable as bracing members, even if a pretension force is applied, as they tended to go slack after a few cycles at moderate level shaking and begin to impose impact loading and additional axial elongation in the rods. Ghanaat

CHAPTER 2. LITERATURE REVIEW

[55] conclude that the efficiency of the rod system diminishes due to the slackening of rods and can be expected to break during successive impacts, although this was not observed during the actual testing carried out by Ghanaat [55].

Rolled hollow sections have been widely reported as an effective means of resisting seismic loading in X-braced CBFs, showing stable hysteretic behaviour and satisfying code specified limits on permitted slenderness [59, 123, 134, 58]. This stable hysteretic behaviour of these members is reported as being beneficial in terms of energy dissipation up until the onset of buckling of the members, where significant strength degradation occurs in the members. However, Wijesundara [134] notes that of the members considered in his study, tubular members suffered the least strength degradation when compared to others. Wijesundara [134] also documents a report by Lee and Bruneau [80] where experimental data is collected from various publications, [4, 6, 11, 72, 130, 139], and from these, the energy dissipation of various braces is reported along with the loss of strength of each of the cross section types, following the onset of buckling. From experimental data, Black et al. [11] ranked the sections tested in order of effectiveness for a given slenderness as follows:

- Circular hollow section.
- Rectangular hollow section.
- I-Shape section.
- T-Shape section brace.
- Double angle brace.

The determining factor of the effectiveness of the brace member in the above studies is the local buckling capacity of the cross section along with the capacity of the section after the onset of buckling. Methods of preventing this buckling and loss of strength are possible by using, for example, a newly developed buckling-restrained brace, or by the filling of hollow sections with a mortar material to improve its buckling capacity. On the other hand, careful selection of brace properties such as $c/t\epsilon$ ratios, $\bar{\lambda}$ and material properties could prevent or minimise this buckling. A study into the effect of filled sections compared to hollow sections was conducted by Goggins [56], where monotonic testing was carried out in both tension and compression on hollow sections followed by the testing of infilled members. Goggins [56] concludes that when compared to the hollow sections, the filled sections exhibit higher buckling capacity and significant post buckling capacity. It was noted, however, that under tensile loading, the presence of mortar infill can cause a reduction in the ductility of the brace member by preventing ductile necking from occurring. A review of Buckling Restrained Braces (BRBs) is provided by Uang and Nakashima [125] which looks at the composition and performance of BRBs. A BRB consists of a steel core section that yields in tension and compression. A hollow section is placed around this section to prevent the buckling of this member followed the infilling of the section with mortar [102]. Uang and Nakashima [125] note some advantages and disadvantages of this system by Shuhaiar et al. [111]. The advantages are that the BRBs provide large, stable hysteresis loops at high-level seismic inputs, they offer design flexibility as both the steel core and the casing can be easily tuned and also that these braces can act as replaceable fuses in a structure. Some of the disadvantages of these BRBs are that they are proprietary along with lower field erection tolerances than that of conventional braced frames [125], but the principal and most critical point for this report is the presence of large residual deformations. The advantage of these braces has also been documented in [34, 35], whereby comparing a building built with BRBs with a similar building with MRF, a reduction of 50% in the weight of steel was observed along

with a reduction of 30 to 50% of the inter storey drifts, which is beneficial from an economic point of view and also that code drifts are satisfied more easily. It should be noted that the aforementioned study only compared a building with BRBs to a similar building with MRFs and not a building with CBFs.

Brace Slenderness

Since the brace slenderness has been identified as the single most important parameter governing a brace's behaviour, it is necessary to examine this property in detail. Brace slenderness is a term which describes two types of slenderness of a brace member: global brace slenderness and local slenderness. In addition to these two types of slenderness of the brace, also governing the brace behaviour are hysteretic behaviour, ductility and energy dissipation. It will become clearer how all of these terms are interrelated in the overall performance of a bracing member under cyclic loading.

The global slenderness of a bracing element is a function of the brace cross-section and effective length as given by:

$$\lambda = \frac{kL}{i} \quad (2.1)$$

where k is the effective length reduction factor for the given brace end conditions, L is the length of the brace and i is the radius of gyration. Eurocode 3 (EC3) [20], defines the slenderness in terms of its normalised slenderness $\bar{\lambda}$ which is given in Equation 2.2.

$$\bar{\lambda} = \frac{kL}{i} \frac{1}{\lambda_1} \quad (2.2)$$

where λ_1 is defined by the squash load of the member [20]. For seismic design, EC8 [18] imposes limits on the non-dimensional slenderness of a brace, where it must be between the values of 1.3 and 2.0 for X-braces and less than 2.0 for diagonal braces, with the upper level aiming to ensure satisfactory hysteretic behaviour [44]. The appropriateness of these limits will be discussed in due course.

The effective length reduction factor k is a function of the end restraint of the brace. Astaneh-Asl et al. [6] conducted physical testing on double-angle braces and examined the effect of the end restraint of the gusset plate. These test specimens were designed using the current American code provisions at the time of publication [1], and it was concluded that a value of 0.5 should be used for the effective length factor, k , for these double angle braces. A study by Roeder et al. [102] also examined the effect of the end restraint on tubular brace members and concluded that the energy dissipation capacity depended highly on the end connection, where it was suggested to use an effective length factor of 1.0 for corner gussets designed according to the design procedure set out by Roeder et al. [103]. Zayas et al. [139] compared the experimental behaviour of fixed and pinned brace members under cyclic loading, and it was shown how fixed ended braces showed superior performance in terms of hysteretic behaviour, strength deterioration and energy dissipation when compared with the pinned-end braces.

Khatib et al. [75] reports that most researchers in the US and Japan [11, 55, 91, 129] favour the use of stocky, low slenderness brace members as opposed to braces having large slenderness, as stocky braces exhibit full stable hysteresis loops, which allows them to dissipate more energy. On the other hand, slender members, which are often favoured in Europe, can exhibit low buckling capacity along with pinched hysteresis behaviour. The relation of the performance of the bracing member to global slenderness has also been reported in numerous recent publications

[44, 45, 60, 58, 59, 80, 90, 120].

However, this behaviour of slender members is considered advantageous also [72], as the buckling of the compression members in the structure will increase the forces in the tension members and cause them to yield and dissipate energy. Tremblay and Lacerte [121] also present an argument for the desirable behaviour of more slender members, where the elastic global buckling of the member will result in less damage. In addition to this, several reports have documented how the ductility of a brace member can be directly related to its slenderness. Tremblay [120] proposed an equation that related the ductility of a brace to the brace slenderness, while Goggins [56] and Nip et al. [90] proposed similar equations that related the ductility to the global and local slenderness of the brace member. This equation proposed by Tremblay [120] is a linear representation implying braces with higher slenderness exhibit higher ductility than that of stocky members. Goggins et al. [59] notes that this relation proposed by Tremblay [120] agrees well with the findings of Jain et al. [73], and experimental work by Elchalakani et al. [43], and it resonates the equations proposed by Nip et al. [90]. Elghazouli et al. [45] reports that this relation between high ductility capacity and slender members indicates better performance of slender members, but that seismic codes generally impose an upper limit on the allowed slenderness, which can be as low as 1.3 or 1.5 for the normalised slenderness. The reason for the reduced ductility capacity in braces with low slenderness is due to the higher strain demands experienced in their plastic hinges, whereas slender braces have reduced strain demand [58, 120]. Experimental work by Goggins et al. [58] concludes that the energy dissipation of a brace member increases with decreasing brace slenderness, whereas brace ductility decreases.

Elghazouli et al. [45] reports that the purpose of this upper limit in codes is to prevent elastic buckling of the member, reduce the effects of pinched hysteresis and sudden loading on the structure, whereas Lee and Bruneau [80] note that seismic codes introduced in the US in the 1990's were based on the philosophy that braces with low effective slenderness have superior seismic performance, and that stocky braces can significantly contribute to energy dissipation when in compression. Elghazouli et al. [45] performed a number of tests on braces with slenderness values outside of the code specified ranges, and concluded that the braces demonstrated satisfactory seismic performance. Goggins et al. [60] notes that despite the lower energy dissipation capacity of these slender members, a higher fracture resistance along with other practical and design advantages leads to the recommendation of the possible relaxation of code imposed slenderness limits. The design advantage of this approach is that when $\bar{\lambda} \geq 2.4$, the capacity of the frame can be assumed to be that of the tension member as the compression provides little to or no capacity in its buckled state. For $1.5 < \bar{\lambda} < 2.4$, 30% of the buckling capacity of the brace can be added to the tension brace for the overall capacity of the frame [60].

In addition to the global slenderness of the brace members, another equally important parameter that also affects the energy dissipation of brace members is the local slenderness. This is defined as the ratio of width-to-thickness ($c/t\epsilon$) in EC3, and some cross-sections, along with their corresponding c and t dimensions, are shown in Figure 2.2, where ϵ is a term related to material strength as per EC3.

Brace members with a low global slenderness are more susceptible to local buckling than slender members, as for a given thickness, stocky members have a wider section and therefore increasing the local slenderness. Tremblay et al. [123] note how previous research and observations after recent earthquakes shows that the RHS sections are prone to early fracture due to local buckling, as during local buckling there is an increased strain in the corner edges of the

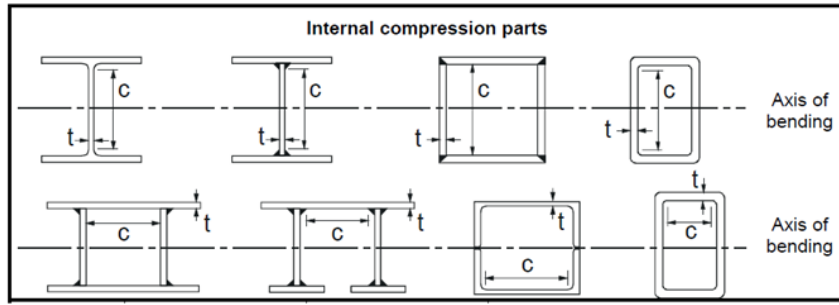


Figure 2.2: Local slenderness parameters of various cross-sections [20].

section, and subsequent cyclic loading eventually leads to crack initiation in these areas to cause the failure of the brace, as shown in Figure 2.3.

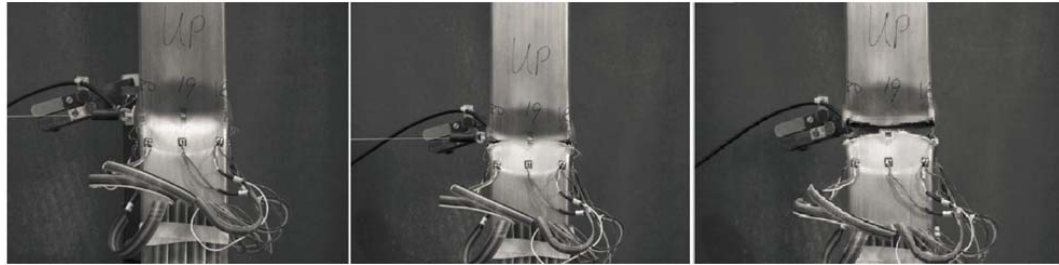


Figure 2.3: Progression of brace failure through local buckling [90].

As previously mentioned, Nip et al. [90] proposed equations that related brace ductility to local and global slenderness. These expressions by Nip et al. [90] show that for members with high local slenderness, the ductility capacity, μ_Δ , of the brace was low and did not vary significantly through increasing global slenderness for a constant ratio of width-to-thickness ratio. For low local slenderness, the test results by Nip et al. [90] demonstrate that braces with low local slenderness have increased displacement ductility capacity, μ_Δ , and this increases for an increase in global slenderness, $\bar{\lambda}$, as shown in Figure 2.4. These relations between width-to-thickness ratio with ductility and fracture have been noted in other studies [58, 59]. Experimental testing by Zayas et al. [139] also reported that the onset of local buckling in tubular members caused the rapid deterioration in members, and hence, the use of brace members with lower $c/t\epsilon$ ratios is preferable.

Gusset Plates

The behaviour and design of the gusset plate connections has been the focus of much research for many years. Lai [79] provides a review of how the 30° concept for determining the maximum stress in the gusset plate cross section, which is shown in Figure 2.5 for both welded and bolted brace connections. Experimental test observations by Wyss [137] and Whitmore [132] provided the basis for what formed the design approach for gusset plates for many years. The use of this effective section method came about as during the experimental work carried out by Whitmore [132], it was observed that linear beam theory could not be applied to the design of these gusset plates, hence a more rational approach to the design was developed.

More recent developments in the design and sizing of gusset plates are discussed in English

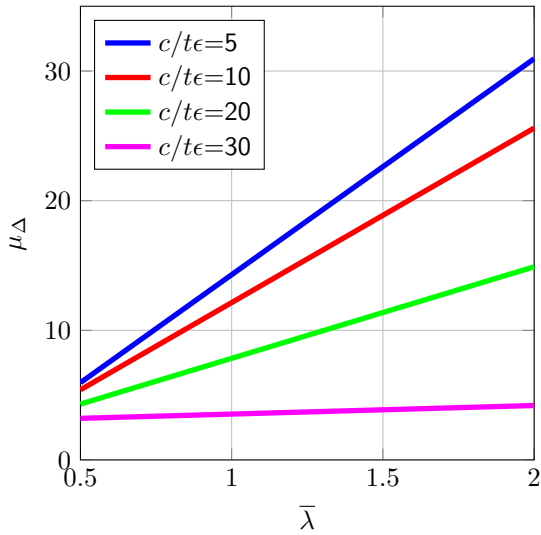


Figure 2.4: Displacement ductility, μ_{Δ} , versus global member slenderness, $\bar{\lambda}$ (Adapted from Nip et al. [90]).

[46] and English and Goggins [47], where the basis for sizing the gusset plates to allow the ductile out of plane buckling of the brace member is reported. The two methods discussed by English [46] are the linear offset method, as proposed by Whitmore [132], and the elliptical clearance method, which has been more recently proposed by Lehman et al. [81], and are both shown in Figure 2.6. English [46] reports how this linear clearance method tends to produce larger, thicker gusset plates than the corresponding elliptical clearance method. Experimental work carried out by Yoo et al. [138] demonstrated that the larger gusset plates produced by the linear clearance method restricted the ductility capacity of the plate and caused relatively early fracture due to failure of the interface welds between the gusset plates and the beam and column. Conversely, the gussets plate that were sized using the elliptical method were much smaller and thinner, and were shown to have much more ductility capacity where failure occurred by tearing of the brace member, rather than failure of the actual gusset plate.

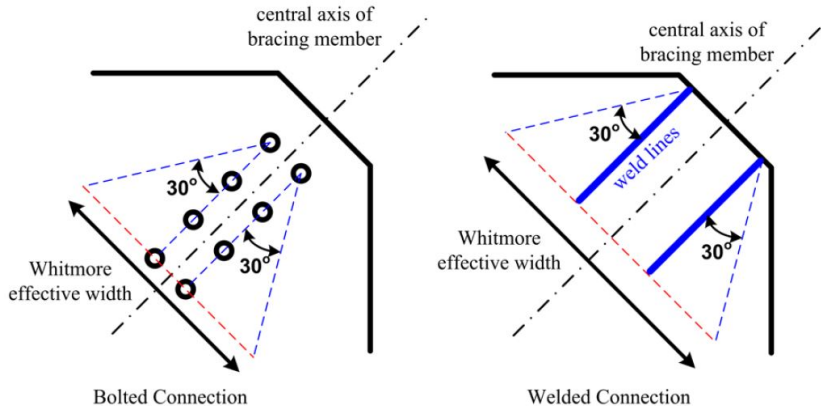


Figure 2.5: Illustration of the 30° concept (Adapted from Lai [79]).

2.3.3 Brace Response Parameters

Material Type and Forming

The two most common types of material that have been used and reported in previous research are hot-rolled and cold-formed carbon steel. Goggins [56] provides a comprehensive review into the research on cold-formed sections and the influence of the cold-working on the yield strength of the material. From this, it is seen that the cold-working affects the yield strength of the material through the pinching of the corners of the tubular members, which causes a slight increase in yield strength, and hence, a change in overall yield strength of the brace. This has been incorporated into design codes such as Eurocode 3 [21], American standards [3] and Canadian code of practice [40]. The details of these design equations are not discussed here, but merely highlighted that these are equations used in steel design when using cold-formed steel members.

In addition to the two types of forming that have been noted, the actual material type plays an equally significant part in the seismic behaviour when considering brace properties. The comparison of different material types when subject to cyclic loading was performed by Nip et al. [90]. This program consisted of cyclic testing of hot-rolled carbon steel, cold-formed carbon steel and cold-formed stainless steel to compare the differences in cyclic performance of hot and cold-formed members along with carbon and stainless steel material. The results of these experiments show that stainless steel specimens exhibit higher tensile and compressive resistance, and also maintain a higher tensile stiffness when compared to that of the carbon steel members. The stainless steel members also required a greater number of cycles to induce fracture compared to the carbon steel members. This was especially prominent for members with a low local slenderness and a high global slenderness, as previously noted in Section 2.3.2. The energy dissipation capacity of each of these brace types was reported as similar by Nip et al. [90], although the higher number of cycles the stainless steel members could sustain contributed to a slightly higher overall energy dissipation capacity of these braces.

Overstrength

In seismic design, it is important for the purposes of capacity design that the actual strength of a system is known. The reason for this is to be able to properly assess the behaviour of a system and the distribution of forces within the system and, hence, be confident in that the inelastic behaviour during an earthquake will occur in the intended locations. In seismic design, there are many causes of overstrength. For example, this already been highlighted in the cold-working of brace members discussed in Section 2.3.3. Causes of overstrength in a system are as follows:

1. Material properties.
2. Cold-working.
3. Dimensional tolerances.
4. Strain rate.
5. Design assumptions.

The overstrength due to the material properties is due to the definition of the nominal yield strength of steel grades. For a certain grade of steel, S275 in Europe for example, this indicates that the minimum strength of this is 275 N/mm^2 , not exactly 275 N/mm^2 , therefore, the actual material yield strength is likely to be greater than this.

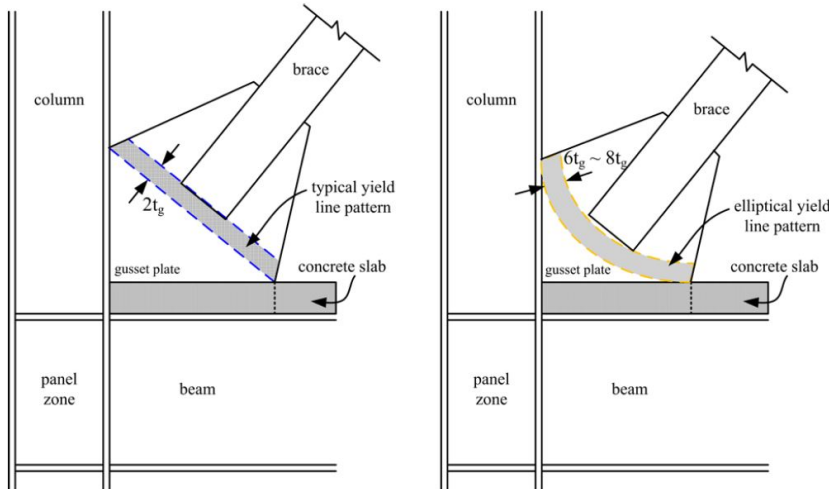


Figure 2.6: Yield line clearance approaches for out-of-plane buckling (Adapted from Lai [79]).

Cold-working overstrength has previously been encountered in this section, where it was observed that the yield strength at the corners of the tubular members can increase slightly due to the cold working. The provisions in numerous codes of practice [3, 21, 40] are also noted for calculating the actual yield strength of the cross-section due to the cold-working.

The dimensional tolerance overstrength relates to the accuracy of the member dimensions provided, which is used in the calculation of the response properties of the brace member. These tolerances are usually specified by a code of practice, such as EN 10210-2:2006 [22]. The actual consequences of these limits on dimensions of a brace section were reported in a recent experimental investigation [90], where none of the measured samples matched the dimensions specified on the identification label. For example, a sample labelled as 60x60x3mm actually measured at 59.87x59.75x2.76mm. This gives a cross-sectional area reduction of 54.2mm^2 , which corresponds to a 7.9% reduction in cross sectional area of the original nominal dimensions. Although these differences may not be large, it is necessary to acknowledge that significant differences in these may lead to inaccurate results. The final contributor to overstrength in the dynamic loading of steel members is the strain rate at which the loading is applied. This is due to the difference in yield strengths that are observed which during a short duration loading as opposed to the same loading over a longer duration. The effect is that the yield strength of the brace is slightly greater in the short impulse-like loading compared to the longer duration loading.

The effects of these sources of overstrength have been well documented in recent research of steel tubular members for braced frames. In a series of monotonic tests on short members by Goggins et al. [59], the ratios of the actual yield strength to the nominal yield strength ranged from 1.19 to 2.21, averaging at 1.49 with a COV of 0.21. Elghazouli et al. [45] reported how the observed test values for the tensile yielding of a series of braces was approximately 30% greater than predicted when using the actual yield strength, hence highlighting the need to consider the other sources of overstrength discussed above. Tremblay [120] conducted a series of testing on twenty seven RHS specimens and found the ratio of actual yield strength to nominal yield strength to be on average 1.29 times greater with a COV of 0.16. These tests also included the various grades of steel and cold-formed members.

The overstrength due to design assumption refers to the design assumption that is currently used in EC8, where the contribution of the compressive brace is ignored but accounted for in the overstrength factors specified.

It is clear from the results obtained from the various tests listed above that overstrength needs to be taken into account in seismic design of braced frames. Eurocode 8 [18] specifies a value $f_{y,max}$ for use in design of dissipative zones, which are the braces members in CBFs, as:

$$f_{y,max} \leq 1.1\gamma_{ov}f_y \quad (2.3)$$

where γ_{ov} is the overstrength factor, whose default value is equal to 1.25. However, this is the Eurocode's recommended value, but as it is a nationally determined parameter, a country's individual National Annex may stipulate an alternative value. The 10% increase is due to the strain hardening effect and the γ_{ov} is due to the possibility that the actual material strength may be higher than the nominal yield strength of the material. Combining these together it is seen that the increase is approximately equal to 37.5% of the nominal yield strength, which is in line with the values observed in the studies noted above.

Post-Buckling Compressive Strength Degradation

During seismic loading, there is continuous loading of a brace member in tension and compression. During this loading, for moderate to large earthquakes there is tensile yielding of the brace and compressive buckling of the brace. Figure 2.7 shows a typical load displacement response of a brace member subject to symmetric displacement-controlled cyclic loading. It is seen that over subsequent cycles of tensile yielding and compressive buckling, there is a gradual deterioration of the compressive strength of the brace member. Tremblay [120] notes how after buckling has occurred in the brace during the first cycle, the compressive strength decreases as a plastic hinge is formed near the mid-length of the brace. During subsequent cycles, the compressive strength of the brace is degraded significantly due to the Baushinger effect and also due to the residual out-of-plane deformations from previous cycles [11].

Tremblay [120] collected data from nine previous investigations of various cross-section types, resulting in a data set of 76 tests being used for discussion. Lee and Bruneau [80] concluded that for a variety of cross-section types, tubular cross sections were shown to exhibit the least degradation of compressive strength, while W-shaped sections were shown to suffer severe degradation. In all of the test results discussed in Tremblay [120], the maximum compressive strength of the braces was reached at the first occurrence of buckling. The lateral deformation and plastic hinging of the brace when further compressive load was applied resulted in increased lateral deformation and plastic hinging of the brace, and hence the loss in compressive strength.

Tremblay [120], Goggins et al. [59] and Nip et al. [90] all provide plots of experimental data along with predictive equations, to predict the post-buckling compressive strength of a brace at a certain ductility level. Figure 2.8 shows the equations developed in these studies for a given level of ductility, where the ratio of compressive strength to yield strength ($v = F_{cr}/Af_y$) is plotted versus normalised slenderness ($\bar{\lambda}$). Since these equations are a function of μ , this plot also changes for each value of μ , where more severe loss of compressive strength is seen for higher ductility levels.

Nip et al. [90] compares the results of experimental testing to the predictive equations proposed by AISC [2] and Tremblay [120]. From this comparison, Nip et al. [90] concludes that the

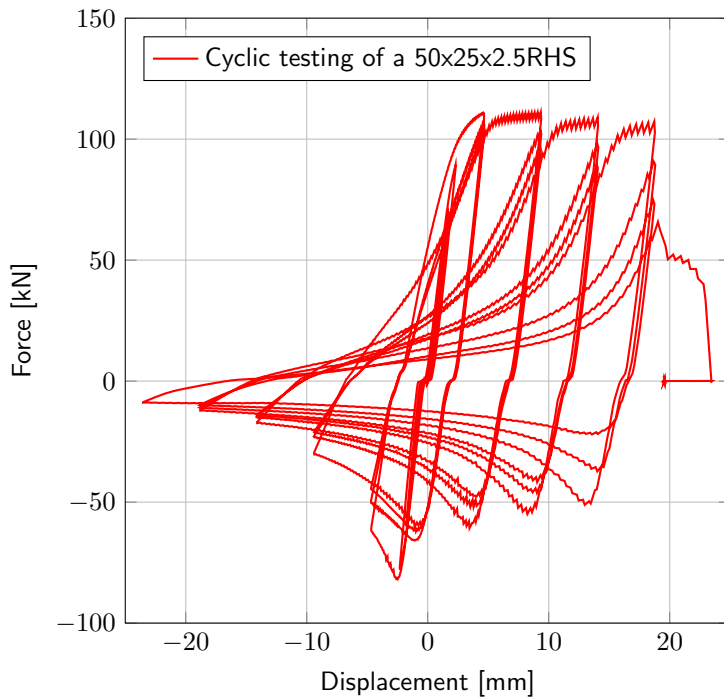


Figure 2.7: Typical load displacement response of a RHS brace member [59].

predictive equations proposed by Tremblay [120] provides a good estimate of the post-buckling resistance, while AISC [2] provides satisfactory predictions. Goggins et al. [59] also compared the results of experimental testing with the predictive equations provided by AISC [2], Tremblay [120] and Nakashima et al. [88], and in addition, provided predictive equations based on the experimental work provided. Goggins et al. [59] remarks that the curves provided by Tremblay [120] and Nakashima et al. [88] are in general agreement with each other, with the exception that Tremblay [120]'s prediction overestimates the post-buckling compressive strength at ductility level of 5. It was noted however, that the predictive equation provided by AISC [2] provided good predictions at this ductility level of 5 for slenderness greater than 0.5, although it significantly underestimates the post-buckling compressive strength at a ductility level of 2.

Fracture Life

Once local buckling occurs in the plastic hinge of a specimen undergoing compressive loading, there is an increase in the strains in the corners of the RHS section at the point of local buckling. These strains eventually cause yielding and after a few cycles, cracking and fracture of these corners occurs in the brace. This cracking of the corners of the brace causes the brace to lose its tensile capacity and hence complete fracture of the brace occurs [90, 120], as illustrated in Figure 2.3. The number of cycles it takes for this fracture is a function of numerous properties. Local buckling is a function of width-to-thickness ratio as previously discussed in Section 2.3.2, but Tremblay [120] notes that local buckling also depends on the global slenderness of the brace as well as the applied displacement history.

Tang and Goel [118] presented one of the first equations to predict the fracture life of brace members, and it is suggested that the fracture life is proportional to the global slenderness of the brace, and inversely proportional to the square of the local slenderness, but this was noted to only be applicable to inverted-V braced frames. Experimental testing by Gugerli and Goel [62]

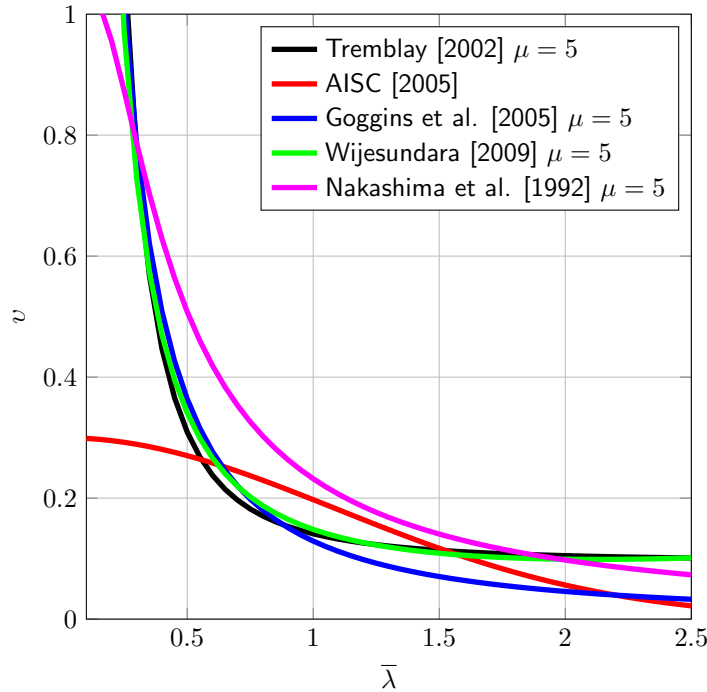


Figure 2.8: Normalised compressive strength versus slenderness prediction equations at ductility level of 5.0 [2, 59, 88, 120, 134].

also concluded that the life of a specimen up to fracture increases with the slenderness ratio of the member. Nip et al. [90] proposed a numerical model for brace members which was verified against experimental testing. Using this model, the number of cycles to failure was investigated for a range of global and local slenderness values. The results are in parallel with Tang and Goel [118]'s predictions, where the number of cycles to fracture increases with global slenderness, and decreases with local slenderness values. Tremblay [120] proposed the following equation to predict the fracture life of a brace member based on the total ductility reached at fracture, which is the sum of the peak ductility's reached in both compression and tension;

$$\mu_f = 2.4 + 8.3\bar{\lambda} \quad (2.4)$$

Although the comparison with experimental data shows good correlation [120, 123], Tremblay [120] concludes that the results indicate slender braces exhibit better fracture life than stocky members, as Equation 2.4 is a linear relationship, but notes that the results suggest that the local slenderness does not have a significant effect on the fracture, which is in contradiction to other studies previously discussed [90, 118]. Huang and Mahin [67] performed a numerical study of the fracture ductility of brace members and the factors governing this. It was concluded that fracture ductility of brace members was more sensitive to the width-to-thickness ratio (i.e. local slenderness) than to global slenderness of the brace. It was then suggested that previous observations of ductility increasing with slenderness may have been indirectly as result of available cross sections with large global slenderness values rather than a direct function of the global slenderness. It is then apparent that expressions that notice this occurrence should be used rather than ones which have not observed this trend, such as Equation 2.4. Another similar type expression to Tremblay [120] was presented and calibrated against experimental results [4, 110]. This expression presented by Shaback and Brown [110] takes into account numerous properties of the brace, including global slenderness, width-to-thickness ratio and the

yield strength of the material. Goggins et al. [58] noted this dependence of the fracture ductility on the global slenderness as well as the local width-to-thickness ratio, and from the testing carried out, expressions were proposed that related to the fracture ductility to each. Nip et al. [90] developed this proposal by Goggins et al. [58] using their experimental results, along with additional physical test and numerical simulation results to propose a new expression which depended on both global and local slenderness, and a product of the two. The expressions developed by Nip et al. [90] are as follows:

$$\begin{aligned} \text{Hot-rolled carbon steel: } \mu_f &= 3.69 + 6.97\bar{\lambda} - 0.05(c/t\epsilon) - 0.19(\bar{\lambda})(c/t\epsilon) \\ \text{Cold-formed carbon steel: } \mu_f &= 6.45 + 2.28\bar{\lambda} - 0.11(c/t\epsilon) - 0.06(\bar{\lambda})(c/t\epsilon) \\ \text{Cold-formed stainless steel: } \mu_f &= -3.42 + 19.86\bar{\lambda} + 0.21(c/t\epsilon) - 0.64(\bar{\lambda})(c/t\epsilon) \end{aligned} \quad (2.5)$$

2.4 Post-Earthquake Residual Deformation

2.4.1 Introduction

When a brace member undergoes seismic loading in moderate to large earthquakes, there are typically many cycles of elastic and inelastic behaviour induced in the brace members. This axial yielding induced in members is beneficial for energy dissipation. However, once loading ceases in the brace, the final position of the frame relative to the initial, unloaded brace's position may be altered. That is, the frame may experience some residual drift. Figure 2.9 shows a typical bilinear representation of a hysteresis loop for a structural system. The yield displacement and maximum displacement for this loop are shown as Δ_y and Δ_{max} , respectively. However, if during this loop, the loading was ceased after a positive loading, the unloading would return from the maximum displacement (Δ_{max}) to a displacement $\Delta_{r,max}$ which is termed the residual deformation (Δ_r).

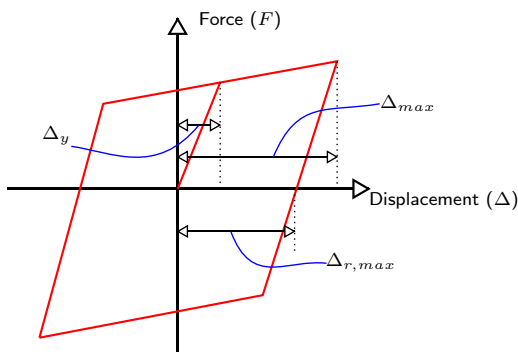


Figure 2.9: Typical bilinear hysteresis model.

When a brace undergoes a series of these loops shown in Figure 2.9, significant residual displacements may remain in the brace after the loading has been applied to the brace. Goggins [56] reported from shaking table testing of CBF brace members, that one of the tests set-ups did not recover its original vertical position after the excitation was applied (Figure 2.10). From Figure 2.10, it is seen that a residual displacement of approximately 4% was observed in the test frame.

Christopoulos and Pampanin [30] note from past earthquake observations, shake table tests and analytical studies indicate that most structure designed to modern codes of practice will sustain some form of residual deformations after loading, even if the structure performed as

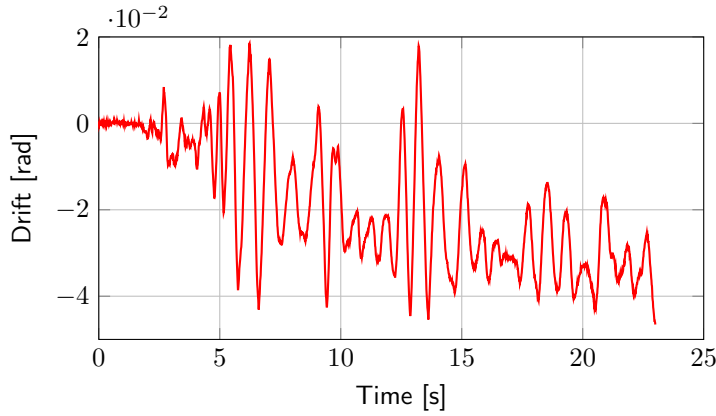


Figure 2.10: Interstorey drift measured from a CBF subjected to El-Centro earthquake record (PGA=2.0g) [56].

expected. This is noted by Christopoulos and Pampanin [30] as an unfortunate and unavoidable result of inelastic seismic response. A review of some studies in the field of psychology by McCormick et al. [85] provides an interesting conclusion when considering a structure's functionality and impact on human life after a major seismic event. Tests that consisted of asking subjects standing on a floor with an initial inclination, and to adjust the inclination until they perceived the floor to be horizontal were carried out. The study concluded that the minimum inclination perceptible by humans is approximately 0.0052 radians. McCormick et al. [85] also reported that at a hearing of 100 residents in Ashiya city, in Japan, after the 1995 Hyogoken-Nanbu earthquake, residents reported being conscious of inclinations between 0.005 and 0.006 radians, with inclinations of 0.008 radians causing serious consciousness of the inclination along with dizziness and headaches. In addition to the effects these residual drifts have on habitability, McCormick et al. [85] reported that the residual drifts present in a 17 storey MRF building after the 1995 Northridge earthquake in the US, went unnoticed during the assessment of the building and were only discovered when the elevators failed to operate because of out-of-plumbness during the re-occupancy. Clearly, this warrants serious consideration when examining the response of structures such as CBFs to seismic loading, and the development of systems with improved seismic performance.

2.4.2 Post-Earthquake Performance Assessment

In the aftermath of a serious earthquake, the final state of structures is of concern. Christopoulos and Pampanin [30] report how current methods of seismic design assess the performance of a structure on the basis on the adherence to code specified drift limits, along with cumulative energy dissipated during the response to seismic excitation. However, the final state of the structure is equally important to these performance factors as it is the final state that will have immediate effect on the status of the building after an earthquake.

Discussions by Priestley [98] and Macrae and Kawashima [83] are summarised in Christopoulos and Pampanin [30], where the importance of residual deformations when assessing the performance of a structure are given, emphasizing on the difficulty and cost associated with the straightening of structures after an earthquake before the repairs to the structure can be carried out. McCormick et al. [85] concluded that in Japan, it was generally cheaper to construct a new building than it was to repair a building that sustained residual drifts greater than 0.5%.

From the above comments, it is seen that residual displacements play an important role in the seismic performance of a structure, with Priestley [98] noting that it is arguable that residual displacements are ultimately more important than the maximum displacements or drifts experienced in the assessment of a structure, given the difficulties associated with straightening a bent building after an earthquake. The above remarks regarding post-earthquake performance assessment relate to the considerations regarding residual deformations and final position of a structure, and by no means is this discussion exhaustive with regard to the global assessment of a structure.

2.4.3 Performance-Based Design

Vision 2000 Approach

Priestley et al. [99] reports how in recent years, there has been increasing interest in defining specific seismic performance levels or objectives for structures. The performance levels defined in the Structural Engineers Association of California (SEAOC) "Vision 2000" document [109] are as follows:

- **Level 1: Fully Operational** - Facility remains in operation with negligible damage.
- **Level 2: Operational** - Facility continues in operation but with minor damage and disruption to non-essential services.
- **Level 3: Life Safe** - Life safety is protected while damage is moderate to extensive.
- **Level 4: Near Collapse** - Life safety is at risk, damage is severe with structural collapse prevented.

Using these definitions, the objectives of design can be determined for a series of different levels of seismic intensities or design levels, which are based on annual probabilities of exceedance. Using these earthquake design levels and performance levels, SEOAC [109] defines a relationship which is shown in Figure 2.11.

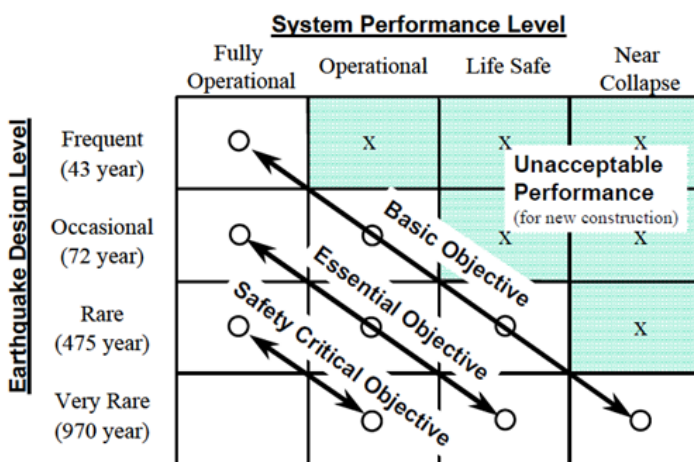


Figure 2.11: Relationship between earthquake design level and performance levels [109].

Using this relationship proposed in Figure 2.11, the design of a structure can be tailored to meet the required level of performance for a given earthquake design level, based on the specified

design objective for the structure which is decided by the designer and client. These design objectives are agreed in terms of acceptable parameters of the structures behaviour during the seismic excitation. Figure 2.12 shows a plot of the base shear versus the displacement for a series of performance levels, and illustrates the performance levels outlined in Figure 2.11 for a given building.

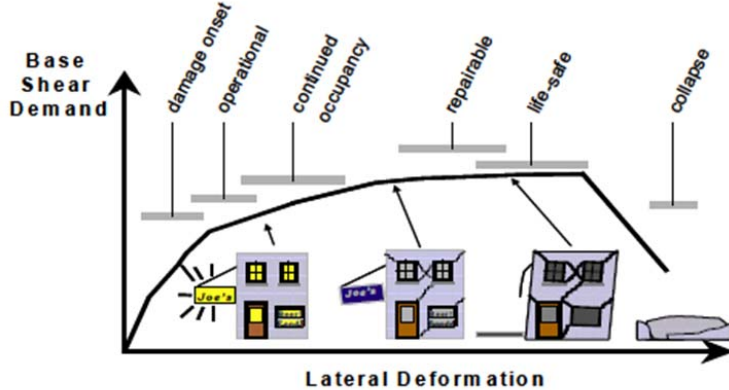


Figure 2.12: Building performance levels [89].

While this proposed method of performance-based design provides a basis for conceptual design of structures, it does not provide a complete description of performance. The details of these deficiencies to this proposed method have been discussed in Priestley et al. [99], and are not discussed in detail here. It does however note that, one measure of performance that has not been included that ought to be, is residual drifts in structures, as this is an important measure of performance and assessment, as was already discussed in Section 2.4.2. The definition of such performance goals for a structure is discussed in Section 7.4, and examples of performance goals are given in Table 7.2.

Residual Deformation Approach

As previously discussed, the Vision 2000 [109] approach to performance based design does not provide a complete description of performance. This is because the main parameter used to define the structure's behaviour are quantities such as ductility and energy dissipation, which are effective when the main objective is to avoid collapse. However, these parameters are not very effective when trying to characterise the structural integrity of the building following seismic excitation [30, 32]. As a result of this, an alternative performance-based design approach has been proposed by Christopoulos and Pampanin [30]. This performance-based design approach has been based on previous work by Christopoulos et al. [32] and Pampanin et al. [96] that developed a residual deformation damage index (RDDI), which is an index defined as a function of damage to structural and non-structural components.

The development of this residual deformation damage index by Christopoulos et al. [32] and its recommendation to be included as an addition to the existing performance-based design approach has led to the development of a new performance matrix by Christopoulos and Pampanin [30]. This combines the residual deformation damage index with the performance-based design index. This gives a three-dimensional performance domain in terms of residual drift, maximum drift and seismic intensity, as shown in Figure 2.13.

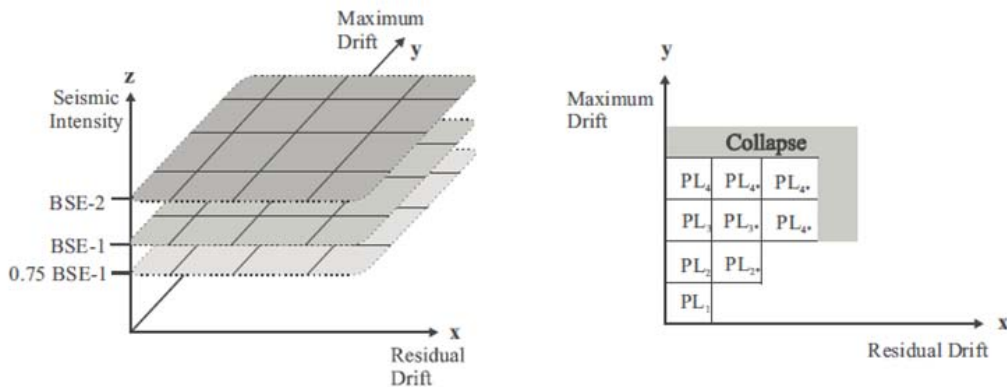


Figure 2.13: Performance domain based on residual deformations approach and Vision 2000 approach [30].

For a given level of seismic intensity, there exists a set of performance levels plotted as a function of residual drift and maximum drift, which is shown in Figure 2.13 on the right-hand side. Combining these plots of residual versus maximum drift performance levels for each level of seismic intensity gives the performance domain with explicit consideration of residual drift presented in Christopoulos and Pampanin [30].

2.4.4 Factors Governing Residual Displacement

The relation of maximum and residual drifts to seismic intensity was previously discussed in Section 2.4.3 in terms of a performance based design approach. While the parameters governing the maximum drifts experienced are well known and accounted for in design methodologies, the parameters influencing the residual drifts experienced by a structure are not as clear. The focus of this section is to examine some of the work conducted in order to establish a relation between structural properties and the residual drifts observed.

A numerical study into structural properties that influence the occurrence of residual deformations was undertaken by Kawashima et al. [74]. This involved taking a series of SDOF oscillators and subjecting them to a series of dynamic analyses using a ground motion record and observing the residual drift present in the system at the end of the analysis. The structural properties that were varied were system ductility, period and the bilinear factor, which is the ratio of the post-yield stiffness to the initial elastic stiffness for a simple bilinear system. Their study concluded that of the three of these, the bilinear factor was the most influential, whereas the bilinear factor approached zero, the occurrence of residual deformation was more pronounced. A similar study was conducted by Christopoulos et al. [32], where again the factors investigated were the bilinear factor, system ductility and period. This study reported the critical dependence of residual displacement on the bilinear factor, where it was noted as being critical as it approaches zero and becomes negative, which indicates significant PDelta effects in the structure.

From the studies by both Kawashima et al. [74] and Christopoulos et al. [32], it is concluded that the bilinear factor is the most influential structural property when considering the occurrence of residual drifts. This is demonstrated by the diagram presented in Kawashima et al. [74], and shown in Figure 2.14, where it is evident how much influence the bilinear factor (b) has on the residual displacement as it approaches a negative value. Plotted in this figure is the ordinate

Q , which represents the ratio of the actual to the maximum possible residual displacement. The actual displacement is determined from the numerical analysis for a given SDOF structure, with the remaining displacement at the end of the analysis taken as the actual value. The maximum possible residual displacement is a theoretical term which is determined from the following expression:

$$\Delta_{r,max} = \begin{cases} (\mu - 1)(1 - b)\Delta_y & \text{if } b(\mu - 1) < 1 \\ \left(\frac{1-b}{b}\right)\Delta_y & \text{if } b(\mu - 1) \geq 1 \end{cases} \quad (2.6)$$

where Figure 2.9 illustrates the meaning of each of these terms. Figure 2.14 illustrates that as the bilinear factor approaches zero and becomes negative, the actual residual drift approaches the maximum possible for that hysteretic rule.

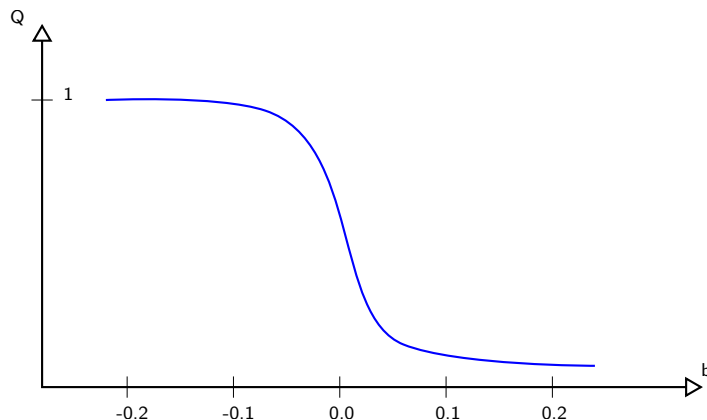


Figure 2.14: Influence of post-yield stiffness on residual displacements (Not to scale, adapted from Kawashima et al. [74]).

The dependence of the residual deformations on the hysteresis rule adopted was also observed in Christopoulos et al. [32], with lower residuals observed for systems with the Takeda hysteresis rule when compared with the Elasto-Plastic bilinear model. This is shown in Figure 2.15 where there is a greater ratio of residual to maximum displacement observed for the Elasto-plastic than the Takeda rule. The label “alfa” in Figure 2.15 corresponds to the bilinear factor labelled b here. This concurs with previously mentioned observations in many publications that BRBs sustain large residual deformations, which has a large stable hysteresis loop similar to the elasto-plastic loop here, which have been shown to result in larger residual deformations than systems with stiffness degrading hysteresis, such as the Takeda model.

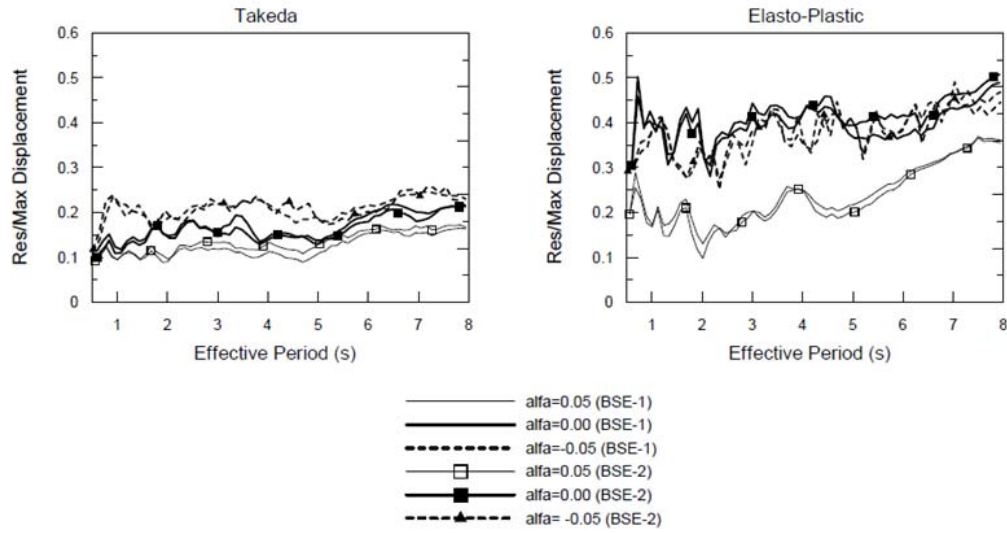


Figure 2.15: Comparison of hysteresis rules in residual displacement response spectra [30].

2.4.5 Seismic Design Considerations

Methods of Mitigation

As has been noted in the preceding sections, residual deformations represent an undesirable performance parameter in a structure's response to seismic excitation. Pettinga et al. [97] recognised the findings by previous research [30, 32, 96] into the main parameters influencing residual displacements, and used a series of simple approaches to attempt to reduce these residuals induced in a structure. These methods do not include methods of post-tensioning to achieve self-centering, which will be discussed in Section 2.5.

The techniques that were investigated by Pettinga et al. [97] to reduce the residual displacements in structures were to:

1. Use different reinforcement materials with beneficial features in their stress-strain behaviour.
2. Re-designing the section geometry and properties of the primary seismic resisting elements.
3. Introduce a secondary elastic frame to act in parallel with the primary system.

These provisions were then investigated using a series of monotonic and cyclic moment-curvature and non-linear time history analyses. Pettinga et al. [97] noted how previous research presented in Section 2.4.4 concluded that the post-yield behaviour was the main influencing factor in the residual displacements experienced by a structure. This was then used as the basis by which to improve the performance of a structure with respect to residual deformations for the methods 1 and 2 mentioned above. These methods involved an attempt to increase the post-yielding stiffness of a system by altering the section level characteristics by means of changing material properties, geometry and arrangement of reinforcement in concrete structures. The various grades of steel available in North America were used in the analyses, and the results showed that the steel grades that exhibited greater strain hardening contributed more to the post-yield stiffness of the section. Pettinga et al. [97] concludes that residual displacements

could be reduced for the section if the designer was able to specify the type of reinforcement used in the section, but the reduction in residual deformations is noted to be small, although Pettinga et al. [97] remarks that these small reductions may be enough to move the system into a higher performance level. It is worth pointing out that this increase in post-yield stiffness is beneficial for reducing residual deformations, but it also has the knock-on effect of increasing the demand in the non-dissipative zones. Hence, if such methods were to become more widely used as a means of mitigating residual deformations, the overstrength factors used in capacity design would also need revision.

Buckling restrained braced frames (BRBFs) are known to exhibit large stable hysteresis loops, which are very beneficial from an energy dissipation point of view, but BRBFs have been shown to be vulnerable to residual deformations compared to other systems, such as moment resisting frames [48, 97]. Recent work by Kiggins and Uang [76] is discussed by Pettinga et al. [97] as a possible method of reducing residual deformations in structures that use BRBFs. This involves using a secondary internal gravity moment resisting frame that remains elastic throughout the seismic loading. The performance of the structure is enhanced with a reduction in both maximum drifts and residual drifts observed for the system incorporating the secondary system. Figure 2.16 shows the results of a BRBF subjected to near-field earthquake ground motion set, and from this it can be seen that residual and interstorey drifts are significantly reduced when the secondary system is incorporated into the structure.

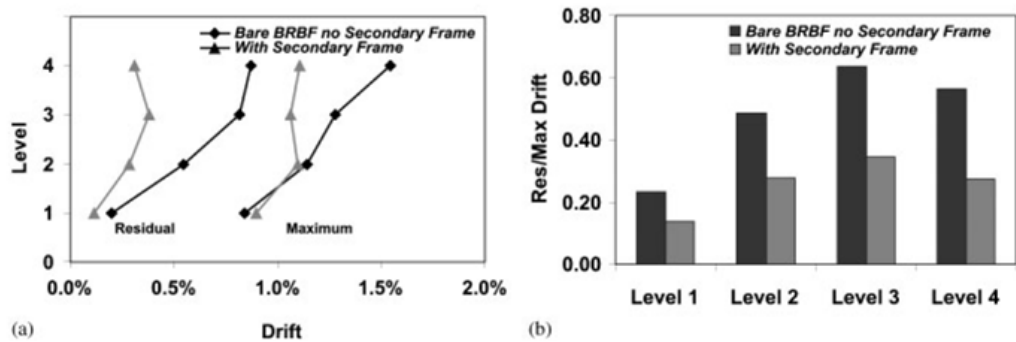


Figure 2.16: BRBF with and without secondary MRF [97].

Design Procedures

While it is important to note the existence of residual deformation in structures discussed in the previous sections, it is important that these residual deformations can be eliminated or reduced in new structures. This leads to the need for this reduction to take place at the design stage for new structures. Some methods that have been proposed by other researchers to attempt to reduce the residual deformations observed in new structures have been discussed already. But these methods are design considerations that a designer may or may not choose to incorporate into a design method. A more direct approach to this would be to incorporate these considerations directly into a design methodology that could be codified and used by designers for future structures.

Such a method has been proposed in Christopoulos and Pampanin [30], where it is concluded that the residual deformations can be estimated based on the maximum deformations of the structure during loading, the expected post yield stiffness if the structure, and if elasto-plastic

hysteresis is used, then the effective structural period. This method of using displacements as the design parameters as opposed to forces is a method that has been utilised in the Direct Displacement-Based Design (DDBD) method. The design method will be discussed in detail at a later stage, hence the design procedure to include consideration of residual deformations proposed by Christopoulos and Pampanin [30] will be discussed generally. However, it is important to note that the DDBD method is based on a target design displacement set at the start of the method and the structure is then designed to achieve that displacement during loading. The basic concept proposed by Christopoulos and Pampanin [30] is that the residual drift could be estimated as a ratio of the maximum drift induced in the structure during loading. Using this estimate of residual drift of the structure from the target drift set using the DDBD method, the structure can be designed to that level of performance. If it is found that the residual drift is not acceptable for the performance level required, the target drift could then be reduced to ensure the residual drift falls within the specified limits for the structure.

2.5 Self-Centering Systems

2.5.1 Self-Centering Mechanism

It has been discussed in detail how residual deformations have been identified as an unwanted result of seismic loading on a structure. Methods of accounting for residual deformations in performance-based design of structures were observed in Section 2.4.3, while methods of mitigation were identified in Section 2.4.5. While these methods aimed to provide a better understanding of residual deformations in terms of accountability in design methods, and the reduction by using certain structural systems, none of these systems provided a way of completely eliminating these residual deformations from the structure. A more ambitious design objective would be to have the structure return to its original position after seismic loading, which would obviously ensure that residual deformations are not a major issue. This idea has led to the development of self-centering systems, which can effectively sustain seismic loading and the structural systems return to their original vertical position after the earthquake.

During the 1990's, a multi-million dollar program known as PRESSS (PREcast Seismic Structural Systems) was undertaken by leading research institutes in the US and Japan with the goal of developing a low-cost precast concrete building that would comply with building codes, and be able to withstand the forces of a major earthquake with minimum damage resulting [61]. The result of the PRESSS program was the development of a hybrid system that was capable of resisting seismic loading, showing stable response up to interstorey drifts of 4% during experimental testing, but also re-centered itself after loading by means of a post-tensioning system within the frame. This is achieved by a rocking system (Figure 2.17), where the beams and columns are allowed to rock against each other during seismic loading. A series of post-tensioned steel strands are then placed unbonded inside the beams to provide an elastic restoring force for the system, which closes the joints and any cracks that opened during the seismic loading [114].

The force-deformation behaviour of this system is as follows in Figure 2.18. The post-tensioned steel strands remain elastic at all times during the seismic loading and, hence, provide an elastic restoring force for the system. The energy dissipation for these systems comes in the form of specialised energy dissipaters or elements that are designated to undergo inelastic behaviour during rocking, which in turn dissipates energy from the system, while the beam and columns remain elastic. Combining these two hysteretic loop behaviours together results in the behaviour shown in Figure 2.18, which is the known as the "flag-shaped" hysteresis loop. This provides

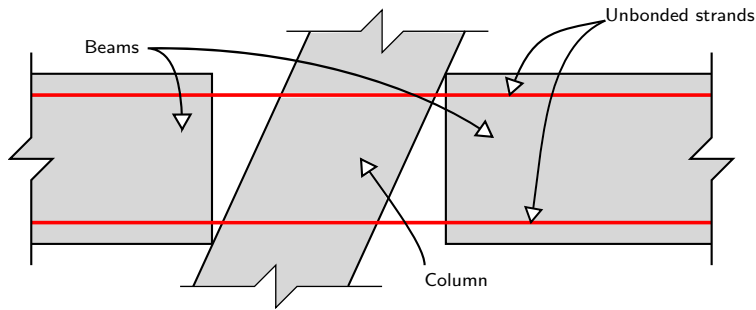


Figure 2.17: PRESSS frame rocking system (Adapted from [99]).

both energy dissipation and self-centering behaviour during cyclic loading.

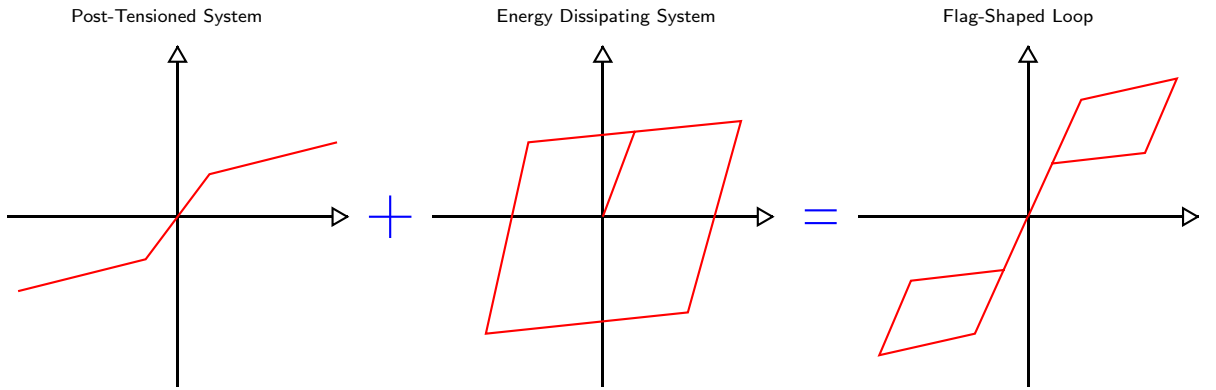


Figure 2.18: Composition of a flag-shaped hysteretic loop.

This technology has been applied in practice, such the “Paramount” building in the Mission district in San Francisco (Figure 2.19), which is an \$87 million, 40 storey residential building constructed using the PRESSS technology, while other structures such as a 4 storey media center in Los Angeles and a 3 storey parking structure at Stanford University in California also use this technology [112].

While this PRESSS system developed in 1990’s has been widely tested in the concrete community, it has also inspired similar ideas in the use of steel structures as methods of resisting earthquake loading. The following section describes numerous systems that have been developed by researchers in the use of technology similar to PRESSS in steel structures.

2.5.2 Self-Centering Steel Systems

Self-Centering Moment Resisting Frames

The self-centering moment resisting frame (MRF) connection detail proposed by Ricles et al. [100] is a development of the MRF connection detail that was used prior to the 1994 Northridge earthquake in California. It introduces a series of post-tensioned strands into the beams along with a top and bottom bolted angle cleat at the connection. This replaces the field welded beam flanges and shear tab that were used previous to the 1994 earthquake. Figure 2.20 illustrates the principal differences between the pre-1994 MRF connection and the new self-centering detail, and shows how the shear tab and flange welds that were previously used have been replaced with



Figure 2.19: Paramount building in San Francisco [115].

a top and bottom cleat for moment capacity. The post-tensioned strands running through the connection provide the self-centering capability that will ensure there are no residual deformations at the connection after an earthquake has occurred.

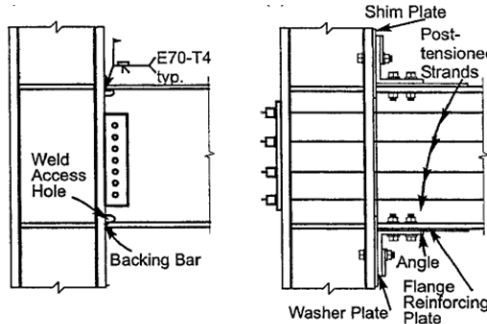


Figure 2.20: Comparison of the connection details prior to the 1994 Northridge earthquake (L) and the developed self centering system (R) for MRF's [100].

One of the main benefits of this type of connection is that when the moments from the earthquake are induced, it is the top and bottom angles that yield and dissipate the energy at the connection, while the beams and the columns remain elastic. Therefore, after the earthquake has taken place, the angles at the connection can be easily removed and replaced [52]. It is also important to note that in order to ensure the self-centering capability of the connection, the post-tensioned strands must be designed to remain elastic at all times [101]. Although the specific arrangement shown in Figure 2.20 has been documented in numerous publications by the same research group, other researchers in this area have developed similar arrangements with the same objective of eliminating residual deformations. These alternate arrangements still

utilise the post-tensioned strands, but differ in the mechanism by which energy is dissipated at the connection. Lin et al. [82] developed and tested a connection detail that used beam web friction devices to dissipate energy, whilst Iyama et al. [69] developed a connection detail that used bottom flange friction devices, so as the device would not interfere with the supported floor slab. Christopoulos et al. [31] developed a similar system to Figure 2.20, where the energy dissipating mechanism was through a series of coupled Dywidag bars that yielded in both tension and compression, and were restrained from buckling along their length. This concept was verified experimentally and both a numerical model and design procedure for this arrangement have been developed. Kim and Christopoulos [77] then tested and developed a design procedure for a system that used friction devices on both top and bottom flanges similar to that of Christopoulos et al. [31]. It is evident from the above research that MRFs with self-centering behaviour is a well-developed area within seismic design of steel structures.

Self-Centering Concentrically Braced Rocking Frame

Another system that has been developed is the self-centering concentrically braced rocking frame. Figure 2.21 shows how this arrangement consists of a building composed of concentrically braced frames that permits the rigid body rotation of the entire building [104]. This is similar to a PRESSS wall system, discussed by [108], that uses a precast wall with post-tensioned strands running down the height to provide self-centering after the rocking behaviour of the wall.

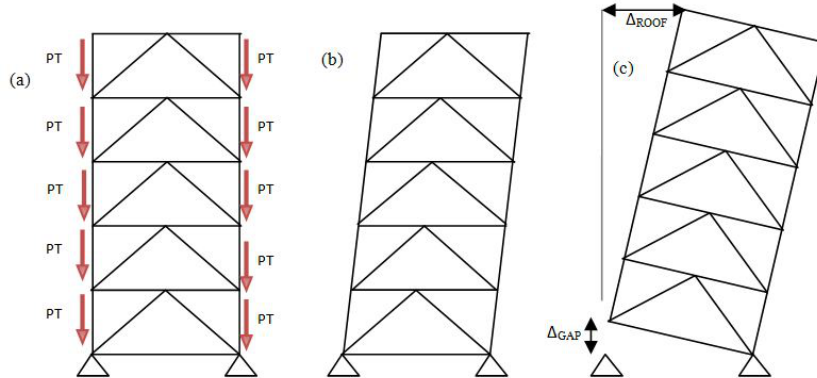


Figure 2.21: (a) Schematic of rocking frame (b) elastic response (c) rigid-body rotation
(Adapted from Roke et al. [104]).

During earthquake loading, the beams, columns and braces are designed to remain elastic under the design earthquake, with uplift permitted in the building. This uplift is then restored by the gravity loads and the post-tensioning forces in the columns of the building. The energy is dissipated at the connection through a hysteretic damping device that is activated by the relative displacement at the connection cause by uplifting of the building.

Self-Centering Friction Damping Brace

A self-centering friction damping brace (SC-FDB) is a structural element that has been developed for use in a concentrically braced frame system. It utilises both Nitinol wire strands and friction damping as a mechanism of energy dissipation. Figure 2.22 shows a SC-FDB, and from this, it is observed that the brace is composed of two elements, or blocks, which are then connected via a series of Nitinol strands across a friction damping interface between the blocks.

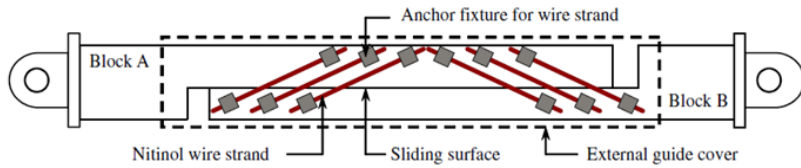


Figure 2.22: Mechanical configuration of SC-FDB [140].

Figure 2.23 shows an illustration of the combination of the mechanism of energy dissipation in the SC-FDB. By adding the friction interface in the element, the energy dissipation characteristics are greatly enhanced. Zhu and Zhang [140] performed a series of analyses on SC-FDB's, where comparison of SC-FDB's with BRB's in two buildings, (a three and six storey), are performed. It was concluded that the results of nonlinear time-history analyses (NLTH) analyses for the SC-FDB's performed well in terms of controlling residual deformations when compared with the results obtained for an identical building using BRBs.

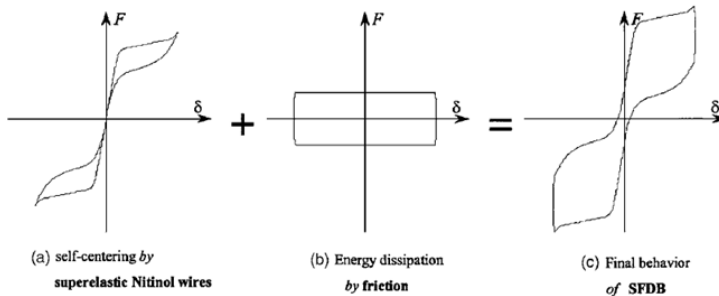


Figure 2.23: Illustration of self-centering mechanism of SC-FDB [141].

Self-Centering Steel Plate Shear Wall

Recent research by Clayton [37] has developed the concept of a self-centering steel plate shear wall (SC-SPSW) that uses the concept of a rocking moment resisting frame connection as discussed earlier. Figure 2.24 shows an arrangement of this system as presented in Clayton et al. [38], and from this, it is seen that the same mechanism of self-centering as the MRFs is utilised, whilst the shear plate is the method of energy dissipation. This is achieved through the shear buckling and development of tension field action in the plate during seismic loading [36]. The steel shear plate then serves as a replaceable fuse after moderate to large earthquakes, after the building has returned to its original position.

Analytical modelling by Clayton et al. [38] showed that the proposed performance-based design method was capable of producing 3 and 9 storey buildings that could meet predefined performance levels. Clayton et al. [38] also noted how the SC-SPSW was able to withstand interstorey drifts of up to 4% without any damage to the frame members or the post-tensioning system, although significant damage is noted in the replaceable fuse due to repeated shear buckling and energy dissipation.

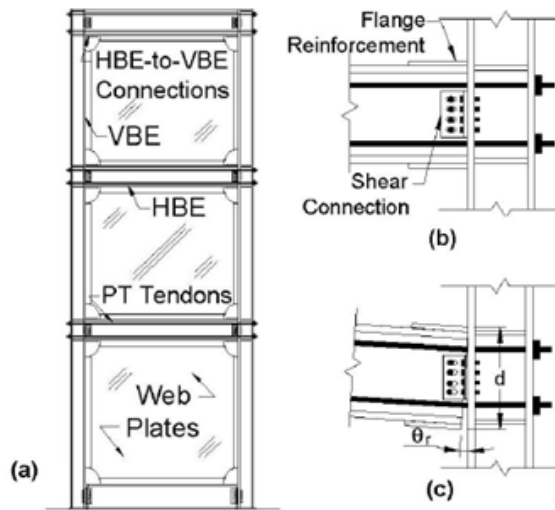


Figure 2.24: Elevation of (a) SC-SPSW, (b) post-tensioning at beam-column connection, (c) post-tensioned connection after gap opening [38].

Self-Centering Energy Dissipating Brace

Another bracing element that has been recently developed is the self-centering energy dissipating (SCED) brace. This brace, shown in Figure 2.25, has been developed and tested by Christopoulos et al. [33] and Tremblay et al. [124]. It consists of two rectangular steel bracing members, and a series of post-tensioned strands running between the steel members that are connected to the end-plates at either end of the element. In addition to these, the brace has a friction energy dissipating mechanism added to enhance the energy dissipating characteristics of the brace. The two steel members are then guided by a series of guiding elements as they move past each other during loading when the post-tensioned strands begin to elongate.

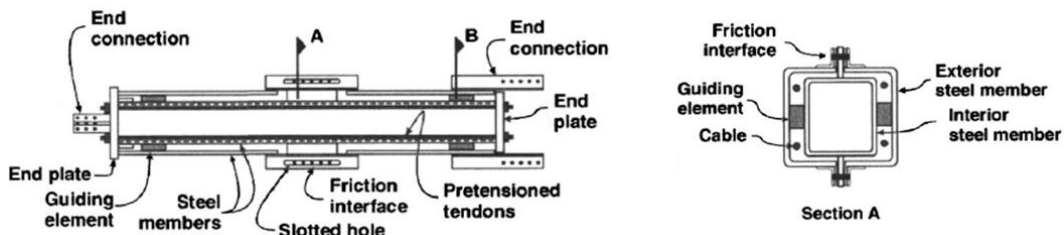


Figure 2.25: SCED brace composition (Adapted from [33]).

The purpose of the post-tensioned strands inside the brace element is to provide a self-centering mechanism to the brace after loading has occurred to eliminate any residual deformations that may remain due to the relative extension of the member during loading, therefore giving the brace enough force to recover the resisting friction force. Christopoulos et al. [33] remark that these post-tensioned strands must remain elastic during loading to ensure that the strands do not undergo any plastic deformation and that the self-centering capacity of the brace remains intact.

Numerous publications [25, 26, 124] have used this SCED developed by Christopoulos et al.

[33] in a number of design situations, and then compared them with other systems such as MRFs and BRBs. Tremblay et al. [124] compared the response of a two, four, eight, twelve and sixteen storey buildings composed of SCED braces with identical buildings that utilised BRB's using NLTH analyses. Tremblay et al. [124] found that the peak storey drifts in the SCED brace buildings were reduced compared to the buildings with BRB's, and that residual deformations in the SCED brace building were eliminated, and therefore the SCED building offered a better resistance to collapse under the maximum considered earthquake. However, it was noted by Tremblay et al. [124] that the SCED brace building could induce floor acceleration pulses in the buildings which may cause damage to non-structural elements within the building, and that the system's analysis depended on accurate values for damping in the building, and hence concluded that more accurate values for the system damping are required.

2.6 Summary

This literature review presented a detailed description of the concepts relevant to this thesis. This was first seen where the performance of CBFs during past earthquake was discussed and the shortcomings of these CBFs were highlighted. The behaviour of CBFs was discussed in detail and the parameters that affect the response at both a global frame and local brace level were presented, with the effects that each of these parameters had on the performance of the CBFs noted.

The post-earthquake residual deformations that are observed in structures following moderate to large earthquakes was then presented. It was evident that recent developments in the field have allowed for a more rational approach to performance-based design that will consider the final state of the structure after an earthquake. Factors that influence the occurrence of residual deformations were outlined, along with some findings of studies that have aimed at reducing the occurrence of residual deformation through alternative design detailing.

A review into the development of self-centering systems was presented where it was observed how the concept of self-centering systems stemmed from initial work in both concrete frame and wall systems in the early 1990's, and then later expanded into steel systems. A number of self-centering systems that have been developed for steel systems were discussed and the mechanics for each of these systems compared and contrasted. From this review, it is seen that while many self-centering systems have been presented for different types of structural systems, a limited number of systems are available for braced frame structures. The available systems that were encountered previously consist of relatively complex or proprietary systems, which somewhat limits their application to the field of earthquake engineering. Hence, there is a clear need for a simple robust system for braced systems that can be implemented by providing slight modifications to the existing system that has performed relatively well over the past few decades. Therefore, the focus of this research is to provide a simple but effective solution for CBF structures that can be incorporated easily into the existing system.

Chapter 3

Mechanics of Self-Centering Concentrically Braced Frame

3.1 Introduction

The influence of global brace slenderness ($\bar{\lambda}$) on the behaviour of braces in CBFs was discussed extensively in Section 2.3.2. Here it was shown by numerous researchers and test program findings that the global slenderness of the brace has a great influence on the brace behaviour and the response of the bracing system subjected to earthquake loading. Testing by Nip et al. [90] concluded that more slender braces can exhibit greater displacement ductility and also fracture life than stockier braces. The main challenge with using slender braces in CBFs is that codes of practice, such as EC8 [18], impose limits on the braces that can be used, with more slender braces falling outside this range. Elghazouli et al. [45] conducted a number of shake-table tests on braces with slenderness values outside of the code specified limits, and it was concluded that the braces exhibit satisfactory performance. Reasons for these limits in EC8 [18] were reported by Elghazouli et al. [45] as to prevent the elastic buckling of the braces, reduce the pinching in the hysteresis loops and also to reduce the impact loading caused during this pinching behaviour. Considering the reasons listed above, one would question what exactly the performance goals of a typical CBF designed to EC8 actually are? It has long been considered that systems with the maximum amount of energy dissipation characteristics possible are the best performers in earthquakes. This may very well be true for most systems, but what use is a building that exhibited large amounts of yielding and energy dissipation during an earthquake, if more practical performance goals, such as the usability of the building post-earthquake are not met? This relates back to Section 2.4, where performance-based design procedures have been established to give more appropriate ways to define seismic performance objectives. Section 2.4.3 then expanded on this where Christopoulos and Pampanin [30] developed the concept of performance-based design to explicitly include the residual deformations in the system after an earthquake. This consideration of the residual deformation in systems as a performance objective has led to the development of many self-centering systems in steel structures throughout the 2000's, which aim to mitigate these residual deformations.

This chapter focuses on the introduction of the proposed new self-centering system developed during this research. The philosophy behind the design is first discussed, followed by the mechanics of the system. The equations that describe the behaviour of the system and its various components are examined followed by discussion of the cyclic behaviour based on these equations.

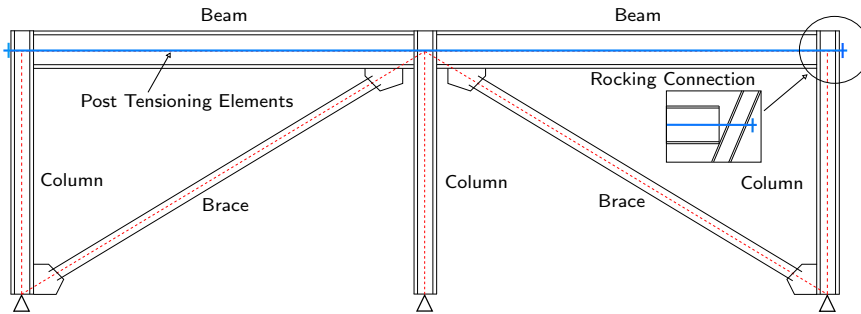


Figure 3.1: Schematic of proposed Self-Centering Concentrically Braced Frame (SC-CBF).

3.2 SC-CBF Arrangement

Numerous different systems for self-centering to achieve the flag-shaped hysteresis loop have been discussed in Section 2.5, where it was seen that these systems are made up of two components: the post-tensioning (PT) arrangement, or method of re-centering, along with a method of energy dissipation in the system, which is through a braced frame arrangement. One option for PT in buildings is to PT down the building vertically to achieve entire building rocking behaviour that was seen in Figure 2.21, or another option was to place the PT elements along the beams to achieve a rocking connection type behaviour.

For this proposed self-centering concentrically braced frame (SC-CBF), the rocking connection used by Christopoulos [29] and Clayton et al. [36] is employed as a self-centering mechanism, and the lateral movement of the frame imposes the axial displacements on the diagonal bracing members, which results in the tensile yielding and compressive buckling of the braces. The general concept is depicted in Figure 3.1.

In terms of behaviour, the lateral movement of the frame will induce a force in both the tension and compression braces, causing the tension brace to yield and dissipate energy, and the compression member to buckle, dissipating very little energy depending on its normalised slenderness ($\bar{\lambda}$). The rocking connection behaviour depends on the beam-column connection movement during lateral movement. Initially the connection is held closed by the initial axial force in the PT strands and the frame behaves essentially as a MRF until a connection moment is generated that will force the connection to open, which is termed decompression, and then the stiffness of the connection changes. This stiffness is due to the axial elongation of the PT strands because of the beam-column connection gap-opening. The mechanics of the system in terms of hysteretic behaviour are examined, where Figure 3.2 shows a schematic of the combined response of the individual components of the system in the global SC-CBF behaviour. This shows how the combination of the brace response to lateral loading combined with the frame's bilinear elastic response due to the rocking behaviour gives rise to the flag-shaped behaviour exhibited by self-centering systems.

In order to achieve this type of behaviour, a critical assumption is made about the behaviour of the bracing members, which is that the compressive resistance of the brace is relatively small in comparison to its tensile capacity. This was highlighted previously as having a number of behavioural characteristics that design codes typically try to avoid. However, it was subsequently shown that the behaviour of these slender braces can have numerous other advantages in design. In addition to those advantages, we can now use this system in a PT arrangement to give a new self-centering system. The plot in Figure 3.2 represents the lateral pushover force (F) applied

to a SC-CBF such as the one shown in Figure 3.1 and this is plotted against the roof lateral displacement Δ .

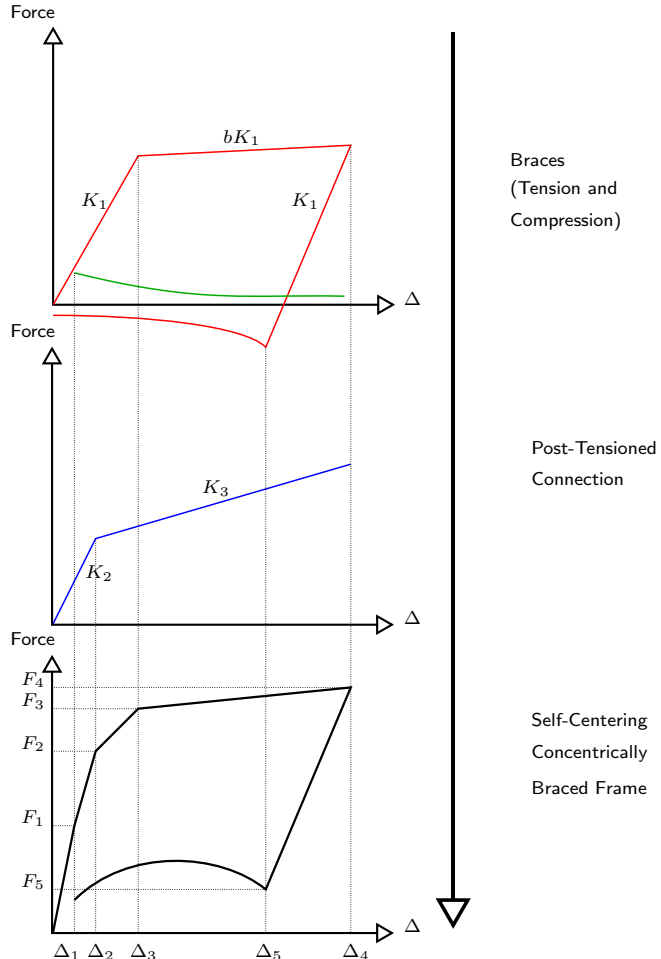


Figure 3.2: Hysteresis of proposed Self-Centering Concentrically Braced Frame (SC-CBF).

For the system shown in Figure 3.2, where the gap opening of the rocking connection is presumed to occur during the pushover before the yielding of the tension brace, we can derive some equations that describe the fundamental behaviour of the system. During the pushover, the first event to occur is the buckling of the compression brace at Δ_1 . Following this, the system is reduced to the combined stiffnesses of the PT connection, which essentially behaves as a rigid moment connection, and the axial stiffness of the tension brace. Following decompression of the rocking connection, which is when the beam-column connection begins to open at Δ_2 , the stiffness of the system is now reduced to the post-decompression stiffness of the connection in addition to the axial stiffnesses of the tension brace. This stiffness is maintained up until Δ_3 when the brace yields in tension and begins to dissipate energy. The system then has a combined stiffness of the post-yield stiffness of the brace as well the post-decompression stiffness of the connection. This stiffness is maintained until Δ_4 which is the maximum displacement experienced by the system. During unloading, the stiffness is the combined stiffness of the elastic tension brace's stiffness and the post-decompression stiffness of the connection until Δ_5 , which is when the tension has now been pushed into compression and buckles, allowing the frame to move in the opposite direction and begin the same cycle with the other brace in the opposite direction. The

stiffness present in the system after Δ_5 is attributed to the post-buckling compressive resistance of the compression member, which is a function of the normalised slenderness ($\bar{\lambda}$) and ductility of the brace member, which was discussed in Section 2.3.3 and illustrated in Figure 2.8. Hence, for more slender members, the post-buckling compressive strength degrades quicker and the stiffness of the system is reduced compared to a more stocky member. Using this flow of events, the quantities F_1 to F_5 shown in Figure 3.2 can be written as follows:

$$F_1 = (K_1 + K_1 + K_2)\Delta_1 \quad (3.1)$$

$$F_2 = F_1 + (K_1 + K_2)(\Delta_2 - \Delta_1) \quad (3.2)$$

$$F_3 = F_2 + (K_1 + K_3)(\Delta_3 - \Delta_2) \quad (3.3)$$

$$F_4 = F_3 + (bK_1 + K_3)(\Delta_4 - \Delta_3) \quad (3.4)$$

$$F_5 = F_4 - (K_1 + K_3)(\Delta_4 - \Delta_5) \quad (3.5)$$

Using these expressions for the behaviour of the SC-CBF, the self-centering of the system can now be defined. Similarly to the mechanics of the self-centering PTED connection developed by Christopoulos [29], the equations describing the behaviour can be substituted into each other to determine a condition which will give self-centering behaviour. For this system, this is such that the force at Δ_5 is greater than zero to ensure the brace is allowed to buckle at a positive global force and, hence, give the desired flag shaped behaviour. Substituting Equations 3.1 to 3.4 into Equation 3.5, the following expression is obtained:

$$F_5 = K_1(\Delta_3 + \Delta_1 + b\Delta_4 - b\Delta_3 - (1/v)\Delta_3) + K_2(\Delta_2) + K_3(\Delta_4 - \Delta_2 - (1/v)\Delta_3) \quad (3.6)$$

where the factors b is the strain hardening in the steel bracing members, and v is the normalised compressive strength of the brace, which is used to eliminate the Δ_5 term from the expression. Now the condition for self-centering as the formation of the flag-shaped loop, which is represented by:

$$F_5 \geq 0 \quad (3.7)$$

The factors that determine whether this condition is met are the design parameters, which will be discussed later, but by choosing a combination of bracing and PT connection properties, a system that exhibits the intended behaviour of the SC-CBF can be achieved. BRBs may be used to give more hysteretic energy dissipation during loading, but the level of post-tensioning that may be required to satisfy the condition for self-centering above would be so large that beam buckling would become an issue in design, hence, highlighting another reason for using more slender braces.

3.3 SC-CBF Hysteretic Properties

3.3.1 Brace Response

The first set of parameters under consideration for the SC-CBF is the brace response. Consider a simple diagonal brace shown in Figure 3.3, if a horizontal roof displacement Δ is applied to the frame and assuming small rotations of the frame, an expression for the horizontal stiffness can be formed, as follows:

$$(L + \epsilon L)^2 = (B + \Delta)^2 + (H)^2 \quad (3.8)$$

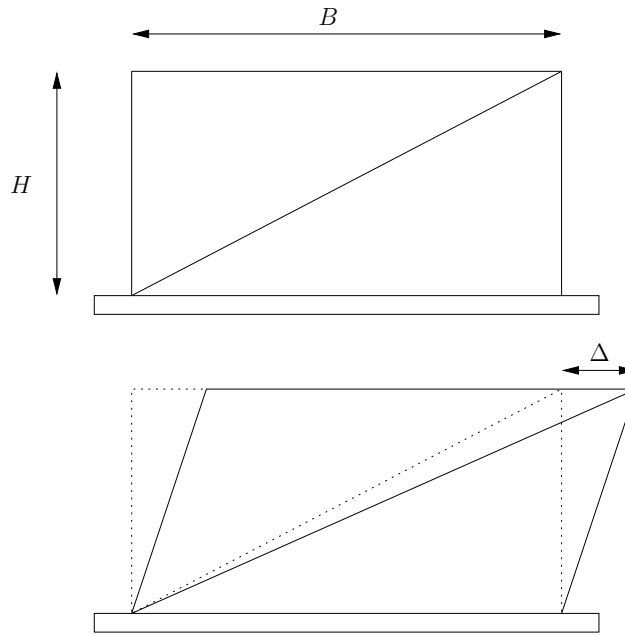


Figure 3.3: Displacement Δ applied to the roof of a CBF.

where L is the length of the brace, B is the bay width, H is the storey height and ϵ is the axial strain in the brace. This can be expanded to the following:

$$L^2 + 2\epsilon L^2 + \epsilon^2 L^2 = B^2 + 2B\Delta + \Delta^2 + H^2 \quad (3.9)$$

and assuming $\epsilon^2 \approx 0$ and $\Delta^2 \approx 0$, the horizontal displacement of the frame can be expressed as:

$$\Delta = \frac{\epsilon L^2}{B} \quad (3.10)$$

and the lateral stiffness, K_1 , can be given by:

$$K_1 = \frac{A_{br}EB}{L^2} \quad (3.11)$$

where A_{br} is the cross-sectional area of the brace and E is the Young's modulus.

Using this expression for the initial stiffness of the bracing elements, expressions for the displacements at brace yielding and buckling (Δ_3 and Δ_1) can be developed. Using the expression for the horizontal roof displacement as a function of the axial strain in the brace yields:

$$\Delta = \frac{\epsilon L^2}{B} = \frac{\sigma L^2}{BE} \quad (3.12)$$

and at tensile yield this gives the expression for Δ_3 :

$$\Delta_3 = \frac{f_y L^2}{BE} \quad (3.13)$$

and at buckling, the expression for Δ_1 is given by:

$$\Delta_1 = \frac{\chi f_y L^2}{BE} \quad (3.14)$$

where χ is the compressive reduction factor for the relevant buckling mode, as per Eurocode 3 [20].

It has been noted that the contribution of the compressive brace to the hysteretic frame response strongly depends on its slenderness. However, during seismic loading, where many cycles of inelastic deformation have occurred, the compressive braces contribution has been significantly reduced. Broderick et al. [13] reported that for braces with $1.5 \leq \bar{\lambda} \leq 2.4$, the ultimate frame resistance of the frame can be estimated by the tensile resistance plus 30% of the compression braces buckling capacity. And for more slender braces, this compressive brace contribution may be ignored.

3.3.2 Frame Response

During the elastic range of loading, the PT connection acts as if it were fully rigid at each connection. It is upon decompression that the frame is acting more like a pinned frame, with small rotational stiffness at the gap-opening connections. Up until decompression of the connections occur, the stiffness of the SC-CBF contributed from the frame is effectively the elastic horizontal stiffness of the frame. From the principal of virtual work for a two-bay frame, shown in Figure 3.1, the horizontal stiffness can be determined as:

$$K_2 = \left(\frac{H^3}{8EI_c} + \frac{H^2B}{24EI_b} \right)^{-1} \quad (3.15)$$

where E , I_b and I_c are the Young's modulus, beam second moment of area and column second moment of area, respectively.

If the bending moment in each connection at decompression (M_c) is given by:

$$M_c = \frac{P_{T0}b_h}{2} \quad (3.16)$$

where P_{T0} is the initial post-tensioning applied to the PT elements, then the moment at the four connections in the frame shown in Figure 3.1 is the total moment that needs to be generated by the frame pushover in order to achieve decompression at the rocking connections. Thus, the following expression can be formed:

$$4M_c = K_2 \Delta_2 H \quad (3.17)$$

and by substituting in for the various terms yields:

$$\Delta_2 = \frac{2P_{T0}b_h}{K_2 H} \quad (3.18)$$

3.3.3 Connection Response

Upon decompression, it is the beam-column connection behaviour that will determine the stiffness, K_3 , in Figure 3.2. One of the characteristics of this rocking connection in framed systems is that during rocking, there will be a series of gaps opening at each connection. These gaps (Δ'_g) cause the frame to expand slightly and, hence, induce other forces in the beams and columns of

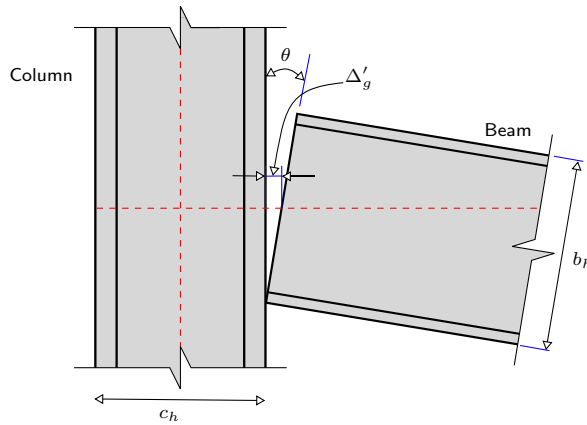


Figure 3.4: Beam-column rocking connection.

the frame. Figure 3.4 shows the connection between a beam and column undergoing rocking. At each of these connections, the gap opening at the connection, measured at the centreline of the beam, is given by:

$$\Delta'_g = \theta(b_h/2) \quad (3.19)$$

where θ is the rotation of the connection and b_h is the height of the beam. Since the frame being described is a 2-bay frame, symmetric about the central column, the elongation caused by these gap openings will be accommodated by the exterior columns. The elongation that takes place at each of the external columns is Δ_g and is given by:

$$\Delta_g = 2\Delta'_g = \theta b_h \quad (3.20)$$

Christopoulos [29] derived a relation that took into account this behaviour at the beam-column connection. Figure 3.5 shows the diagram used by Christopoulos [29]. During the rocking of the connection, a gap opens up at each of the connection which induces forces in the exterior columns, but also in the PT elements that are connected to both columns that are being pushed out. This increase in force in the PT elements will in turn induce forces in the beam elements, as the gap opening does not pull the beam in tension since the beam are not connected. This is represented in Figure 3.5 by inserting a rigid link when the column are expanded by an amount Δ_g on each side. However, this increase in axial force in the beam then causes an axial shortening in the beams, δ_b , which then in turn reduces the axial force in the PT elements. Once the system finally reaches equilibrium, Christopoulos [29] gives the relation to be:

$$\delta_b k_b = (\Delta_g - \delta_b) k_c + 2(\Delta_g - \delta_b) k_{pt} \quad (3.21)$$

where k_b , k_c and k_{pt} are the axial stiffness of the beam, flexural stiffness of the columns and axial stiffness of the PT elements, respectively.

This can then be rearranged into the form:

$$\delta_b = \frac{\theta(b_h)}{\Omega} \quad (3.22)$$

where:

$$\Omega = 1 + \frac{k_b}{k_c + 2k_{pt}} \quad (3.23)$$

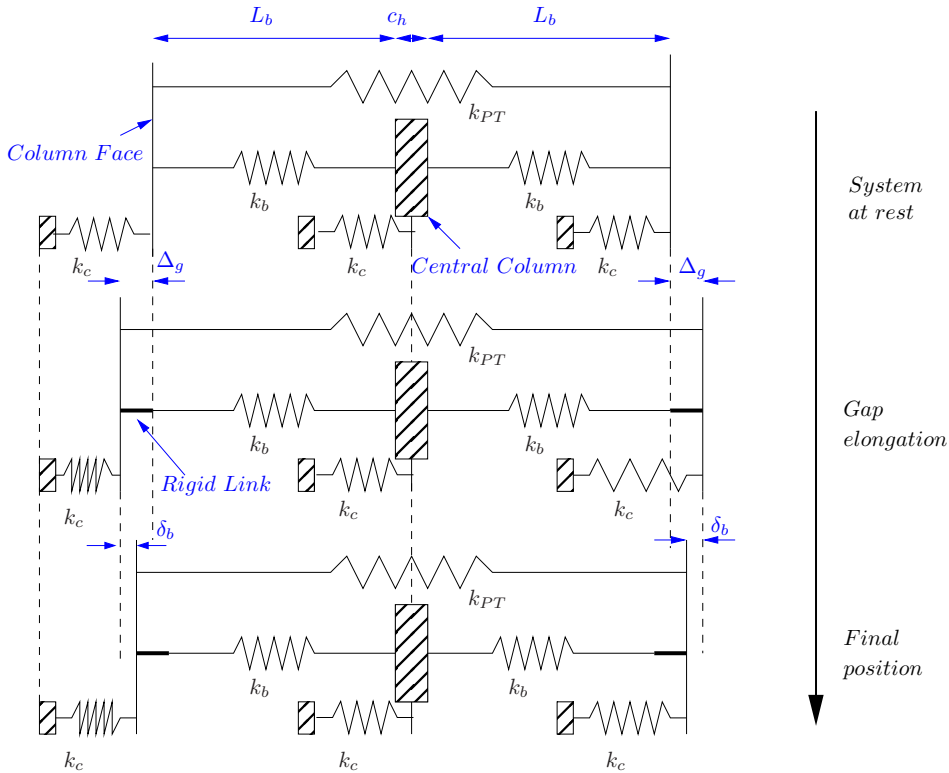


Figure 3.5: Spring model of system expansion (Adapted from Christopoulos [29]).

Since the increase in PT force is what effectively determines the post decompression stiffness of the connection, these relationships can now be formed into an equation that represents the increase in PT force, and in turn the connection stiffness. This increase in PT force is directly related to the roof displacement, so as the frame displacement increases, there is a slight increase in connection moment following decompression. The force in the PT elements can be represented as follows:

$$P_T = P_{T0} + 2k_{pt}(\Delta_g - \delta_b) \quad (3.24)$$

and substituting in the Equations 3.21, 3.22 and 3.23 gives:

$$P_T = P_{T0} + 2k_{pt}\left(1 - \frac{1}{\Omega}\right)\frac{b_h\Delta}{H} \quad (3.25)$$

where P_{T0} is the initial PT force applied manually to the elements by hydraulic jacking.

Using Equation 3.25, the moment in the connection is written as follows:

$$M_c = \frac{b_h}{2} \left(P_{T0} + 2k_{pt}\left(1 - \frac{1}{\Omega}\right)b_h\theta \right) \quad (3.26)$$

giving the rotational stiffness of a connection after decompression (k_r^θ) to be:

$$k_r^\theta = k_{pt}\left(1 - \frac{1}{\Omega}\right)b_h^2 \quad (3.27)$$

Clayton et al. [36] derived the following expression for the post-decompression stiffness of a

rocking frame:

$$K_3 = \frac{\sum k_r^\theta}{H^2} \quad (3.28)$$

which for a two bay frame consisting of 4 rocking connections gives the following expression for the post-decompression stiffness of the frame:

$$K_3 = 4k_{pt}(1 - \frac{1}{\Omega}) \frac{b_h^2}{H^2} \quad (3.29)$$

Examining the expression developed for K_3 a little further, it is seen that K_3 can be easily increased by increasing the axial stiffness of the PT elements, which can be easily achieved by increasing the cross-sectional area of the PT elements by increasing the number of strands. Section 2.4.4 discussed the factors influencing the residual displacement present in structures, and from this, it was concluded the post-yielding stiffness of a structure was the most significant factor. That is, when P-Delta effects become significant, the post-yield stiffness becomes negative and large residual displacements begin to become more likely. Normally the post-yield stiffness can not be easily increased, as for steel structures it usually represents the strain hardening in the yielding steel elements. The fact that the post-yielding, or post-decompression in the case of the SC-CBF, can be easily increased by increasing the area of the PT elements is a significant advantage of the SC-CBF alone, without even considering the already advantageous flag-shaped hysteretic behaviour it exhibits. An expression can then be setup to check the P-Delta effects for a frame as follows:

$$\frac{\sum k_r^\theta}{H^2} - \frac{mg}{H} \geq 0 \quad (3.30)$$

3.4 Parametric Study

Using the expressions derived in Section 3.3 for the SC-CBF, a parametric study may be conducted to investigate the influence of certain design parameters on the salient response behaviour. To do this, a single storey SC-CBF similar to that shown in Figure 3.1 is analysed, where member sizes are chosen to represent typical member sizes of braced frames used in buildings. These include, European section sizes IPE600 for the beams, HE320B for the columns and 100x100x6.3SHS for the braces. The PT arrangement is chosen to be two no. 30mm diameter strands with a total initial PT force of 500kN.

Some of the response parameters that are of interest are the force, F_3 , defined in Equation 3.3, as this represent the system 'yielding', and force F_5 , defined in Equation 3.6, as this represents the final point on the flag-shaped loop and must be greater than zero in order to achieve the flag-shaped loop, as was outlined in Equation 3.7. Other response parameters include the post-decompression stiffness, K_3 , defined in Equation 3.28, which plays an important role in the self-centering behaviour of the frame. In order to examine the sensitivity of these response parameters, the design parameters that will be examined are the initial PT force, P_{T0} , and the axial stiffness of the PT elements, k_{PT} . These are varied and the sensitivity of the aforementioned response parameters are plotted in Figure 3.6.

As can be seen in Figure 3.6a, the dependence of the pushover force value F_3 increases almost linearly with increasing P_{T0} . This is to be expected as this increasing P_{T0} force will in turn increase the lateral capacity of the PT system and, in turn, the SC-CBF. Figure 3.6b shows the dependence of the force F_5 on the initial P_{T0} , where again it is seen that the condition required for self-centering outlined in Equation 3.7 can be met by altering the initial PT force to ensure the flag-shaped behaviour of the SC-CBF. Figure 3.6c shows the sensitivity of the force

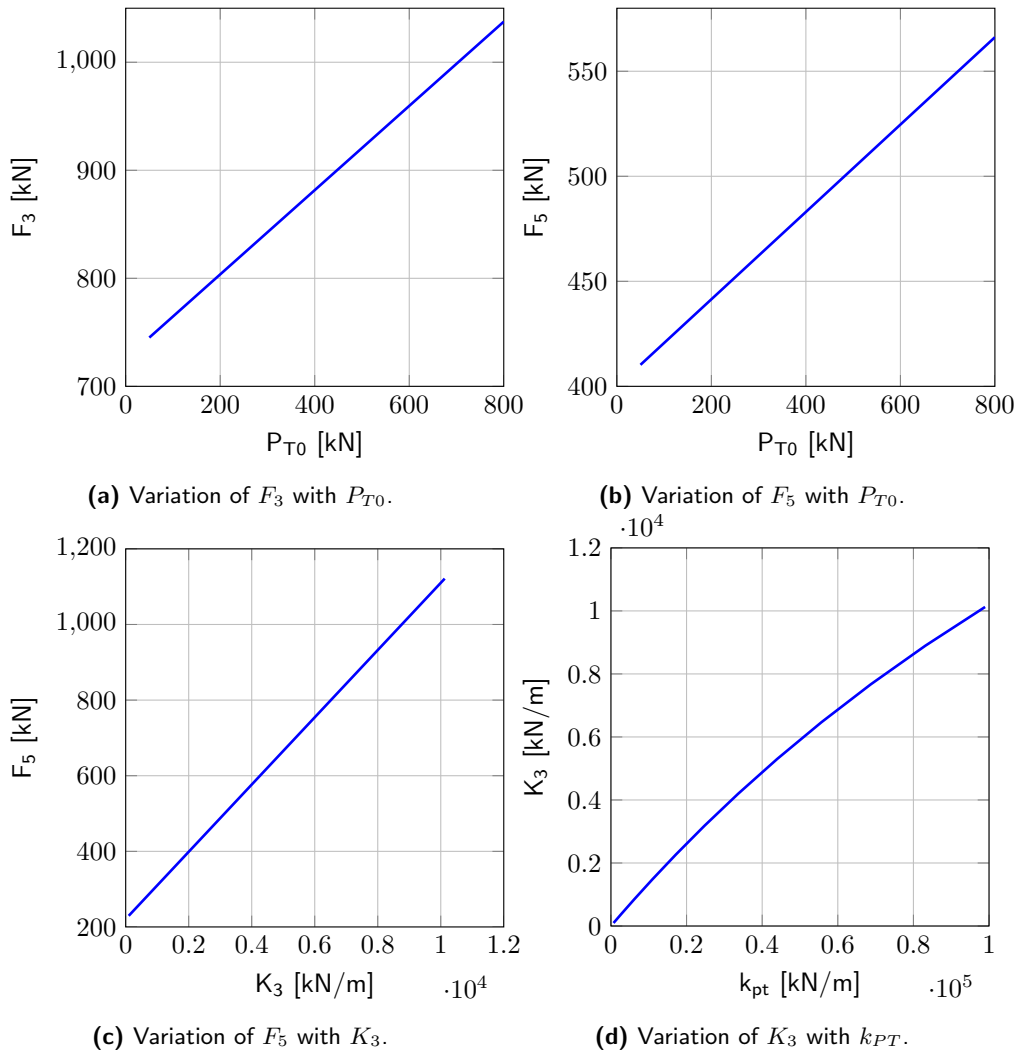


Figure 3.6: Sensitivity of response parameters to design parameters.

F_5 to the post-decompression stiffness, while Figure 3.6d shows the sensitivity of this stiffness to the axial stiffness of the PT elements. This suggests that in order to satisfy the flag-shaped loop condition, the post-decompression stiffness may be altered, but in order to do this another design parameter such as the axial stiffness of the PT elements must be altered.

The result of the plots shown in Figure 3.6 demonstrate that in order to meet the self-centering and flag-shaped loop conditions for the SC-CBF, simple design parameters can be altered to achieve the desired behaviour.

3.5 Summary

This chapter presented the principal concept being developed in this thesis. It was first outlined how the individual systems of both the CBF and the PT system were combined together to give the flag-shaped hysteretic behaviour for the SC-CBF. The detailed behaviour of each of these systems was then discussed, where analytical expressions were developed to describe the complete behaviour of the CBF and the PT system individually and, thus, give equations to describe the

CHAPTER 3. MECHANICS OF SELF-CENTERING CONCENTRICALLY BRACED FRAME

complete behaviour of the SC-CBF. A parametric study was then conducted on some of the variables discussed in the development of the analytical expressions. The study showed how the response parameters of interest are affected by chosen design parameters, which is critical to the correct proportioning of the system to achieve the flag-shaped loop and self-centering behaviour.

CHAPTER 3. MECHANICS OF SELF-CENTERING CONCENTRICALLY BRACED FRAME

Chapter 4

Experimental Setup and Design

4.1 Introduction

This chapter outlines the design and detailing of a physical test setup for the SC-CBF concept described in Chapter 3. This involves testing a SC-CBF with quasi-static pushover cycles in order to demonstrate the anticipated flag-shaped response. A number of removable brace specimens are used in order to carry out numerous tests and, hence, validate the concept. This chapter first describes the layout of the test frame and the specific details that are necessary for the SC-CBF testing. The concept behind the design of the members is also presented briefly with the detailed calculations for the frame available in Appendix A. The chapter finally describes the instrumentation layout in the frame and the testing protocol to which the frame will be tested.

4.2 Overview of the Test Frame

The general layout of the SC-CBF to be tested is shown in Figure 4.1. It consists of a single storey SC-CBF with PT elements located between the beam flanges above and below the storey containing the braces. This is chosen for the test frame as it better represents the behaviour of an arbitrary storey SC-CBF in a multistorey structure. This section describes the test frame and the specific details associated with it. These details are described and justified with reference to similar experimental programs using a similar beam-column rocking connection detail. An outline of the proposed testing sequence is then presented, and the frame is designed accordingly from there.

4.2.1 Layout of the Frame

As previously mentioned, the test frame was chosen as a single storey SC-CBF with PT elements placed in the beams above and below the storey containing the braces to represent a substructure from a multistorey SC-CBF building. Apart from the primary goal of characterising the general behaviour of the SC-CBF and validating the concept, a number of other factors influenced the layout of the test frame. Firstly, the working space of the testing facility at NUI Galway limited the overall size of the frame. Hence a single storey, representative of an arbitrary storey in a multi-storey SC-CBF, was tested to give a better representation of the behaviour of a SC-CBF in a real structure. In addition to geometric constraints, there were also the constraints of the testing equipment. The largest capacity actuator available at the structures testing laboratory at NUI Galway was a 750kN, 250mm stroke actuator. It was necessary to ensure that adequate displacements could be achieved during the experiment to examine the SC-CBF behaviour at

CHAPTER 4. EXPERIMENTAL SETUP AND DESIGN

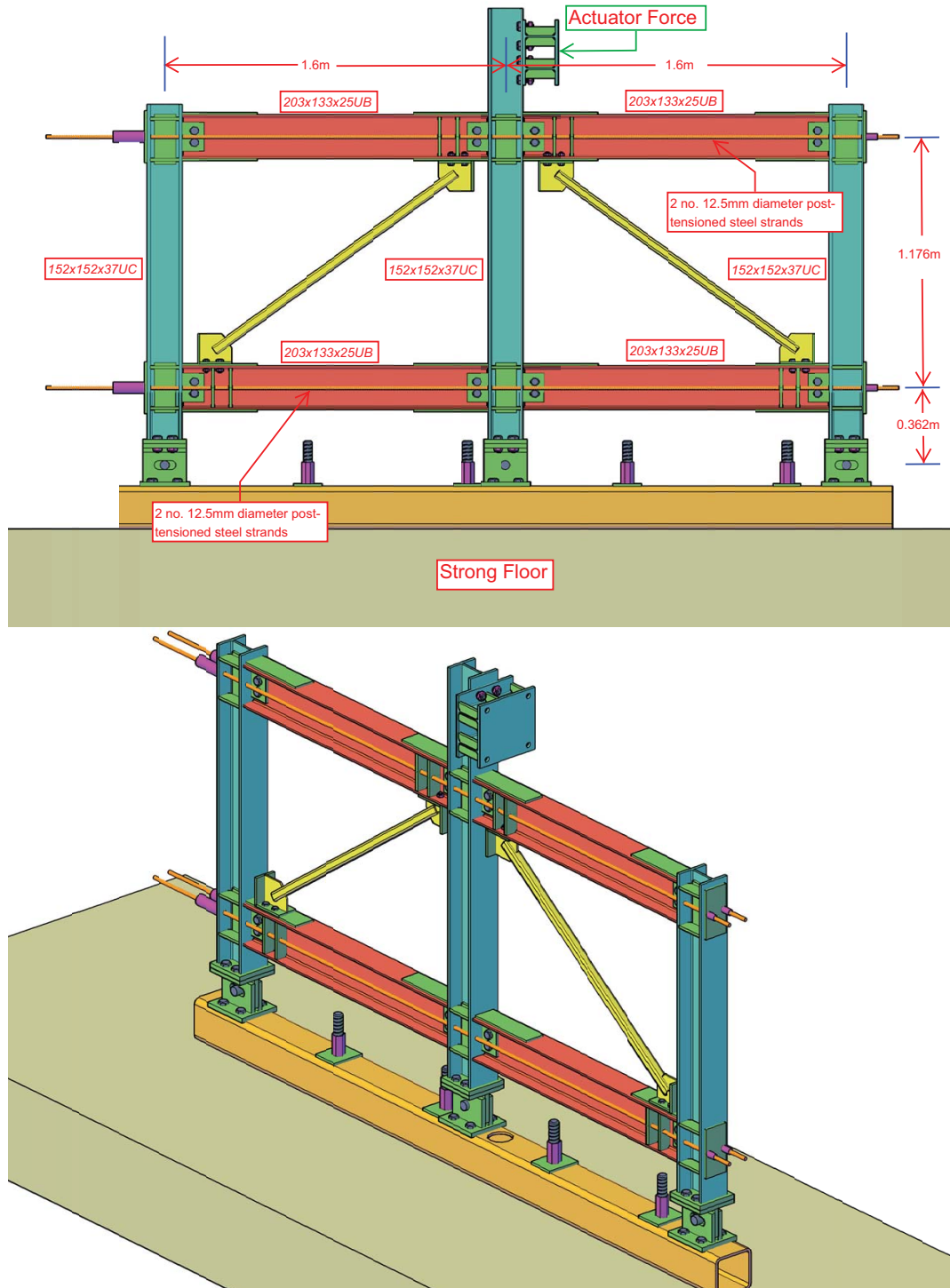


Figure 4.1: Front elevation (top) and general layout (bottom) of test frame.

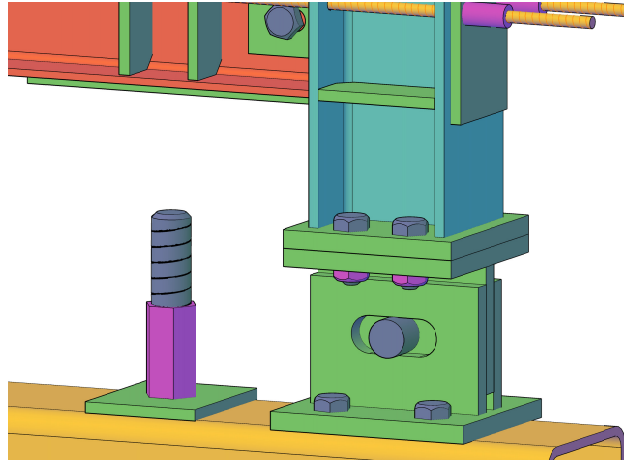


Figure 4.2: Roller connection at outer columns of test frame.

large interstorey drift levels. With these two design issues in mind, a single storey SC-CBF substructure was the most logical option and, hence, was selected as the layout for testing. Figure 4.1 shows a front elevation of the test frame and from this the general concept of the experimental program is shown, which consists two bays of 1.6m and a storey height of 1.176m. More detailed drawings are provided in Appendix B.

4.2.2 Base Connection of the Frame

Since the test frame is that of a single storey SC-CBF substructure representative of an arbitrary storey in a MDOF structure, one particular feature needs to be accommodated. Section 3.3.3 discussed and derived the behaviour of the rocking connection that is used in the SC-CBF. In this discussion, it was highlighted that once the beam-column connection begins to open, the frame as a whole begins to expand due to the connection gap opening. Since the test frame is an arbitrary storey in a structure, this expansion of the SC-CBF needs to be accommodated. This is similar to the testing of a self-centering steel plate shear wall system by Winkley [136]. During this test program of a 1-bay frame, one of the columns was restrained with a pinned connection and the other a pinned roller connection in the direction of loading. The pinned roller connection was designed to accommodate a horizontal translation due to frame expansion from the rocking connection. The amount of translation the connection needed to accommodate was estimated from a numerical model of the test frame. Using the maximum translational displacements recorded in the numerical simulation, the pinned roller connection could be designed to accommodate this translation. For the testing of the SC-CBF, a similar approach to the one used by Winkley [136] was adopted, where the simulation in the OpenSees [86] numerical model to be discussed in Chapter 6 was used to approximate the maximum translation of the two exterior connections. Figure 4.2 shows the general concept of this roller connection, where for the outer column of the frame, the base connection is pinned, but with room for expansion of the frame.

4.2.3 Testing Sequence

Figure 4.1 shows the front elevation of the test frame setup. This frame is to be pushed and pulled laterally by the actuator, which is attached to the top of the centre column. During loading, the compression brace buckles and the tension brace yields, dissipating hysteretic energy, while the rocking frame then provides the bilinear elastic hysteresis that gives the overall



Figure 4.3: Typical connection of brace gusset plate to beam-column connection [79].



Figure 4.4: Beam-only gusset plate connection presented in Berman and Bruneau [10].

flag-shaped behaviour of the SC-CBF. For this test frame, the rocking frame is first to be tested without any bracing members to characterise its bilinear elastic behaviour. Since this rocking frame has a bilinear elastic response, no inelastic behaviour should occur during loading of the rocking frame by itself. Hence, it can be reused for many tests with numerous different braces. In order to make the frame reusable, the brace members must be easily replaced. Hence, they are bolted to the top and bottom flanges of the beams, as opposed to welded which is what is traditionally used. Figure 4.3 shows a typical connection of traditional CBFs to the beam-column connection, where the two edges of the gusset plate are welded to the flanges of the beam and column.

Another development in the connection of braces is presented in Berman and Bruneau [10], where a buckling restrained brace is connected to the beam only. This connection type, shown in Figure 4.4, is the type of connection that is used in the design of SC-CBFs, where the gap opening of the beam-column connection is not restrained by a gusset plate that is welded in place to the surrounding frame. As with the gusset plate shown in Figure 4.4, the gussets used in the test frame presented here are bolted to the beam, rather than welded. This means that a set of braces are easily attached and removed from the frame for testing. Using this rocking frame, a number of different braces can be used and tested to examine the behaviour of the SC-CBF with braces of different cross sectional sizes.

Table 4.1 gives a list of the proposed braces to be tested and the corresponding normalised slenderness (λ) of each, which are based on the nominal properties of the specimens. Each brace type has two specimens to be tested, hence, 8 brace tests and 1 bare frame test are to be conducted, giving a total of 9 tests. For the calculation of the slenderness, an effective length coefficient of 1.0 is used, as was suggested by Lehman et al. [81]. From Table 4.1, it can be

seen that the slenderness range of the braces tested ranges from 1.03 to 2.21, which covers the range of slenderness values permitted by EC8, with the most slender brace falling just outside the range. It is necessary to examine the behaviour of slender braces in a SC-CBF setup, as more slender braces are preferred for this arrangement due to their higher fracture ductility. In addition, it is necessary to ensure that all section sizes chosen are of Class 1 classification, as per Eurocode 3 [20], as this classification is a requirement for high ductility class CBF structures in Eurocode 8 [18]. Furthermore, the flag shaped loop of the SC-CBF is dependent on the compressive contribution of the braces, where no buckling of the braces would result in the flag shaped hysteretic loop not being achieved.

Table 4.1: Details of braces to be tested.

Specimen ID	Section Size	Grade	$\bar{\lambda}$	Testing Sequence
B1	20x20x2.0 SHS	S235	2.21	1, 4
B2	25x25x2.5 SHS	S235	1.70	2, 3
B3	30x30x2.5 SHS	S235	1.39	5, 7
B4	40x40x4.0 SHS	S235	1.03	6, 8

4.3 Design of Test Frame

The detailed calculations for the final design of the test frame are given in Appendix A, whereas this section is limited to the discussion of the final design.

4.3.1 Beams and Columns

The final member sizes for the beams and columns were chosen to be 203x133x25UB and 152x152x37UC for the beams and columns, respectively. UK section sizes were chosen due the availability of these sections in Ireland at the time of testing. Ideally, European H and IPE sections or American W-sections would be used as these would correspond to the section sizes that would be available in countries where systems such as the SC-CBF would be employed. However, the sections chosen have very similar sizes to sections used in Europe, so it is concluded that using UK sections will have no implications on the performance of the frame.

4.3.2 Beam Shear Connection

Since it is intended that the beams in the SC-CBF will be allowed to rock freely against the face of the column to provide the self-centering behaviour of the PT system, there must be no moment resistance in the connection of the beams and columns. However, this still leaves the problem of transferring the shear force from the beams to the columns. In other similar systems, such as the self-centering frame developed by Christopoulos [29], this relied on the shear resistance provided by the friction between the beam flanges and the column face, with the energy dissipating couplers placed at the beam flanges doubled as a safety measure in the case of the friction resistance being exceeded. While there is some resistance provided by this friction interface, large shear forces are being transferred from the vertical component of the brace axial forces to the columns, which results in large shear forces acting through this connection. Therefore, a special shear tab is designed in Appendix A.3 to transfer this shear force from beam to column but also permit the rotation of the beam against the column, via slotted bolt holes. The layout of this shear tab is shown in the detailed drawings in Appendix B.

4.3.3 Beam Flange Reinforcement

During rocking of the beam against the face of the column at maximum drift, there will be effectively one flange of the beam in contact with the column. Hence, it is necessary to ensure that the flanges of the beams have adequate capacity to transfer the axial forces in the beams across the joint. This is done by adding beam flange reinforcement to the top and bottom of the beams. These reinforcement plates will need to be sufficiently wide to allow connection of the braces to the beams later, but also allow a space in which a weld from the plate to the beam flange can be placed.

It is also necessary to ensure that no local yielding occurs at the beam flanges during rocking, as observation from testing by Garlock [51] reported that local yielding in the beams would be detrimental to the intended behaviour of the self-centering frame. This is also true for the beam webs, where local yielding or buckling of the beam webs will cause a sudden loss in PT force. During testing by Winkley [136], this problem of web yielding was mitigated by keeping the beam web away from the column face by inserting shim plates between the beam flanges and column face, thus the beam web does not come into contact during rocking. A similar but alternative method is employed in this test setup, where instead of inserting more plates to keep the beam webs at a distance from the column face, an 8mm notch has been cut back into the beam web to keep it at a distance from the column face. It is envisaged that this notch will have the same effect as inserting plates between beam flanges and column. On the other hand, it simplifies the fabrication process.

4.3.4 Panel Zone Reinforcement

During rocking of the connection, there are large forces acting across the panel zones of the columns. Backing plates have been inserted in the column webs to transfer the force of the beam flange into the column. In addition, it is necessary to check the panel zone behaviour of the connection and ensure that the column remains completely elastic during loading.

4.3.5 PT Strands and Anchorage

The location at which the PT elements are connected to the test frame are its anchor points. The two critical parameters associated with this are the spacing of the PT strands and the anchorage points. The spacing of the PT elements is important as up until now, these PT elements have just been idealised as a single element along the centreline of the beam. These PT elements are then placed symmetrically about the centre of the beam to avoid any eccentric action. The spacing of the elements is then important as to not interfere with any of the other elements of the system, such as the beam shear tab, and also to allow for sufficient space for two load cells to be placed adjacent to one another to monitor the force in the PT strands during testing. As a result of this, it was chosen to space these PT elements 90mm apart. In addition to this spacing, a 12mm plate is also attached to the anchor points to avoid any local yielding of the column flange under PT forces.

The actual PT strands selected consist of 7-wire standard strand with 12.5mm nominal diameter typically used in concrete prestressing, for which details can be found in BS 5896:1980 [14]. The anchorage system used is shown in Figure 4.5, which consists of a set of grips that hold the PT strands in place and maintain the load. However, these anchors shown in Figure 4.5 are temporary anchors and will gradually lose the initial load over time. This was deemed satisfactory for the testing, as it will occur over a short time period, but for future use, more



Figure 4.5: PT anchorage system used in test frame.

Table 4.2: Brace details.

Specimen		B1	B2	B3	B4
Section		20x20x2.0SHS	25x25x2.5SHS	30x30x2.5SHS	40x40x4.0SHS
A	mm^2	134	209	259	535
b	mm	20	25	30	40
t	mm	2.0	2.5	2.5	4.0
Class		1	1	1	1
L	mm	1437.6	1435.1	1432.6	1395.3
$\bar{\lambda}$		2.12	1.70	1.39	1.03

permanent anchor systems may be sourced for use in the SC-CBF system. The initial force that is to be installed in these strands was chosen to be 80kN, as this was deemed to be sufficient to demonstrate the flag shape for all specimens, but also enough so that the strands were well below their breaking load, as stated in BS 5896:1980 BSI [14].

4.4 Specimens

This section describes the properties of the specimens to be tested and the design of the gusset plates used for each of these specimens.

4.4.1 Braces

As previously mentioned, four grade S235 hot-rolled steel square hollow section (SHS) sizes manufactured in accordance with EN 10025:2004 [19] are selected for this experiment. Some details of these braces are shown in Table 4.2, with a more detailed table given in Table C.1 of Appendix C. From this table, it is seen that the slenderness ranges from 1.03 to 2.21, which covers the range of slenderness values permitted in Eurocode 3 [20]. The lengths of these braces are taken as the lengths of the tubular section that forms each brace given on the detailed drawings shown in Appendix B, where the effective length factor k is taken to be 1.0.

4.4.2 Gusset Plates

Since the gusset plates used here are not the same as traditional gusset plate connections, as shown in Figure 4.3, an alternative method of connecting the braces to the beams is employed. This consists of using the gusset plate type shown in Figure 4.4, where the gusset plate is designed using conventional design methods, but it is provided with a vertical stiffener to replicate

CHAPTER 4. EXPERIMENTAL SETUP AND DESIGN

conventional gusset plates. It was initially intended to use gusset plates that had no stiffeners attached to the free vertical edge and design these gusset plates according to the experimental and numerical findings of English [46]. However, at the time of design of the frame, sufficient evidence and verification work had not been carried out to justify the use of free edge gusset plates. This is because the primary goal of this experiment is to investigate the performance of the SC-CBF's self-centering behaviour and validate the concept, and not the behaviour of the gusset plates. It was therefore decided to use a connection type that had been developed and tested, such as the work by Berman and Bruneau [10], where the gusset type shown in Figure 4.4 has been tested when used to connect buckling restrained braces to a surrounding test frame.

These gusset plates were designed using the elliptical clearance method presented in Roeder et al. [103], and the following checks for each gusset plate are presented in Table C.2.

- Whitmore yielding.
- Block shear.
- Whitmore fracture.
- Thornton buckling.
- Free edge length
- Net section fracture
- Weld lengths.

The final dimensions for each gusset plate are shown in the drawings presented in Appendix B, where the additional vertical stiffener is shown, as per the gusset plates used by Berman and Bruneau [10].

4.5 Coupon Specimen Design

In addition to the testing of the SC-CBF frame, it is necessary to perform a number of coupon tests on the specimens to characterise the actual material strength, as oppose to the characteristic material strength. This is done by testing a number of samples from the offcuts, which were supplied along with the test specimens, and cut up into small samples and tested prior to full testing on the full frame. The coupon testing was performed on the samples cut from the section sizes listed in Table 4.1 in accordance with EN 10002-1:2001 [17].

Since the B4 brace specimen had a wall thickness equal to or greater than 4.0mm, it was sized using the provisions outlined in Annex D of EN 10002-1:2001 [17], and since the remaining 3 brace specimens had a wall thickness less than 4.0mm, these were sized using Annex B of the same standard. The dimensions of the coupons that were cut from each specimen are given in Table 4.3. Typically, EN 10002-1:2001 [17] states that coupons are to be cut with a certain width for the gauge lengths and a wider width for the ends that are to be gripped by the testing apparatus. However, since the specimens to be tested are of small size, it is not possible to cut the coupons to this shape and to the required tolerance. Hence, EN 10002-1:2001 [17] allows the use of single width coupons specimens. Since each of the off-cuts that were received from the manufacturer were 600mm long, it was possible to cut 3 coupons from each face of the section size. This resulted in 12 coupons for each brace size and a total of 48 for all section sizes.

The drawings for the coupon specimens, together with mill certificates supplied by the fabricator, are attached in Appendix D.

Table 4.3: Details of coupons cut from each brace section.

Specimen ID	Section Size	B	t	L_0	L_t
		[mm]	[mm]	[mm]	[mm]
B1	20x20x2.0 SHS	12.0	2.0	95.0	200.0
B2	25x25x2.5 SHS	15.0	2.5	95.0	200.0
B3	30x30x2.5 SHS	15.0	2.5	95.0	200.0
B4	40x40x4.0 SHS	20.0	4.0	95.0	200.0

4.6 Loading Protocol

4.6.1 Coupon Testing

The loading protocol that is used for the coupon specimens is also stipulated by EN 10002-1:2001 [17], where it consists simply of a pull straight to failure test, rather than cyclic loading. CEN [17] specifies the allowable loading rates to be used for the specimens, where a slow loading is used for the initial elastic and yielding region of the stress strain curve, followed by a faster strain rate when the specimens have yielded. Each of the specimens had a gauge length of 95mm, which was set in the test machine and remained constant throughout the test. This was used to determine the loading rate for the specimens, which was set at 0.024mm/sec up to an extension of 4mm and then 0.475 mm/sec until fracture. This corresponded to a strain rate of 0.00025s^{-1} and 0.005s^{-1} as per EN 10002-1:2001 [17].

4.6.2 Test Specimens

The loading that is used for the testing of the specimens in the test frame is a cyclic loading history stipulated by ECCS [42]. This consists of a number of cycles that gradually increase until failure of the specimens. The loading protocol is dependant on an estimate of the yield displacement as the amplitude of its cycles are defined as multiples of this. Using this estimate the cycles are defined as follows:

- One cycle at a ductility of 0.25.
- One cycle at a ductility of 0.50.
- One cycle at a ductility of 0.75.
- One cycle at a ductility of 1.00.
- Three cycles at a ductility of 2.00.
- Three cycles at a ductility of $2n+2$, where $n=1, 2, 3 \dots$

Using the estimate of yield displacement obtained from the coupon testing prior to specimen testing, the ductility levels to be input into the testing control system can be estimated for each specimen individually. This is shown in Figure 4.6 up to a ductility of 6, where the actual testing will proceed in a similar fashion until the specimen has fractured.

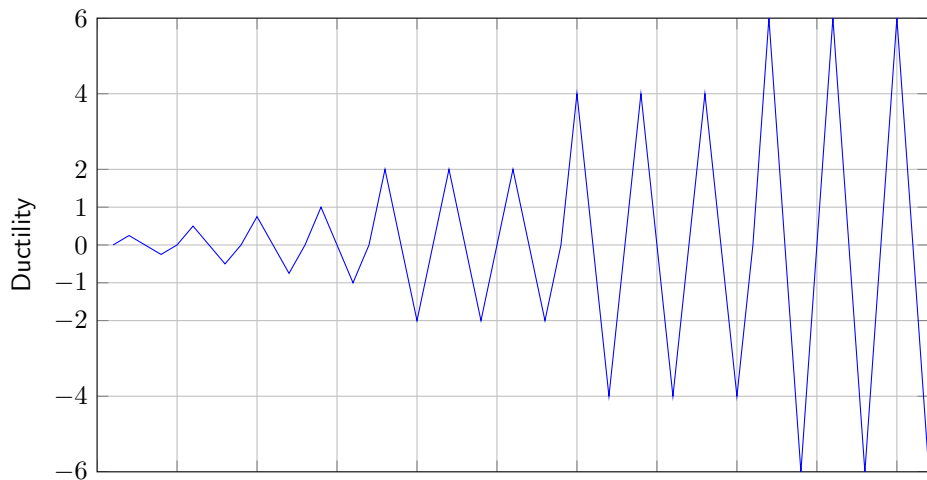


Figure 4.6: Waveform of the ECCS loading protocol as per ECCS [42].

4.7 Instrumentation

The decision of the final instrumentation layout is influenced by two variables - the required ordinates to be recorded from each test and the availability of instruments and software to record them. Since there are many ordinates that are of interest in this test frame, the main ones for which the instruments are designed to reflect are:

- Pushover force and roof displacement.
- Beam-column connection gap opening.
- Forces in PT strands.
- Expansion of base roller connection.
- Beam and column member strains.
- Brace strains.
- Brace out-of-plane movement.
- Stiffness of the laboratory reaction frame.

A summary of the instrumentation employed is given in Table 4.4 with their locations indicated in Figure 4.7. Each of the aforementioned ordinates are to be recorded in each test and will be reported in the Chapter 5. However, firstly a brief outline of reasons for considering the aforementioned ordinates is given.

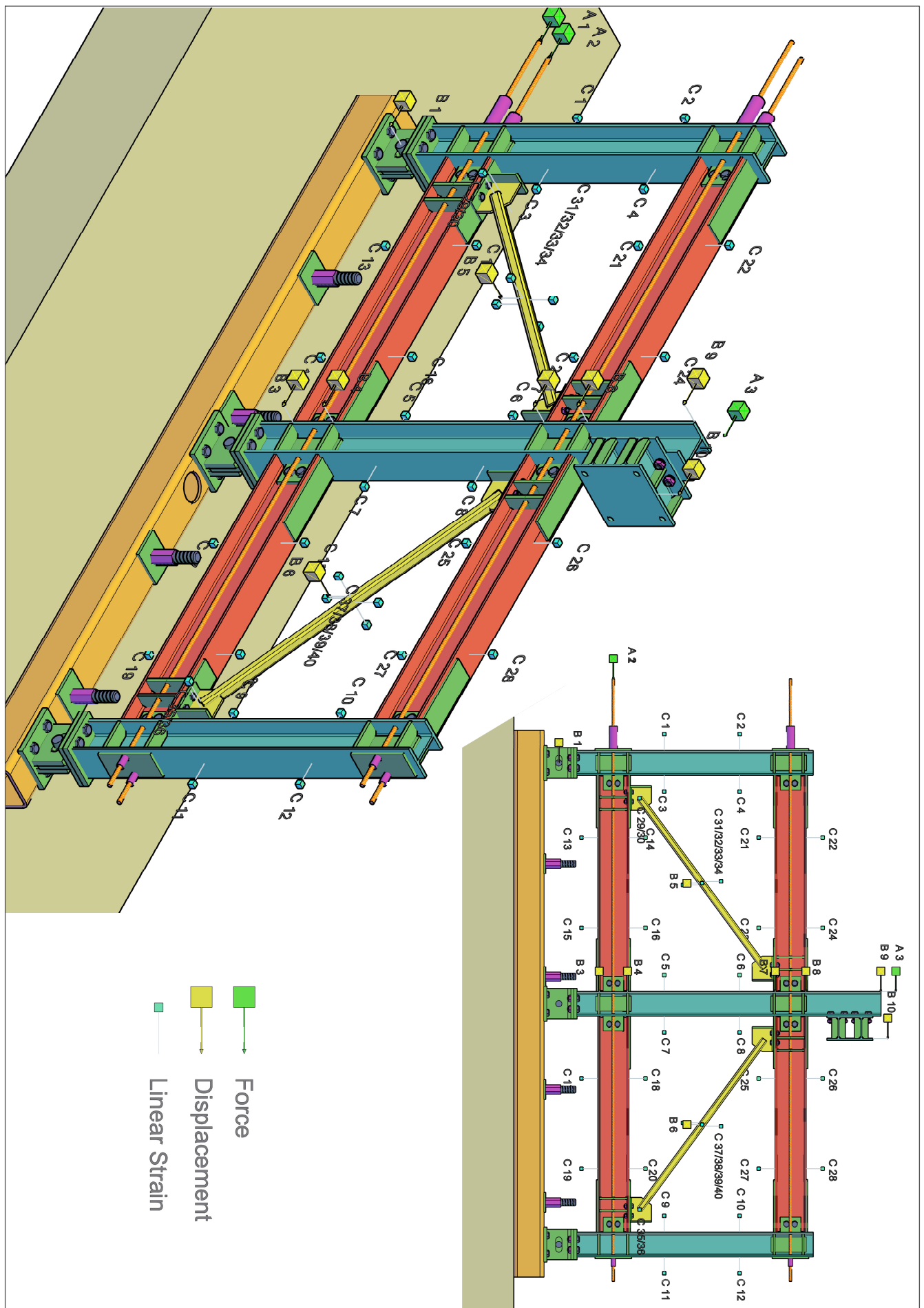


Figure 4.7: Layout of the test frame instrumentation.

CHAPTER 4. EXPERIMENTAL SETUP AND DESIGN

Table 4.4: Test frame instrumentation details.

Instrumented Area Label	Instrument ID	Load Cells A	LVDT B	Strain Gauges C	Channels
PT Strands	A1-A2	2			2
Reaction Frame	B10		1		1
Roller Connections	B1		1		1
Beam-Column Gap	B3-B4, B7-B8		4		4
Actuator Force	A3	1			1
Actuator Displacement	B9		1		1
LHS Column	C1-C4			4	4
Centre Column	C5-C8			4	4
RHS Column	C9-C12			4	4
Lower LHS Beam	C13-C18			4	4
Lower RHS Beam	C17-C20			4	4
Upper LHS Beam	C21-C24			4	4
Upper RHS Beam	C25 C28			4	4
Brace Net Section LHS	C29			2	2
Brace Net Section RHS	C30			2	2
Brace Midpoint RHS	B5, C31-34		1	4	5
Brace Midpoint LHS	B6, C35-38		1	4	5
Total					52

Pushover force and roof displacement

It is necessary to record the pushover force and displacement as is measured in the load cell and linear variable displacement transducer (LVDT), respectively, of the 750kN actuator for two reasons. Firstly, to be able to record the specified displacements and the resulting force to monitor the system during testing to ensure the expected performance of the system is similar to that predicted. Secondly, to be able to plot the response of the frame and demonstrate the flag shaped behaviour of the test frame, which is fundamental to the SC-CBF's behaviour.

Beam-column connection gap opening

The gap opening of the beam-column connection is again fundamental to the behaviour of the SC-CBF, as it is the opening of these gaps that cause the increase in the force in the PT system, which then forces the system to re-center. By recording the displacement of the top and bottom flanges of both upper and lower beams relative to the central column, this gap opening can be observed. Furthermore, the connection rotation, which also corresponds to the interstorey drift of the frame, can be calculated.

Force in PT strands

Since the gap opening behaviour at each of the beam-column connections causes an increase in PT force, which ultimately gives the SC-CBF its self-centering behaviour, it is necessary to monitor the force that develops in these. This is useful to demonstrate the concept of the gap opening connection, but it is also used as a safety measure. While the tests are to be carried out, the force in the strands are to be monitored to ensure that the breaking load, as specified by BS 5896:1980 [14], is not exceeded. If it is observed that the force being generated by the strands is higher than the predefined limit of 75% of the breaking load, the test is to be stopped

to avoid the possibility of strand fracturing. In addition to this, the gradual losses in the PT strands can be monitored, as the anchorage systems used are intended to be temporary anchors and, hence, the force is anticipated to drop gradually between tests.

Expansion of base roller connection

Since the test frame is idealised to represent an arbitrary storey in a multi-storey building, the connection at the base of the frame was detailed in order to best represent this. This was achieved by allowing the outer columns space to expand during testing, as is anticipated due to the gap opening behaviour of the frame. Hence, it is necessary to monitor the roller connections displacement to demonstrate the frames expansion during tests.

Beam and column member strains

As the primary goal of the test is to demonstrate that SC-CBF can undergo numerous horizontal cycles, which yield and damages the brace specimens, while the rest of the structure remains elastic and returns to its original position, the strains generate in the beams and columns are of interest. This is firstly to monitor that these elements do not exceed their yield strains and remain elastic during the tests, but also to calculate the forces within these elements. This is done by monitoring the strains in opposite flanges at the same location to which the section forces can be obtained. From here, the bending moments and shear forces can be estimated for each member.

Brace strains

Since the brace members are expected to yield in tension and buckle in compression, the strains in the braces are recorded to demonstrate this. The gauges are placed at midpoint of the brace and at the net section. The gauges at the net section are placed there as this region is expected to remain elastic and the large deformations associated with local and global buckling, which are expected to occur at the midpoint of the brace, are not expected to occur here.

Brace out-of-plane movement

When the brace members experience global buckling while subjected to compressive axial loading, the gusset plates are designed to force them to buckle out of plane. This can be problematic in an actual building in terms of non-structural components and the allowance of sufficient space to permit buckling to take place freely, as was discussed in Section 2.2. The out-of-plane lateral deformation of the braces is recorded to demonstrate this and also to later validate models that are used to show this for future designs.

Stiffness of the laboratory reaction frame

It was observed that during a previous test setup at the same test facility at NUI Galway, the reaction frame from which the actuator is supported has a certain degree of lateral flexibility. Subsequently, additional elements were employed in the frame to increase its lateral stiffness. Nevertheless, the relative lateral displacement of this frame is recorded such that this measured lateral stiffness of the frame can be accounted for when evaluating test data.

Considering these, and the availability of instruments and channels in the data acquisition system, the final test frame instrumentation is listed in Table 4.4, where the labels listed here are shown along with their location in the diagram of the test frame in Figure 4.7. This results in a total of 52 channels to be recorded during each test.

4.8 Summary

This chapter presented the design and layout of the proposed test frame of a SC-CBF, which is shown in Figure 4.8 setup in the structures laboratory in the Engineering Building at NUI Galway prior to any testing. The general design concept of the frame was first discussed with issues such as the frame layout and base connection presented. These were important parameters as it is necessary to create a representative sample of the SC-CBF frame that had adequate boundary conditions which reflected the actual behaviour in multi-storey structures.



Figure 4.8: Final test frame setup in the lab at NUI Galway prior to testing.

The design details of the various elements of the test frame was discussed along with the relevant documentation included in Appendices A, B and C. The brace specimens, as well as the gusset plates, were described in detail, as these form the principal difference between each of the tests to be carried out. Coupon specimen design and sizing was discussed along with the loading protocol for these specimens. The loading protocol to be used for the main testing is presented, where it is seen the that this consists of repeated cycles of increasing amplitude until failure of the specimens occurs. Finally, the instrumentation layout is presented, where it was seen that a total of 52 channels are to be recorded during each test, with ordinates from both the test frame and test specimens to be logged.

Chapter 5

Experimental Results and Observations

5.1 Introduction

This chapter describes the findings from testing of the SC-CBF test frame under quasi-static loading for a range of specimens. The material testing carried out on the coupons cut from the specimen off-cuts is first reported, followed by the substructure testing carried out on all the specimens in the test frame.

Testing is performed on the coupons and the actual values for the yield strength and Young's modulus are reported for each brace section. For the specimen testing, a description of each individual test is provided along with any observations recorded during each test. The input displacement cycles, some plots of the test results and other observations made during the testing are reported.

5.2 Coupon Specimen Testing

5.2.1 Test Setup

The coupons were cut and labelled according to the following system, C(1)(2)(3). Here (1) corresponded to the section ID, where 1, 2, 3 and 4 represented specimens B1, B2, B3 and B4, as seen in Table 4.3. (2) represented the face from which each of the coupons were cut and starting at the face with the seam weld, were labelled A, B, C and D in a clockwise fashion. The last number, (3) corresponded to which number from that face was cut, as three coupons were cut from each face of each brace.

The specimens were tested using an Instron 8500 Digital Control Test Machine (Figure 5.1) and were tested to failure. Prior to testing, the exact specimen dimensions were measured using a vernier callipers, and are presented in the results. As reported in Section 4.6.1, each specimen had a gauge length of 95mm, which was set in the test machine and remained constant throughout each of the tests, and was used to calculate the loading rate for the specimens.



Figure 5.1: Instron 8500 Digital Control Test Machine.

5.2.2 Specimen Results

From the coupon testing, a number of parameters are obtained. The first of these was the final width and thickness (b_f and t_f) of the coupons where necking fracture had occurred. The percentage reduction of the cross section area (Z) is then reported by expressing the difference in necking cross sectional area (S_u) and original area (S_0) as a percentage of the original area. Also reported, is the percentage elongation at fracture (A), which expresses the extension at fracture as a percentage of the original gauge length. Using the stress-strain plots that are obtained from the loading apparatus, the initial modulus (E), 0.2% proof strength (f_y) and maximum strength (f_u) of each of the coupons are obtained. An example plot of the stress-strain obtained from the C2D1 specimen is shown in Figure 5.2.

The full set of results and measurements from each of the specimens along with the mean values for each are shown in Tables E.4 - E.1 of Appendix E. Photographs of the fractured specimens are shown in Figures 5.3.

Final values for the yield strength, ultimate strength and Young's modulus are to be reported. Table 5.1 compiles the average values for yield strength, f_y , modulus of elasticity, E , and ultimate strength, f_u , from coupon testing for each brace cross-section, where the yield strength is the 0.2% proof strength, as defined by CEN [17]. It can be seen that the actual material strength of the braces is higher than the nominal strength expected from S235 steel, which is 235 MPa. For the Young's modulus values reported from this coupon testing, it is believed that due to the uniform width of the coupon specimens, yielding was not only confined to the intended distance between the grips in the test machine shown in Figure 5.1, but also within the grips of the machine, as was observed in a number of tests.

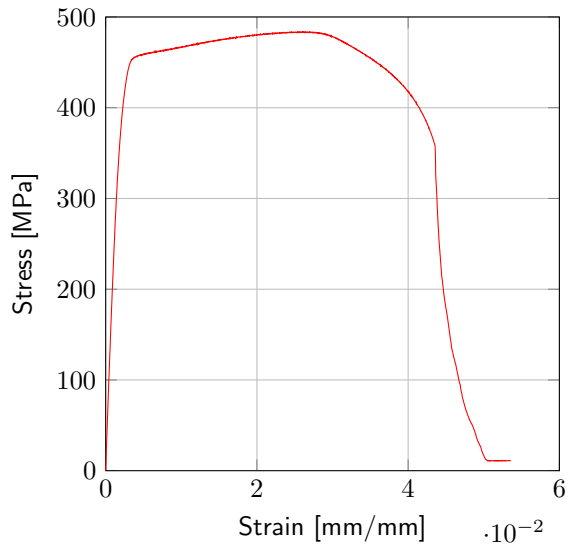
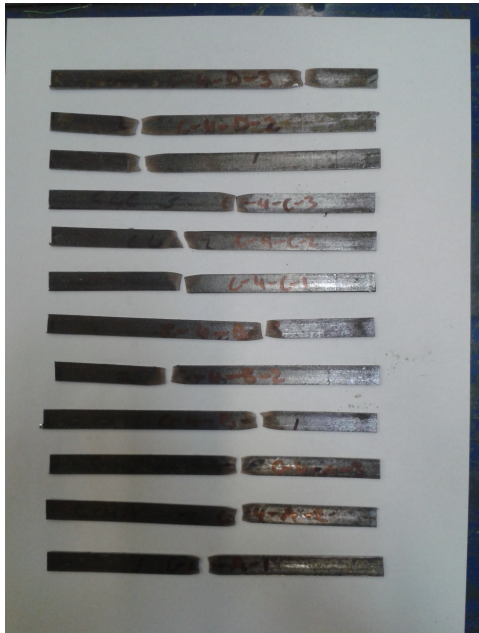


Figure 5.2: Example stress-strain plot for coupon C2D1.

Table 5.1: Summary of test results for all coupons.

Specimen ID	Specimen	f_y [MPa]	E [GPa]	f_u [MPa]
C1	20x20x2.0 SHS	433.34	231.11	437.05
C2	25x25x2.5 SHS	469.22	216.83	493.92
C3	30x30x2.5 SHS	449.37	214.82	469.57
C4	40x40x4.0 SHS	411.21	163.06	428.66

CHAPTER 5. EXPERIMENTAL RESULTS AND OBSERVATIONS



(a) Fractured C1 specimens.



(b) Fractured C2 specimens.



(c) Fractured C3 specimens.



(d) Fractured C4 specimens.

Figure 5.3: Fractured coupon specimens.

5.3 Specimen Testing

5.3.1 Overview

A total of nine tests have been carried out on the test frame which consists of eight brace specimens and one bare frame test, which are detailed in Table 5.2. This section will present the results of each test in the order in which they were tested and describe the loading and observations from the test along with the plots of the following, when available:

1. Pushover force versus drift.
2. Post-tension (PT) force versus drift.
3. Beam-column gap opening versus drift.
4. Moment-rotation due the PT elements at the beam-column connection.
5. LHS brace out-of-plane (OOP) displacement.
6. RHS brace out-of-plane (OOP) displacement.

The strain gauge data from each of the brace specimens tested (C29 to C40, as per Table 4.4), are plotted in Appendix F, and are not discussed in this chapter. The abbreviations in the legends of the plots of the gap opening refer to the position of the instrument on the frame (Figure 5.4) and stand for lower beam bottom flange (LBBF), lower beam top flange (LBTF), upper beam bottom flange (UBBF) and upper beam top flange (UBTF). This notation will be used throughout the reporting of these results.



Figure 5.4: LVDT instrumentation on upper beam-column connection.

Table 5.2: Summary of test specimens.

Specimen ID	Brace Section Size
B0	-
B1A	20x20x2.0 SHS
B1B	20x20x2.0 SHS
B2A	25x25x2.5 SHS
B2B	25x25x2.5 SHS
B3A	30x30x2.5 SHS
B3B	30x30x2.5 SHS
B4A	40x40x4.0 SHS
B4B	40x40x4.0 SHS

The drift values in the plots described above are calculated based on the gap opening at the connection and corresponds to the interstorey drift, or rotation of the storey and are calculated as follows:

$$\theta = \frac{\delta_t - \delta_b}{b_h - t_f} \quad (5.1)$$

where t_f is the thickness of the beam flange and δ_t and δ_b are the gap openings measured at centre of the top and bottom flanges of the beam, respectively.

This is done as initial testing of the frame showed a degree of flexibility associated with the test setup that was causing skewed results when the actuator displacement was used for the plots. This flexibility was caused by the looseness in various parts of the frame that were identified during preliminary tests. Efforts were made in the preliminary test runs to reduce the effects these sources of error had on the results, (e.g. manufacturing new pins with tighter tolerance for the base connections), such that useful data was still obtained.

5.3.2 Specimen B0

Description of the Test

The first test that was carried out was titled B0, as it corresponds to the bare frame and contains none of the brace specimens listed in Table 5.2. This was in order to first determine the behaviour of frame with the PT elements installed, and demonstrate the bilinear elastic behaviour of the frame. Thus, when combined with diagonal braces, the energy dissipation of the braces and the self-centering of the PT system can be distinguished.

Displacement Cycles and Loading Rate

Since there are no yielding elements in the bare frame test, it is not possible to calculate the displacements required from the ECCS loading protocol. It was then decided that the yield displacement for the first specimen test be used as a reference, which was B4B. This resulted in a cyclic loading up to the ECCS ductility cycle of 26 and was loaded at a rate of 0.5mm/s.

Plots of Test Results

Figure 5.5 shows the plots of the data obtained from the test, as previously outlined. The OOP displacement of the braces are omitted as there are no braces employed in this frame. Figure 5.5a shows a plot of the pushover force against drift of the frame, where the frame experienced a maximum drift of 1.78%. It is seen that the hysteresis of the frame is a bilinear elastic response with very little energy dissipation due to the elements remaining elastic, where the small amount of area under the curves shown in Figure 5.5a is due to the friction and flexibility of the test frame setup. This plot demonstrates the behaviour of the frame is close to what is anticipated in Chapter 3, where the only difference is a slight unexpected kink in the pushover force versus drift response plot at approximately -0.25% drift. This behaviour occurs in only one direction of the testing and is not believed to be a characteristic of the self-centering frame, but rather a consequence of the sources of error encountered in this test setup, which are discussed in Section 5.5.

Figure 5.5b shows a linear variation in PT force against drift, where it is seen that the increase in drift causes an increase in the PT force due to the gap-opening behaviour of the frame. This gap opening of the frame is further demonstrated in Figure 5.5c, where the gap opening at the frames flanges is clearly seen. This shows the rocking behaviour of the connections in the frame and that this rocking of the connection results in an increase in the PT force. Figure 5.5d shows a plot of the connection moment due to the PT system versus drift. This plot

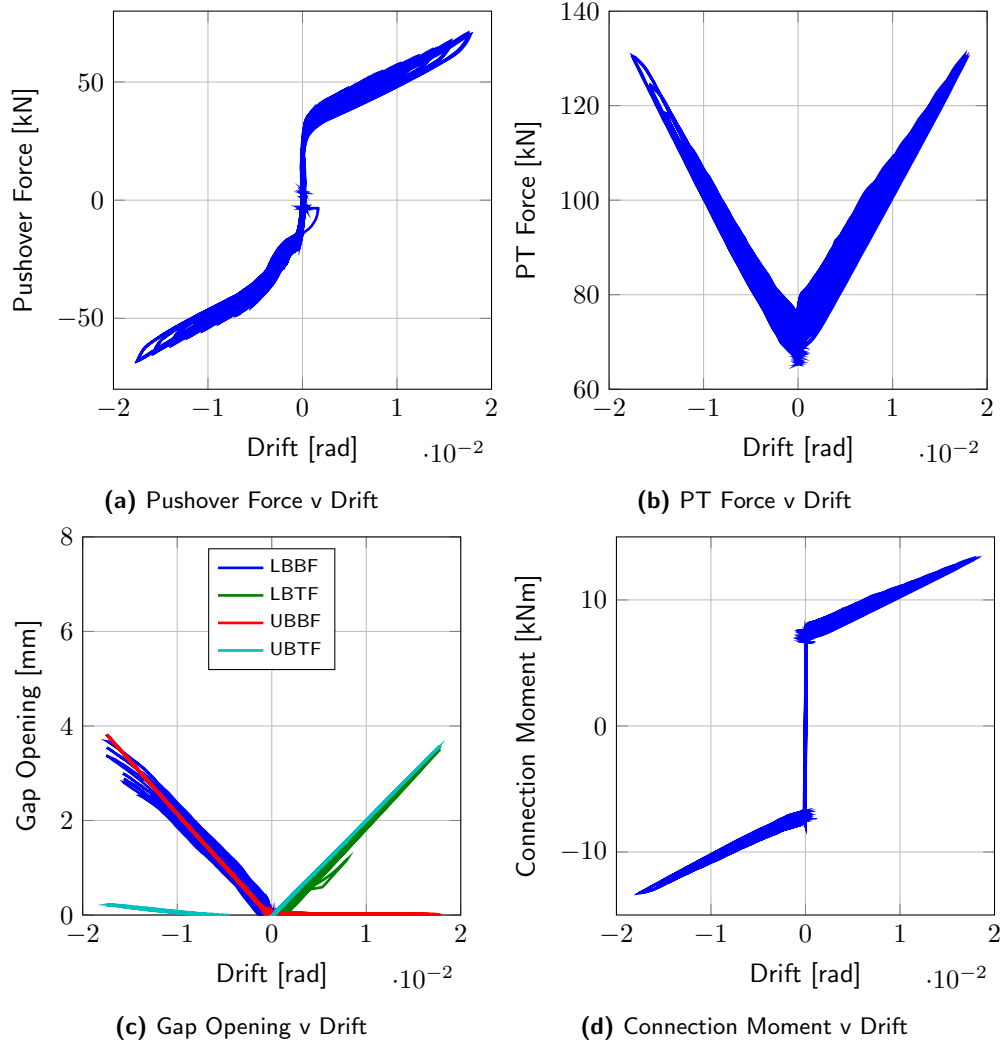


Figure 5.5: B0 test results.

shows that a moment of approximately 8kNm is required to open the connection and allow the frame to displace horizontally beyond the initial elastic deformation of the PT frame. This is in line with the theory developed in Chapter 3, where the term decompression moment was used to describe this moment required to allow the beam-column connection to open. The initial deformation of the PT frame is relatively little in comparison to the displacements that are experienced by the frame after decompression, whereby using the OpenSees model that will be discussed and compared to this test data in Chapter 6, the gaps at the beam flanges begin to open at a pushover force of 33.4kN, which can be seen in Figure 5.5a, where the total horizontal displacement of the frame at this point is 1.27mm. Since the PT frame behaves essentially as a MRF up until decompression, this displacement of 1.27mm should correspond to that of an equivalent MRF with fully rigid connections. It is seen that an equivalent MRF with the same section sizes as the SC-CBF displaces 1.45mm horizontally when a 33.4kN lateral force is applied to it. Hence, it can be concluded that the initial elastic deformation of the SC-CBF is due to the elastic response of the PT frame, and is very small in comparison to the displacement beyond connection decompression.

Test Observations

During this test, it was observed that there was a degree of unintended movement in the test frame. This was partly due to the pinned and roller connections at the base not being perfect pinned conditions. Efforts were made to reduce the effect, for example, by fabricating new pins with a tighter fit to reduce any looseness in the connection. However, a relatively small degree of flexibility persisted and was accounted for during the remaining tests. Secondly, it can be seen in Figure 5.5b that the PT force in the strands is gradually decreasing during the test by roughly 5 to 10kN. This was thought to be due to the frame being tested at high displacement cycles for the first time. A loss of 10kN in the strands would correspond to a shortening of 0.88mm (i.e a change in strain of $275\mu\epsilon$) between the two anchor points, and since the frame is being tested for the first time, and the rocking connection is being opened and closed constantly, it is thought that this has caused the slight reduction in PT force over the duration of the test.

5.3.3 Specimen B1A

Description of the Test

This was the first test to be carried out on the full SC-CBF frame consisting of both braces and self-centering frame system. The braces employed were formed from 20x20x2.0SHS. In addition to the instrumentation in the bare frame test (B0 test), there are also strain gauges associated with the brace members. That is, 52 sensors in total were employed as detailed in Section 4.7. During installation of the braces, the data acquisition system was set to record the installation and tightening of the bolts that connect the brace specimens to the test frame. This permitted quantification of any additional forces that may be induced in the specimens due to a lack of fit during the installation. For these specimens, the strains were of the order of $195\mu\epsilon$ and $164\mu\epsilon$ in the LHS and RHS braces, respectively. These strains equate to an initial tension force of 5.49kN and 4.61kN in the braces. Before full testing was commenced, a preliminary run was conducted within the elastic range to ensure everything was in order with the data acquisition system, and that it was logging the results as expected.

Displacement Cycles and Loading Rate

The ECCS loading protocol was used, as outlined in Section 4.6.2, where the yield displacement was established from the coupons test results discussed in Section 5.2.2. An additional 5mm was added to each of the cycles during this test to account for the lateral movement observed in the pinned connections at the column bases of the frame during the B0 test. This 5mm was justified by performing a number of low level elastic tests on the B1A specimen to establish the amount of movement of the pinned connection. In addition to this, the loading rate of the test was increased to 1mm/s in order to reduce the test time and the loss of load in the PT strands, giving a test cycle to the ECCS ductility cycle 26, as with B0, and a higher loading rate.

Plots of Test Results

Figure 5.7 shows the results of the test on the specimens. Figure 5.7a shows the pushover force against drift, where it can be seen that the bilinear behaviour of the self-centering frame is evident, in addition to the energy dissipation associated with the brace specimens. This is seen by the fact that the pushover force required to cause any significant displacements is much higher than that of the bare frame test. In addition, Figure 5.6 shows a single loop of the response of the pushover force versus drift of the B1A test frame, where the flag shaped loop of the self-centering system can be seen in addition to the hysteretic energy dissipation of the

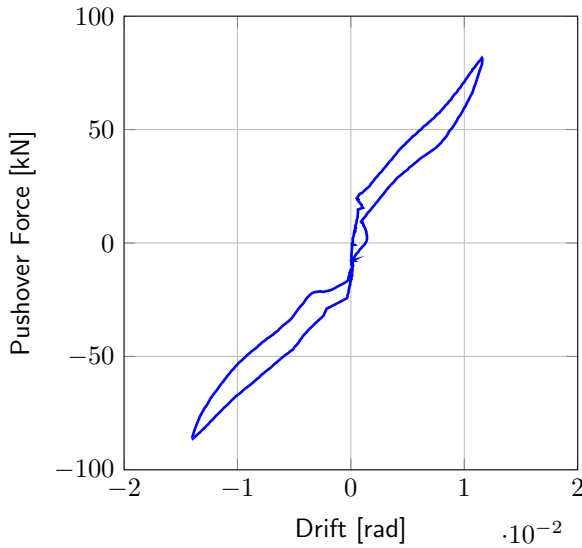


Figure 5.6: Single loop of B1A specimen at 1.2% interstorey drift.

brace specimen. Since the B1A brace specimens are the most slender of all the brace specimens, it dissipates a relatively little amount of hysteretic energy where the pinching behaviour of the braces due to the large number of cycles is also evident.

Again, it can be seen in Figure 5.7b that the PT force increases as expected with drift. The gap opening of the connection causing the increase in PT force is shown in Figure 5.7b. However, the recording of the gap opening at the LBBF instrument shows unusual results, where it was later discovered after testing that the clamp holding this instrument in place had gradually come loose during testing and was no longer recording accurate measurements. The results are included nonetheless and the general trend can still be seen to be the same as the other instruments measurements.

The decompression moment required to achieve this gap opening is also shown in Figure 5.7d and the values remain unchanged from the previous bare frame test, where the same decompression moment is required for the bare frame as is for the frame with test specimen. Figure 5.7e and 5.7f show the OOP displacement of the left and right braces. These plots are such that the two braces buckled in two different directions, but the peak magnitude of the OOP displacement at mid-length is the same for both braces. Referring to Figure 4.1, the right hand brace buckled in the direction going into the page and the left hand brace buckled in the direction coming out of the page. This can be seen in the photo of the test specimens during testing in Figure 5.8.

Test Observations

The test specimens used in this test did not fracture after the completed cycles, which gave a drift of 1.71% in the positive direction and 1.98% in the negative direction. This unsymmetrical loading is observed in the test frame as the actuator position was not perfectly at the zero point before loading, hence, it displaced more in one direction than the other. Although attempts were made to mitigate this issue in the initial elastic runs, and by adding 5mm to the displacement cycles, it was difficult to accurately assess the looseness of the frame in either direction with a small amplitude test, and is more evident after many large cycles have been carried out. Severe pinching can be seen in the hysteresis loops (Figure 5.7a), as these braces represent the most

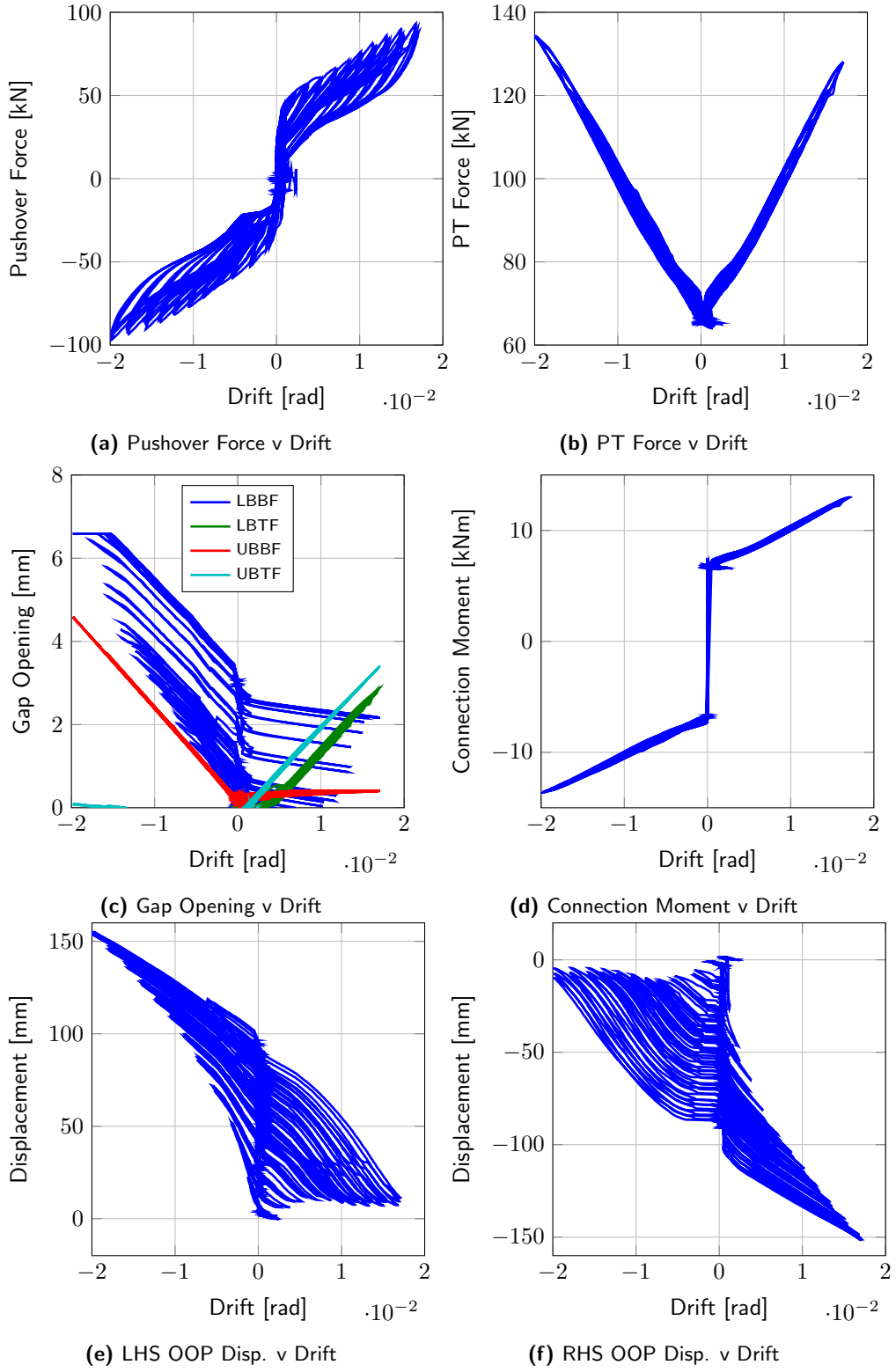


Figure 5.7: B1A test results.



Figure 5.8: Buckling out of plane of the B1A specimens.

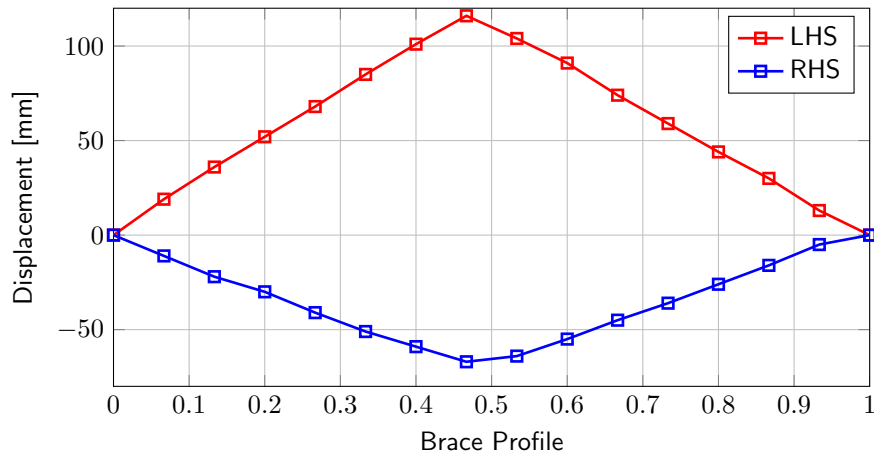


Figure 5.9: Displaced profile of the B1A specimens after testing.

slender braces in the test setup.

As these brace specimens had not fractured after the cycles were completed, final measurements for the displacement profile of the braces could be taken along the brace specimen to give the plots shown in Figure 5.9. These braces showed a residual OOP deformation after testing due to the many cycles of inelastic behaviour induced during testing. That is, after many cycles of tensile yielding, the braces have elongated axially, and when the frame returns to its original position, there is a permanent OOP deformation present. In addition to the axial elongation, the plastic hinge developed at the midpoint of the braces during global member buckling influences the OOP deformation remaining in the braces throughout the test. This is because the hinge developed at the brace midpoint does not fully recover its inelastic rotation upon picking up tension. Hence, a residual lateral deformation persists in the braces. This can be seen in Figures 5.7e and 5.7f, where it is seen that when the braces return from the compressive cycle and into the tensile cycle, there is still a residual OOP displacement throughout the test for both braces. This behaviour along with the fact that the frame was displaced further in the negative direction than the positive (1.78% and 1.98%), can explain why the OOP deformation remaining in the braces after testing is larger in the LHS brace than the RHS brace, as shown in Figure 5.9. In addition to this OOP displacement in the brace, some degree of necking was observed after testing at the midpoint of both braces, although there was no evidence of any significant local buckling.

5.3.4 Specimen B2A

Description of the Test

This test consisted of the first test on the 25x25x2.5SHS specimens, which were the next section size up from the B1 specimens. The instrumentation setup was the same as that of the B1A specimens described in Section 5.3.3, which meant a total of 52 channels were to be recorded. The tightening of the bolts that connect the braces to the frame was recorded to observe the increase in strain in the braces due to the bolt tightening. For these specimens, the strains were of the order of $58\mu\epsilon$ and $112\mu\epsilon$ in the LHS and RHS braces, respectively. These strains equate to an initial tension force of 2.55kN and 4.92kN in the braces. In addition, the test frame was run through a low amplitude cycle to ensure that the acquisition system was working correctly before full testing was commenced.

Displacement Cycles and Loading Rate

The loading cycle performed was as described by the ECCS protocol with an additional 5mm added in to account for frame movement. The loading was again set at 1mm/s to decrease the total test time.

Plots of Test Results

Figure 5.10 shows the results of the test on the specimens. There are only three of the desired plots available for this test due to difficulties during the test with the instrumentation. The available plots are the pushover force, PT force and connect moment versus drift. The reasons for the lack of data from this test are discussed in the next section. However, the main trends from the plots in Figure 5.10 are still noted. The pushover force versus drift plot in Figure 5.10a shows the flag shaped loop and with the energy dissipation of the braces clearly seen compared to the bare frame. Figure 5.10b shows the PT force versus the drift in frame and the increase in force can be seen to increase from the initial value with drift. Figure 5.10c shows the connection moment for the PT strands versus the drift and shows that the self-centering frame is again independent of the brace specimens and provides the bilinear elastic moment connection to give the self-centering behaviour of the frame.

Test Observations

Numerous observations and adjustments have been made to the results of this test in order to make the reporting of the results presentable. This is due to the fact that the LVDT instruments LBBF and UBBF were accidentally moved during the testing and it was not possible to calculate the drift angle for the entire test. It was, however, possible to obtain presentable data for a portion of the test. This corresponded to the drift cycles 1.08%, 1.25% and 1.35% in the positive direction, and this is what is presented in Figure 5.10. The gap opening and brace OOP displacements are not presented in Figure 5.10 as the resulting plots from the portion of the test plotted do not show any relevant data. While not ideal, the basic trends in the available plots in Figure 5.10 can still be observed in the test data.

During the actual test, it was noted that the RHS brace fractured fully during the first cycle of the ECCS ductility 26 cycle, and since the instrumentation that was documenting drift of the frame was lost at this stage of the test, it is not possible to determine the exact drift this corresponds to. However, from measurements in the previous test (i.e. B1A), the amplitude of the cycle corresponding to an ECCS ductility of 26 gives an interstorey of 1.63%, which can be used as an approximation for this test. The LHS brace did not fracture after 3 cycles at this cycle level and was observed to show some necking at the midpoint, although no significant local buckling was evident. The test was then concluded after the end of the three ECCS ductility 26 cycles.

5.3.5 Specimen B2B

Description of the Test

As with the previous test reported, this was a test of the 25x25x2.5SHS brace specimens. The same instrumentation setup as before was used, where all 52 channels were recorded. However, for this specimen, the instrumentation was corrected and a complete data set for the test was obtained allowing for proper evaluation of the 25x25x2.5SHS specimens. For these specimens, the strains were of the order of $123\mu\epsilon$ and $160\mu\epsilon$ in the LHS and RHS braces, respectively. These

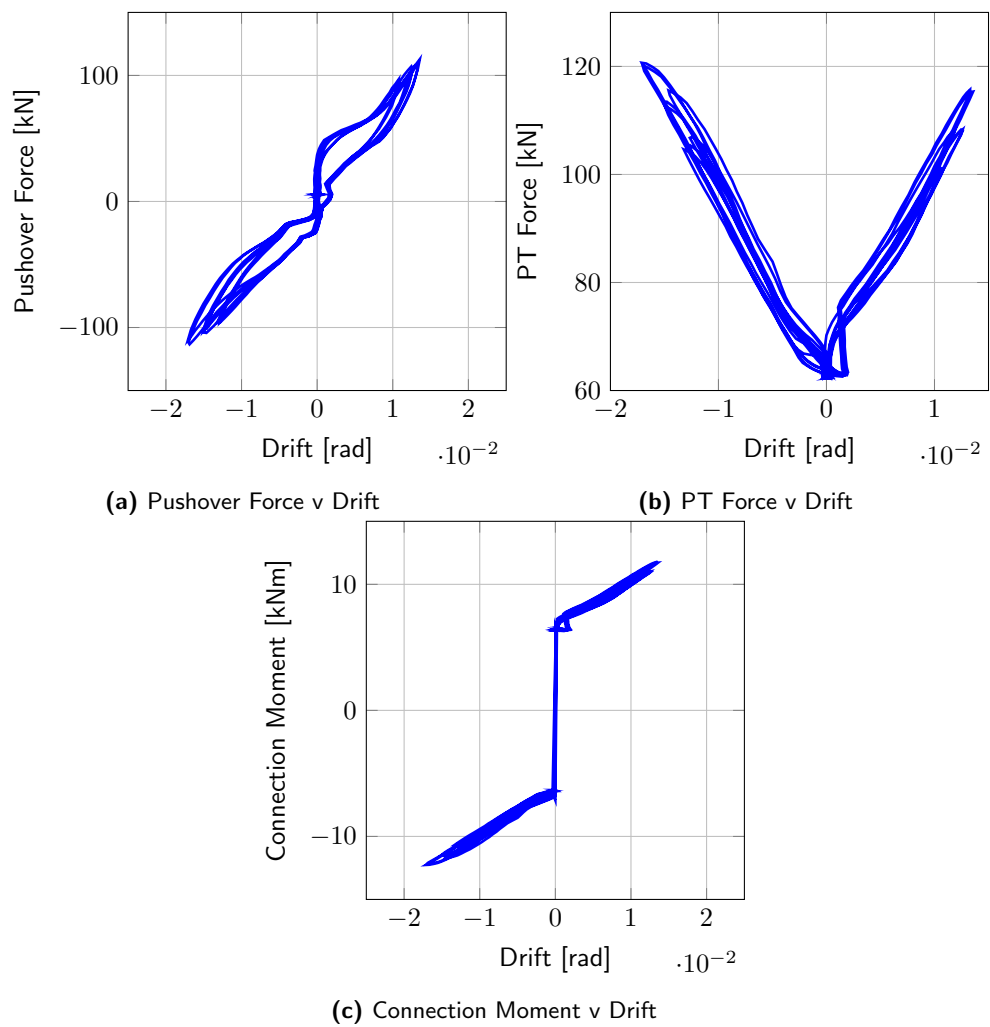


Figure 5.10: B2A test results.

strains equate to an initial tension force of 5.40kN and 7.02kN in the braces. Again the frame was cycled through an initial low level elastic run to determine if all the instrumentation was in correct working order before the full test was commenced.

Displacement Cycles and Loading Rate

The displacement cycles were as before for the B2A specimen with the ECCS loading at 1mm/s and an additional 5mm included to account for the flexibility of the frame.

Plots of Test Results

Figure 5.11 shows the six plots of the results from the test specimens. Figure 5.11a shows the hysteresis of the frame where it can be seen that the specimen again exhibits a full flag shape loop with degrading loops due to the pinching of the braces, which is similar to the portion of the data available shown in Figure 5.10 for braces of the same cross-section. The same general trend with regard to the PT force, gap opening and connection moment is seen in Figures 5.11b to 5.11d, where the PT force increases with drift as expected, the gap opening of the beam column connection (Figure 5.12) is the same and symmetrical, and the connection moment due to the PT force also shows the bilinear elastic hysteresis. The brace OOP displacements shown in Figures 5.11e and 5.11f show the expected trend, although the LHS brace displaces much further (approximately 15%) than the RHS brace despite the frame being displaced to similar drifts in either direction (2.54% in the positive and 2.31% in the negative). The difference in OOP displacement could be due to the LHS brace not recovering as much straightness as the RHS brace during tensile loading, as can be seen in Figure 5.11e, where a relatively large residual deformation remains in the brace throughout the testing, especially when compared to the RHS brace.

Test Observations

The necking of the RHS brace at 1.95% drift in the positive direction can be seen in Figure 5.13, where tearing of both braces occurred during the second cycle of 2.54% in the positive direction and 2.31% in the negative direction. The LHS brace fully fractured first during the third cycle at this drift cycle followed by the RHS brace in the reverse cycle.

5.3.6 Specimen B1B

Description of the Test

This test is the second that utilises the 20x20x2.0SHS specimens, which are the most slender specimens employed in this study. The instrumentation setup was as per the previous test and all 52 channels of data were logged. The bolts were tightened and the strain readings of the braces were taken during this process. For these specimens, the strains were of the order of $44\mu\epsilon$ and $156\mu\epsilon$ in the LHS and RHS braces, respectively. These strains equate to an initial tension force of 1.24kN and 4.39kN in the braces.. During the initial preliminary runs on the frame within the elastic range, which were carried out to ensure that everything was in order before the main test was carried out. It was noted that the response of the frame was not symmetric, i.e. the frame was picking up more force in one direction than in the other. It was thought that this was due to the zero point on the actuator being slightly out, as the actuator was adjusted in order to fit the specimens into the frame when the bolt holes did not align exactly. The actuator zero point was adjusted to give a more symmetric initial elastic response of the test frame and from there the main test sequence was run.

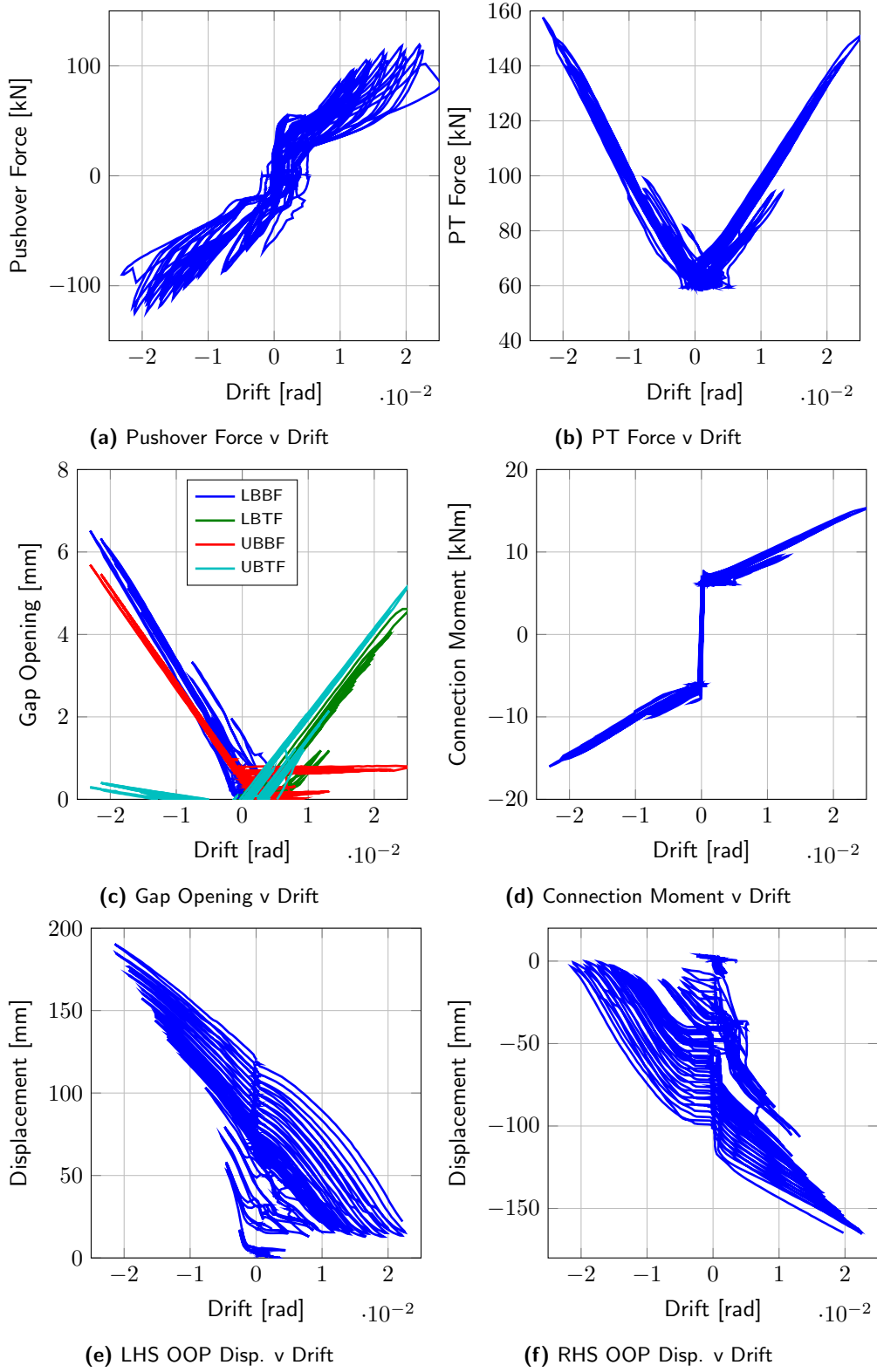


Figure 5.11: B2B test results.

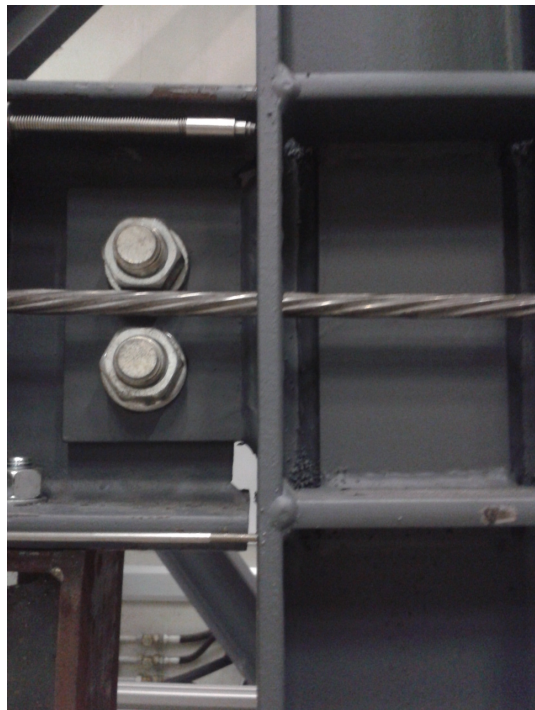


Figure 5.12: Gap opening of upper beam bottom flange during B2B testing.



Figure 5.13: Necking of RHS brace during B2B testing.

Displacement Cycles and Loading Rate

As previously mentioned, the zero point of the actuator was adjusted to give a symmetric force displacement response in the preliminary runs. Apart from this, the displacement cycles were as before for the B1A specimen with the ECCS loading at 1mm/s, and an additional 5mm included to account for the flexibility of the frame.

Plots of Test Results

Figure 5.14 shows the plots for the test. As it can be seen when comparing to the plots previously seen, this test specimen performs in the same way as the previous test, exhibiting the flag shape etc. and showing the gap opening and self-centering behaviour of the frame. However, despite the efforts made in the preliminary elastic runs to adjust the zero point of the actuator to give a more symmetric response, the frame displaces slightly more in the negative direction than the positive (2.23% in the positive and 2.05% in the negative direction). Upon closer examination of the actuator force and displacement readings from the full test, it was observed that the frame was still not exactly at the zero point and there was still a few millimetres of extra looseness in the frame in the negative direction, compared to the positive direction, that was not obvious from the initial elastic runs used to correct the position of the actuator prior to testing. Although this extra looseness is only of the order of 3 to 4mm, it is still sufficient to cause the differences in the maximum drifts of the frame.

Figure 5.14c shows a sudden offset of the results for the UBBF LVDT reading as this instrument slipped out of position during the test but was quickly rectified, albeit in a slightly different position or stroke of the LVDT, for the remainder of the test. Hence, the data is offset for some of the test but the magnitudes and slope are still the same.

Test Observations

The specimens observed the same response as the B1A specimens in that the same flag shape was observed and the other plots showed the same trends. Unlike the B1A specimen, these B1B specimens were loaded until full fracture, which for the RHS brace was during the 3rd cycle of the 2.05% drift cycle, and for the LHS brace, the fracturing occurred during the 2nd cycle of the 2.23% drift cycle. In the drift cycles prior to full fracture, there was some degree of necking in both specimens observed at the midpoint of the braces although there was no obvious tearing of the braces prior to full fracture. No local buckling of the braces was obvious during the compressive cycles of the braces prior to full fracture.

Despite the slightly unsymmetrical drift cycles imposed on the frame, the maximum OOP displacement of the braces is quite similar with the LHS brace having a maximum of 162.2mm, and the RHS having a maximum of 166.5mm. It is to be expected that the RHS brace displaced more OOP than the LHS brace as the drift in the positive direction was slightly larger than the negative direction.

5.3.7 Specimen B3A

Description of the Test

This test was the first on the 30x30x2.5SHS specimens and was carried out in the same fashion as the other braces. All 52 channels were recorded and the brace strain gauges data documented

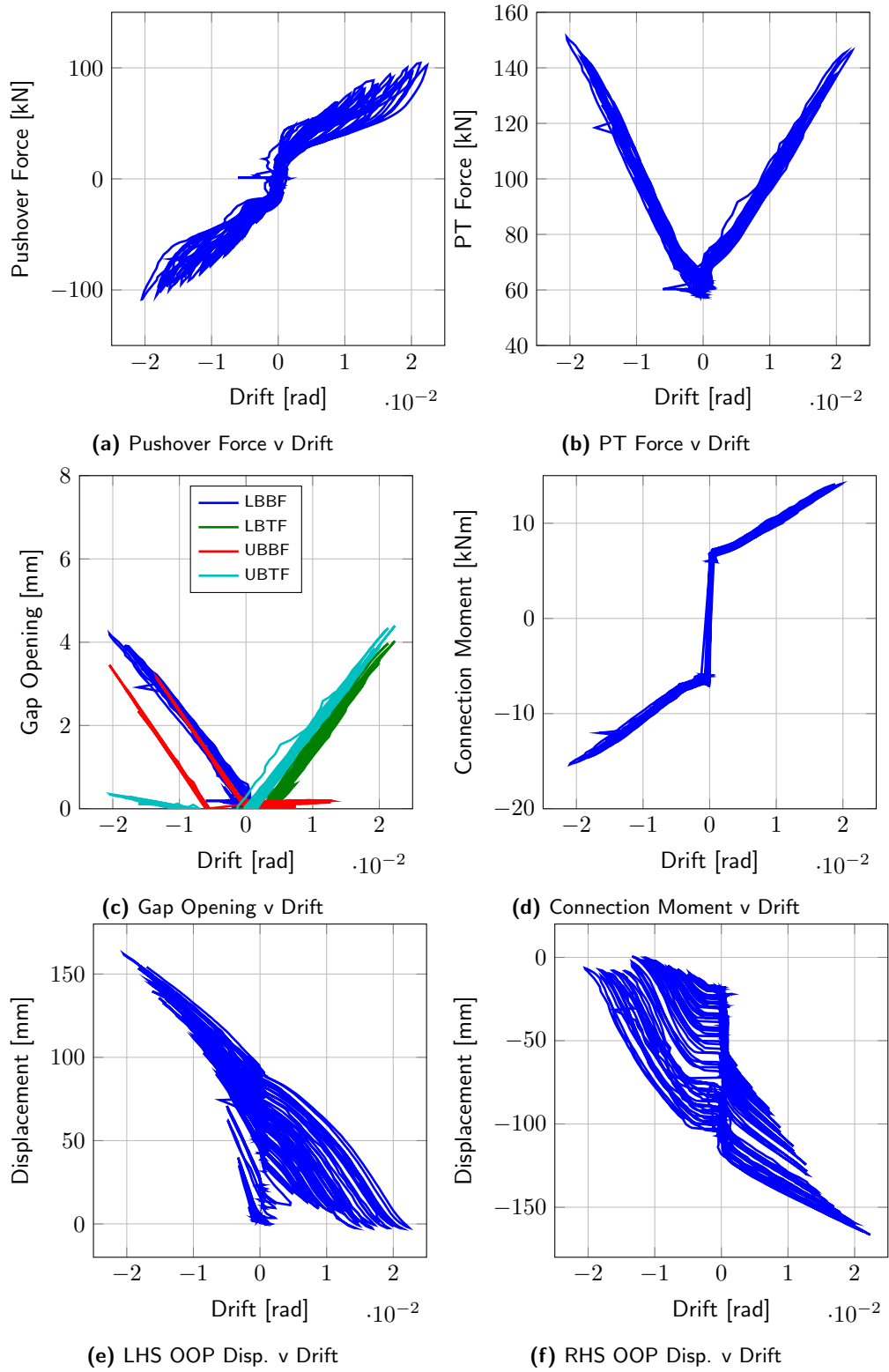


Figure 5.14: B1B test results.

CHAPTER 5. EXPERIMENTAL RESULTS AND OBSERVATIONS

during the tightening of the bolts. For these specimens, the strains were of the order of $118\mu\epsilon$ and $103\mu\epsilon$ in the LHS and RHS braces, respectively. These strains equate to an initial tension force of 6.42kN and 5.60kN in the braces. Again, it was necessary to adjust the position of the actuator to fit the specimens into the test frame initially. Also, the preliminary runs showed asymmetric response of the frame initially and was picking up more load in one direction. Hence, adjustments to the actuator zero point were carried out until a symmetric response was obtained as before with the B1B specimens.

Displacement Cycles and Loading Rate

After adjusting the zero point of the actuator to give a symmetric force displacement response in the preliminary runs, the displacement cycles were as before with the ECCS loading at 1mm/s and an additional 5mm included to account for the flexibility of the frame.

Plots of Test Results

Figure 5.15 shows plots of the response of the frame. It is obvious from looking at the data obtained for the LVDT on the upper beam, bottom flange connection measuring gap opening and the two string pots measuring OOP displacement at the midpoint of the braces in Figures 5.15c, 5.15e and 5.15f, that there is a problem with this data. In particular, there is a lot of noise in the string pot data and the LVDT data is not logging correctly. In any case, these have been included as, for the OOP displacements, the general trend of the plots is the same as before and shows the behaviour and movement of the braces during buckling.

The other plots exhibit similar characteristics as expected with the flag shape evident along with the increasing PT force with drift, and the bilinear elastic connection moment resulting from the PT system. There is, however, a limitation to the data plotted in Figure 5.15b, where the positive drift values do not exceed 2.63%, whereas the PT force is still seen to be increasing. This is due to the LBTF LVDT, from which the drift is deduced, has reached its maximum stroke and cannot record any larger displacements at the connection. It can be concluded however, that the overall behaviour is as expected, as the same PT force values are recorded despite LVDT reaching a maximum displacement.

Test Observations

As seen in the plots in Figure 5.15, the string pots measuring the OOP displacement were producing a lot of noise, but are included nonetheless as they show the general trend of the brace buckling. In addition to this, there was a sudden movement of the frame during testing which resulted in the RHS brace string pot falling off the specimen during testing, which can be seen in the sudden jump in Figure 5.15f. It was quickly reattached and the test continued, but it should be noted in any case. In addition to this, the channel corresponding to the C27 strain gauge went offline during the test. It was investigated after testing where the gauge was brought back to producing results again. However, no data has been logged for this channel for this test.

The RHS brace began to show local buckling (Figure 5.16) during the 1st cycle at drift 2.00% and the LHS followed in the reverse cycle. The LHS brace fractured during the 2nd cycle at drift 2.30% and tearing began in the RHS brace during the 3rd cycle at the same drift level. The RHS brace then fractured during the first cycle at drift 2.63% and is shown in Figure 5.17.

The maximum OOP displacements of the braces are difficult to assess as there is a lot of noise in the data shown in Figures 5.15e and 5.15f. A maximum value can still be obtained from

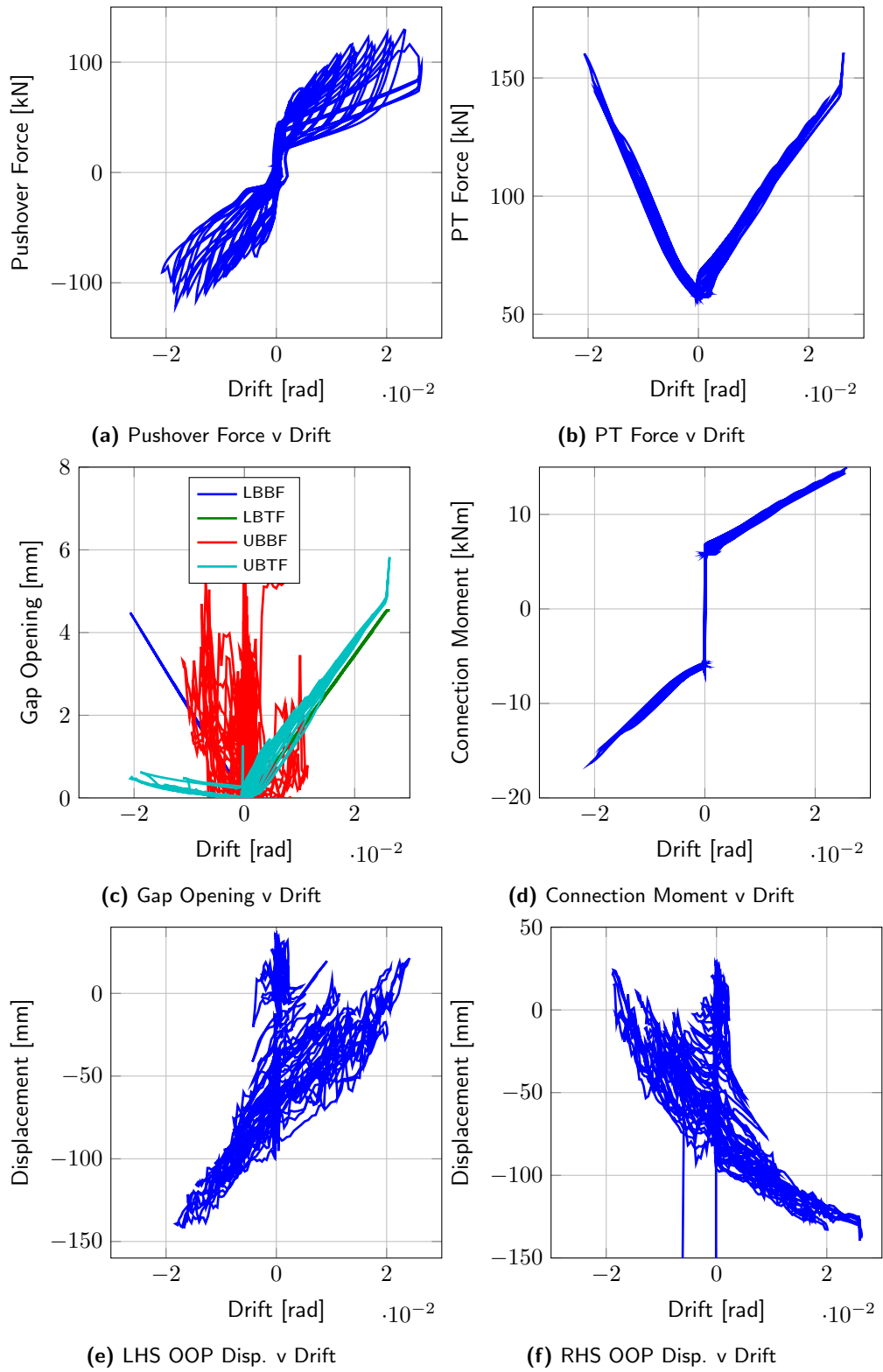


Figure 5.15: B3A test results.



Figure 5.16: Local buckling in the B3A RHS brace.

these plots, although upon closer inspection it is seen that the data is not zeroed correctly. This is evident from the plots showing a positive value for the OOP displacements of the braces when they are in tension, which is not expected. Hence, these values are displayed to show a trend in the behaviour, and not exact values.

5.3.8 Specimen B4A

Description of the Test

This was the first test on the largest specimen fabricated from 40x40x4.0SHS. All 52 channels were recorded during the test. However, slight adjustments were made in an attempt to improve the quality of the data obtained. As was seen in the previous B3A test, the LVDT at the lower flange of the upper beam produced a lot of noise and unusable data. This was checked prior to testing and the instrument seemed to work. In addition, it was swapped with the LVDT on the roller connection as it was felt that it was more important to record the gap opening at the beam column connection. During this process, it is believed that the calibration of the LVDT on the roller connection was lost as the results produced were at a much larger magnitude than the typical displacements, but with the same trend. In addition to this, the instrument slipped during testing and reached its maximum stroke, thus rendering the results obtained effectively useless for the test. For these specimens, the strains were of the order of $62\mu\epsilon$ and $39\mu\epsilon$ in the LHS and RHS braces, respectively. These strains equate to an initial tension force of 6.97kN and 4.38kN in the braces.

As before, the actuator was adjusted to fit the specimens and the zero point then adjusted to give a symmetric response during initial runs. As mentioned in Section 5.3.7, the C27 strain gauge was fixed and results were obtained for this test.

Displacement Cycles and Loading Rate

After adjusting the zero point of the actuator to give a symmetric force displacement response in the preliminary runs, the displacement cycles were as before for the B3A specimen with the



Figure 5.17: Fractured B3A RHS brace.

ECCS loading at a rate of 1mm/s and an additional 5mm included to account for the flexibility of the frame.

Plots of Test Results

Figure 5.18 shows the plots of the B4A test specimens. It can be seen that the UBBF instrument did not produce legible results and its data is thus discarded for the evaluation of the frame. Again, the string pots used to measure the OOP displacement of the braces was producing very noisy results again, although the general trend of the brace buckling behaviour versus drift is seen nonetheless. Apart from these problems, the general behaviour of the self-centering frame is seen in the plots of pushover force, PT force and connection moment due to the PT system. This again shows the frame was providing the intended self-centering behaviour, with much more energy dissipation in this specimen due to the stockier brace size.

Test Observations

As outlined in the test description, the LVDT on the lower flange of the upper beam was producing noisy readings that are not of much use, but are included nonetheless. Similarly with the string pot readings of the braces OOP displacement. These are included in the plots (Figure 5.18e and 5.18f) as the general trend of the data is still evident, despite the noise present in the data.

The RHS brace buckled suddenly during the 1st cycle, at ECCS ductility 18 with the LHS brace following in the reverse cycle but not in the same sudden manner as the RHS brace. The complete ECCS loading up to an ECCS ductility cycle of 30 was performed on the specimen, without any brace fracturing, although some local buckling is evident in the specimens (Figure 5.19). The test was stopped as the actuator was at minimum stroke and could not pull the frame any further than about 96mm, where the actual target displacement for the last cycle was 103mm. The final buckled brace specimens are shown in Figure 5.19, and a plot of the displaced shape of these braces is shown in Figure 5.21. It should be noted that in order to remove the RHS brace from the frame without cutting it, it was necessary to move the actuator

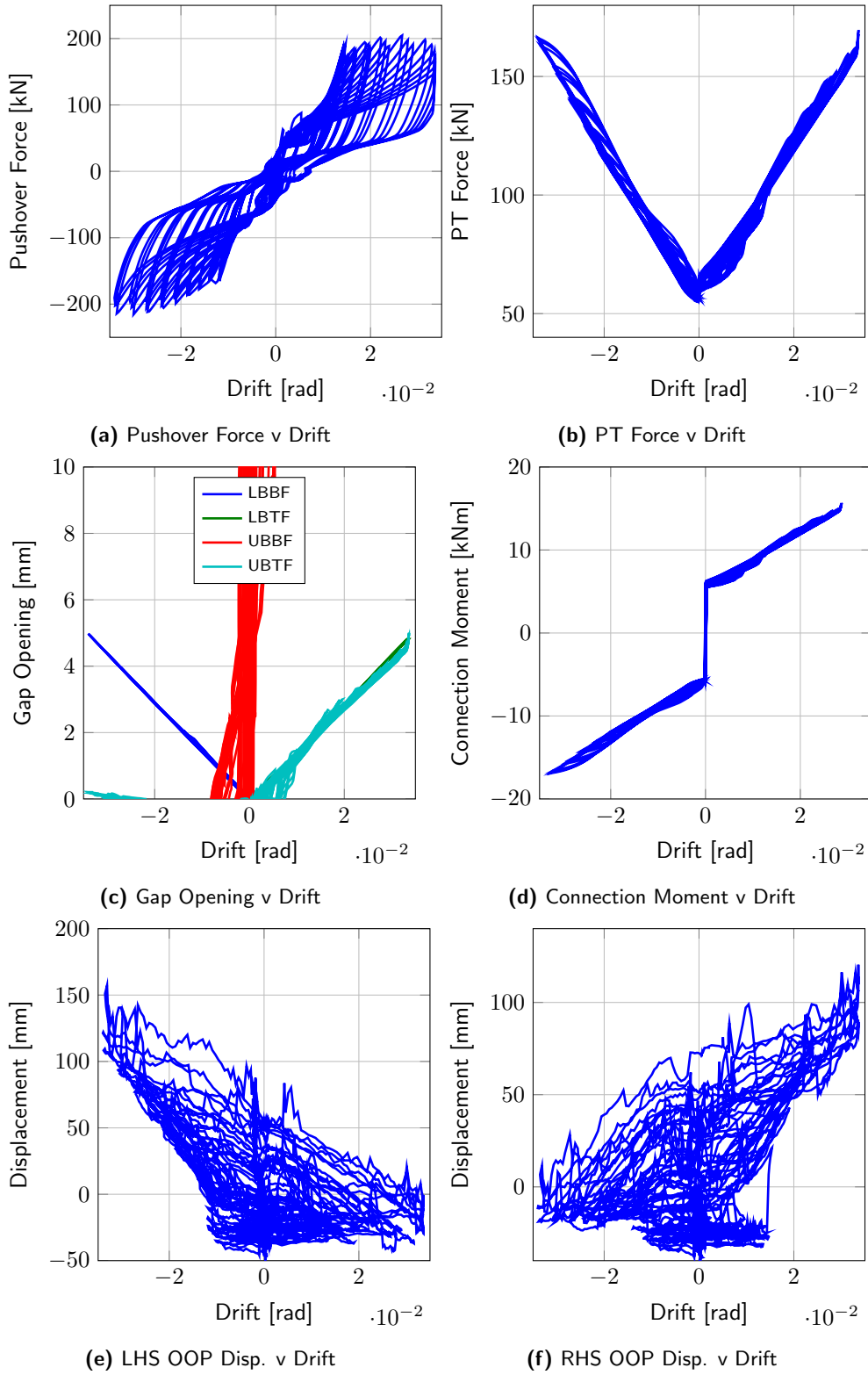


Figure 5.18: B4A test results.



(a) B4A LHS brace local buckle.

(b) B4A RHS brace local buckle.

Figure 5.19: B4A local buckling of braces.



Figure 5.20: B4A specimens after testing.

approximately 50mm. This was so that the force in the brace preventing the bolts being removed was relaxed. This caused a slight relaxation in the final displaced shape as can be seen in Figure 5.21 when compared to that of the LHS brace.

5.3.9 Specimen B3B

Description of the Test

This was the second test be performed on the 30x30x2.5SHS section size. Due to a limited number of instruments available at the time of testing, a reduced number of instruments were used for the brace specimens. This meant that just the strain gauge channels labelled C31, C33, C37 and C39 were recorded for the braces, with all the other channels recorded as per usual. This does not affect the final data set or the conclusions that can be drawn from the test, as these instruments omitted are not critical to the evaluation of the frames behaviour, but it does mean that a reduced set of data is available for later modelling comparisons. However, since the B3A specimens were fully instrumented, the omitted data from this test can be interpreted from the test on the other B3A specimens. For these specimens, the strains were of the order of $75\mu\epsilon$

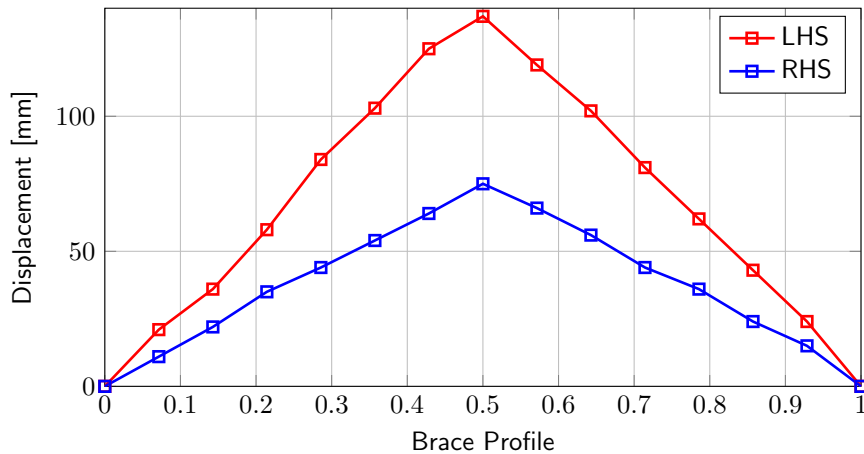


Figure 5.21: Displaced profile of the B4A specimens after testing.

and $54\mu\epsilon$ in the LHS and RHS braces, respectively. These strains equate to an initial tension force of 4.08kN and 2.94kN in the braces. Before the full testing of the specimens commenced, a low amplitude cycle was conducted to ensure that the frame was picking up similar load in both directions, and from this, the zero point of the actuator was adjusted to ensure that the loading would be symmetric.

Displacement Cycles and Loading Rate

The input displacement cycles were as before for the B3A specimen with the ECCS loading at a rate of 1mm/s and an additional 5mm included to account for the flexibility of the frame.

Plots of Test Results

Figure 5.22 shows the results from the testing on the specimens. As before with the B3A specimens, this B3B specimens shows the expected flag-shaped behaviour in Figure 5.22a, although it can be seen that the drift is slightly larger in the negative direction (2.97% in the negative and 2.52% in the positive). Again, this is due to the actuator not being perfectly zeroed prior to testing as was evident once a full large cycle data set of the actuator force displacement was obtained. In addition to this, it is observed that the drift in the positive direction reaches a maximum value, while the PT force is still increasing. This is due to the LBTF LVDT reaching its maximum displacement, which was also observed in the B3A specimens test, and hence, higher drifts are not reported. From the plot of connection moment versus drift, it can be seen that the decompression moment has reduced slightly when compared to other tests. This is to be expected as many cycles have been carried out on the specimens using the test frame, hence a slight reduction in strand force is to be expected. In addition, the anchors used are intended to be short term anchors and this test on the B3B specimens was conducted nearly 2 months after the PT force was initially applied to the strands.

Test Observations

In addition to the obvious trends that this test specimen showed, a smaller observation can be made from the plots in Figure 5.22. This is seen in Figure 5.22e and 5.22f where the plots show the OOP displacement of the braces against drift of the frame. These brace specimens are a stockier section size with a higher buckling capacity than the previous B2 and B1 specimens, and from observation of the OOP displacement in the initial displacement cycles, it can be seen

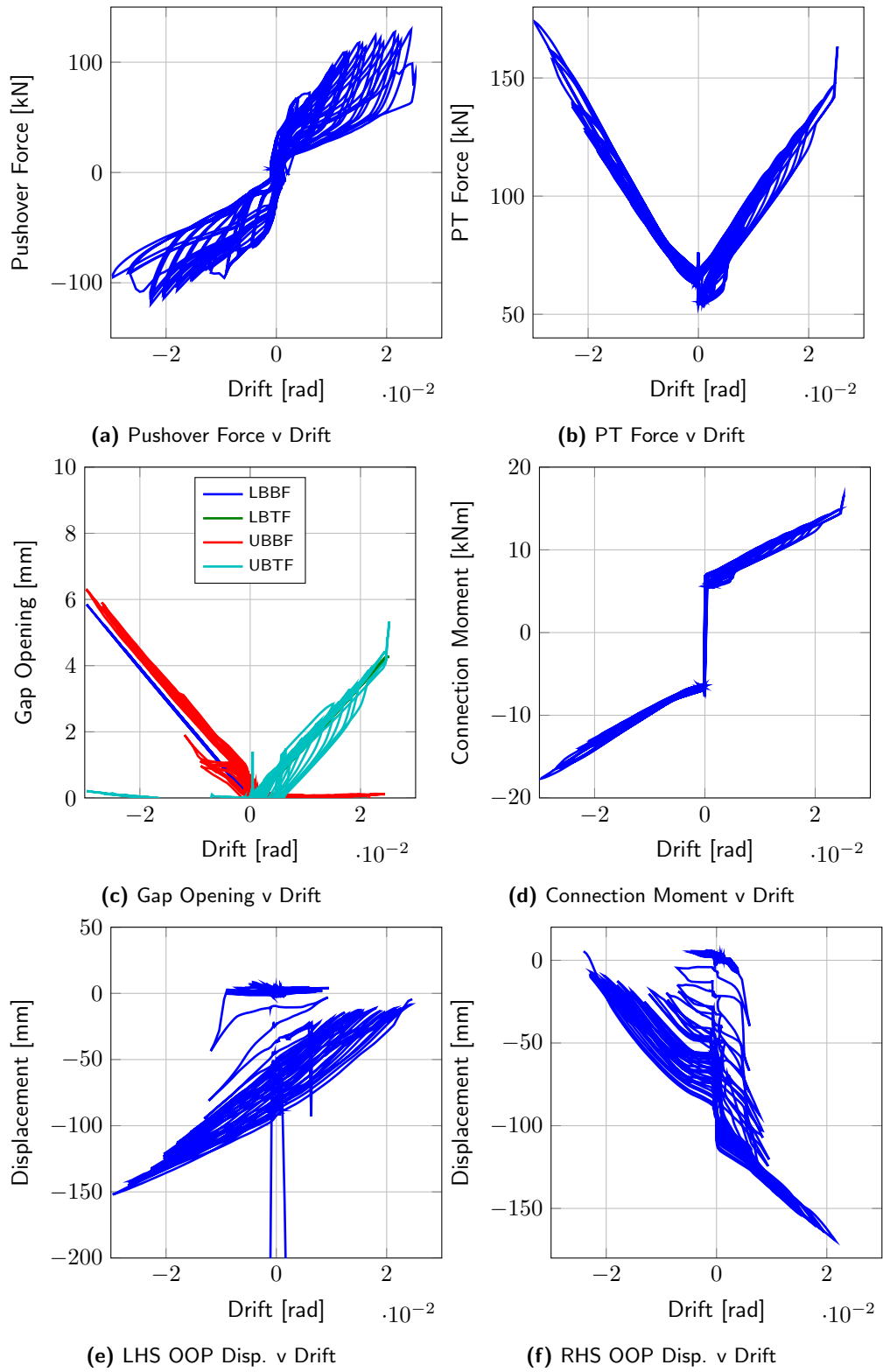


Figure 5.22: B3B test results.

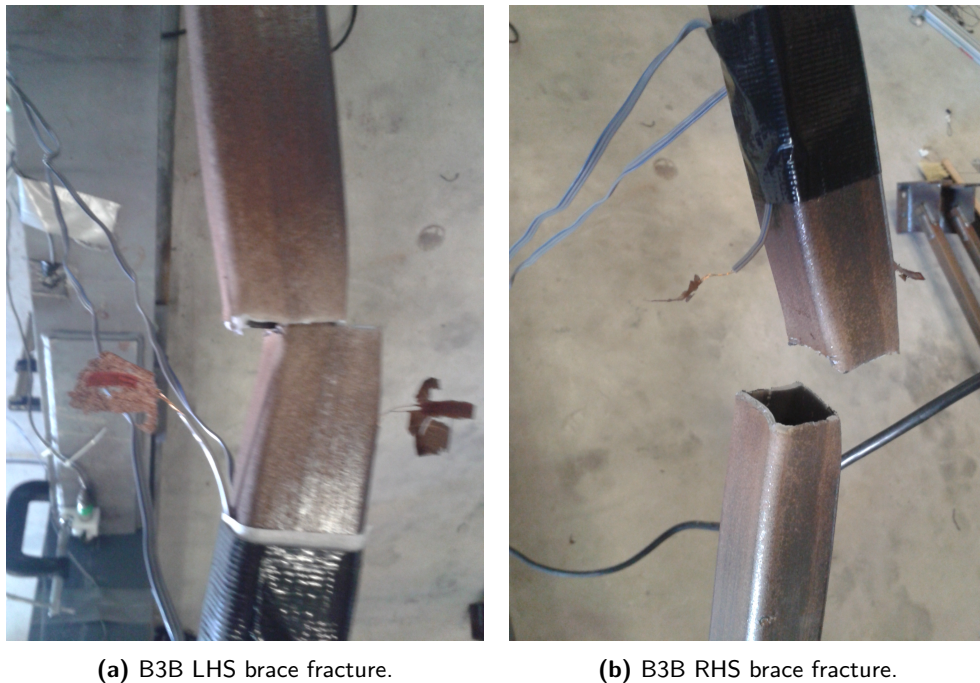


Figure 5.23: B3B fractured braces.

to be very low and eventually increases quickly. This was observed visually during the testing, where the braces kicked out of plane quickly after a few cycles. This was the same for both braces, where the corresponding drifts in Figure 5.22e and 5.22f at which this observed buckling occurred are -0.95% and +0.45% for the LHS and RHS braces, respectively.

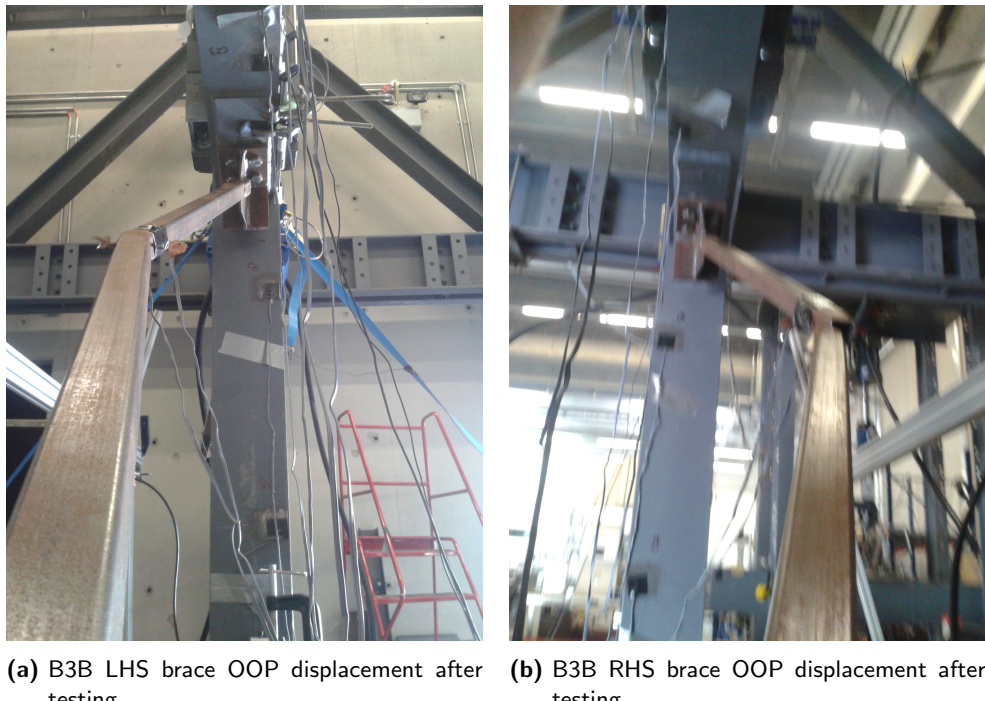
During the actual testing, there was a loss of actuator pressure due to a power trip in the laboratory. This resulted in the test being paused during the third cycles of the ECCS displacement ductility 16 cycle while the system was being restored to complete the testing. The LHS brace's stringpot magnet fell off the brace during the second ECCS displacement ductility 16 cycle, hence there is a spike in the LHS braces OOP displacement at midlength of the brace in Figure 5.22e. The testing was paused at the end of this cycle in order to reattach the magnet, and then continued as per usual.

During the first cycle of drift 1.90%, there was some necking observed in the RHS brace and during the second cycle at the same ductility, local buckling began to occur in both braces. Severe local buckling was observed in both braces during the first cycle of 2.20% drift and upon loading in tension during the reverse cycle, the RHS brace fractured fully. The LHS brace fractured later during the second cycle of 2.45% drift on the frame. Figure 5.23 shows a picture the fractured braces after testing, and Figure 5.24 shows a picture along the braces after testing showing their OOP displaced shapes.

5.3.10 Specimen B4B

Description of the Test

This was the second of the 40x40x4.0SHS specimens to be tested. As with the B3B specimens, a limited number of strain gauges were available at the time of testing, hence a reduced number



(a) B3B LHS brace OOP displacement after testing. (b) B3B RHS brace OOP displacement after testing.

Figure 5.24: B3B OOP displacements after testing

of channels were recorded. The channels recorded were the same as the B3B test, where just the C31, C33, C37 and C39 strain gauge channels were recorded for the braces. Again, this reduced number of channels is not critical, as the complete data set was recorded during the B4A test. For these specimens, the strains were of the order of $31\mu\epsilon$ and $149\mu\epsilon$ in the LHS and RHS braces, respectively. These strains equate to an initial tension force of 3.48kN and 16.74kN in the braces.. It is thought that this initial force in the brace is also due to the lack of fit of the test specimen during the initial installation in addition the bolt tightening. Before the full testing of the braces commenced, a low amplitude cycle was conducted to ensure that the frame was picking up load symmetrically, and based on this, the zero point of the actuator was adjusted to ensure that the displacement cycles would be symmetric.

Displacement Cycles and Loading Rate

The input displacement cycles were as before for the B4A specimen with the ECCS loading at a rate of 1mm/s and an additional 5mm included to account for the flexibility of the frame.

Plots of Test Results

Figure 5.25 shows a plot of the test results obtained from the B4B specimens. As expected, the test shows the usual flag-shaped behaviour of the frame and demonstrated the self-centering as before with the B4A specimens. In contrast to the B4A test, the OOP displacements at the midlength of the brace were recorded much more accurately, with the noise present in the B4A data being rectified and the OOP displacement of the braces can be seen more clearly. Similarly to the B3B specimen, the buckling of the braces after a few cycles of relatively little OOP displacement can be seen. This was observed visually during the testing where the braces kicked out of plane relatively quickly when buckling in compression and straightened in tension, as expected, during the subsequent cycles of loading. The drift values at which this buckling

occurred are -1.05% and +1.10% for the LHS and RHS braces, respectively. It is also observed that the recordings of positive drifts are again limited by the maximum displacement capacity of the LVDT documenting it which was also observed during the B3A and B3B specimen tests.

Test Observations

As with the previous test on the B4 specimens, fracture of the braces was not achieved. This was due to the actuator stroke reaching its maximum capacity and the frame could not be pushed any further past the maximum drifts in either direction, which were 2.66% and -2.76%, to cause brace fracture. The result of testing was the local buckling of the two specimens, which is shown in Figure 5.26. The final state of the test frame with the B4B specimens is shown in Figure 5.27 and a picture along both braces showing the OOP displacement is shown in Figure 5.28.

5.4 Summary of Test Results

With all the specimens tested and documented in detail in the preceding sections, this section summarises the data from each test and compares some of the values reported in the tests to theoretical predictions. Table 5.3 summarises salient response parameters for each test, where the values for maximum and minimum drift are reported for each of the specimens. The maximum PT force in either direction is also reported, as well as the base shear force in each direction. The maximum absolute OOP displacement at the mid-length of the braces are also shown for each of the brace specimens, with the exception of B0, where no brace specimens were inserted in the test frame and B2A where difficulty with the instrumentation during the test meant only a limited amount of data was available. Also presented in Table 5.3 is the total energy dissipated (E_d) by each of the test specimens during testing, and also an indication of whether or not full fracture of the brace specimens occurred for each of the tests. This can be calculated by the following expression:

$$E_d = \int_0^{t_{max}} F dv \approx \sum_{i=0}^{t_{max}} \frac{F_{i+1} + F_i}{2} (v_{i+1} - v_i) \quad (5.2)$$

where t_{max} is the total test time, F is the lateral force and v is the relative lateral displacement of the frame. These values of dissipated energy shows the difference in energy dissipation for each of the specimens, where it can be seen that the stockier braces such as the B4B specimens dissipate much more than the more slender members due to the fatter hysteretic loops and the characteristic pinching behaviour of more slender members reducing their total energy dissipation. The energy dissipated up to a drift cycle of 1.5% is also documented in Table 5.3, where a similar trend can be observed for each brace specimen. Figure 5.29 shows this trend, where it can be seen that there is a clear relationship between energy dissipation and normalised slenderness of the brace members. Also shown in Table 5.3 is the dissipated energy normalised by the elastic energy stored in the braces, where again, the difference in energy dissipation between the different normalised slenderness ratios is evident.

The maximum PT force for each of the test specimens is also shown in Table 5.3 for both the positive and negative drift cycles imposed on the frame. These values observed in the tests can be compared to those predicted by the expression developed for PT force in Equation 3.25, which is rewritten here for convenience:

$$P_T = P_{T0} + 2k_{pt}(1 - \frac{1}{\Omega})b_h\theta \quad (5.3)$$

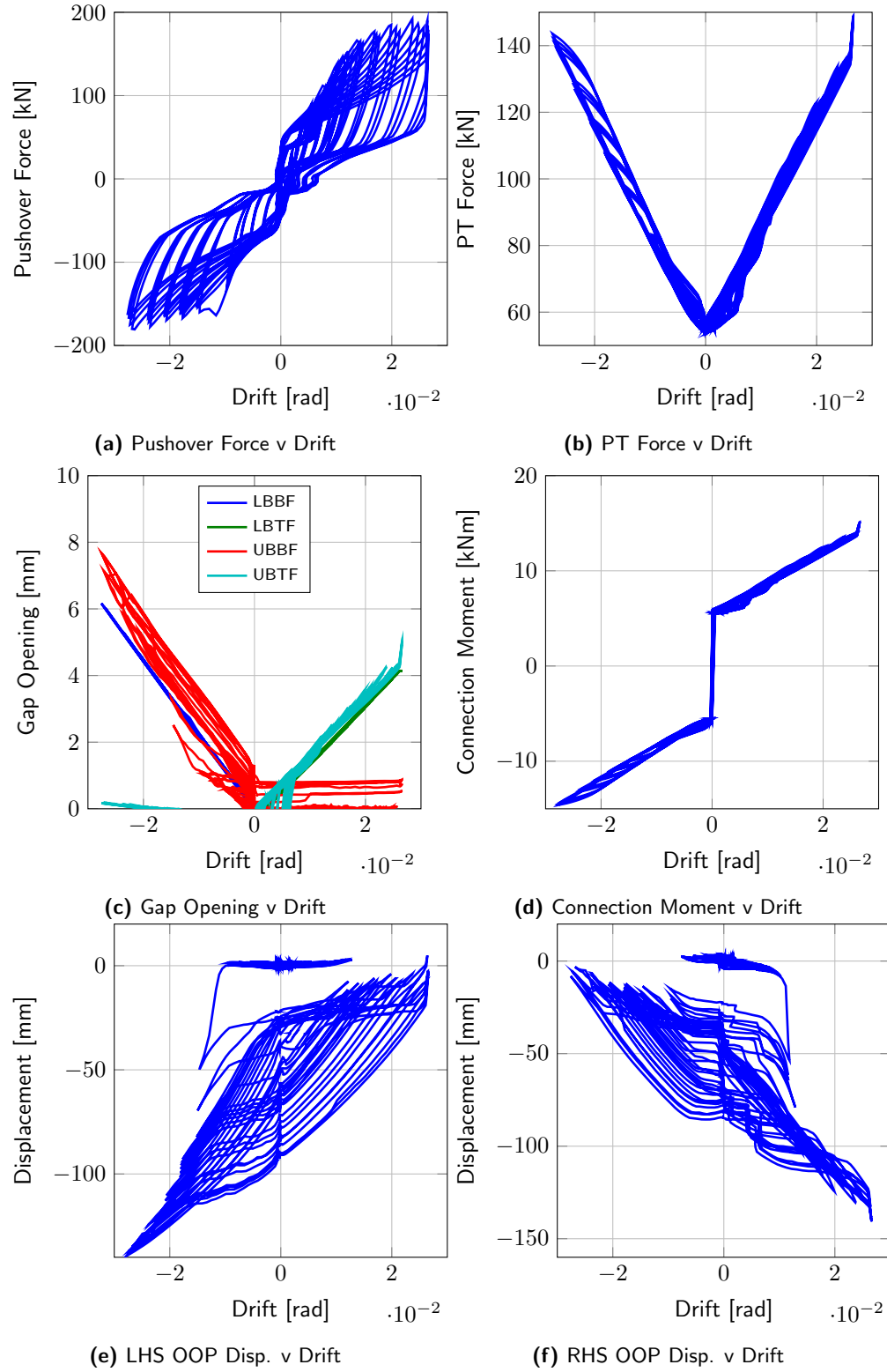


Figure 5.25: B4B test results.



(a) B4B LHS brace local buckling.



(b) B4B RHS brace local buckling.

Figure 5.26: B4B local buckling of braces.



Figure 5.27: B4B specimens after testing.



(a) B4B LHS brace OOP displacement after testing.



(b) B4B RHS brace OOP displacement after testing.

Figure 5.28: B4B OOP displacements after testing.

Table 5.3: Summary of test results.

Specimen ID	B0	B1A	B2A ^a	B2B	B1B	B3A ^b	B4A ^c	B3B	B4B
Drift (+)	[%]	1.78	1.71	1.35	2.54	2.23	2.63	3.37	2.52
Drift (-)	[%]	-1.75	-1.98	-1.69	-2.31	-2.05	-2.07	-3.40	-2.97
Fracture ^d	-/-	-/-	-/R	L/R	L/R	-/-	-/-	L/R	-/-
Pushover Force (+)	[kN]	70.9	93.2	112.5	119.4	107.4	129.4	204.6	129.5
Pushover Force (-)	[kN]	-68.1	-96.8	-113.3	-125.0	-108.5	-121.6	-215.6	-119.3
PT Force (+)	[kN]	129.8	127.8	115.8	151.4	146.1	160.5	169.5	163.1
PT Force (-)	[kN]	130.5	133.9	120.5	157.6	151.1	160.3	166.4	173.7
LHS OOP	[mm]	-	155.1	-	190.3	162.2	141.9	157.4	152.1
RHS OOP	[mm]	-	151.4	-	165.6	166.5	139.4	120.5	139.0
Total Dissipated Energy	[kNm]	2.31	7.72	-	14.61	10.43	16.64	71.93	18.05
Dissipated Energy ^e	[kNm]	-	2.10	-	7.60	4.90	10.35	14.64	11.43
Dissipated Energy/Elastic Energy	-	26.86	-	49.91	62.59	59.39	37.84	65.57	44.38
M_c (+)	[kNm]	7.2	6.5	6.5	6.2	6.1	5.7	5.6	5.3
M_c (-)	[kNm]	-7.3	-6.9	-6.6	-6.6	-6.5	-6.3	-5.7	-5.6
$M_{c,max}$ (+)	[kNm]	13.2	13.0	11.7	16.4	14.1	15.9	14.8	13.8
$M_{c,max}$ (-)	[kNm]	-13.3	-13.6	-12.3	-16.0	-14.8	-14.4	-16.9	-14.6
k_r^θ (+)	[kNm]	339.0	382.4	383.8	400.8	399.0	379.8	321.6	375.5
k_r^θ (-)	[kNm]	340.6	339.9	330.4	407.4	392.9	391.3	339.4	373.3

^aValues represent data in Figure 5.10, and not complete data set due to limited data available from test.

^bBrace OOP data not accurate due to noise and is estimated visually from Figure 5.15e and Figure 5.15f.

^cBrace OOP data not accurate due to noise and is estimated visually from Figure 5.18e and Figure 5.18f.

^dL/R indicates full fracture in both LHS and RHS brace whereas -/- indicates no fracturing of either.

^eEnergy dissipated up to 3 cycles nearest 1.5% drift.

CHAPTER 5. EXPERIMENTAL RESULTS AND OBSERVATIONS

The values for the PT force prediction are then compared to the observed values in Figure 5.30, where the value being plotted on the y-axis for the percentage difference is given by:

$$\text{Percentage Difference} = \frac{(\text{Predicted} - \text{Actual})}{\text{Actual}} \% \quad (5.4)$$

Figure 5.30 shows that the prediction made using Equation 3.25 for the maximum PT force is within 10% for all but two of the tests, with tests B4A and B4B falling outside this range, but still remaining within 20% of the observed value.

The post-decompression stiffness of the self-centering frame (k_r^θ) is calculated in both directions for each test. The values of k_r^θ , calculated from the decompression moment (M_c) and the maximum moment ($M_{c,max}$), are given in Table 5.3 for each test. These are compared to the prediction equation developed in Equation 3.27, which is rewritten here for convenience:

$$k_r^\theta = k_{pt}(1 - \frac{1}{\Omega})b_h^2 \quad (5.5)$$

and the percentage difference between the test values and the prediction are shown in Figure 5.32, where it is observed that all the values recorded in the test fall within 15% of the calculated value. This demonstrates the accuracy of the developed expression in Equation 3.27 for the determination of K_3 of the frame. This has been previously discussed as being critical for the susceptibility of a structure to PDelta effects, which have been shown to be a major factor in the occurrence of residual deformations.

The maximum absolute OOP displacements of the braces are also shown in Table 5.3. These can be compared to a simple expression proposed by Tremblay [120], which predicts the OOP displacement, and is given by:

$$\Delta_{OOP} = \frac{1}{\sqrt{2}} \sqrt{\Delta_a L} \quad (5.6)$$

where Δ_{OOP} is the OOP displacement, Δ_a is the axial displacement of the brace and L is the length of the brace. Figure 5.31 shows a plot of the percentage difference, as calculated by Equation 5.4, for each of the tests except B0 and B2A for the reasons noted in Table 5.3. Figure 5.31 shows that, in general, Equation 5.6 tends to underestimate the maximum OOP displacement of the braces, with the exception of B4A, B4B and B3B. Although Equation 5.6 underestimates the OOP displacement for most of the braces, the predicted values are still within approximately 20% of the actual values observed in the test.

5.5 Sources of Error

As is the case with most experimental testing setups, there are a number of sources of error that effect the results and do not give the ideal behaviour of the frame as intended. Some of these sources of error have been documented and reported during the test results in Section 5.3 and their effects accounted for when interpreting the final results.

The main source of error was the looseness of the frame during testing. This mainly stemmed from the pinned connection under the central column not being a perfect pinned connection and hence allowing some lateral movement between cycles. This was observed during the initial preliminary test runs and a pin with new diameter was manufactured in order to give a better fit with less lateral movement. Nevertheless, there was still some degree of undesirable of movement during the initial cycles after the pin was installed and, hence, the input displacement were modified

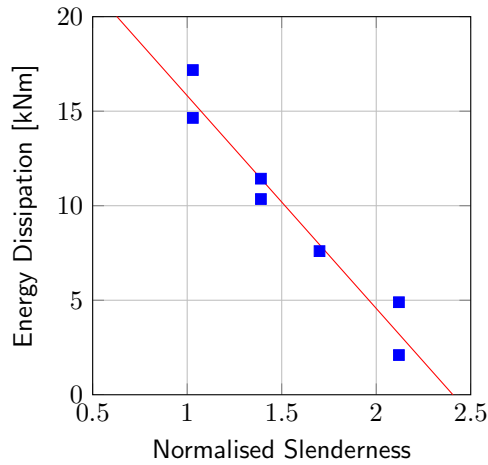


Figure 5.29: Energy dissipation to 1.5% drift versus normalised slenderness.

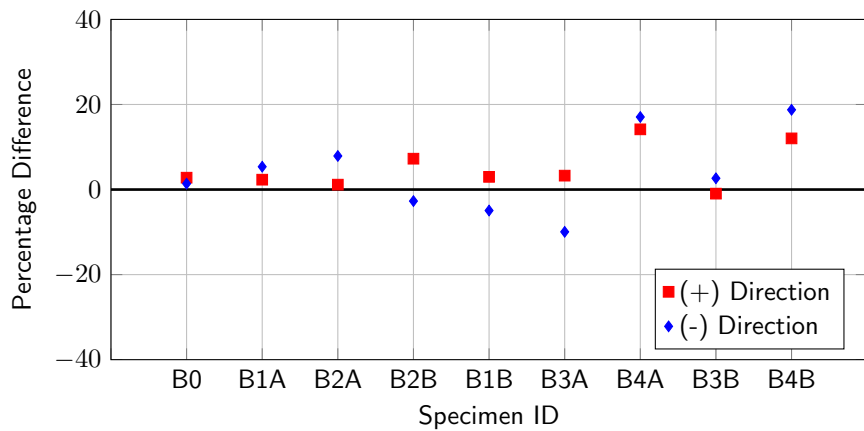


Figure 5.30: Percentage difference of PT forces for each test.

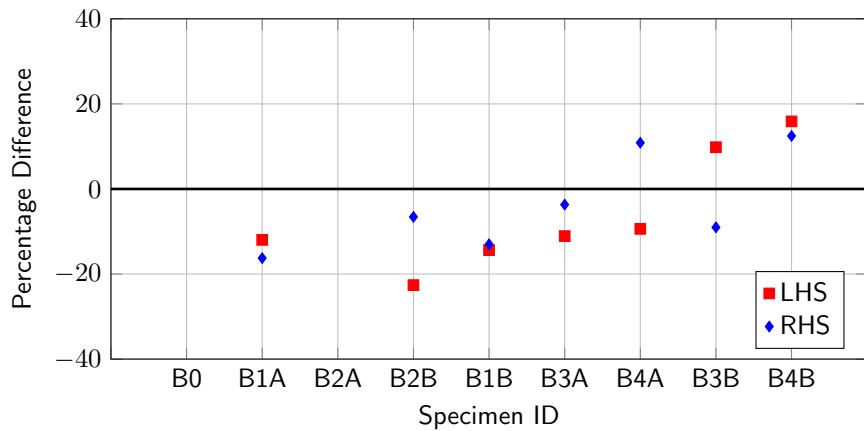


Figure 5.31: Percentage difference of brace OOP displacements for each test.

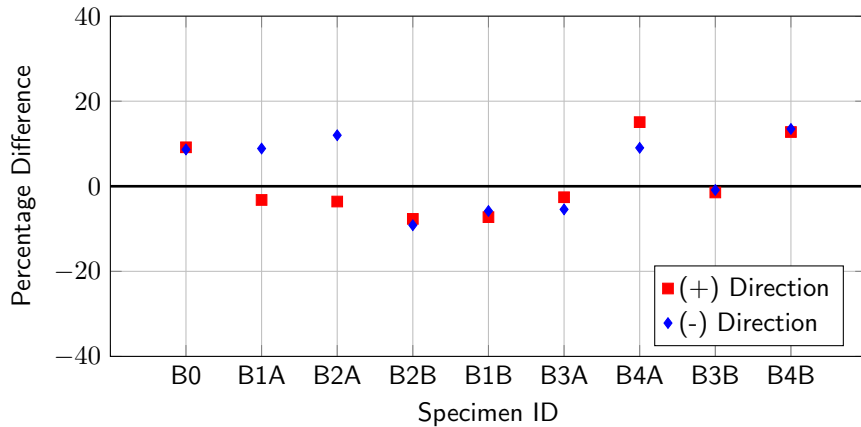


Figure 5.32: Percentage difference of k_r^θ for each test.

to account for the lateral slipping still being observed in the initial preliminary run by adding an extra 5mm to the amplitude of the input displacement waveform for each cycle in both directions.

Upon reviewing the video footage recorded of the testing, it was seen that there was also some unexpected movement in the vertical direction of the left and right hand side columns. This occurred due to uplifting of the column by a few millimetres as a result of the pin at the column base being slightly smaller than the hole it went through. This also allowed the frame to move laterally an extra few millimetres. Furthermore, the beam-column shear tab connection showed a little looseness in that it had a degree of slippage in the vertical direction, and hence provided a degree of movement when the shear from the braces was being transferred through the connection.

Although these additional source of lateral movement observed in the test frame outlined above are problematic for any test, they are not critical when collecting and reporting data from the test frame. This is because the measurement of horizontal displacement or drift was taken from the LVDT's at the beam column connection, so while the frame may also be moving due to these loosenesses mentioned above, the readings used when reporting the results are in terms of relative measures.

5.6 Summary

This chapter first presented the results from the coupon testing that was performed on the off-cuts obtained from each of the brace specimens. The test setup used to test the coupons was first described, followed by the summary of the results obtained, where a complete set of test data is included in Appendix E.

The results of each of the specimens tested in the test frame were then presented. For each of these tests, plots of the results obtained were reported, as well as a description of each test. This included a brief description of each test and the loading cycles that were used to test the frame. The plots of the test data describing the primary behaviour of the system were then presented and a discussion of the findings from the physical experimental testing was presented, which included a description of any observations during the test and the mode of failure for each of the brace specimens. A discussion into the sources of additional unexpected movement in

CHAPTER 5. EXPERIMENTAL RESULTS AND OBSERVATIONS

the test frame that led to some additional flexibility and unwanted behaviour of the test frame was included. This discussion of the test results highlighted a number of important parameters in relation to the behaviour of the SC-CBF. Firstly, the flag-shaped hysteretic behaviour of the frame was demonstrated throughout the testing of all the brace specimens, which is a critical finding of the experimental testing as it validates the self-centering nature of the novel SC-CBF system developed as part of this research. In addition, the gap opening behaviour at the beam flanges in the beam-column connections was demonstrated and the associated behaviours, such as the increases in PT force and the bilinear moment-rotation behaviour of the connection, were also verified. These conclusions successfully demonstrate the behaviour of the SC-CBF is as anticipated from the theoretical developments in Chapter 3.

The salient response parameters of each test were then collected and documented, and comparisons of the test data with previously developed theory were made. The maximum drifts, pushover force, PT forces, and decompression moments were reported for each test. The test values for OOP displacement, PT force and decompression stiffness of the frame were compared to the theoretical values in the relevant expressions reported. It was shown that the test values and predicted values were very close, with the PT forces being within 10% for most of the tests and the OOP displacements generally within 15% of the calculated values. The total hysteretic energy dissipated by each set of brace specimens during each test was also documented, where it was demonstrated that the brace members with a lower normalised slenderness dissipate more energy than the more slender braces, which is to be expected. The post-yield stiffness of the system were also collected from each of the tests and compared to the theoretical values using the expressions developed in Chapter 3. It was seen that the comparison between the theoretical value and the observed experimental values was excellent, with all the values within 15% of the calculated value. This demonstrates the reliability of the post-decompression stiffness in the SC-CBF system, which is fundamental to the behaviour of the system.

CHAPTER 5. EXPERIMENTAL RESULTS AND OBSERVATIONS

Chapter 6

Numerical Modelling of a SC-CBF

6.1 Introduction

This chapter presents the numerical modelling of the SC-CBF frame described in Chapter 4 and 5, which was developed using OpenSees. The modelling of the individual components that make up the SC-CBF frame are first reviewed and these are combined to give the proposed model for the SC-CBF. This is then compared to the analytical expressions derived in Chapter 3 for a simple push-pull analysis to show the model behaves as expected. This model is then validated by comparing the results of the SC-CBF test frame experiments reported in Chapter 5 to give a model that can be used for more extensive analysis of the SC-CBF. A brief discussion of the extension of this model to be used in dynamic analyses in order to evaluate its performance under seismic loading is also discussed.

6.2 Braced Frame Modelling

6.2.1 Braces

The numerical modelling of braced frames has been the focus of much research for the past few years. Numerous parameters have been established that affect the behaviour of the brace within a frame, and these have been identified and calibrated experimentally by many researchers [127, 134, 105].

One of the main difficulties in modelling bracing elements is the ability to accurately capture the effect of brace buckling on the system. Uriz [126] proposed a model in OpenSees [86] that was able to capture this global buckling behaviour for the test specimens used for the calibration. Salawdeh [105] then developed this model using numerous test results from the experiments conducted by Goggins [56] to verify the accuracy of this model proposed by Uriz [126], along with some further recommendations. The model uses the Giuffré-Menegotto-Pinto material model [50] for the steel brace material model, which is labelled Steel02 in OpenSees. This material model accounts for kinematic and isotropic hardening within the steel, as well as accounting for the Baushinger effect during repeated loading. The nonlinear beam-column element proposed by Spacone et al. [113], which is based on the force formulation, is used to model the bracing elements. This element considers the spread of plasticity along the element during loading, as oppose to user defined locations of plastic behaviour, such as the lumped plasticity approach. The advantage of this distributed plasticity approach is that inelastic deformations can take place at any location along the length, rather than user specified locations when using lumped plasticity.

When using this beam-column element for modelling steel braces, the cross section is modelled using a series of fibers along the width and thickness of the section. The integration of this element is based on the Gauss-Lobatto quadrature rule, where a polynomial of order $2p - 3$ is interpolated around p integration points along the element. The two remaining modelling parameters that have significant impact on the brace model behaviour is the number of elements used to model the brace, and the initial imperfection of the brace midpoint, as proposed by Uriz [126]. A minimum number of 2 elements are necessary to cause brace buckling, because a single element will load to compressive yield repeatedly without buckling, which is not the case for conventional tubular braces. This is where the use of the initial imperfection of the brace was proposed by Uriz [126], whereby specifying a small initial imperfection at the center node of the brace elements, the brace will be forced to buckle during the analysis, which is what is expected. A complete breakdown of the composition of the brace elements is shown in Figure 6.1.

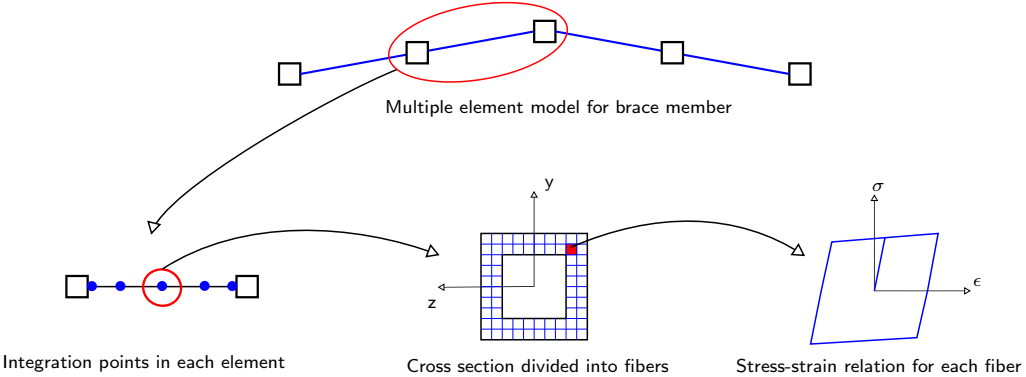


Figure 6.1: Illustration of the composition of the brace member model.

Using the above modelling methods, a number of parameters need to be specified when modelling the braces, such as the number of elements to use, number of integration points and cross section fibers. Uriz and Mahin [127] noted that by using a small amount of fibers in the cross section, there is an increase in sensitivity in the bending moment and axial forces interaction in the element. The behaviour is more sensitive to the number of fibers around the perimeter of the cross section, hence a minimum of 10 to 15 fibers was recommended along the depth of the brace. Salawdeh [105] proposed an expression for square and rectangular hollow sections which depended on the dimensions of the brace to result in the same size fibers around the perimeter for each cross section size. This meant that for smaller cross sections, less fibers could be used and for larger sections, more be used. This expression is given below, where h and b are the brace height and width (in mm), respectively, to give a number of fibers n that have the same physical size regardless of the cross section size.

$$n = \frac{2(h+b)}{3} \quad (6.1)$$

The initial deformation that is required in order to cause the brace buckling is another important parameter. However, it is still relatively open to interpretation. Uriz and Mahin [127] recommended using an imperfection of between 0.05-0.1% of the brace length. On the other hand, in a study by Wijesundara [134], the recommended value was 0.5% of the brace length. Salawdeh and Goggins [106] noted how these values did not accurately represent the buckling load of some of the brace specimens used in that study. For the study by Salawdeh and Goggins

[106], which used test data from Goggins [56] and Nip et al. [90], it was proposed that an initial imperfection of between 0.1 and 1.0% gave the best comparison with the test data in terms of the initial buckling load of the member, where a lower magnitude of imperfection was used for members with a lower slenderness, and a higher magnitude of imperfection was used for more slender braces.

The number of integration points per element is also an important parameter, where Uriz and Mahin [127] reported that using just 2 integration points results in a significant loss of compressive strength in the post buckling range. This was reported to be due to an under integration of the element when using 2 integration points. Hence, a minimum of 3 integration points was recommended by Uriz and Mahin [127]. Similarly, Salawdeh and Goggins [106] also suggested a minimum of 3 integration points could be employed, but noted that by using more integration points per element, less elements could be used. As mentioned previously, a minimum of two elements is required to include the initial imperfection in the buckling brace. This is to be increased if asymmetric buckling of the brace is expected [127], as may be the case with X-braced CBFs. Salawdeh and Goggins [106] conducted a study on the effect of the number of brace elements on the response of the element by comparing 2, 4, 8, and 16 elements and performing a cyclic load on the brace. A similar study was conducted by Santagati et al. [107] where the number of elements investigated was 2, 4, 6, 8 and 28 elements. Both of these studies showed that increasing the number of elements did not have a significant effect on the response of the braces and that a minimum of two should be used when modelling brace members.

While the modelling parameters listed above have been shown to give relatively accurate predictions of the brace response, Uriz and Mahin [127] reported some limitations to using this fiber based modelling. These include the fact that one of the principal assumptions for this element type is that plane sections remain plain and do not distort locally. This is known to be untrue, as there is significant local buckling and deformation in tubular members during buckling, especially in stocky bracing members. Uriz [126] compared the results of the numerical model to those of an actual test where non-compact sections were used. The comparison showed that the results of the numerical prediction with OpenSees diverged quickly from those that were observed during the experiment. Uriz [126] concluded that these modelling parameters described above are not valid for sections that are prone to local buckling, although the effect it has on strength degradation and fracture life may be compensated for in a different way. Also, Eurocode 8 [18] stipulates that only compact, or Class 1, sections may be used for tubular brace members in structures classified as high ductility (denoted DCH in EC8 [18]), which somewhat reduces the significance of this limitation of the brace model. Another issue with this modelling is that initial stress states are assumed to be zero, which is known to be untrue since during the manufacturing process of the sections, residual stress can be as high as 40-80% of the yield stress for certain steel sections [127]. Also during the initial installation, additional stresses can be imposed due to a lack of fit, where during the testing carried out in Chapter 5, it was observed that strains of up to $195\mu\epsilon$ were induced in the braces, which is approximately 17.6% of the yield strain.

6.2.2 Gusset Plate Connection

Another parameter which has been one of the shortcomings of many numerical models in CBFs is the modelling of the connection of the braces to the beam and column via a gusset plate. Traditionally, this connection was modelled as a pinned connection due to the gussets permitting out-of-plane buckling of the braces quite easily and also that numerical models were more focused on accurately capturing brace behaviour without giving significant consideration to the rotational

stiffness of the connection. Wijesundara [134] utilised a model consisting of rigid links, to represent the beam, column and gusset plate rigid zone connection, followed by a nonlinear element of length equal to two times the thickness of the gusset plate, which corresponds to the linear clearance method, to represent the yielding behaviour of the gusset plate. A similar approach was proposed by Hsiao et al. [66], where the gusset plate was represented by a rotational spring stiffness that can be determined from the dimensions and properties of the gusset plate. This study by Hsiao et al. [66] compared the results of a pinned connection, rigid connection and a connection with rotational stiffness to experimental test data. The results showed that the pinned connection underestimated the response while the rigid connection overestimated it. The best match was obtained by inserting three rigid links to represent the rigid zone provided by the beam, column and gusset plate. The connection between the braces and this rigid zone was via a zero-length element with a rotational stiffness determined from the properties of the gusset plate. Figure 6.2 depicts the proposed connection model by Hsiao et al. [66].

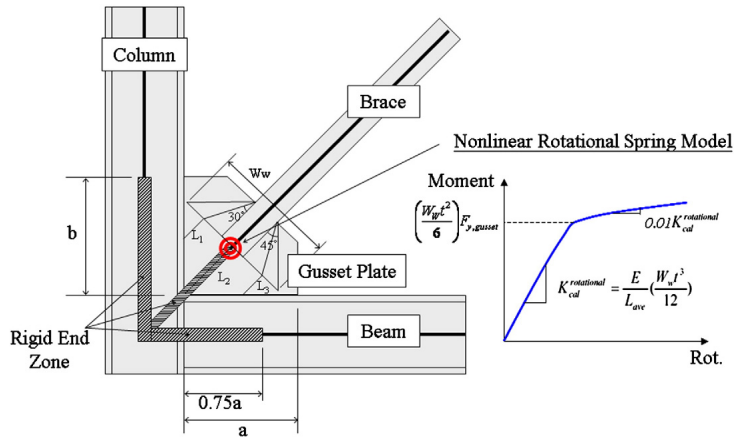


Figure 6.2: Proposed gusset plate connection model by Hsiao et al. [66].

6.2.3 Low Cycle Fatigue Modelling

When braces are subjected to repeated cycles of inelastic behaviour, plastic hinges form in the braces which can induce very large rotational demands and subsequently large strain histories. Continued cycles of these strains can cause rupture in the brace due to low cycle fatiguing of the material. Local buckling within a bracing element significantly increases these local strain demands on the braces and further reduce its fatigue life. This resonates the findings from Section 2.3.3, where it was observed that members more prone to local buckling exhibited a lower fracture life compared to other more compact sections. As previously observed in Chapter 2, the performance of a CBF depends mainly on the performance of its braces. Hence, it is paramount that this effect of low cycle fatigue be accounted for in the numerical modelling of braced frames.

Uriz [126] developed a procedure to account for this low cycle fatiguing effect that could be incorporated into the fiber-based numerical modelling parameters previously discussed for modelling in OpenSees. Since the strain histories of each individual fiber in a cross section, shown in Figure 6.1, are tracked during the analysis, the method proposed by Uriz [126] uses these strain histories to model the fatiguing of the section. A damage index based on Miners rule is proposed for each individual fiber in the cross section, and using a modified rainflow cycle counting method, the damage induced in the fiber under repeated loading is accumulated. Once the fatigue life has been exhausted, which corresponds to the damage index equalling unity, the strength of that

individual fiber is set to zero, effectively removing it for the subsequent cycles of loading. The exact details of this method and how it has been implemented are not discussed here as it has been extensively discussed elsewhere [105, 127, 24].

What is necessary, however, is the parameters used when implementing this low cycle fatigue model into a material in OpenSees. Two parameters are needed to use this, ϵ_0 and m . ϵ_0 is a parameter that approximately indicates the strain amplitude at which one cycle on a virgin piece of that material will cause fracture, whereas m is another parameter which indicates the sensitivity of the logarithm of the total strain amplitude to the logarithm of the number of cycles to failure. These parameters are determined from experimental data and need to be specified in OpenSees by the user depending on the material type and cross sections used. Uriz [126] proposed a range of values for ϵ_0 and m for different cross sections based on the experimental data available at the time. While the results of numerical analysis match the experimental fracture life reasonably well for the sections tested (wide flange sections, hollow structural sections, buckling restrained braces and reinforcing bars), Salawdeh and Goggins [106] cite that only a single section type (6" x 6" x 3/8" HSS) was used to calibrate these coefficients proposed by Uriz [126] for a tubular steel bracing element, which where $\epsilon_0=0.095$ and $m=-0.458$. Salawdeh and Goggins [106] proposed a new set of parameters for the low cycle fatigue of brace members using the experimental work by Goggins [56] and subsequently verified these results using independent testing completed by Nip et al. [90]. The values proposed by Salawdeh and Goggins [106] are $\epsilon_0=0.19$ and $m=-0.5$.

Santagati et al. [107] also conducted a study to determine suitable parameters for use in the low cycle fatigue model proposed by Uriz [126]. This study used a total of 32 specimen results from various experimental programmes to calibrate the parameters. An important aspect to note about the work by Santagati et al. [107] is the assumption that $m=-0.458$, which was proposed by Uriz [126], is constant throughout the calibration, leaving just one variable to be determined in ϵ_0 . Santagati et al. [107] recommends the use of $\epsilon_0=0.07$ for numerical analysis, as this was the lowest value for ϵ_0 obtained throughout the whole set of data, where $\epsilon_0=0.17$ was the maximum and $\epsilon_0=0.12$ was the mean value.

6.3 PT Connection Modelling

When modelling self-centering systems, one of the new concepts that has to be modelled is the behaviour of the rocking beam-column connection in the frame. Since the development of precast rocking concrete systems throughout the 1990's, a number of models have been developed to capture the behaviour of the connection. Christopoulos [29] provides a brief summary of these various models where defining a discrete moment-rotation behaviour for the connection was first utilised by some researchers. Christopoulos [29] then developed 3 methods of modelling the rocking connection in PTED¹ frames and compared these to experimental results. Firstly, a simple model (Figure 6.3) that just involved two rotational springs was investigated and compared to the experimental results from a connection sub-assembly. These results are discussed in Christopoulos et al. [31], and the numerical model developed captures the behaviour of the sub-assembly, both with and without the energy dissipating bars used in the PTED system, with reasonable accuracy.

The drawback to using the bilinear relation developed for the rotational springs employed in this sub-assembly is that when applied to an actual frame, they do not capture the gap opening effect of the frame expansion during connection rocking, as was discussed in Section 3.3.3. These

¹MRF's developed by Christopoulos [29] that self-center by using the rocking connection described here.

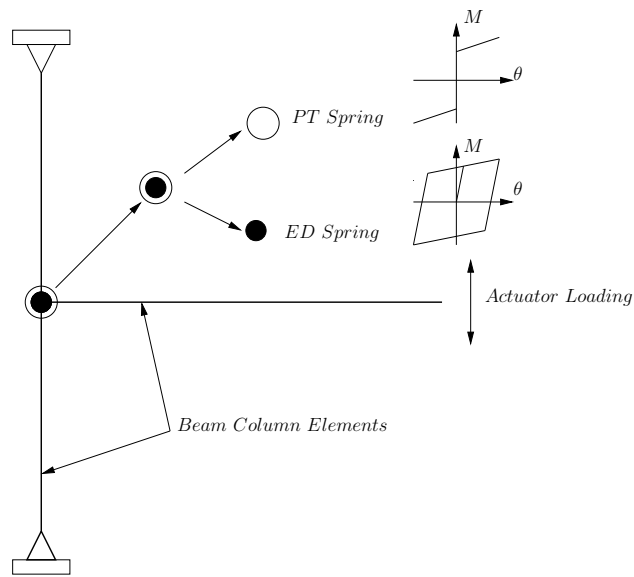


Figure 6.3: Rotational spring model for PTED connection sub-assembly (Adapted from Christopoulos [29]).

rotational springs were then modified to account for this and compared to the experimental results from a 2 bay PTED frame assembly test. The results from the model accurately matched those from the experiment, hence making this modelling of the connection appropriate for PTED frames. Christopoulos [29] reports that although the global behaviour of the frame is accurately captured using the rotational springs at the connections, the effect of the beam depth is not captured directly, but is accounted for in the rotational spring definition. However, the forces induced in the beams and columns due to the gap opening is not captured. Hence, an improved model that accounts for both the beam depth and the forces induced in the system due to the column's restraint is then proposed by Christopoulos [29].

This model proposed by Christopoulos [29] to account for beam depth in the PTED is shown in Figure 6.4. It uses a series of nodes at each connection to capture the behaviour via numerous rigid link offsets and contact springs (CT Springs). The contact springs are placed at the flanges of the beams and are modelled as compression only springs to simulate the rocking of the beam flanges against the column face. The PT elements are modelled as truss elements with an initial strain and are connected to the exterior columns to clamp the beams and columns together, as in the physical assembly. Clayton [37] developed a similar model to this for the shear wall system discussed in Section 2.5, and verified these numerical results to experimental results observed by Kim and Christopoulos [78] and Garlock et al. [53]. Kim and Christopoulos [78] conducted a study into the accuracy of these methods of modelling PT connections in self-centering systems, citing that such models are necessary to enable accurate global response prediction for both other researchers using PT connections and practising designers. Kim and Christopoulos [78] concluded that these methods of connection modelling developed by Christopoulos [29] capture the behaviour of the PT connections reasonably well within the design drift range, but finite element models should be employed to investigate the behaviour beyond the design drift limits to investigate failure mechanisms that aren't possible in more simple models. Recommendations are also made for the number and axial stiffnesses of the springs that achieve satisfactory results without causing numerical difficulty for general systems that use the PT connection.

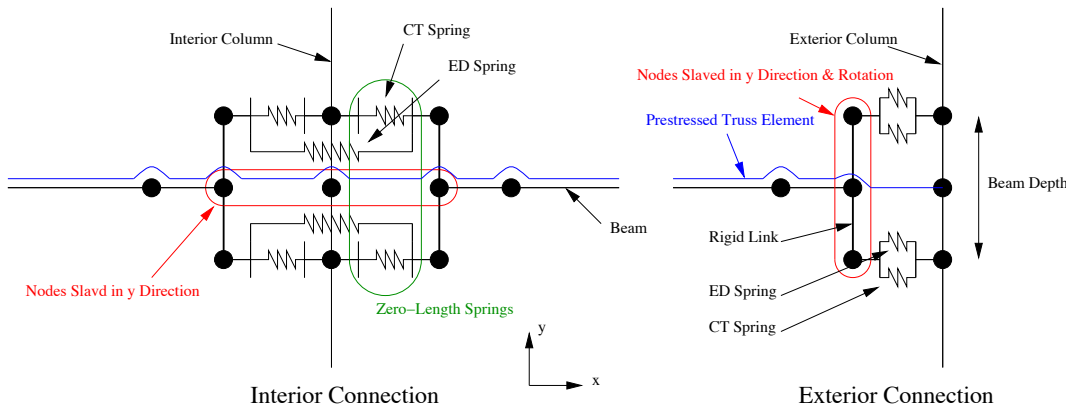


Figure 6.4: Spring model accounting for beam depth (Adapted from Christopoulos [29]).

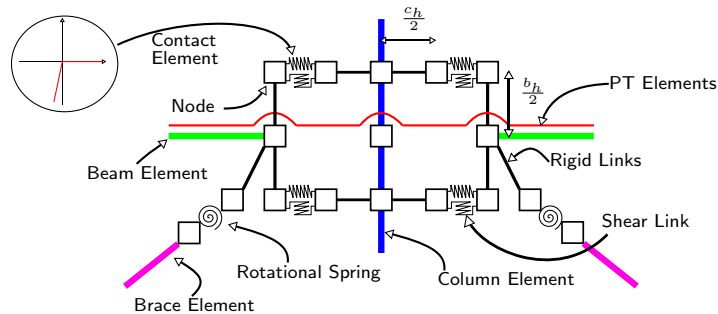


Figure 6.5: Proposed spring model connection used for SC-CBF arrangement.

The successful application of this rocking connection that accounts for beam depth in numerous different systems by different researchers [29, 37, 78] demonstrates its applicability to rocking connections in self-centering frames.

6.4 Proposed SC-CBF Model

The modelling of both braced frames and PT connections using OpenSees has been discussed, and from this, it is seen that a vast amount of information is available on the modelling and validation of these models. Since the proposed SC-CBF is a combination of both a CBF and PT connection frame, these modelling parameters are then combined to give a numerical model for the SC-CBF. Figure 6.5 shows a schematic of the nodes and springs used in the connection of the middle column to the corresponding beams, columns and braces.

For the brace members, 4 nonlinear force-based elements with 5 integration points per element are used to model the braces, and these elements have a 0.5% initial camber to induce global lateral buckling of the braces. The corotational transformation is used to model the braces due to the large displacements experienced during buckling, as proposed by Uriz [126]. The braces are modelled with a series of fibers across the cross section with 20 fibers along the width and depth of the brace and 5 fibers along the thickness of the brace section. Each of these fibers consists of a material model, which for the steel is the Giuffré-Menegotto-Pinto material model, or Steel02, as labelled in OpenSees. This material is assigned a yield strength equal to the material property assumptions and a post-yield stiffness ratio of 0.005 is assumed. The low-cycle fatigue model proposed by Uriz [126] is used to model the fatigue of the brace elements with the fatigue

parameters ϵ_0 and m proposed by Santagati et al. [107] are used. The parameters for the fatigue model proposed by Salawdeh [105] are also considered valid for the modelling of the braces, but since 4 elements are used for these braces, and 2 elements are used by Salawdeh [105], it is not possible to use these. This is because the parameters developed by both Salawdeh [105] and Santagati et al. [107] are for different numbers of elements, (Santagati et al. [107] uses 4 elements per brace), where different strains are being tracked in the elements. Since this strain in the elements is not actually the real strain because of the assumption that plane sections remain plane during buckling, this represents a pseudo-strain in the element. Thus, when using the low cycle fatigue parameters proposed by the authors listed, it is vital that the same number of elements and fibers are used such that the same pseudo-strain is being tracked for the fatigue model.

The connection of the braces to the beams and columns has often been considered a pinned connection in the past, whereas in actual fact it is not. Taking this fact that there is some rotational stiffness present in the gusset plates, a preliminary rotational stiffness of 10kN/m has been assigned to the gusset plate connection. This value is a reasonable assumption if compared to a rotational stiffness value that would be obtained from a typical gusset plate using the formulas given in the connection model proposed by Hsiao et al. [66] in Figure 6.2. During analyses where a gusset plate size and dimensions are known, this stiffness may be changed to a bilinear model with the properties proposed by Hsiao et al. [66], instead of the nominal value assumed initially.

The beam and column members are also modelled using force-based beam column members with one element per member, and 5 integration points along each element. 5 fibers are used along the flange width and web depth and 2 fibers used along flange and web thickness's. The material model is the Steel02 material model, as with the brace members. The P-Delta transformation is used for the columns in order to take into account the second order geometry effects caused by gravity loads during lateral loading. The beam elements, however, use a linear geometric transformation.

The PT elements are modelled using truss elements and the bilinear steel material model, labelled Steel01 in OpenSees. This material is then used to form the PT element material using the initial strain material, initStrain, which essentially applies an initial strain to the steel material. The initial PT force P_{T0} in the tendons after elastic shortening of the beams is converted into a strain using simple mechanics and, hence, applied to the material. Due to the fact that there is an initial strain in the PT elements but not the beams, there is a small loss in the PT force before lateral loading even begins in OpenSees. This is because the force present in the PT elements gets reduced due to the axial shortening of the beams. Hence, it is necessary to apply an artificial increase in the initial strain applied to the PT elements material in OpenSees to account for this. The following expression gives $\overline{P_{T0}}$, which is the force to be applied to the element in order to give the intended force being present:

$$\overline{P_{T0}} = \frac{P_{T0}}{1 - \frac{k_{pt}}{k_{pt} + k_b}} \quad (6.2)$$

where k_{pt} and k_b are the axial stiffnesses of the PT elements and beams, respectively.

The contact springs placed at the beam flanges which make up the rocking connection are modelled using zero-length elements. These springs are assigned a material model called elastic no-tension material, which essentially means it is a contact spring as a large stiffness is applied in compression. Hence, the contact springs nodes are free to move apart, but are met with a large stiffness when put into compression. These contact springs have no resistance in rotation,

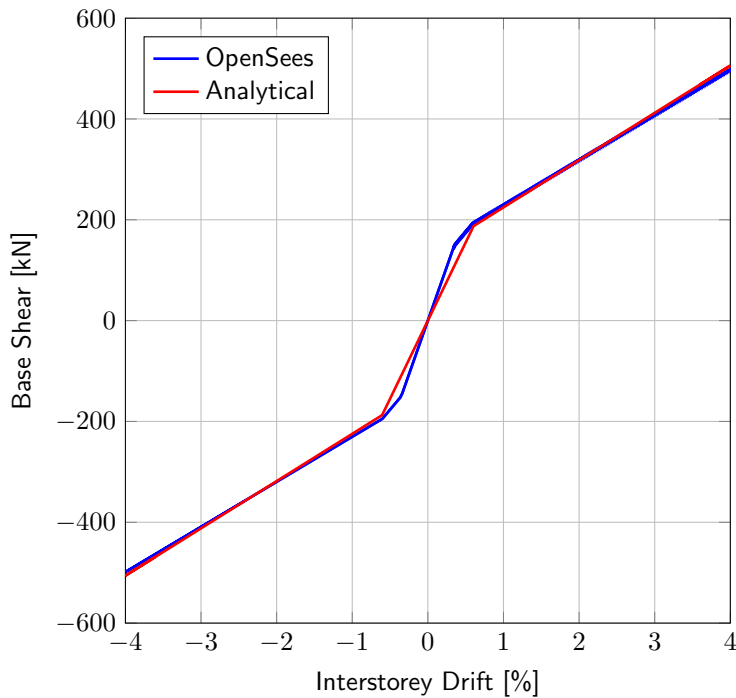


Figure 6.6: Base shear versus interstorey drift for the SC-CBF with PT elements only.

but the shear resistance is made very large in order to prevent the shear force causing large displacements. The shear force in these springs can then be monitored to calculate the connection shear force. The compressive stiffness of these contact springs was reported by Kim and Christopoulos [78] to be a sensitive modelling parameter, where it was suggested to use a value between 10 and 20 times the axial stiffness of the beam elements to avoid any convergence issues.

6.4.1 Response of a PT Frame

The response of a 2 bay frame with no braces is examined when subjected to a static cyclic load. The example frame has a bay width of 6m and a storey height of 3.2m. The beams that are used in this example are the European Sizes IPE600 and the columns are HE320B. The PT arrangement consists of 2 no. 30mm diameter cables.

The beams and columns are modelled using the aforementioned force-based element, whereas the PT elements were modelled using the truss element with a 500kN initial force applied. The base connection of the frame is modelled as pinned at the base of all three columns and the frame is cycled through an interstorey drift of $\pm 4\%$. Figure 6.6 shows the base shear versus interstorey drift for the frame when modelled in OpenSees. This demonstrates the bilinear elastic behaviour of the PT frame without and bracing elements.

Figure 6.6 also shows the comparison between the OpenSees analysis and the analytical prediction using the equations derived in Section 3.3. It is seen that the analytical expressions predict the response very well for the SC-CBF with only PT elements present. On the other hand, the analytical expression developed slightly underpredicts the initial stiffness of the PT frame. This is due to the assumption made in the derivation of this expression that all four rocking connections

decompress at the same time, whereas the OpenSees model demonstrates that while they are close together, they are not exactly at the same location. This is not critical to the frames behaviour as the final decompression point is accurately captured and the post-decompression stiffness is excellently matched, which is a more critical aspect of the frames behaviour.

6.4.2 Response of a SC-CBF

Using the same frame setup seen in the previous section, two tubular steel braces are now added to the model to examine the response of a complete SC-CBF, as discussed by O'Reilly et al. [93] and O'Reilly et al. [95]. Two 100x100x6.3-HSS brace members are inserted to the model with the modelling parameters previously outline in this section. Figure 6.7 shows the response of the SC-CBF, and it is seen that there is now the increase in base shear and energy dissipation due to the axial yielding of the braces under cyclic loading. Furthermore, the frames exhibits the intended self-centering behaviour that is expected from the SC-CBF.

Figure 6.7 shows the comparison between the numerical results from OpenSees and the analytical results from the equations previously derived. From this, it is seen that the analytical expressions derived for the SC-CBF compare well with the results obtained from the OpenSees simulation. The initial stiffness of both the analytical and numerical predictions match each other closely during positive direction loading, although the displacement at which the reduction in lateral capacity due to the RHS brace buckling are different, with the numerical model's RHS brace buckling at a larger displacement than determined by the analytical expressions. This difference in lateral displacement at which buckling first occurs is relatively small although the impact it has on the lateral load capacity plot is more pronounced, with the additional capacity provided in the numerical model leading to a difference in capacity at around +0.5% drift. However, once the RHS brace buckles, and the frame is pushed towards the target drift of 4%, the two plots approach similar lateral load capacities, limiting the influence of this difference in capacity between the two plots at the design drift level.

When the frame is being pushed from the +4% back through the zero drift point and into negative direction loading, the analytical expressions assume the same initial stiffness and buckling displacement as in the positive direction, which is evident in the fact that the two plots of positive and negative loading for the analytical model are mirror images of each other. For the LHS brace in the numerical model, which has been elongated through tensile yielding in the positive direction, the buckling capacity for this member is much less as the brace now has a longer length and hence, buckles more easily. For the RHS brace, which has been buckled in compression in the positive direction, this brace must restrengthen before it can pick up load in the negative direction. Noting these two remarks, it can be seen that the load capacity of the numerical model when being unloaded from the positive peak, and into the negative direction is somewhat different to the idealised capacity of the analytical expressions as the LHS brace has buckled much earlier than the analytical model and the RHS brace is still straightening out before it can pick up load in tension for this cycle. If the frame is pushed in the negative direction initially, followed by the positive direction, the same behaviour is observed in reverse. Considering the above discussion, it can be concluded from Figure 6.7 that the modelling parameters previously described accurately capture the behaviour of the SC-CBF.

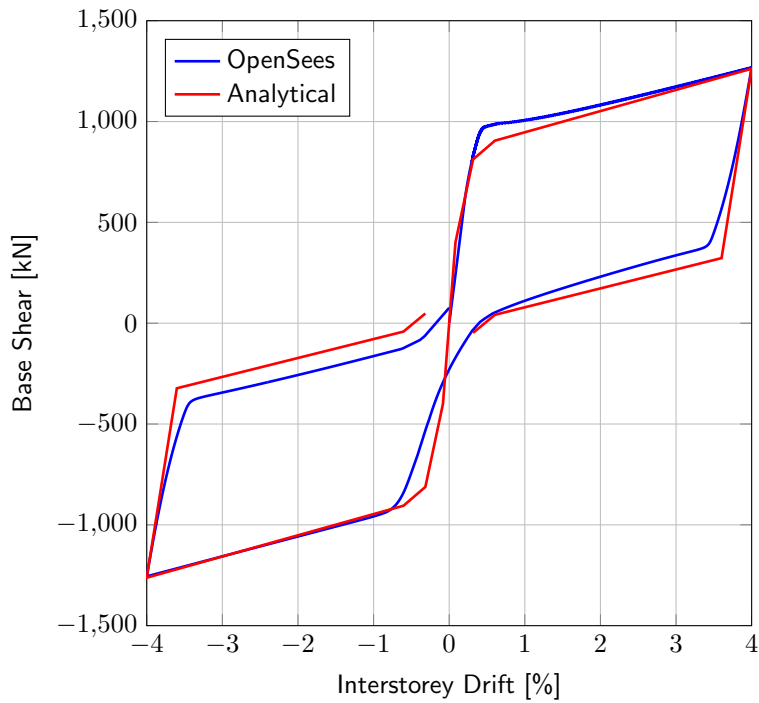


Figure 6.7: Base shear versus interstorey drift for the SC-CBF.

6.5 Validation of Proposed Model

6.5.1 Overview

In this section, the proposed SC-CBF model outlined in Section 6.4 is validated through comparisons with the experimental testing performed on a SC-CBF test frame described in detail in Chapter 5. The model developed for the test frame is first presented followed by comparisons of salient response parameters from the model with the test frame for each of the specimens tested.

6.5.2 Modelling of SC-CBF Test Frame

As the test frame presented in Chapter 4 is a slightly alternative arrangement, as it is arranged to suit laboratory conditions, a special model is developed for this test as opposed to the model used to demonstrate the behaviour of the SC-CBF in the previous section. A schematic diagram of the model is shown in Figure 6.8, where the same modelling parameters outlined in Section 6.4 are used for this model.

This model is then compared to the test results presented in Chapter 5 for each of the specimens tested, where the section sizes are changed in the model between tests. As the PT force was observed to be decreasing during the tests from the initial 80kN, the actual measured initial PT force at the time of testing was used in each of the models.

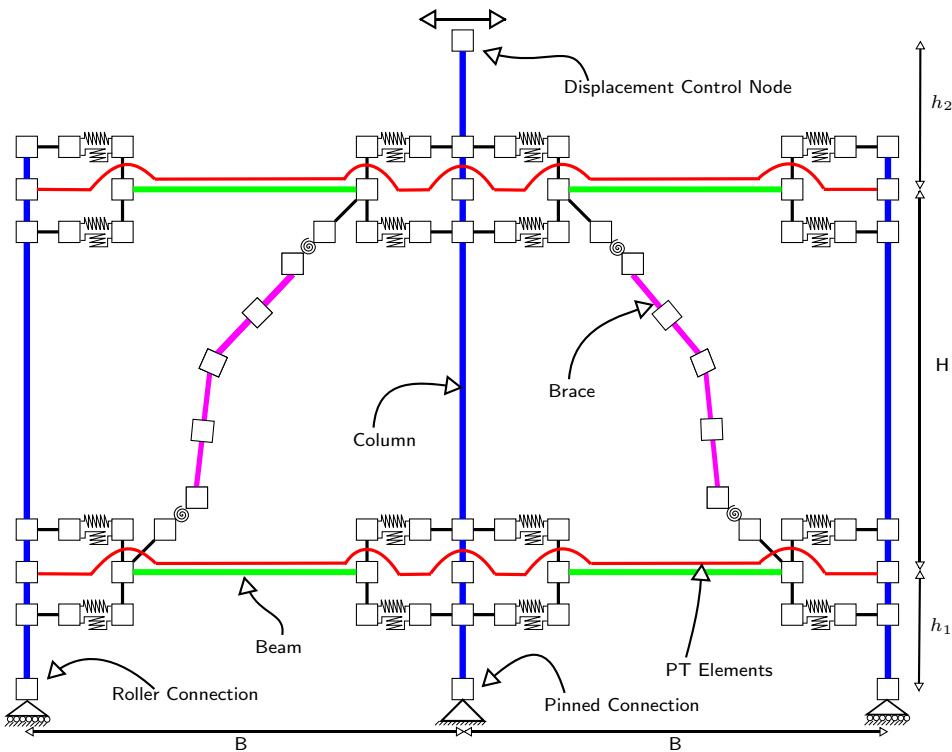


Figure 6.8: Test frame model used for SC-CBF model validation.

6.5.3 Model and Test Results Comparisons

Specimen B0

Comparisons of the results from the physical experiment, discussed in Section 5.3.2, and the numerical model in OpenSees are shown in Figure 6.9 for the bare frame (i.e. specimen B0). It can be seen that the plot of the pushover force versus drift in Figure 6.9a are in good agreement with the same initial and post yield stiffness. The slight kink in the plot of the test results in the negative direction is due to the looseness of the physical test frame (that is, additional movement in the pin connection at the column bases due to manufacturing tolerances), and is not thought to be an actual characteristic of an idealised frame behaviour. Figure 6.9b shows the plot of PT force variation versus drift, where it can be seen that these plots show reasonable agreement. The differences are primarily due to the gradual loss in PT force during testing, as was reported in Section 5.3.2, and it is evident that this loss is causing the gradual deviation from the numerical models results with increasing cycle amplitude. There are some loops in the test data which are not present in the numerical model in Figure 6.9a, as there are no dissipating brace specimens in the system. This was documented during the experiment as a result of the friction and flexibility of the test frame setup employed, and not a characteristic of the SC-CBF's behaviour.

Figure 6.9c shows the plot of the gap opening at the beam flanges and shows that the numerical model and test results are in good agreement, as the magnitude and slope of the results from numerical model and physical test are similar. Figure 6.9d shows the connection moment due to the PT force and again it is seen that the numerical model and physical test match very well. It also evident from this graph that the PT force is reducing, as the decompression moment is slightly reducing over repeated cycles. However, this is not critical when demonstrating the

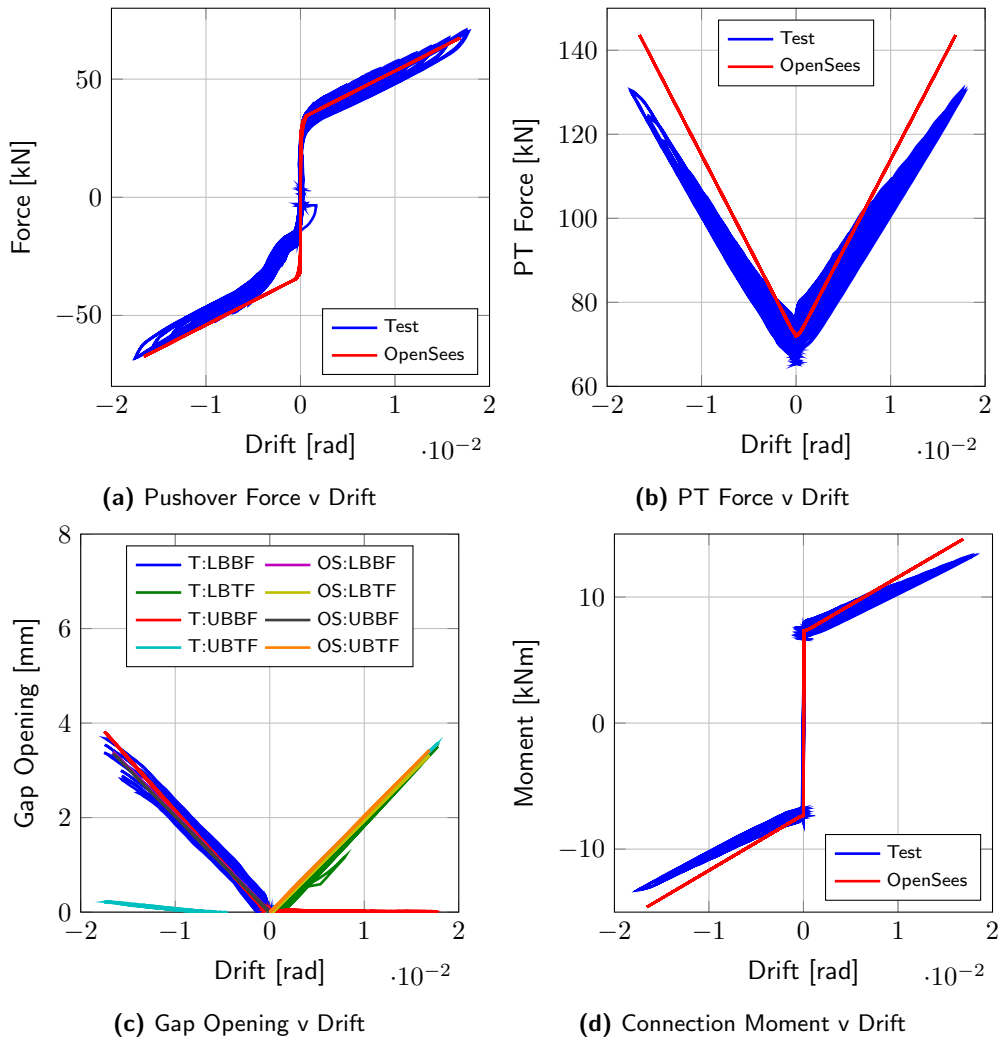


Figure 6.9: B0 test and model comparison.

accuracy of the numerical model to mimic the salient features of the response of an idealised frame.

Specimen B1A

Figure 6.10 shows the comparison of the test results from specimen B1A, which contains 20x20x2.0SHS members, with the OpenSees model. It should be noted initially that as there was a significant amount of unintentional looseness and flexibility in the physical test frame, the input displacement cycles were not exactly what the test frame experienced, although attempts were made to minimise this effect on the system ductility as discussed in Section 5.3.3. The outcome of this is that for the numerical model, where there is no additional flexibility or looseness, the input displacement is exactly what is experienced by the frame. Hence, it will be observed in this test specimen results, and all specimens, that the displacement amplitude during cycles do not match between experiment and model. This is not critical as it is the general trend of the response parameters that are of interest. This is demonstrated in Figure 6.10a, where the general shape and amplitudes of the force-drift hysteretic behaviour for the physical test and the OpenSees numerical model are similar despite having different cycle amplitudes. This shows

that the model and the test frame are in good agreement, although there is a small difference in post-decompression stiffness, where the test shows a slightly larger stiffness than the numerical model. This is due to the post-decompression stiffness being slightly larger than anticipated, as was observed in Figure 5.32.

For the variation of PT force with drift, Figure 6.10b shows a very good agreement between the two plots and for the gap opening displacement in Figure 6.10c, the amplitudes and slopes are similar with the exception of the bottom flange LVDT on the lower beam. This was reported in Section 5.3.3 to be due to the instrument gradually becoming loose during the test and hence returning incorrect results. However, the trend is still evident. The plot of connection moment in Figure 6.10d again shows excellent agreement between model and test.

Figure 6.10e and 6.10f show the out-of-plane (OOP) lateral displacements of the brace elements at midlength during loading. During the actual testing, the braces buckled in opposite directions (i.e from the point of view of the top diagram in Figure 4.1, the LHS brace buckled out of the page and RHS brace buckled into the page). When specifying the initial imperfection in the brace elements used in the OpenSees, the direction in which this imperfection forces the brace to buckle needs to be specified. Since it was observed from testing which directions the braces buckled, the initial imperfection was specified in order to represent this. It can be seen that the model predicts this buckling behaviour very well, thus demonstrating the validity of the brace modelling in the SC-CBF model.

Specimen B2A

As discussed in Section 5.3.4, problems with the instrumentation during testing meant that only a limited amount of test data is available to discuss this specimen, which is a 25x25x2.5SHS. It is presented here nonetheless, and the plots of the comparison between the test and OpenSees model can be seen in Figure 6.11. Due to the lack of a complete data set it is difficult to make definite comments about the comparisons. Nonetheless, the same general trend for each of the plots is observed as for the B1A specimen. The connection moment versus drift plots shows excellent agreement, as does the change in PT force. The OOP displacements of the braces seem to follow the same general trend of the OpenSees, but these are just small observations. The gap opening plots in Figure 6.11 show a reduced data set from the test as these instruments were not recorded for the whole test.

Specimen B2B

Figure 6.12 shows the comparison between the test results obtained from the B2B specimen (25x25x2.5SHS) and the numerical model. A complete data set was obtained during the test and hence the model can be better evaluated using these results. Figure 6.12a shows the pushover force against drift and it can be seen that the test results and the model are in good agreement, although the post-decompression stiffness can be observed to be slightly larger in both directions, which can be related to the higher post-decompression stiffness observed in Figure 5.32 for this test. Similarly the numerical model predicts with very good accuracy the PT force and the connection moment, as seen in Figure 6.12b and 6.12d. The brace OOP displacements are also well represented by the model although the numerical model appears to under-predict displacements at the brace midpoint by approximately 15mm for a given drift level, (i.e. at maximum drift).

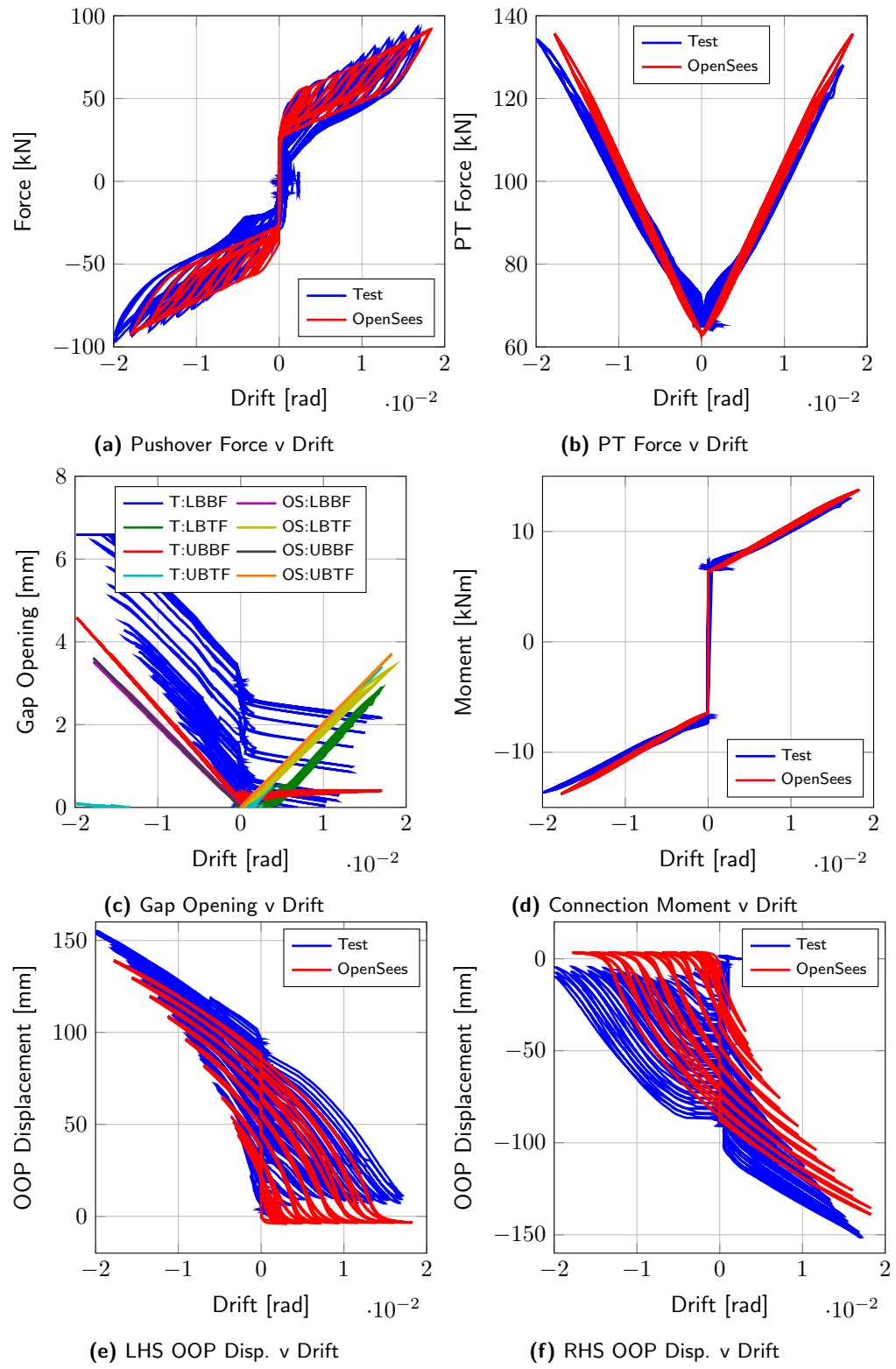


Figure 6.10: B1A test and model comparison.

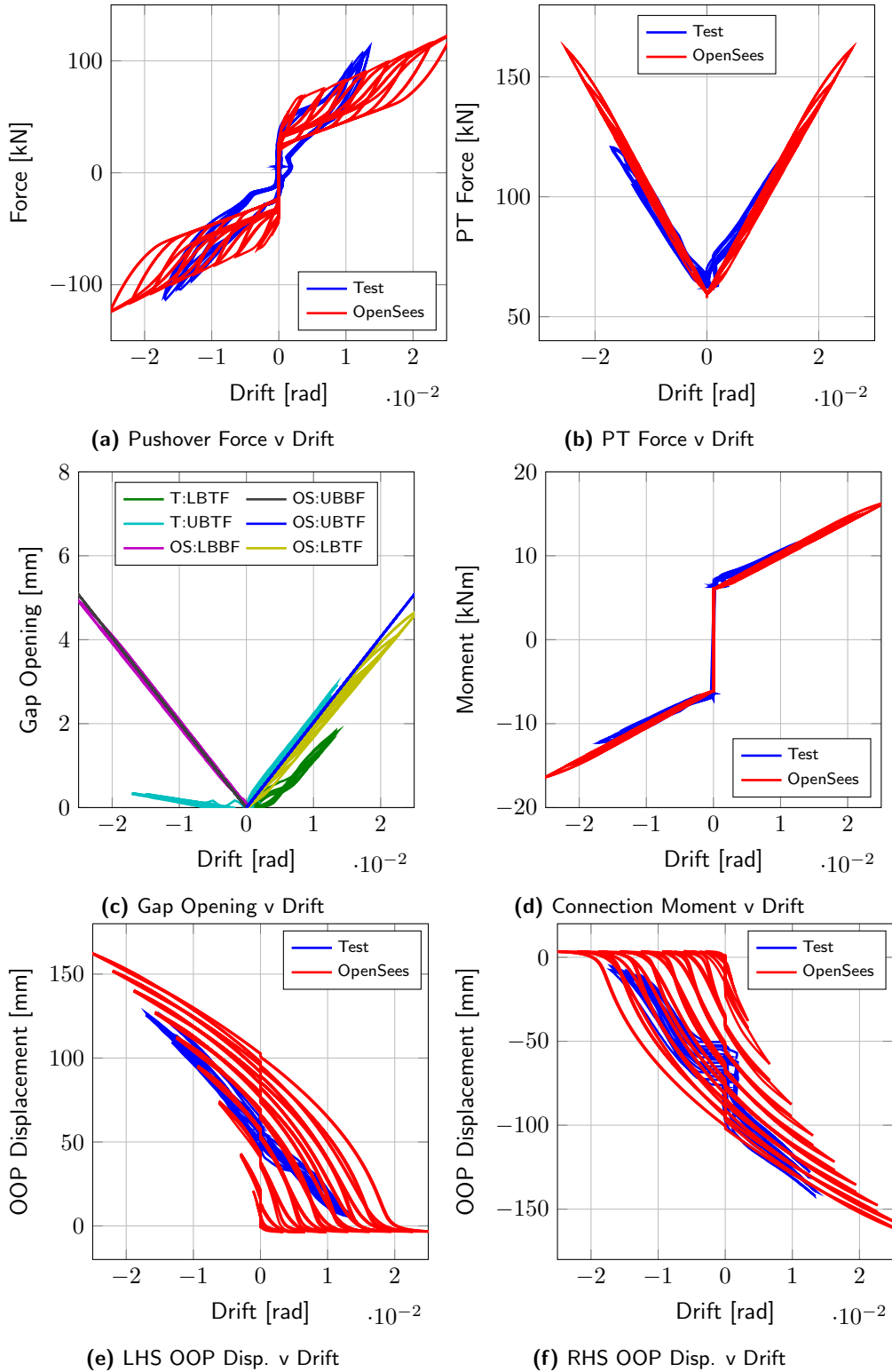


Figure 6.11: B2A test and model comparison.

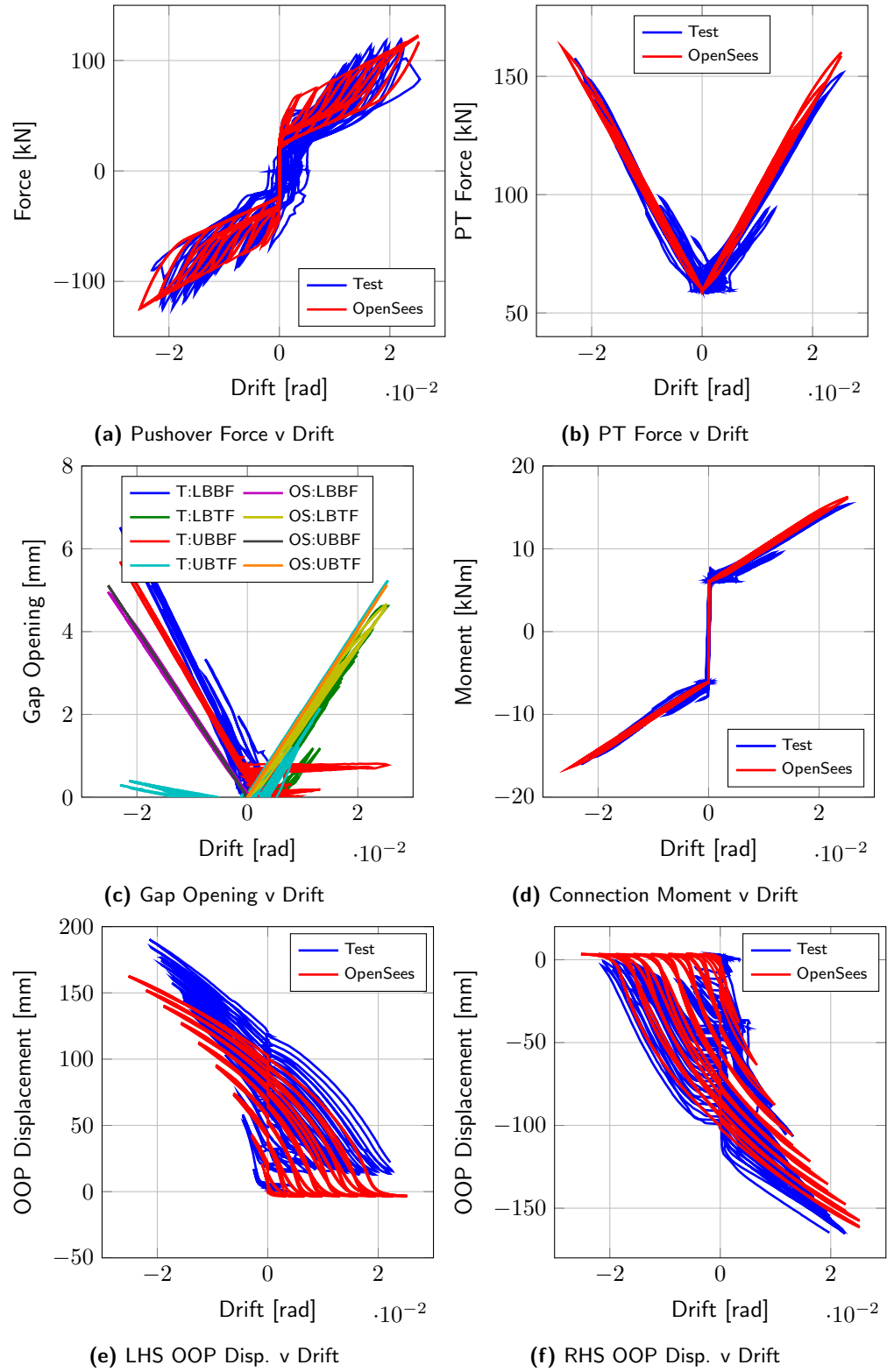


Figure 6.12: B2B test and model comparison.

Specimen B1B

Figure 6.13 shows the comparison between the test results and OpenSees model for the B1B specimen, which contains 20x20x2.0SHS brace members. Again it is seen from the plots of pushover force and PT force versus drift that the model provides a satisfactory prediction of the response when compared to the test results. The plots of connection moment and gap opening also demonstrate this fact also. Furthermore, the brace OOP displacements are well represented, as seen in Figure 6.13e and 6.13f.

Specimen B3A

Similar to other tests, the numerical model predicts the salient behaviour of the test frame very well for B3A specimen with 30x30x2.5SHS braces as is evident in Figure 6.14. It is noted once again, that the LVDT measurements that produce the values for the gap opening were not reading properly during testing. Hence, one of the plots in Figure 6.13c gives incorrect readings. Also, the string pots used to measure the OOP displacement of the braces were producing a lot of noise, but the results were included as the general trend of the buckling is still obvious and matches the model very well. The post-decompression stiffness of the test frame is seen to be slightly higher to that of the OpenSees model. Consulting Figure 5.32, it is seen that the test value is slightly higher than predicted for this test also.

Specimen B4A

Figure 6.15 shows the comparison between the B4A test specimen (40x40x4.0SHS) and the OpenSees modelling. The plot of pushover force versus drift in Figure 6.15a shows reasonable agreement between the physical test and the numerical model. The PT force and connection moments are closely predicted by the numerical model at the full range of drifts imposed. The brace OOP displacements recorded during the physical tests contain a lot of noise, similar to the B3A test specimens. However, they are shown here again as the general shape and trend of the results is still evident. The plots are offset slightly, as when the data was zeroed in the post processing, the amount of noise in the data meant that the zeroing was not very accurate. The results are included in any case.

The plots of the PT force and gap opening versus drift show some area under the loops from the OpenSees model, which doesn't actually correspond to energy dissipation, but the way in which the experiment was setup, as the gaps were not opening as originally anticipated. This is due to the pushover force being applied to the central column only, and since the B4B specimens are very low slenderness, the gap opening in the frame is restricted. This causes the unexpected behaviour seen in the gap opening plots and also in the PT force plots for the OpenSees model and the physical test results. If the pushover force being applied to the frame is over the three columns and not just via the central column, as it would be more common in a design situation, this issue of gap opening restriction is overcome and the frame behaves as expected. This was observed during further analysis using the OpenSees model to investigate the cause of this behaviour observed in the numerical model and physical test for the B4B specimens. It is therefore concluded that this observed behaviour is not an issue when considering the response of the SC-CBF for future designs, but rather a limitation of the current test setup.

Specimen B3B

Figure 6.16 shows the comparison between the B3B specimens (30x30x2.5SHS) and the OpenSees modelling. As with the previous test result comparisons, the modelling is shown to be a good

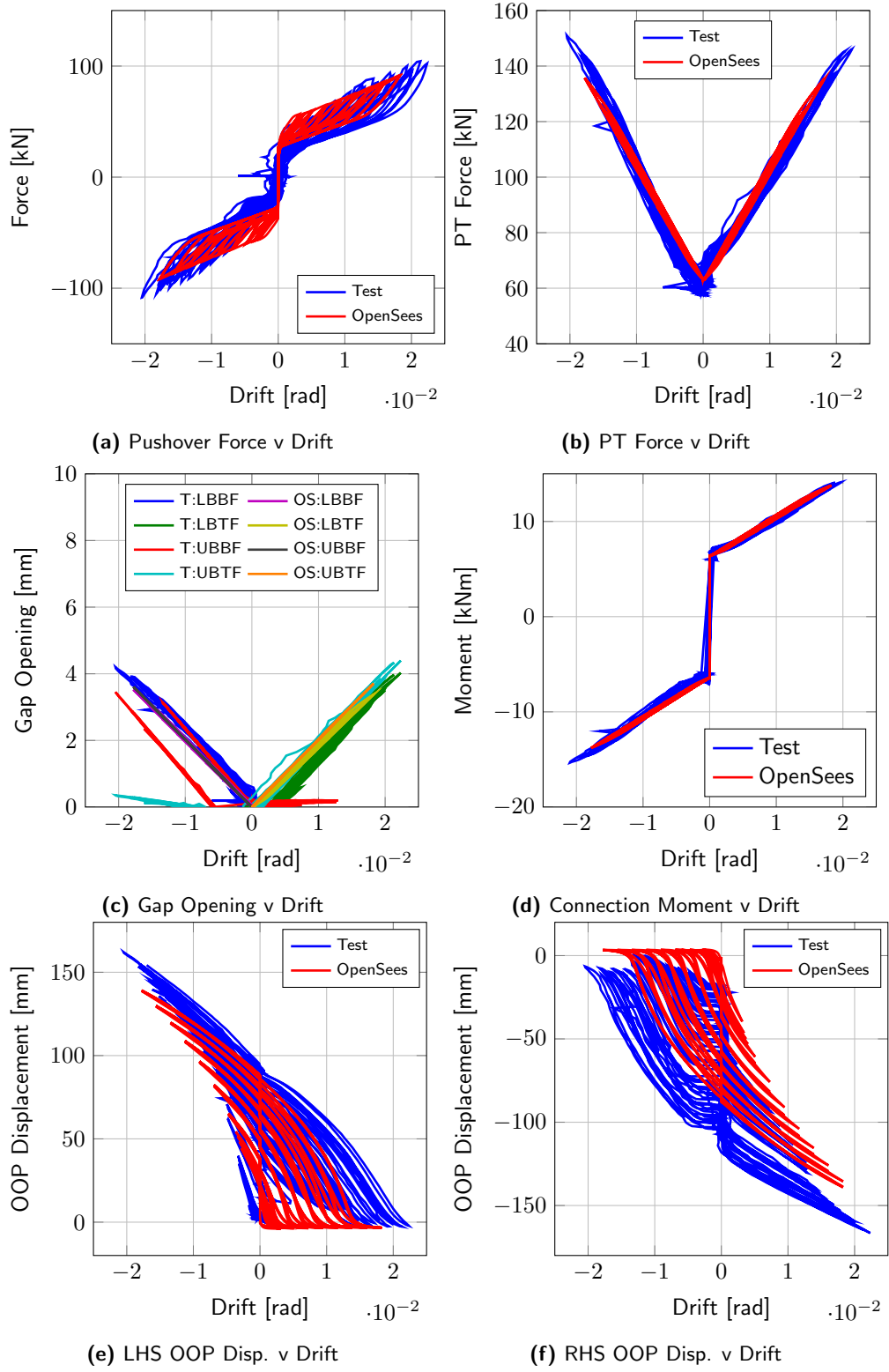


Figure 6.13: B1B test and model comparison.

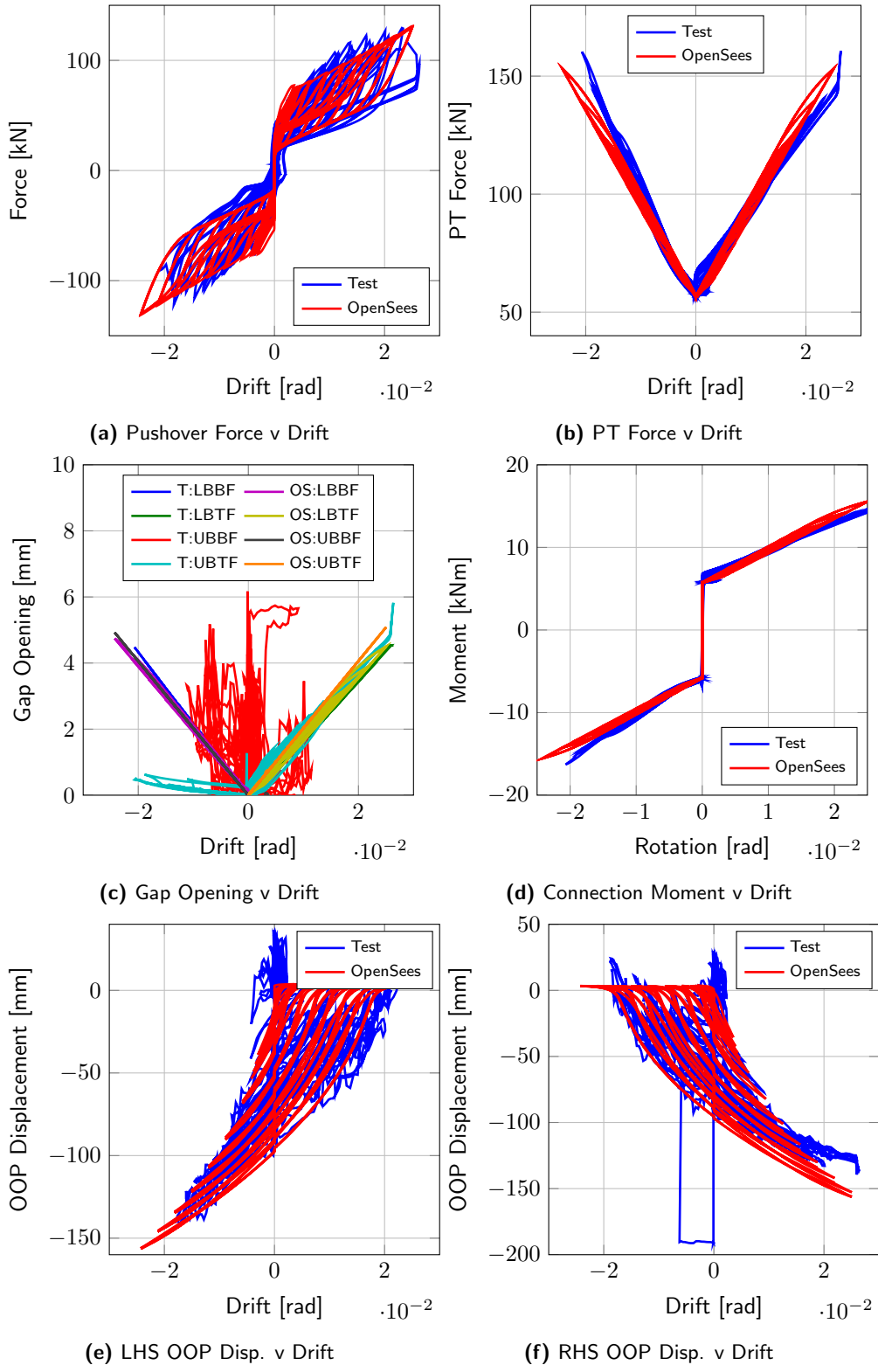


Figure 6.14: B3A test and model comparison.

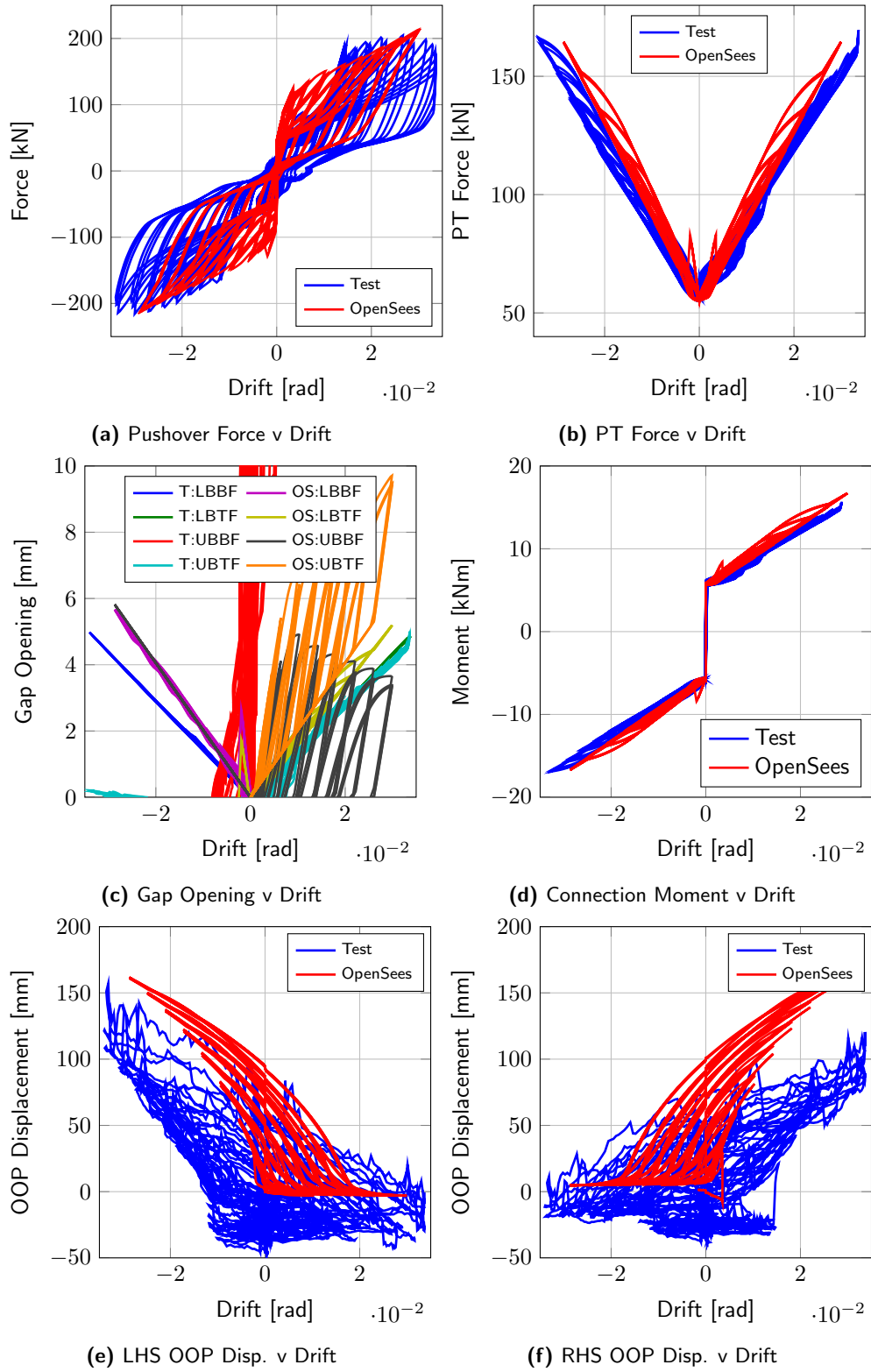


Figure 6.15: B4A test and model comparison.

predictor of the behaviour of the test specimens. The pushover force versus drift plot shows good matching and the same matching is evident in the plots for PT force and connection moment. In contrast to the previous test on the T3 section sizes, the issue with the instrumentation was resolved for this testing and a better match can be seen as the noise associated with the brace OOP string pots has been resolved and the quality of data from the LVDT's placed on the beam flanges has been improved. Therefore, the comparison between the gap opening and the braces OOP displacements with the OpenSees modelling can be demonstrated more easily and as expected, there is good agreement between the two.

Specimen B4B

Figure 6.17 shows the comparison between the second set of T4 braces (40x40x4.0SHS) and the OpenSees modelling. As with the B3B specimens, the instrumentation issue that hampered some of the comparisons that could be drawn from the B4A test specimens have been rectified for this test. In summary, the model shows a good prediction of pushover force, PT force and connection moment as expected. The gap opening and the brace OOP displacements of the test specimens are then seen to be in good agreement with the OpenSees modelling. The peculiar results from the OpenSees modelling with regard to the PT force and the gap opening has been previously discussed for the B4A specimens, where it was seen that this unusual behaviour is due to a limitation of the test setup, rather than an actual characteristic of the SC-CBF.

6.6 Modelling of SC-CBF for Dynamic Analysis

Since the purpose of developing this numerical model for the SC-CBF and validating it against data from pseudo-static physical experimental results is to use the model to perform a series of dynamic analyses to evaluate the performance of the SC-CBF under seismic loading, it is necessary to discuss this modelling expansion.

In addition to the nodes and elements described in Section 6.4, a P-Delta dummy column is included in the model to incorporate the second order geometry effects present due to the gravity loading. This consists of lumping all the gravity loading in the form of a force in a single column outside the structure in the vertical direction and slaving it to the nodes of the actual structure. Thus, P-Delta forces from the tributary mass associated with each frame are accounted for. These column members are modelled using stiff elastic beam-column elements and using the P-Delta transformation to model the second order effects.

The analysis options in OpenSees are a very important part of nonlinear time history (NLTH) analyses. Firstly, a gravity analysis is performed, where the gravity loads are applied to the structure and kept constant throughout the earthquake. This is done using a simple load pattern and a 10-step incremental static loading. The Transformation constraints are used, RCM numberer, BandGeneral system of equation solver, Newton iteration algorithm with a Norm Displacement Increment convergence test with a 1×10^{-6} tolerance and 10 maximum number of iterations. All of these analysis objects and their documentation can be found on the OpenSees command manual [86]. Once this gravity loading is applied, the pseudo-time is reset and an earthquake ground motion can be applied to the structure.

An eigenvalue analysis of the structure is performed to obtain the natural circular frequency of the first mode of vibration. Using the natural circular frequency obtained from the eigenvalue analysis, 3% stiffness-proportional Rayleigh damping is applied to the last committed stiffness

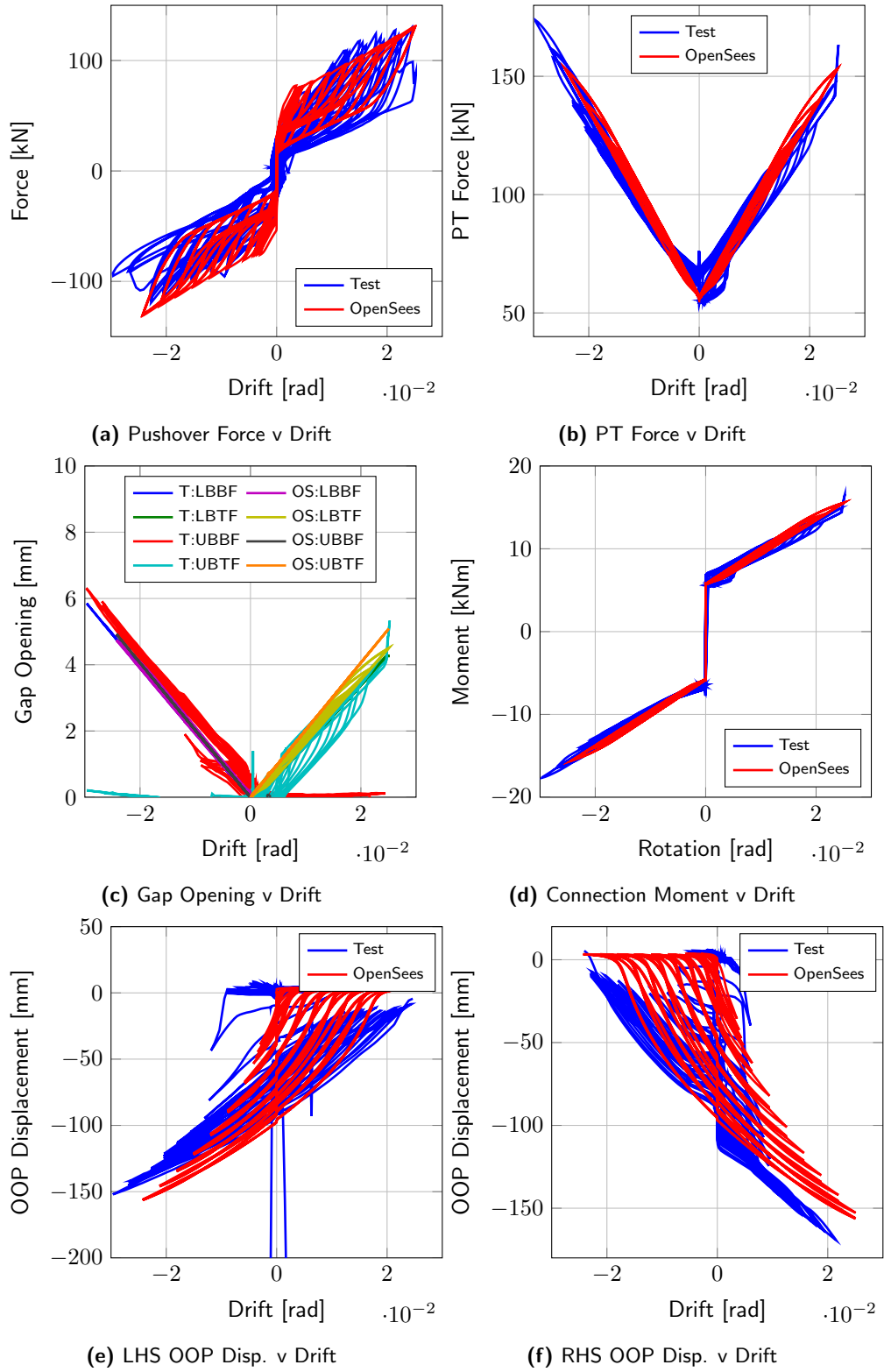


Figure 6.16: B3B test and model comparison.

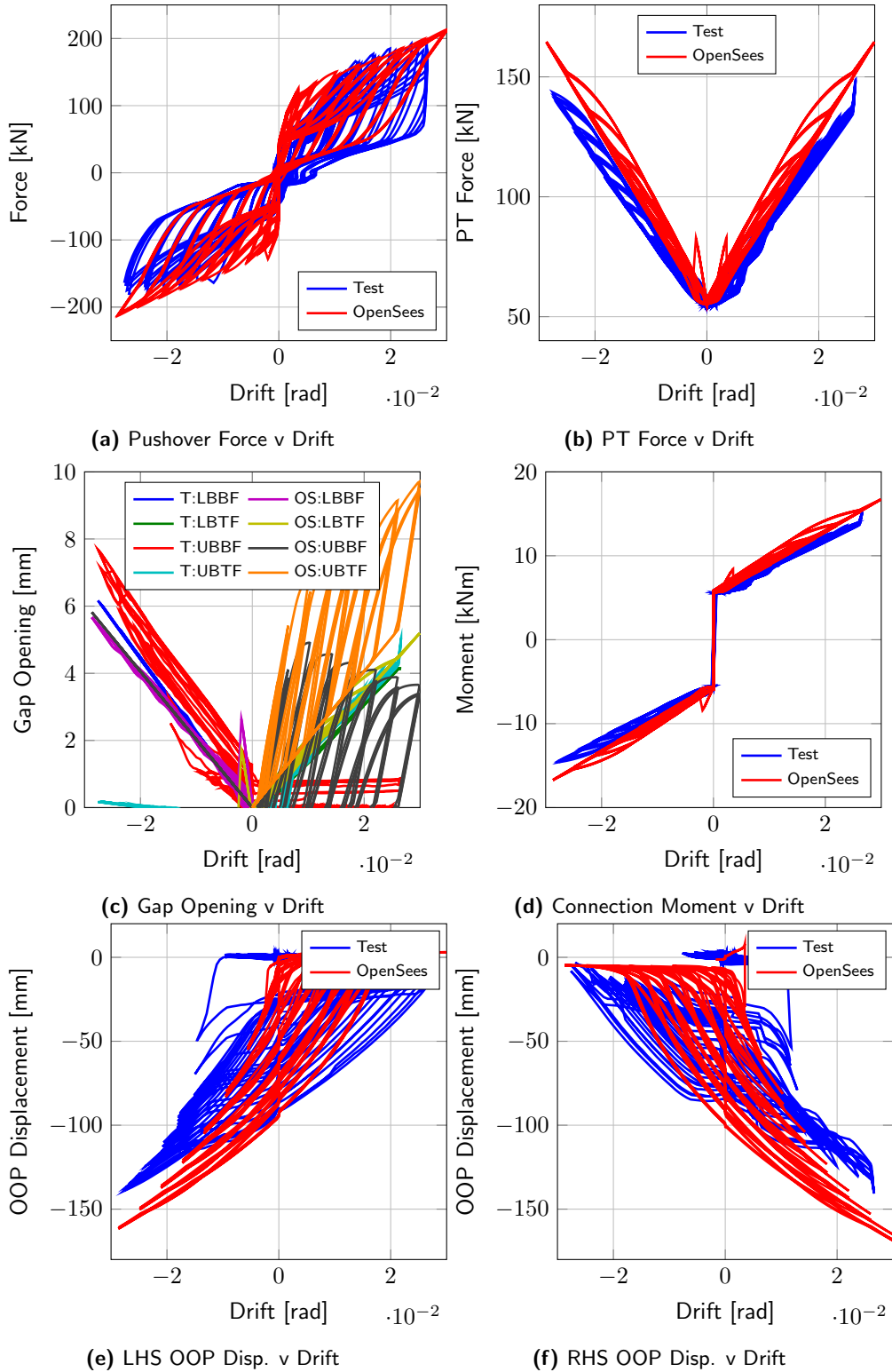


Figure 6.17: B4B test and model comparison.

matrix of the model, as this represents the typical value for elastic damping used in steel structures [27]. The last committed stiffness matrix is to be used as this is the stiffness matrix from the last increment of the analysis which has converged to the prescribed tolerance, making it correct for the previous step of the analysis. The last committed stiffness matrix is to be used as it is wildly inappropriate to use initial stiffness for nonlinear analysis as this leads to huge damping forces which dampens most of the response, giving the illusion that the structure performs well, when in actual fact it may not have. The current stiffness matrix will still be converging during the analysis so it is not guaranteed to be correct at that step and given that when small analysis increments are used, the last committed stiffness matrix is satisfactory to use. However, since the coefficients used in the Rayleigh damping model are based on initial stiffness, it is necessary to update these at every step of the analysis, as the stiffness matrix is changing. This requires a lot of computation as an eigenvalue analysis is required at every step of the analysis to calculate the new coefficients. Charney [23] discusses the various implications of Rayleigh damping and concludes that using the coefficients calculated from initial stiffness eigenvalue analysis to be a reasonable approach when they are applied to the tangent stiffness of the system. Hence, this approach is adopted to save on computation time.

For the NLTH analysis, the initial objects are defined similar to the gravity loading except that this is now a dynamic analysis with a uniform excitation (ground motion) being the loading. A procedure is then set up here to ensure convergence of the analysis is as quick as possible. As before, the Transformation constraints, RCM numberer and UmfPack system of equation solver are used. The accelerated Newton iteration scheme KrylovNewton is used with an EnergyIncr test object that has a tolerance of 1.0×10^{-7} and a maximum of 100 iterations. As this is a transient analysis, a different integrator is needed from the static integrator used in the verification of the numerical model. The most common integrator is Newmark's γ and β , method whereby varying γ and β , a different scheme is employed with unconditional stability guaranteed for certain values of γ and β . Another feature of these types of integrators is the amount of numerical damping that they possess. A notable example of the occurrence of numerical damping in numerical integrators is in the so-called "Wilson-θ method" [135]. It provided a convenient method of numerical integration until the discovery of large numerical damping in the method that was damping the response, and which more importantly, the user had no control over. Since then, another numerical integrator was developed by Hilber et al. [65] which is unconditionally stable for linear problems and allowed the user control over the amount of numerical damping present in the integrator. Numerical damping is sometimes desirable in an integrator in order to damp out the higher spurious modes that have little or no effect in reality, but can be problematic in numerical modelling. This is employed in the numerical modelling of the SC-CBF as when the contact elements at the beam flanges come into contact and the stiffness suddenly changes, there is a sharp change in the nodal accelerations which may cause the model to fail the convergence test, and the model will not work². Hence, numerical damping is employed by using the Hilber, Hughes and Taylor integrator with $\alpha = 0.2$, which is not a very large value, to mitigate this convergence problem in the contact springs.

The initial time-step that is chosen in the analysis is 0.001s, and the analysis is started in these increments until the end of the earthquake. An additional 40s of no excitation is added to the end of an earthquake record to let the structure vibrate freely and return to rest at its final position. This is necessary to get the correct value of the residual displacement present, as the structure may still be shaking at the end of an earthquake record and not be at its final resting position, which is what is of interest. The following scheme is then set up for the analysis to help

²Personal communication with Dr. Frank McKenna.

the model run quicker, by altering the analysis objects wherever the model doesn't converge, and reverting back to the quicker analysis once the time steps of difficulty have been converged. The procedure is:

- Divide the initial time-step by 2.
- Divide the initial time-step by 10.
- Divide the initial time-step by 100.
- Divide the initial time-step by 10 and increase maximum number of iterations to 500.
- Divide the initial time-step by 100, increase maximum number of iterations to 500 and reduce test tolerance down to 1.0×10^{-5} .

If the model is still not converging after these steps, the problem lies elsewhere in the model. It was found on a few occasions that the analysis is sensitive to the post yield stiffness ratio of the steel material models, where the smaller the ratio was, the more difficulty that arose in convergence.

6.7 Summary

A numerical model for a SC-CBF was developed and validated with experimental test data in this chapter. The numerical model developed in OpenSees was first developed by considering all the existing research into the modelling of both CBFs and PT systems individually and then combining them to give a model of the complete CBF. This model was then compared to the analytical expressions developed in Chapter 3 for the SC-CBF system by performing cyclic pushover analyses.

The numerical model was then validated by comparing the results of physical testing of a single storey SC-CBF, which was tested quasi-statically, to the results obtained from 9 different brace specimens. It was then seen that the numerical model captured very well, the salient behaviour of the physical SC-CBF measured in the tests and thus, it was concluded that the developed model is valid for performing more extensive studies on the design and behaviour of SC-CBFs. A short note on the expansion from the static model, developed to validate the model into a dynamic model which can then be used for more extensive studies to analyse the response of SC-CBF to earthquake loading, was also included.

Chapter 7

Towards a Performance-Based Design Approach for SC-CBFs

7.1 Introduction

This chapter aims to expand on some of the concepts presented in Chapter 2 in terms of performance-based design (PBD) and design for seismic loading when using the SC-CBF. Previous efforts of incorporating the SC-CBF into a PBD framework are first discussed along with some areas in which this approach can be furthered to develop it into a more comprehensive approach. This is brought about by recent work in the hazard definition and seismic design approaches. It is not intended to conduct any calculations or perform any numerical analysis in this chapter, but to develop a framework for the PBD of SC-CBFs that can be developed and tested in future studies.

7.2 Previous Efforts and Suggested Improvements

Performance-based design of structural systems is not a new concept in earthquake engineering. The first attempts to incorporate some kind of performance goals were discussed in Section 2.4.3, where the “Vision 2000” document [109] provided the basic framework for many PBD frameworks, such as the expansion to consider residual deformations present in structures by Christopoulos and Pampanin [30]. This allowed for the design approach to consider a series of performance goals for a structure, both during and after an earthquake, at various earthquake intensity levels. This approach to design for self-centering systems was seen in the work by Clayton et al. [36] where performance goals were set for different seismic hazard levels for a self-centering steel plate shear wall system (Section 2.5.2), and evaluated using numerical analysis with a set of design spectrum compatible ground motions. This approach was utilised for the SC-CBF system by O'Reilly et al. [94], where the recently developed direct displacement-based design (DDBD) approach was trialled as a more rational design approach for the PBD of SC-CBFs.

O'Reilly et al. [94] showed that the DDBD procedure could be used as a tool for the PBD of SC-CBFs, as the evaluation of a 3-storey building for two different seismic hazard levels showed positive results when compared to the performance goals initially set out in design. This study, and more recent work since its publication, has led to this framework proposal for these SC-CBFs and how the PBD may be improved from the work in O'Reilly et al. [94]. The areas that are to be discussed and expanded on in this chapter consist of three main areas. The first of these is

the seismic hazard assessment and the selection of ground motion sets that best represent the seismic hazard associated with a certain design location for a structure. The second is in the area of performance limit states for the structure, as while it is necessary to accurately represent the seismic hazard of a design site, as this corresponds to one of the axes in the PBD framework in Section 2.4.3, it is also necessary to describe in detail the acceptable performance limits states of the structure. These range from ordinates that are relevant during the earthquake, such as interstorey drift, to ordinates that are relevant after an earthquake, such as residual drift when adopting the more recent developments in PBD by Christopoulos and Pampanin [30], as these represent the other axis (or axes) of the PBD framework (see Figure 2.13). The last area of discussion for this framework is in the area of designing structures for a given seismic intensity in order to satisfy certain corresponding performance goals. This is critical, as without a reliable seismic design method that can produce structural designs that will satisfy the performance goals for each seismic hazard level, the PBD frameworks do not carry out their basic function.

These three areas will be discussed in the following sections to form a complete PBD framework for which the SC-CBF systems can be designed. This will then be summarised into a process that can be applied to a series of SC-CBFs in future studies.

7.3 Seismic Hazard Analysis

7.3.1 Introduction

One of the main concepts in PBD is the use of different acceptable damage states for different levels of seismic intensity. Therefore, it is important that these levels of seismic intensity be represented correctly within an appropriate framework. The typical code approach to seismic hazard is first discussed, followed a more rational approach to the definition of seismic hazard for a given location.

7.3.2 Typical Code Approach

Typically, a seismic design code, such as Eurocode 8 [18], will specify a design level earthquake that will be represented by a reference probability of exceedence in 50 years. A probability of 10% exceedence in 50 years is suggested in Section 2.1(1) of Eurocode 8, which from the Poisson model of recurrence gives a return period of approximately 475 years, although Bommer and Pinho [12] notes that this has been rather arbitrarily selected to give a return period of 475 years, and the value of 10% is taken by statisticians to be “meaningful”. Hence, this results in the 10% in 50 years hazard level being selected and does not directly imply that the design life of a structure is 50 years [12]. This hazard level corresponds to the damage control state (Level 2), and the other two states, serviceability (Level 1) and life safety (Level 3), are specified in terms of this reference Level 2 intensity. The ratios between these seismic intensity measures can vary from country to country, with Priestley et al. [99] noting that for Europe and New Zealand, the ratio between the Level 2 and Level 1 intensity levels are 0.4 and 0.167, respectively. Similarly in the United States, it is typical to derive the Level 3 intensity by multiplying the Level 2 intensity up by 1.5. Some of the drawbacks to this approach are discussed in Priestley et al. [99], where it is noted that for areas of high seismicity, this approach of factoring up and down the Level 2 seismicity to get the corresponding Level 1 and Level 3 seismicities works well in general, but are not so relevant for areas of infrequent, high intensity shaking. It is therefore necessary to be able to better represent the three levels of seismicity such as to be able to apply a PBD framework.

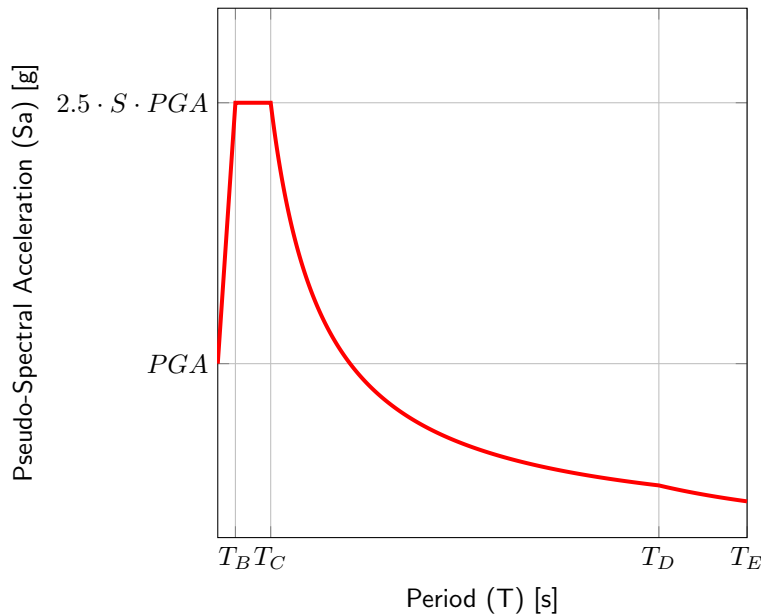


Figure 7.1: Eurocode 8 design spectrum.

Once the levels of seismic intensity have been defined, it is then necessary to represent these intensities in the form of a design spectrum that typically represents the variation of pseudo-spectral acceleration (S_a) with structural period. This way, the design of a structure using a code such as Eurocode 8, becomes a rather straightforward process. The way in which these design spectra are formed is by using code defined equations that depend on peak ground acceleration (PGA), soil type and bracketed magnitude, where magnitudes less than 5.5 use one type of spectrum and magnitudes greater than 5.5 use another. These expressions, given in Equation 7.1 for Eurocode 8 and shown in Figure 7.1, vary from country to country and the general shape is based on characteristics of previously recorded ground motions. Chopra [27] noted how expressions were initially developed from observing the El Centro ground motions from the 1940 earthquake in southern California, and the basic characteristics of the motion formed the general shape for future design spectra, as it was one of the first earthquakes from which high quality data was recorded.

$$\begin{aligned}
 0 \leq T \leq T_B : S_A(T) &= PGA \cdot \left[1 + \frac{T}{T_B} \cdot (\eta \cdot 2.5 - 1) \right] \\
 T_B \leq T \leq T_C : S_A(T) &= PGA \cdot S \cdot \eta \cdot 2.5 \\
 T_C \leq T \leq T_D : S_A(T) &= PGA \cdot S \cdot \eta \cdot 2.5 \cdot \left[\frac{T_C}{T} \right] \\
 T_D \leq T \leq T_E : S_A(T) &= PGA \cdot S \cdot \eta \cdot 2.5 \cdot \left[\frac{T_C \cdot T_D}{T^2} \right]
 \end{aligned} \tag{7.1}$$

Priestley et al. [99] noted some of the difficulties with the approach of having the spectra for all three levels of seismicity found by taking a certain factor of the Level 2 spectrum. A more rational approach was discussed in Priestley et al. [99] whereby displacement spectra could be developed. This is done by using the expressions developed by Faccioli et al. [49] to find the corner period and displacement of the displacement spectra given the expected magnitude and distance to the causal earthquake. This provided a more rational approach to the generation of design spectra as it incorporated site-specific hazard assessment to develop each spectra for each seismic intensity rather than being based on factors relating the three intensity levels to

each other. While this is an improvement on the Eurocode 8 approach, the resulting spectra generated are still represented by a set of equations that typically dependant on two or three input values, similar to the Eurocode 8 approach.

Bommer and Pinho [12] discuss the shortcomings of typical design codes, where spectral acceleration is anchored to the PGA and soil type despite the fact that PGA has no geophysical significance and it has been well established that the spectral shape is heavily influenced by the magnitude. The option in EC8 of having two “types” of spectra depending on the magnitude is commended by Bommer and Pinho [12], however, it is thought to be an unsatisfactory compromise. Another issue with the Eurocode 8 method of producing design spectra is in the value of the corner period T_D (Figure 7.1). Bommer and Pinho [12] notes how this is a very important value in the generation of design spectra and questions the Eurocode 8 approach of fixing the value of T_D at 2.0s, where the justification for this constant value came from the work by Tolis and Faccioli [119]. Bommer and Pinho [12] noted the dependence of the corner period on magnitude, and reported that although more recent work by Faccioli et al. [49] acknowledges this dependence, additional research into this dependence is urgently needed.

7.3.3 Uniform Hazard Approach

Having discussed the code approach to the generation of the design spectra for each level of seismic intensity being considered, it is necessary to propose a method by which these design spectra are to be generated for the PBD of SC-CBFs. It was seen how the Eurocode 8 approach to the generation of design spectra relied on factors relating each of the spectra, while the approach discussed by Priestley et al. [99] suggested using values obtained from probabilistic seismic hazard assessment (PSHA) of a specific site to develop each of the three spectra for each hazard level. The difficulty with these approaches are that the values at each period in the spectra may not have the same probability of exceedence at another period. This is noted by Gavridou et al. [54] for the Italian seismic code, where the spectrum is anchored based on PGA and soil type, and is independent of magnitude despite the previously mentioned observation by Bommer and Pinho [12]. Thus, the spectra generated by methods that anchor the spectral shape independent of magnitude, despite its influence, cannot be considered of uniform hazard. For example, the spectral value at a period of 0.5 seconds ($Sa(0.5)$) may have exactly a 10% probability of exceedence in 50 years, whereas the Sa at 1.5 seconds ($Sa(1.5)$) may have a different probability of exceedence due to the spectral shapes dependence on magnitude being ignored. This means that the design spectra for this level of seismic intensity is not of uniform hazard at all periods. It is again noted that despite Eurocode 8 providing two types of design spectra which depend on magnitude, it is not a satisfactory remedy to the issue as reported in Bommer and Pinho [12].

An improved approach to using these spectra generated using empirical formulae is to perform a PSHA of the design site and plot the pseudo-spectral acceleration values obtained for each period to give what can be called a uniform hazard spectrum (UHS). The term UHS reflects the fact that each point on the design spectra has the same probability of exceedence as the values at every other period considered, thus making it uniform hazard. The web-based tool developed by the United States Geological Survey (USGS) [128] may be used to form a UHS, for a given probability of exceedence, at the specified location. This is done by specifying the address, or coordinates, of a location along with the soil shear wave velocity at 30m ($V_{s,30}$) for a given probability of exceedence at a certain response period for the site. The result of this disaggregation produces a figure such as the one shown in Figure 7.2. Using this tool for the three hazard levels (50% probability of exceedence in 50 years, 10% probability of exceedence

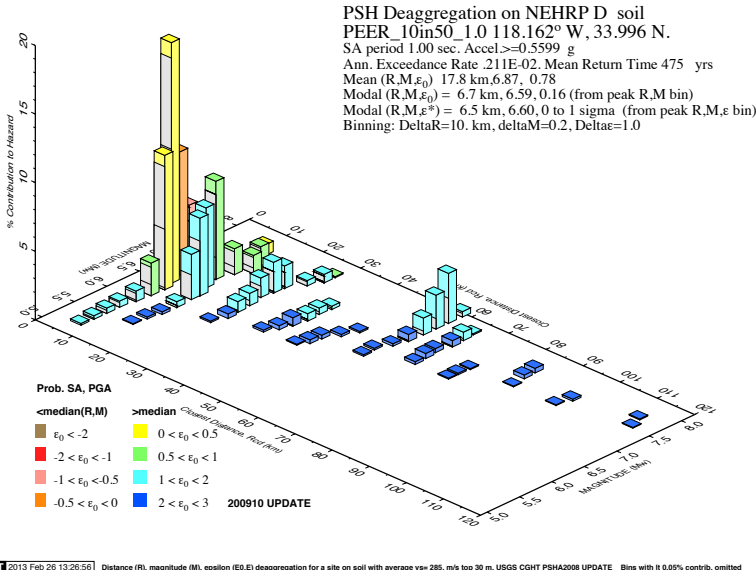


Figure 7.2: Disaggregation plot produced from USGS [128] for the 10% in 50 year hazard level at 1 second for the PEER benchmark site described in Haselton et al. [63].

in 50 years and 2% probability of exceedence in 50 years) and a number of periods, the disaggregation results can be obtained on a plot similar to Figure 7.2 developed for each scenario of hazard and period. The results of the disaggregation for a benchmark site are given in Table 7.1. The aforementioned benchmark site is the PEER benchmark site used by Haselton et al. [63] and is the LA Bulk Mail Facility located in Bell, Los Angeles, California, which has coordinates 33.995N 118.162W when using the USGS disaggregation tool. This site was chosen as it best represents the general characteristics of the Los Angeles area and provides a benchmark site for which comparisons between different studies can be performed.

An improved approach to using these spectra generated using empirical formulae is to perform a PSHA of the design site and plot the pseudo-spectral acceleration values obtained for each period to give what can be called a uniform hazard spectrum (UHS). The term UHS reflects the fact that each point on the design spectra has the same probability of exceedence as the values at every other period considered, thus making it uniform hazard. The web-based tool developed by the United States Geological Survey (USGS) [128] may be used to form a UHS, for a given probability of exceedence, at the specified location. This is done by specifying the address, or coordinates, of a location along with the soil shear wave velocity at 30m ($V_{s,30}$) for a given probability of exceedence at a certain response period for the site. The result of this disaggregation produces a figure such as the one shown in Figure 7.2. Using this tool for the three hazard levels (50% probability of exceedence in 50 years, 10% probability of exceedence in 50 years and 2% probability of exceedence in 50 years) and a number of periods, the disaggregation results can be obtained on a plot similar to Figure 7.2 developed for each scenario of hazard and period. The results of the disaggregation for a benchmark site are given in Table 7.1. The aforementioned benchmark site is the PEER benchmark site used by Haselton et al. [63] and is the LA Bulk Mail Facility located in Bell, Los Angeles, California, which has coordinates 33.995N 118.162W when using the USGS disaggregation tool. This site was chosen as it best represents the general characteristics of the Los Angeles area and provides a benchmark site for which comparisons between different studies can be performed.

Table 7.1: Disaggregation results for the 50%, 10% and 2% in 50 years hazard levels for the PEER benchmark site.

	T	[s]	0.0	0.1	0.2	0.3	0.5	1.0	2.0	4.0
50% in 50 years	Sa	[g]	0.2031	0.3575	0.4591	0.4462	0.3689	0.2257	0.11175	0.04732
	R	[km]	27.4	25.7	27.4	29.6	32.0	37.5	48.9	50.6
	M		6.66	6.56	6.62	6.70	6.80	6.95	7.10	7.20
	ϵ		0.12	0.23	0.27	0.28	0.26	0.31	0.36	0.33
10% in 50 years	Sa	[g]	0.4675	0.818	1.0249	1.0287	0.8806	0.5599	0.2801	0.12074
	R	[km]	13.2	13.0	13.7	14.1	14.3	17.8	28.9	35.4
	M		6.64	6.56	6.62	6.67	6.74	6.87	7.08	7.27
	ϵ		0.64	0.82	0.83	0.79	0.70	0.78	0.98	1.06
2% in 50 years	Sa	[g]	0.8066	1.372	1.7205	1.7551	1.6077	1.0538	0.5113	0.2174
	R	[km]	8.0	8.5	8.7	8.5	7.9	8.9	15.9	26.1
	M		6.64	6.58	6.63	6.67	6.72	6.79	7.00	7.27
	ϵ		1.08	1.26	1.27	1.21	1.10	1.11	1.34	1.54

Returning to Figure 7.2 again, a number of parameters can be noted from this disaggregation plot. Firstly, it is seen that for the given ordinates inputted, the expected spectral acceleration for this return period and spectral period is 0.5599g. From the diagram, it can be seen that this hazard is mainly caused by magnitude 6.6–7.0 earthquakes at a distance of between 8 and 15km. This corresponds to the nearest active fault to the site and is dominating the hazard if the other omitted disaggregation plots are examined. There is, however, a small contribution from a fault much further away, where it is seen that 8.0 magnitude earthquakes at about 60km are contributing to the hazard. This becomes more prominent for longer period disaggregation where the higher periods tend to be influenced more by faults further away. The results of all the disaggregations for all the hazards are given in Table 7.1 are presented for the LA site and plotted in Figure 7.3, where the mean magnitudes and distance are given for each disaggregation. Also shown is a parameter called ϵ , which is a term used in engineering seismology to describe the number of standard deviations an observed logarithmic spectral acceleration is away from the logarithmic spectral acceleration given by a ground motion attenuation model, which is a model that predicts spectral values for a given site location and soil conditions and is based on empirical data collected from previous seismic events. It is computed by subtracting the mean logarithmic spectral acceleration ($\mu_{\ln(Sa(T))}$) from the observed logarithmic spectral acceleration ($\ln(Sa(T))$), and dividing by the logarithmic standard deviation ($\sigma_{\ln(Sa(T))}$), as shown below:

$$\epsilon(T) = \frac{\ln(Sa(T)) - \mu_{\ln(Sa(T))}}{\sigma_{\ln(Sa(T))}} \quad (7.2)$$

This is a relevant parameter in the hazard analysis, as at each period of the UHS, it gives an idea of how many standard deviations away from the median hazard predicted by attenuation relationships the actual UHS for the site is. This is discussed in detail in Baker et al. [9], where a site in Oakland, California is chosen as the design site. Three sets of UHS are obtained via the same method outlined above, and the same values presented in Table 7.1 are presented for the Oakland site. It is demonstrated that using a ground motion attenuation relationship for the site, such as the one presented in Campbell and Bozorgnia [16], and given the magnitude and distance, returns a design spectra roughly equal to the 50% in 50 year UHS. This is to be expected for the Oakland site used in Baker et al. [9], as the ϵ values obtained from the disaggregation are close to zero, meaning the UHS is almost equal to the median spectra obtained

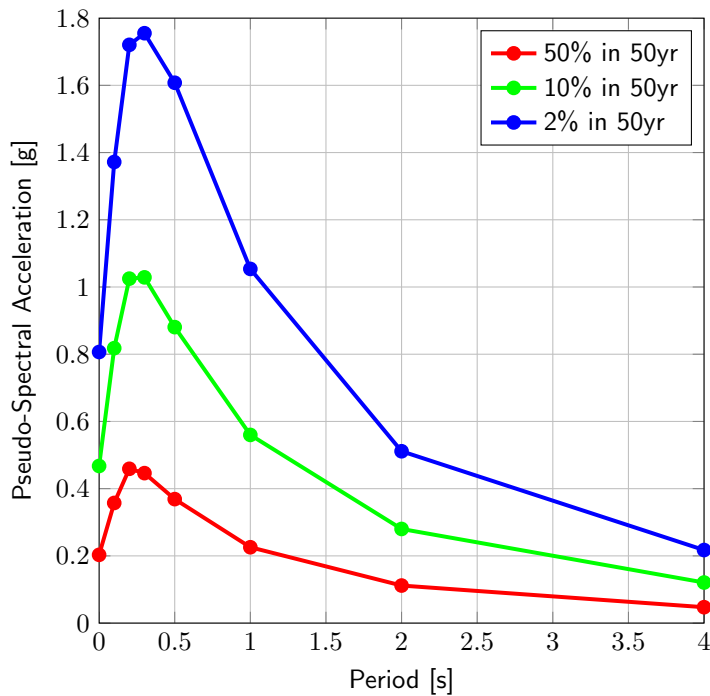


Figure 7.3: Uniform hazard spectra for the PEER benchmark site.

from the attenuation relationship. This means that for higher intensity UHS, the site is capable of producing this level of shaking, but it will need to be ϵ number of standard deviations higher than the median to actually happen.

This is observed also in Table 7.1 for the PEER benchmark site in LA, where the 50% in 50 year UHS gives epsilon values slightly above zero, and the 10% and 2% in 50 year events are higher again. Again, this refers to the fact that the ground shaking produced will need to be ϵ number of standard deviations above the median in order to take place. The main observation to be noted from this is that due to the hazard contribution from various source faults for the site, as demonstrated in Figure 7.2, a UHS cannot be accurately represented by a single ground motion, as a single ground motion is not expected to have a positive ϵ at all periods for a given hazard level. Baker and Cornell [8] describes how since the high frequency portion of the UHS is dominated by small nearby earthquakes, and low frequency is dominated by large distant earthquakes, no single earthquake can be expected to have the same high ϵ value required for a given hazard level across the entire frequency range of the spectrum. Thus, the UHS cannot be accurately represented by a single ground motion, but a set of motions that satisfy the ϵ requirements at every period.

7.3.4 Impacts on Ground Motion Selection

The previous section saw the introduction of a new variable termed ϵ , which is the number of standard deviations an observed logarithmic spectral acceleration of a record is away from the logarithmic spectral acceleration given by a ground motion attenuation model. This term has been primarily used in engineering seismology, but has been more recently adopted into ground motion selection by Baker and Cornell [7], where it is seen to be an indicator of spectral shape of individual records for ground motion selection. Figure 7.4 shows the influence of positive ϵ ,

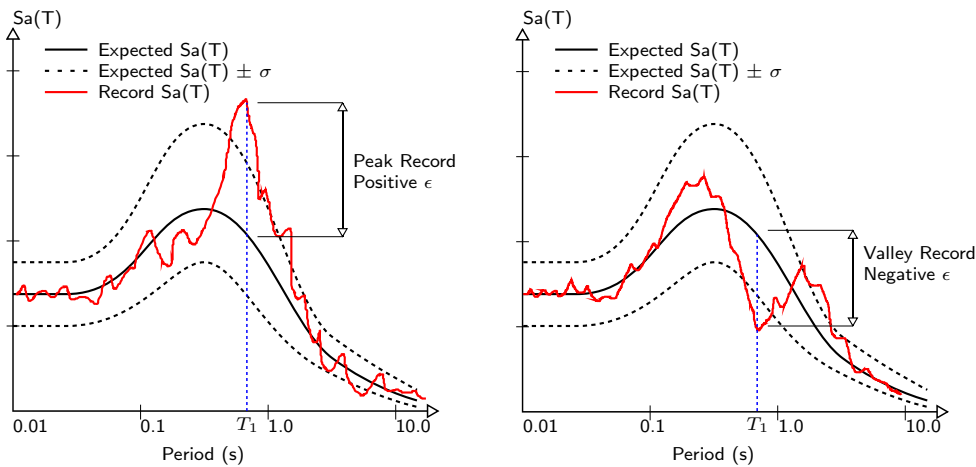


Figure 7.4: Illustration of positive and negative ϵ with respect to the target spectrum
(Adapted from Baker and Cornell [7]).

or “peak records”, and negative ϵ , or “valley records”. In general, a record with a peak ϵ at the fundamental period of interest will produce a record that will decrease in intensity as the period elongates away from the fundamental period into a lower ϵ range. Conversely, records with a negative ϵ will produce higher intensity records as the fundamental period elongates during the record and the ϵ is moving up into higher epsilon values.

Using this definition of ϵ for ground motion records, Baker and Cornell [7] developed a vector-valued ground motion intensity measure that uses both the spectral acceleration at the structures fundamental period along with the corresponding ϵ value, where it is seen the influence of ϵ on structural response is more pronounced than the corresponding magnitude or distance of a record when selecting ground motions records. It was thus suggested by Baker and Cornell [8] that it is more important to select ground motions to match a target spectrum based on the correct ϵ values rather than correct magnitude and distance values. This is demonstrated in the record selection in Welch et al. [131], where the ϵ values of the records chosen were approximated visually to ensure that no peak or valley records existed at the fundamental period of interest in the records selected for that study.

7.4 Performance Limit States

The second area within the PBD framework is the definition of acceptable performance limits states for each of the hazard levels defined in Section 7.3. This involves defining what is acceptable performance for each of the hazard levels and evaluating a structure’s performance to these limits through a series of numerical analyses. This way, a structure can be designed and evaluated within a PBD framework such as the one described in Section 2.4.3.

These limit states, or performance goals, consist of two types. The first is the dynamic response ordinates the structure exhibits under earthquake excitation, such as displacement, and the second is the state in which the members in the structural system remain during the earthquake loading. For the dynamic response ordinates, this is usually specified in terms of the maximum interstorey drift experienced by the structure during the earthquake, and following on from the discussions in Chapter 2, the residual drift is now incorporated as an equally important measure of performance and is one which the SC-CBF system aims to mitigate. For the member

Table 7.2: PBD response ordinate limits.

Hazard Level	Interstorey Drift	Residual Drift
50% in 50 years	Yield drift	0.20%
10% in 50 years	2.50%	0.20%
2% in 50 years	4.00%	0.30%

limit states, this requires knowledge of the systems structural behaviour to be able to assess which elements will remain elastic during an earthquake and which elements will exhibit ductile behaviour and experience some form of damage. Following the principals of capacity design, it is necessary to provide adequate strength in the elements that are not intended to experience damage so that the principal structural system that provides stability is maintained.

The response ordinates consisting of interstorey drift and residual drift must be set for each hazard level. Design codes typically try to limit the amount of interstorey drift in a structure in order to minimise the damage to the non-structural elements in the building. However, in addition to the restriction of structural drift in order to limit the damage to non-structural elements, there is also the issue of structural elements, namely the brace members in the SC-CBF. The approach adopted by O'Reilly et al. [94] was to set the initial design drift to be 2.5% for the 10% in 50 year hazard level and 4% for the 2% in 50 year level, as these correspond to values set out in Eurocode 8 and the study by Clayton et al. [36], respectively. However, if it was found that the brace fracture ductility was exceeded with this design drift, the design drift would need to be reduced in order to avoid the brace members fracturing at the design drift. The maximum interstorey drift corresponding to the yield of the bracing members is set as the limit for the 50% in 50 year hazard level, as it is intended to have no yielding in the structure at this level.

For the residual drift, it is necessary to define some limits, as although the purpose of the SC-CBF is to eliminate residual drift entirely from structure, there may be a small amount remaining after an earthquake. A limit of 0.2% was set for the 10% in 50 year event, as this corresponds with the work by Clayton et al. [36] and Henry [64] for the same hazard level. This is also justified when considering the out-of-plumbness tolerance specified in Eurocode 3 [20] for this type of construction is found to be 0.272%. It is also seen that this value of 0.2% is well below the limit value of 0.5% reported in McCormick et al. [85], which was discussed in detail in Section 2.4. For the 2% in 50 year event, this limit is raised to 0.3% based on engineering judgement and also that these correspond to the values used in other similar studies [36, 64]. For the 50% in 50 year hazard level, a limit of 0.2% is applied as this corresponds to the out of plumbness limit for the structure, although it is anticipated that residual deformations will be minimal at this hazard level, since the structure is designed to remain elastic at this level. A table of the selected response ordinate limits is shown in Table 7.2.

For the member state limits, this is essentially restricting the elements that yield and accumulate damage from the ones that are anticipated to be damaged. As mentioned above, the braces are designed so as to not exhaust their fracture ductility at maximum drift, where the expressions developed by Nip et al. [90], given in Equation 2.5, can be used to determine this limit, which are given as:

$$\begin{aligned} \text{Hot-rolled carbon steel: } \mu_f &= 3.69 + 6.97\bar{\lambda} - 0.05(c/t\epsilon) - 0.19(\bar{\lambda})(c/t\epsilon) \\ \text{Cold-formed carbon steel: } \mu_f &= 6.45 + 2.28\bar{\lambda} - 0.11(c/t\epsilon) - 0.06(\bar{\lambda})(c/t\epsilon) \\ \text{Cold-formed stainless steel: } \mu_f &= -3.42 + 19.86\bar{\lambda} + 0.21(c/t\epsilon) - 0.64(\bar{\lambda})(c/t\epsilon) \end{aligned} \quad (7.3)$$

Table 7.3: PBD member limits.

Hazard Level	Braces	PT Elements	Beams	Columns
50% in 50 years	$\mu \leq 1$	Elastic	Elastic	Elastic
10% in 50 years	$\mu \leq \mu_f$	Elastic	Elastic	Elastic
2% in 50 years	$\mu \leq \mu_f$	Elastic	Elastic	Elastic

Thus, if the design drift exceeds the fracture ductility, then the design drift is reduced accordingly. For the beams and columns in the structure, these are sized so as to remain elastic at all times during loading as these are not part of the energy dissipating mechanism. This is achieved by finding the maximum forces exerted on the system at maximum drift and designing with adequate factors of safety to ensure these elements do not exceed their yield capacity. Similarly, the PT elements in the system are to remain elastic at all times. The PT elements form a critical part of the SC-CBF's behaviour, therefore, it is vital that they remain elastic at all times, and should be designed with an adequate factor of safety. The list of the performance for the structural member is shown in Table 7.3.

7.5 Design Methodologies

7.5.1 Introduction

Having discussed the design limits or performance goals and methods of defining the hazard associated with a given location, it is now necessary to discuss a design method to fit both of these in the PBD framework. This means the design method must be able to utilise the outputs from the hazard analysis at each level of seismic intensity and produce a design that will satisfy the performance limit state requirements at each of these seismic intensity levels. This involves ensuring that drift limits are not exceeded and the inelastic behaviour occurs at the intended locations. Two possible approaches can be used for this, with the first being the code-based [18] design method which will be termed “force-based design” (FBD) and the second being “direct displacement-based design” (DDBD). The differences between these will become apparent in the next two sections, where their approach to the design of SC-CBFs within a PBD framework is discussed.

7.5.2 Force-Based Design as per Eurocode 8

One of the principal features of force-based design is the use of the force modification factor q . Different structural systems are assigned different q factors, as they represent the structural system's ability to undergo ductile behaviour, and these factors are chosen for a particular system based on experimental observations and past performance of the system and, hence, are stipulated by design codes. Since the SC-CBF is a novel system developed as a part of this research, no such force modification factor has been assigned. However, since the yielding elements which will dissipate hysteretic energy during loading are essentially concentric tubular bracing elements, it can be assumed that the force modification factor assigned to CBFs in EC8 is an appropriate factor for the force-based design of SC-CBF's. EC8 assigns a force modification factor of $q = 4.0$ to CBFs. This is a relatively low value when compared to a system such as a moment resisting frame (MRF), which is assigned a value of 6.5. Reasons for this difference include the greater ductility capacity of a MRF compared to a braced frame and also due to the pinched nature of the CBFs hysteretic loops caused by the buckling of its braces.

The first step in designing a structure to EC8 is to obtain an estimate for the period of the structure's first fundamental mode of vibration. Since this is a property that depends on the structure's strength and structural properties, it is not possible to know its value prior to design. Hence, an estimation can be obtained from a height-dependent expression for an initial estimate, with a view to revising this estimation following the first trial design of the structure through modal analysis. This height based expression, given in Section 4.3.3.2.2(3) of EC8, is as follows:

$$T_1 = C_t H^{0.75} \quad (7.4)$$

where H is the height of the structure in meters and C_t is a coefficient equal to 0.050 for CBFs, although for SC-CBFs this value should be revised as the additional capacity and stiffness provided by the post-tensioning arrangement results in a first mode period shortening which would correspond to a slightly smaller value for C_t for SC-CBFs when compared to conventional CBFs. However, this is outside the scope of this project. Thus, Equation 7.4 is used in this study. This expression gives an estimate of the buildings first fundamental mode of vibration, which is then used to obtain pseudo-spectral acceleration ($Sa(T_1)$) from the EC8 design spectrum, which is determined by the location of the structure and site conditions for the structure, as outlined in Section 7.3.2. Using this value of $Sa(T_1)$, the base shear force is obtained from Section 4.3.3.2.2(1) of EC8, which is given in Equation 7.5.

$$V_b = \frac{Sa(T_1)\lambda m}{q} \quad (7.5)$$

where m is the mass of the structure taking into account the dead gravity load and a portion of the live gravity loading. λ is a factor which accounts for the fact that only a portion of the mass m participates in the first fundamental mode of vibration in multi-storey buildings. λ is assigned a value of 0.85 for structures with more than two storeys and a first mode period T_1 less than twice the corner period T_C of the design spectrum. Otherwise, a value of 1.0 is assumed for λ . This base shear force V_b is now distributed along the height of the structure in accordance with the equivalent lateral force (ELF) method. The forces are distributed over the height of structure as per Section 4.3.3.2.3(2) of EC8, and assuming a linear displacement of the structure, the equivalent lateral forces are as per Equation 7.6.

$$F_i = V_b \frac{z_i m_i}{\sum z_j m_j} \quad (7.6)$$

where F_i is the equivalent lateral force at the i^{th} storey of the structure with j number storeys. Using this distribution lateral forces on the structure, the storey shear force (V_i) can be determined from summing the storey forces down the height of the structure.

The displacements of the structure are calculated from a modal analysis of the assumed displaced, or first mode, shape. Using this, the displacement of the structure, where the masses are lumped at each storey i , is given by the following expression:

$$\Delta = \phi Sd(T_1) \Gamma \quad (7.7)$$

where ϕ is the assumed mode shape, which is taken to be linear, $Sd(T_1)$ is the spectral displacement obtained from the design spectrum using the first mode period T_1 . Γ is the participation factor of the mode shape in the response of the structure given by:

$$\Gamma = \frac{\phi^T M r}{\phi^T M \phi} \quad (7.8)$$

where M is the mass matrix and r is a unit vector.

One of the main assumptions in FBD is the use of the force modification factor and that the displacements of the inelastic system are equal to that of the yield displacement multiplied by the force modification factor to account for the increased displacements because of the nonlinear behaviour. This has been discussed in Priestley [98], and is reported that this approach is known to be only true where the fundamental period is longer than the predominant periods of the ground motion. Since braced frames are relatively stiff structures, the natural period is relatively low, which means this assumption, known as “equal displacements” does not always apply to these structures, although for taller buildings where the period is greater than 1s, this equal displacements rule is likely to hold. It can be shown, for short period buildings, that the displacements will be larger by a factor R (Equation 7.9), which should be used when calculating the structure displacements using the FBD method.

$$R = \frac{q^2 + 1}{2q} \quad (7.9)$$

While the method presented above provides a relatively simple codified approach to seismic design, it possess some shortcomings, two of which are of concern for the PBD framework for SC-CBFs. The first of these relates to its actual ability as a design method. This has been extensively discussed in Priestley et al. [99], where the logic behind many of the steps is questioned. This stems from the fact that the FBD method uses lateral force as the driving metric when sizing a structure for lateral loads. This then leads to the decision to use unique force modification for a given structural system, which suggests that every variation of a certain structural system can undergo the same ductility demand as another. Priestley et al. [99] have shown this to be invalid by using the simple case of a SDOF bridge pier as an example. This then leads to the second area which is of concern, which is that lateral force is the driving metric in the design process and the general philosophy of the method is to avoid achieving certain unwanted performance by ensuring that the structure does not reach levels of unwanted behaviour by providing sufficient structural capacity.

For a structural system such as the SC-CBF, using FBD would imply requiring two different force modification factors for the two levels of seismic intensity that are due to cause ductile behaviour in the system. Since there is no procedure for determining these factors, as they are chosen based on experience and observation, this leaves a PBD framework that uses FBD as its design methodology relatively open to interpretation. While FBD may be used in a performance-based design framework for such a system, as demonstrated by Clayton et al. [36], it is acknowledged that some of the shortcomings of the design method may be restraining the effectiveness of such a PBD framework when applied to the SC-CBF system.

7.5.3 Direct Displacement-Based Design

The shortcomings of FBD have been well documented in the literature over the past 20 years with Priestley et al. [99] providing a detailed description of these. Priestley et al. [99] then propose a method termed the direct displacement-based design (DDBD) method, which primarily uses the displacements of a structure the driving metric in the design process rather than forces, as with FBD. In this section, the DDBD method is presented generally and the specific details required for the design of a SC-CBF are added accordingly. Figure 7.5 shows the basic concept of the DDBD method. First, the structure is modelled as an equivalent SDOF system with an effective stiffness K_e , as in Figure 7.5. The design displacement (Δ_d) is then specified and from the knowledge of the building’s layout and material, the yield displacement (Δ_y) can be determined.

This gives a target displacement ductility (μ), and knowing the type of system being used, the equivalent viscous damping (EVD) (ξ) can be determined from Figure 7.5 (c). Using the design displacement (Δ_d) and the EVD, the effective period of the system (T_e) can be determined from the elastic spectral displacement, as per Figure 7.5 (d). From this, the design base shear can be determined and the structure designed and detailed accordingly. This is a brief summary of the DDBD method, and the details of the method when applied to SC-CBFs are now discussed.

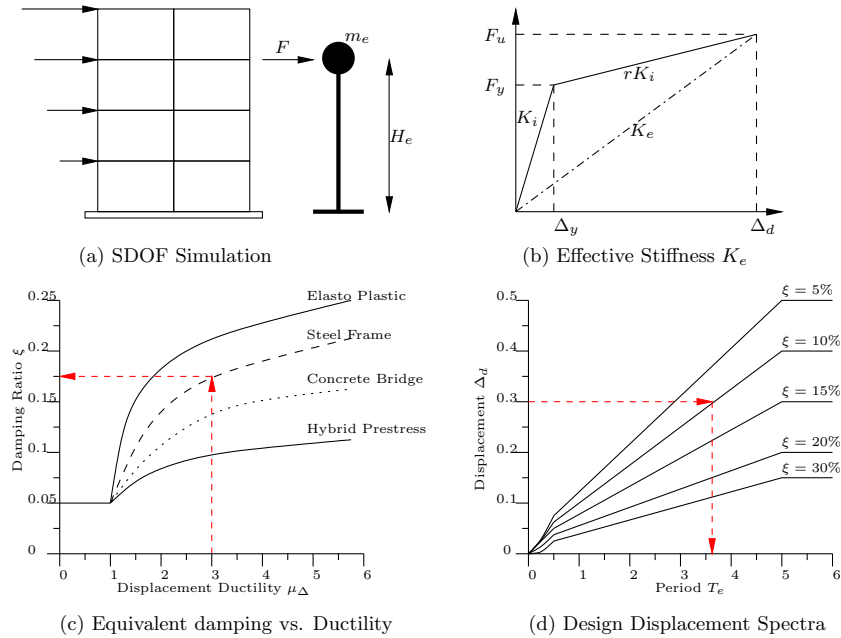


Figure 7.5: Fundamentals of Direct Displacement-Based Design (DDBD).

Design Displacement

One of the first steps in the DDBD method is determining a displacement profile for the structure. For a single storey structure, this is quite simple as it is already a SDOF system, but for a multi-storey structure a transformation to a SDOF is necessary. This is done by assuming a displaced shape for the structure and idealising the MDOF's behaviour as an equivalent SDOF system. Medhekar and Kennedy [87] derives the basis for this transformation from MDOF to SDOF and also note that this is based on the following assumptions:

- The MDOF system has a harmonic response in this assumed displaced shape.
- The base shear developed by the MDOF and SDOF systems is the same.
- The work done by the lateral earthquake force in both systems is the same.

The assumption of displaced shape of the structure depends on what type of system it is (e.g. a frame building, cantilever wall building or a multi-span bridge). For a frame building, Priestley et al. [99] has recommended the use of the following equations for determining the displaced shape δ_i for a frame building:

$$\delta_i = \begin{cases} H_i/H_N & \text{if } N \leq 4 \\ \left(\frac{4}{3}\right) \left(\frac{H_i}{H_N}\right) \left(1 - \frac{H_i}{4H_N}\right) & \text{if } N > 4 \end{cases} \quad (7.10)$$

where H_i is the height of the i^{th} storey in the structure of N storeys.

However, Priestley et al. [99] also states that for CBF structures, a linear displaced shape should be used regardless of the number of storeys in the structure. More recent work by Wijesundara [134] and Salawdeh [105] on the development of DDBD for CBFs have recommended the use of both expressions in Equation 7.10 for CBFs. Since the SC-CBF is a combined system consisting of a CBF and a post-tensioned rocking frame system, the use of Equation 7.10 for the displaced shape must be justified. If we consider the post-tensioned system to act as a bilinear elastic MRF, then the use of Equation 7.10 is justified. In addition, Maley et al. [84] investigated the behaviour of dual BRBF and MRF systems, and from this, it was shown that because the MRF is much more flexible than the BRBF system, by the time the structure has deformed to its design displacement, the CBF has been yielded and provides little contribution to the determination of the deformed shape due to its low post-yield stiffness. The displaced shape is a snapshot of what the structure looks like at the design displacement, hence, the MRF contribution will play a more significant role in determining the displaced shape of such a dual system of CBFs and MRFs. The SC-CBF can be considered to behave similarly and, hence, this justification provided by Maley et al. [84] is cited. It is noted that these expressions for the displaced shape can be further investigated by performing nonlinear time history analyses on a number of different designs and hence evaluating the most appropriate one based on how the actual observed displaced shape compares to the design displaced set out at the beginning of the design process.

Using this displaced shape of the structure, the design displacement (Δ_i) can be determined. The target maximum interstorey drift (θ_d) for a structure is set at the start of the analysis. Using this value and the displaced shape, the displaced shape can be scaled up to give the design displacement as:

$$\Delta_i = \frac{\delta_i}{\max(\Delta\delta_i)} \theta_d h_i \quad (7.11)$$

where h_i is the storey height of floor i .

Yield Displacement

The next step in the DDBD method is the determination of the yield drift of the structure. For CBFs, this depends on the geometry and material properties of the structure. Since the yielding element in the SC-CBF is a CBF, the yield drift calculation is the same. Della Corte and Mazzolani [41] developed an expression for the yield drift shape for a chevron CBF, which took into account the beam flexural deformations in addition to the column axial deformations, which also contribute to the drift of the storey, due to the rotation of the storey from the column axial deformations. Wijesundara [134] developed a similar expression for CBFs with diagonal braces, which is given by:

$$\Delta_{y,i} = \sum_{i=1}^N \left(\left(\frac{\epsilon_{y,1}}{\sin\beta \cos\beta} \right) h_i + \rho \epsilon_{y,2} h_i \tan\beta \right) \quad (7.12)$$

where ρ is the ratio of the design axial force to the yielding force and β is the angle of inclination of the diagonal brace members. The variables $\epsilon_{y,1}$ and $\epsilon_{y,2}$ represent the yield strain of the braces and the columns respectively. Using this expression, the yield displacement profile of the braces can be determined for the SC-CBF.

MDOF to SDOF Transformation: Design Displacement, Yield Displacement & System Ductility

Using the expressions in Equations 7.11 and 7.12 for design displacement and yield displacement profiles, the transformation from MDOF to an equivalent SDOF can now be completed to give Δ_d and Δ_y . This is performed as given in Equations 7.13 and 7.14.

$$\Delta_d = \frac{\sum_{i=1}^N m_i \Delta_{d,i}^2}{\sum_{i=1}^N m_i \Delta_{d,i}} \quad (7.13)$$

$$\Delta_y = \frac{\sum_{i=1}^N m_i \Delta_{y,i}^2}{\sum_{i=1}^N m_i \Delta_{y,i}} \quad (7.14)$$

Using these two values for design displacement and yield displacement, the system ductility can be calculated as follows:

$$\mu = \frac{\Delta_d}{\Delta_y} \quad (7.15)$$

Equivalent Viscous Damping

The next step in the DDBD method is the estimation of the equivalent viscous damping (EVD) of the equivalent SDOF system for the structure at design displacement, as per Figure 7.5 (c). While the DDBD method presents many convenient steps that make it more desirable over the traditional FBD method, one area that is still a “grey area” in the method is the EVD. The notion of EVD being directly related to the area enclosed by a hysteretic loop was first proposed by Jacobsen [70] and forms what is the key concept in the calculation of EVD for structures in DDBD. Priestley et al. [99] provides a discussion into the effect of damping and ductility on the spectral displacement, where the idea of using a spectral displacement spectrum modified by different levels of damping is compared to one that is modified by different levels of ductility for DDBD. The key question being debated is whether or not it is appropriate to use an elastic design spectrum modified for different levels of damping for a structure that behaves inelastically, or whether a design spectrum modified for different levels of ductility is more appropriate.

Chopra and Goel [28] present an argument on why the use of elastic spectra with modified levels of damping is inappropriate for design and examples are presented to demonstrate this for a SDOF bridge bent. Chopra and Goel [28] go on further to demonstrate how using a design spectra modified for different levels of ductility provides a better design for the SDOF bridge bent, and from this it is concluded that spectral displacement spectrum modified for different levels of ductility should be used for design. While this seems like a simple task, this means that each spectrum must be modified for each hysteretic rule considered for each level of ductility considered, which is a task in itself. Another drawback to this approach proposed by Chopra and Goel [28], is the current stage and completeness of the design method. While it may seem logical to use a design method that appears to offer a better design, Sullivan [116] notes how the method is still incomplete and offers no real guidance for systems other than elasto-plastic SDOF oscillators. In addition to this, Priestley et al. [99] note how using the elastic design spectrum means that a single elastic displacement spectrum can be used for all hysteretic rules considered

in design simply by adjusting them to different levels of damping through the reduction factor (R_ξ) in Equation 7.16, where ξ_{evd} is the EVD calculated for the hysteretic rule being considered. Since this approach has been relatively well developed for use compared the other approach, it is adopted herein.

$$R_\xi = \sqrt{\frac{0.07}{0.02 + \xi_{evd}}} \geq 0.55 \quad (7.16)$$

The expression for the EVD of a system is composed of two parts, the elastic damping (ξ_{el}) and the hysteretic damping (ξ_{hyst}), as in Equation 7.17. ξ_{hyst} is an empirical relation for each type of system that is a function of the ductility of the system, as seen in Figure 7.5 (c). ξ_{el} is the elastic damping present in the system, which for systems such as concrete is assumed to be 5%, while for systems such as steel, it is normally assumed to be 3%. Since the EVD of the SC-CBF is related to the EVD of a CBF, it is first necessary to discuss the relationship for calculating the EVD for a CBF before expanding this relation into one that can be used for SC-CBFs.

$$\xi_{evd} = \xi_{el} + \xi_{hyst} \quad (7.17)$$

As noted by Goggins and Sullivan [57], an expression for the EVD of a CBF that accurately predicted the EVD compared to shake-table tests was not readily available at the time of publication. Since then, a model has been developed by Wijesundara et al. [133], which relates the EVD at different ductilities to the normalised slenderness of the braces ($\bar{\lambda}$), where more slender braces have less EVD associated with them due to the pinching hysteretic behaviour of the braces. The expression developed by Wijesundara et al. [133] is given by:

$$\xi_{cbf} = \begin{cases} 0.03 + \left(0.23 - \frac{\bar{\lambda}}{15}\right) (\mu - 1) & \text{if } \mu \leq 2 \\ 0.03 + \left(0.23 - \frac{\bar{\lambda}}{15}\right) & \text{if } \mu \geq 2 \end{cases} \quad (7.18)$$

where the range of braces slenderness values for which this was derived was 0.4 to 1.6, where for slenderness values outside this range, the limit value is used rather than the actual value. This model was developed by estimating an initial EVD value using the expression relating EVD to hysteretic area proposed by Jacobsen [70] for a given pushover cycle ductility level and brace slenderness. This initial estimated value of EVD at each ductility level was then used to calculate an effective mass required for a single storey CBF designed to a EC8 design spectrum. This design displacement was compared to an actual displacement using a series of design spectrum compatible ground motions, and if there was a difference in actual versus design displacements, the initial EVD estimate was adjusted and the analyses rerun until both values within 5% of each other. This resulted in a series of EVD values for a set of brace slenderness values at various ductilities, which had been validated using real ground motion accelerograms. Wijesundara et al. [133] then proposed the equation given in Equation 7.18 as a valid expression to predict the actual EVD in a CBF system, but only within the limits of the slenderness range to which it had been calibrated, where the limit values were to be used outside of this range. Since the development of the model, Salawdeh [105] has recommended using this model for design without imposing such limits on the brace slenderness. While this expression is a good start for calculating the EVD of CBFs, further improvements may be possible. This is seen in Figure 7.6 where for higher ductilities, Wijesundara et al. [133] predicts a value for the EVD larger than the actual EVD measured in shake table tests and NLTH analyses. Conservatism is also present in the use of this expression by Wijesundara et al. [133] in its inclusion in the model DDBD design code [15], where the hysteretic damping term is reduced by a factor of 0.7 to prevent overestimation of the EVD, leading to unsafe designs.

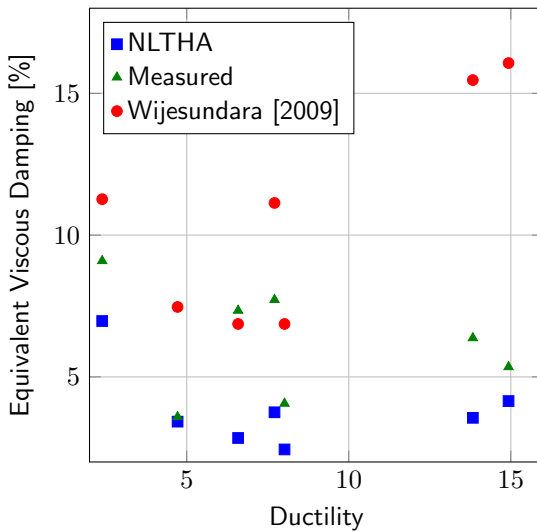


Figure 7.6: Comparison of estimated EVD versus measured shake table values (Adapted from Salawdeh [105]).

Since the SC-CBF is a combination of the PT system and a CBF system, the damping model needs to be adjusted to account for this. In addition, once the EVD has been determined for the MDOF structure, this must then be transformed to the SDOF representation. Maley et al. [84] investigated the DDBD of dual BRBF and MRF systems. For the EVD calculation of this system, a weighted sum of the EVD provided by the MRF and BRBF was used, where the weighting was based on the base overturning moment resisted by each system. In a similar approach, NZCS [92] used a weighted combination of the damping provided by the PT system and the energy dissipating system for the DDBD of PRESSS systems in New Zealand. The same approach is proposed here for the SC-CBF, where the EVD is found by taking a weighted contribution from the EVD's provided by the CBF and the PT system, where the weighting is done by weighting the ratio of the work done by each system to the total work at each floor. The ratio of the storey shear resisted by the PT system is denoted ω , and the storey shear resisted by the CBF system is 1 minus ω . Using this contribution from each of the systems, the system damping is given by:

$$\xi_{sc-cbf} = \frac{\sum_{i=1}^N V_i \Delta_i \omega_i \xi_{pt,i} + \sum_{i=1}^N V_i \Delta_i (1 - \omega_i) \xi_{cbf,i}}{\sum_{i=1}^N V_i \Delta_i} \quad (7.19)$$

where V_i and Δ_i are the storey shear and storey displacement at floor i . For the damping contribution from the PT system, there is no hysteretic energy as the system is bilinear-elastic, so the only contribution is the elastic damping which is taken as 5%, as per NZCS [92].

Effective SDOF and Design Base Shear

Now that the design displacement and EVD have been determined for the structure, this can now be used to find an effective period for the equivalent SDOF system. Entering the elastic spectral displacement spectrum with the design displacement Δ_d , the design spectrum is reduced by a factor R_ξ to account for the level of EVD (ξ_{sc-cbf}) in the equivalent SDOF system. From this, the effective period is read, as shown in Figure 7.5 (d). Using this effective period T_e , the final

steps of the DDBD method can be completed to get the design base shear. This is done by first calculating the effective mass of the system m_e from Equation 7.20, then using this to find the effective stiffness K_e , as per Equation 7.21. The design base shear is then given as Equation 7.22.

$$m_e = \frac{\sum_{i=1}^N m_i \Delta_i}{\Delta_d} \quad (7.20)$$

$$K_e = \frac{4\pi^2 m_e}{T_e^2} \quad (7.21)$$

$$V_b = K_e \Delta_d \quad (7.22)$$

Base Shear Distribution

Once the base shear has been determined for the equivalent SDOF system, it can now be distributed along the height of the structure to find the storey forces (F_i) and shears (V_i). This is done in accordance with Equation 7.23, where the base shear is distributed in accordance with the floor masses and design displacement, as opposed to the storey height as in the FBD method. The storey shears are then found by summing the storey forces down the height of the building.

$$F_i = V_b \frac{\frac{m_i \Delta_i}{N}}{\sum_{i=1}^N m_i \Delta_i} \quad (7.23)$$

The storey shear at an arbitrary storey i is then divided between the CBF system and the PT system according to the shear ratio ω_i at that floor. For the CBF system, the design lateral resistance at a storey i ($V_{cbf,i}$) is given by:

$$V_{cbf,i} = (1 + v) A_{br} f_y \cos \beta \quad (7.24)$$

where v is the ratio of compressive buckling force to tensile yield force plotted in Figure 2.8, which is given by Wijesundara [134] as:

$$v = 0.369 \bar{\lambda}^{-1.819} (2\mu - 1)^{0.39\bar{\lambda}-0.805} \quad (7.25)$$

The resistance provided by the PT system is to be calculated from the following expression:

$$V_{pt,i} = K_2 \Delta_2 + K_3 (\Delta_4 - \Delta_2) \quad (7.26)$$

where K_2 is the elastic lateral stiffness of the PT frame prior to decompression, given in Equation 3.15 for a single storey frame, and K_3 is the post-decompression stiffness given in Equation 3.28. Δ_2 and Δ_4 are the lateral displacements at which decompression occurs and the maximum lateral storey displacement, respectively. The expression in Equation 7.26 therefore describes the hysteresis of the PT system shown in Figure 3.2.

7.5.4 Summary of Design Methodologies

The two possible design methods for the design of SC-CBFs within a PBD framework were presented. The approaches of the two different methods was first described, where it was seen the FBD approach used lateral force as its primary metric and the DDBD method used displacements, hence, the respective names. The advantage of using a FBD approach in for the PBD of

SC-CBFs is that it is a widely used method that appears in most design codes around the world, thus, making it relatively easy for practising engineers to use in the design office setting. The disadvantage to this method is that the displacements of the structure are of secondary concern and are merely a check at the end of an iterative design process. This is of concern when specifying displacement or interstorey drifts as the performance goals in a PBD framework. What is also undesirable about FBD as a method is that the use of unique force modification factors for a system makes it difficult to design for different levels of performance for different levels of seismic hazard. Ideally, different factors should be used for each performance level as three different levels of ductility are expected from each level of seismic intensity. This would require significant more work in order to develop and justify the derivation of such factors for the SC-CBF.

For the DDBD method, the use of displacements as the driving metric in the design method mean that displacements can be specified and designed to for each level of seismic hazard. This was used in O'Reilly et al. [94], where it was seen how the larger design base shear resulting from the specified design drifts and seismic hazard resulted in the design base shear to be used so that the performance goals of each level would be satisfied. This is advantageous for the design method as it involves specifying a design displacement to be achieved by the structure rather than a limit to be avoided when checking the displacement, as with the FBD method. This has the advantage of producing more economical designs as the structures are not over-designed, while still meeting the performance goals.

While the DDBD method appears to be more suited to a PBD framework setting for the SC-CBF, further numerical work is needed to validate the application of such a framework using these design methods.

7.6 Summary

This chapter presented a PBD framework for the design of SC-CBFs. This involved expanding on the concepts introduced in Chapter 2 to incorporate the SC-CBF into such a design framework. Previous studies into the PBD of the SC-CBF by the author was first discussed along with the areas in which the PBD framework could be improved as part of future studies.

The first of these was in the area of seismic hazard analysis of the design location. It was shown how the definition of hazard using the code defined spectra may not result in design spectra of uniform hazard, which is more appropriate for the PBD, as it deals with the different levels of seismic hazard as one of its key features. An improved method of generating the design spectra for the different design intensities was suggested by developing uniform hazard spectra for each hazard level at a given site location. An example of this was provided for the PEER benchmark site in LA, where the USGS online disaggregation tool was used to develop the hazard spectra. The impacts of this method of generating the hazard spectra on the selection of ground motions was then briefly discussed.

The second area that forms a PBD framework is the definition of the limit states that are being adhered to during the design process for each hazard level. This chapter discussed the definition of these performance limits for SC-CBFs, where the two types of ordinates being controlled were discussed. The first of these was termed the response ordinates, which involved the maximum interstorey and residual drift experienced by the structure during earthquake loading. The selection of the limits for each of these for each hazard is presented along with justification of each of these limits, based on previous studies. The second of these ordinates being controlled is the

member limits states. This involves the provision of sufficient capacity in the beams, columns and PT elements such that these elements remain elastic at all times. For the brace members, the fracture ductility for each of these braces is checked against the design ductility and ensured that this is not to be exceeded. If it is found that the brace fracture ductility is being exceeded, the design drift for the structures can be reduced accordingly.

The last part of the PBD framework that was presented in this chapter was the design methodology, which is needed to ensure that a structure can be designed to satisfy the performance limits for the seismic hazards defined for a particular site. Two methods of design were presented for possible use in the PBD framework. The first of these was the code based method, which is termed “force-based design”, as the lateral forces on the structure are used as the driving metric in the design process. The second method was the “direct displacement-based design method”, where it was seen that this method used the design drifts, or displacements, as the driving metric in the design process. The benefits of both methods was seen and was concluded that further analysis and design work should be conducted with each of these methods to validate their use in a PBD framework for SC-CBFs.

Chapter 8

Conclusions and Future Work

The conclusions drawn from the work presented in this thesis on the SC-CBF are presented in this chapter. A summary from each chapter of the thesis is presented along with a brief discussion of the main points presented in that chapter and its relevance to the overall thesis. These points are then collected to summarise the thesis as a whole, and a brief section highlighting the scope for future research on the development of the SC-CBF is presented, with some of the steps that are needed to implement this concept further discussed.

8.1 Summary

8.1.1 Chapter 2: Literature Review

- The behaviour and performance of CBFs in past earthquakes was first discussed, followed by a detailed review into the factors affecting the CBF behaviour at both a global frame level and a local brace member level.
- The occurrence of residual deformations in structures following earthquakes is reviewed, where the factors governing these residual deformations is reported, along with methods of mitigating them by changing small details in the design process.
- The concept of performance-based design in earthquake engineering and the idea of designing structures to performance goals that include the post-earthquake state is introduced as a new development in performance-based design.
- The development of self-centering systems in seismic design of concrete and steel systems is introduced and reviewed. The development of various self-centering systems is presented and the development of steel systems in particular is examined. This sets the stage for development of the research concept presented in Chapter 3.

8.1.2 Chapter 3: Mechanics of Self-Centering Concentrically Braced Frame

- The principal concept being developed in this thesis was presented in Chapter 3. This consisted of combining the conventional CBF, reviewed in Chapter 2, with the self-centering mechanism used in some of the self-centering systems developed for both concrete and steel systems, also reviewed in Chapter 2.

- The detailed behaviour of the SC-CBF was discussed and a series of analytical expressions that describe the behaviour of both the CBF system along with the bilinear elastic self-centering system were presented.
- The combination of these two systems gives the expressions that describe the hysteretic behaviour of the SC-CBF.
- A parameter study was then conducted on some of the variables discussed in the development of the analytical expressions. The study showed how the response parameters of interest are affected by chosen design parameters, which is critical to the correct proportioning of the system to achieve the flag-shaped loop and self-centering behaviour.

8.1.3 Chapter 4: Experimental Setup and Design

- The layout and design of an experimental test setup of the SC-CBF was presented in this chapter. This involves designing a test setup that could accurately reflect the behaviour of a SC-CBF when used in practice, but also be tested within the constraints and limitations of the testing facilities.
- The design of the test frame to account for any unwanted behaviour, and the various implications of the test setup were discussed, and the details listed accordingly.
- The design of test specimens that meant a number of tests could be performed were then detailed, with the key differences between each of the specimens listed. The main focus is that a sufficient range of test specimens be tested as part of the experimentation. This meant that a number of specimens could be used in the same test frame to provide multiple sets of test results.
- The design and sizing of coupon tests to determine the actual material properties of the specimens was listed. The details, and corresponding codes of practice, to which the specimens are to be tested are also outlined. This was conducted such that the exact properties of the material could be assessed when using the data to assess the validity of numerical models.
- The loading protocol to be used for the testing of both the coupon specimens and the brace specimens was outlined, where it was necessary that the testing of the specimens was compliant with the relevant codes of practice to draw conclusions between tests.
- The instrumentation layout to be used in the test frame for each test was outlined, along with the aims and goals of the positioning of each of the instruments used with regards to test data that can be obtained from the frame.

8.1.4 Chapter 5: Experimental Results and Observations

- The results of the coupon testing were first presented, where the material properties of the brace specimens are documented.
- The results of the brace specimens tested in the test frame were then presented for each of the nine tests carried out.
- The results showed that the test frame exhibits the bilinear elastic behaviour when tested without any brace specimens. This is consistent with the derivations for the PT system behaviour when examining and developing the analytical expressions that describe this behaviour.

- The specimen testing displayed the same general trend as with the bare PT frame, but with the added capacity and energy dissipation of the bracing members. This demonstrated that the SC-CBF exhibits a flag-shaped hysteresis and, thus, validates the research concept as a self-centering system.
- The salient response parameters from each test were documented and compared to theoretical approaches discussed in Chapter 3. It was demonstrated that the actual test values for the PT forces, OOP displacements, and post-decompression stiffness were within acceptable limits of the theoretical values. Also documented is the hysteretic energy dissipated by each of the brace specimens, where it was shown that the more stocky brace members showed far more energy dissipation than the slender braces, which is to be expected.

8.1.5 Chapter 6: Numerical Modelling of a SC-CBF

- The modelling of CBFs was discussed extensively, with the various parameters that effect the modelling of the brace members in OpenSees discussed. This includes the initial midpoint deflection of the braces, the material type and the type of elements used. For the modelling of the brace fracture, a low cycle fatigue model for the braces is utilised which attempts to account for the strain life fatiguing of the brace members during repeated cycling, and its implementation into the OpenSees model for the braces is then discussed.
- The modelling of the PT system was presented by first reviewing the attempts of modelling these self-centering systems in other research concepts. A method of modelling the PT system's rocking connection that accurately accounts for the self-centering behaviour of the frame, in addition to the member forces induced into the surrounding frame, was then developed.
- The modelling parameters that describe both the CBF system and the PT system are then combined to give the complete model for the SC-CBF. The response of a simple pushover analysis of this numerical model was found to be very similar to the analytical expressions developed for the SC-CBF in Chapter 3.
- This modelling of the SC-CBF was then expanded to develop an OpenSees model of the test frame. A comparison between the results of the experimentation and the numerical model shows excellent agreement between the two sets of data. This then validates the modelling of the SC-CBF in OpenSees using the developed modelling procedures.
- Since it is intended to use this validated model for the SC-CBF as part of numerical studies to examine the SC-CBF performance under earthquake excitation, a brief discussion into the expansion of the static model validated by experimentation into a dynamic model that can be used for further studies was outlined. This discussed the expansion to a dynamic model in terms of the incorporation of gravity loading and the representation damping in the model. The analysis objects, such as the numerical integrators, were discussed, as well as a strategy to ensure the quick convergence and completion of the dynamic analysis.

8.1.6 Chapter 7: Towards a Performance-Based Design Approach for SC-CBFs

- This chapter outlined a framework that can be developed and tested as part of future studies for the SC-CBF. This involves working the SC-CBF into a performance-based design framework, where different levels of seismic hazard are assigned performance limits

and goals. This aims to incorporate the concepts of performance-based design, discussed in Chapter 2, for the SC-CBF.

- The first area that was examined is the definition and representation of the seismic hazard for a given site at the various seismic intensity levels. This involved assessing the current Eurocode 8 approach to defining seismic hazard and then move to incorporate the recent developments of seismic hazard definition in the form of uniform hazard spectra.
- The second area that was explored is the definition of appropriate performance goals for the SC-CBF for each of the levels of seismic hazard defined. This means that the limits and goals set for each level must be justifiable targets from a structural point of view, but also from a structural member point of view, given the seismic hazard being considered. This means that elements such as the beams, columns and PT elements are to remain elastic at each level to protect the self-centering mechanism of the SC-CBF, but also that the brace members remain ductile at all times, avoiding fracture and also remaining relatively undamaged for more frequent earthquakes.
- The last item that was discussed as a part of the performance-based design framework for the SC-CBFs was the actual design method used. Two methods of design known as force-based design and direct displacement based design were explored as possible options for the framework. The requirement of the methods are that it must be able to deliver a satisfactory design for the SC-CBF which satisfies the performance limits set at the design stage for each of the hazard levels, and can be demonstrated to comply through numerical validation analysis using the model developed in this thesis.

8.2 Conclusions

A novel self-centering concentrically braced frame system has been developed in this thesis, which consists of a relatively simple method of arranging conventional CBFs, along with a post-tensioning arrangement. The system possesses the desirable lateral load resisting characteristics of a conventional CBF, but also ensures the self-centering behaviour following many large cycles of inelastic deformation. This concept was developed using the conventional arrangement of CBF systems together with the recently developed technology in the field of earthquake engineering, which utilises post-tensioning arrangements to provide a secondary elastic system that will ensure the recentering of the structure following large seismic events.

The behaviour of this system was identified theoretically and a series of analytical expressions were developed to describe the behaviour of the SC-CBF system. From the development of these expressions, it was observed that by selecting an appropriate arrangement of brace members and post-tensioning arrangement, the flag-shaped loop is achievable, which validates the system as a self-centering system. This was further demonstrated through the experimental testing of a SC-CBF assembly, where different brace specimens were tested to demonstrate the flag shaped loop and self-centering nature of the frame when loaded through many large cycles of inelastic deformation. The ordinates documented during the experimental testing were then compared to the analytical expressions developed previously to demonstrate the anticipated behaviour of the SC-CBF. This consisted of demonstrating that the PT force increased as anticipated with increased interstorey drift, and also that the post-decompression stiffness was closely matched to the analytical derivations. Both of these comparisons demonstrated the predictability of the SC-CBF's behaviour and, hence, validate the theoretical expressions developed.

A numerical model in OpenSees was developed based on the previous modelling parameters using for both the CBF system and also the PT system. This model was initially compared to the analytical expressions previously developed to demonstrate the accuracy of both the PT frame modelling, and also the SC-CBF modelling. When compared to the experimental testing results, the numerical model captured the behaviour very well, which validates the model for future use in the development of the SC-CBF as a seismic design solution. This development consists of utilising and developing the proposed performance-based design methodology for the SC-CBFs. This involves specifying different performance goals for different levels of seismic hazard to ensure the satisfactory performance of the SC-CBF system. These goals consist of specifying what is considered acceptable interstorey drift and residual drift for the SC-CBF, and also what elements are dissipating hysteretic energy and which ones remain elastic at all times. By ensuring that only the brace members are damaged, the SC-CBF structures can be easily repaired following large seismic events by replacing the damaged brace members, with the rest of the structure remaining undamaged. The further development of this PBD methodology is key to successful implementation of the SC-CBF in the seismic design community, and the proposed design methods outlined in Chapter 7 are intended to be used to validate this as part of future studies.

8.3 Future Work

While the work and findings presented in this thesis represent a step forward in the design and detailing of braced frame structures in seismic areas, there are a number of areas that can be explored as part of future research. These are as follows:

- Carry out extensive analysis using a series of SC-CBF arrangements to demonstrate the PBD framework presented in Chapter 7 can be applied to the SC-CBF. This involves selecting a site location, such as the Los Angeles site discussed in Chapter 7, and using the uniform hazard spectra for this site, select a number of spectrum-compatible ground motions. Using these hazard levels, a SC-CBF can be designed and detailed to meet the design goals using one of the two design methods discussed. The numerical model developed in Chapter 6, and the ground motions chosen for each of the seismic hazard levels can be used to evaluate the performance of the designed structure compared to the initial design goals. This can be carried out for both design methods presented, and for multiple building layouts and storey numbers. Successful results of these analyses will show that each of the designed structures meet the design goals for each hazard level when evaluated using the hazard spectrum matched ground motions.
- Conduct similar testing on different layouts of the SC-CBF to explore more of the factors that influence the behaviour in a real design situation. For example, the actual connection of such a frame to the ground was not properly addressed in the test setup presented in this thesis, as it was intended to represent an arbitrary storey in a MDOF system. Also, the interaction between two storeys in a SC-CBF would also be worth investigating, and validating experimentally.
- Three dimensional nonlinear finite element models could also be developed and validated based on the work conducted in this thesis. This would be worthwhile, as it could lead to further investigation of the failure modes of the self-centering mechanism that cannot be predicted using the simplified OpenSees modelling. This could lead to new suggestions and proposals on the improved designing of the self-centering connection.

CHAPTER 8. CONCLUSIONS AND FUTURE WORK

- If the SC-CBF is to become a serious design option for construction in seismic zones around the world, it is necessary to conduct full-scale shaking table tests on the frame to validate its performance and self-centering under real-time dynamic loading.

References

- [1] AISC. Specifications for the design, fabrication and erection of structural steel buildings. American standard, American Institute of Steel Construction, Chicago, Illinois, 1978.
- [2] AISC. Seismic provisions for structural steel buildings. American Standard ANSI/AISC 341-05, American Institute of Steel Construction, Chicago, Illinois, 2005.
- [3] AISI. Cold-formed steel design manual. American standard, American Iron and Steel Institute, 1996.
- [4] M.H. Archambault, R. Tremblay, and A. Filiatrault. Etude du comportement séismique des contreventements ductiles en x avec profilés tubulaires en acier. Technical Report EPM/GCS-1995-09, Department de Génie Civil Section Structures, Ecole Polytechnique, 1995.
- [5] ASCE. The mexico earthquake 1985: Factors involved and lessons learned, 1986.
- [6] A. Astaneh-Asl, S.C. Goel, and R.D. Hanson. Cyclic out-of-plane buckling of double-angle bracing. *Journal of Structural Engineering*, 111(5):1135–1153, 1985. URL [http://ascelibrary.org/doi/abs/10.1061/\(ASCE\)290733-9445\(1985\)111:5\(1135\)](http://ascelibrary.org/doi/abs/10.1061/(ASCE)290733-9445(1985)111:5(1135)).
- [7] J.W. Baker and C.A. Cornell. A vector-valued ground motion intensity measure consisting of spectral acceleration and epsilon. *Earthquake Engineering & Structural Dynamics*, 34(10):1193–1217, 2005. URL <http://dx.doi.org/10.1002/eqe.474>.
- [8] J.W. Baker and C.A. Cornell. Spectral shape, epsilon and record selection. *Earthquake Engineering & Structural Dynamics*, 35(9):1077–1095, 2006. URL <http://dx.doi.org/10.1002/eqe.571>.
- [9] J.W. Baker, T. Lin, S.K. Shahi, and N. Jayaram. New ground motion selection procedures and selected motions for the peer transportation research program. Technical Report 2011/03, Pacific Earthquake Engineering Research Center, 2011. URL http://peer.berkeley.edu/transportation/wp-content/uploads/2010/09/Baker_et_al__2011__PEER_GM_report.pdf.
- [10] J. Berman and M. Bruneau. Cyclic testing of a buckling restrained braced frame with unconstrained gusset connections. *Journal of Structural Engineering*, 135(12):1499–1510, 2009. URL [http://ascelibrary.org/doi/abs/10.1061/\(ASCE\)1943-541X.0000078](http://ascelibrary.org/doi/abs/10.1061/(ASCE)1943-541X.0000078).
- [11] R.G. Black, B.W.A Wenger, and P.E Popov. Inelastic buckling of steel struts under cyclic load reversals. Technical Report UCB/EERC-80/40, Earthquake Engineering Research Center, 1980. URL <http://nisee.berkeley.edu/elibrary/Text/101000963>.

- [12] J.J. Bommer and R. Pinho. Adapting earthquake actions in eurocode 8 for performance-based seismic design. *Earthquake Engineering & Structural Dynamics*, 35(1):39–55, 2006. URL <http://dx.doi.org/10.1002/eqe.530>.
- [13] B.M. Broderick, A.Y. Elghazouli, and J. Goggins. Earthquake testing and response analysis of concentrically-braced sub-frames. *Journal of Constructional Steel Research*, 64(9):997–1007, 2008. URL <http://www.sciencedirect.com/science/article/pii/S0143974X07001824>.
- [14] BSI. Specification for: High tensile steel wire and strand for the prestressing of concrete. British Standard BS 5896:1980, BSI, London, England, 1980.
- [15] G.M. Calvi and T. Sullivan. *A Model Code for the Displacement-Based Seismic Design of Structures*. IUSS Press, Pavia, Italy, 2009.
- [16] K.W. Campbell and Y. Bozorgnia. Nga ground motion model for the geometric mean horizontal component of pga, pgv, pgd and 5% damped linear elastic response spectra for periods ranging from 0.01 to 10s. *Earthquake Spectra*, 24(1):139–171, 2008. URL <http://www.earthquakespectra.org/doi/abs/10.1193/1.2857546>.
- [17] CEN. Metallic materials - tensile testing - part 1: Method of test at ambient temperature. European Standard EN 10002-1:2001, Comité Européen de Normalisation, Brussels, Belgium, 2001.
- [18] CEN. Eurocode 8: Design of structures for earthquake resistance - part 1: General rules, seismic actions and rules for buildings. European Standard EN 1998-1:2004, Comité Européen de Normalisation, Brussels, Belgium, 2004.
- [19] CEN. European structural steel standard. European Standard EN 10025:2004, Comité Européen de Normalisation, Brussels, Belgium, 2004.
- [20] CEN. Eurocode 3: Design of steel structures - part 1-1: General rules and rules for buildings. European Standard EN 1993-1-1:2005, Comité Européen de Normalisation, Brussels, Belgium, 2005.
- [21] CEN. Eurocode 3: Design of steel structures - part 1-3: General rules - supplementary rules for cold-formed members and sheeting. European Standard EN 1993-1-3:2006, Comité Européen de Normalisation, Brussels, Belgium, 2006.
- [22] CEN. Hot-finished structural hollow sections of non-alloy and fine grain steels - part 2: Tolerances, dimensions and section properties. European Standard EN 10210-2:2006, Comité Européen de Normalisation, Brussels, Belgium, 2006.
- [23] F. Charney. Unintended consequences of modeling damping in structures. *Journal of Structural Engineering*, 134(4):581–592, 2008. URL <http://ascelibrary.org/doi/abs/10.1061/40878%28202%2912>.
- [24] C.H Chen. *Perfomance Based Seismic Demand Assessment of Concentrically Braced Steel Frame Buildings*. PhD thesis, University of California, Berkeley, CA, USA, 2010.
- [25] H. Choi, J. Erochko, C. Christopoulos, and R. Tremblay. Comparison of the seismic response of steel buildings incorporating self-centering energy dissipative braces, buckling restrained braced and moment resisting frames. In *Proceedings of 14th World Conference on Earthquake Engineering*, Beijing, China, October 12-17 2008.

- [26] H. Choi, J. Erochko, C. Christopoulos, and R. Tremblay. Seismic response of 2d and 3d buildings incorporating buckling-restrained and self-centering bracing systems. In *Proceedings of 6th International Conference on Behaviour of Steel Structures in Seismic Areas*, Philadelphia, Pennsylvania, USA, 16th - 20th August 2009.
- [27] A.K. Chopra. *Dynamics of Structure: Theory and Applications to Earthquake Engineering*. Prentice Hall, Upper Saddle River, New Jersey, 2012.
- [28] Anil K. Chopra and Rakesh K. Goel. Direct displacement-based design: Use of inelastic vs. elastic design spectra. *Earthquake Spectra*, 17(1):47–64, 2001. URL <http://earthquakespectra.org/doi/abs/10.1193/1.1586166>.
- [29] C. Christopoulos. *Self-Centering Post-Tensioned Energy Dissipating (PTED) Steel Frames for Seismic Regions*. PhD thesis, University of California, San Diego, CA, USA, 2002.
- [30] C. Christopoulos and S. Pampanin. Towards performance-based seismic design of mdof structures with explicit consideration of residual deformations. *ISET Journal of Earthquake Technology*, 41(1):53–73, 2004. URL <http://home.iitk.ac.in/~vinaykg/Iset440.pdf>.
- [31] C. Christopoulos, A. Filiatrault, Chia-Ming Uang, and B. Folz. Posttensioned energy dissipating connections for moment-resisting steel frames. *Journal of Structural Engineering*, 128(9):1111–1120, 2002. URL <http://ascelibrary.org/doi/abs/10.1061/%28ASCE%290733-9445%282002%29128%3A9%281111%29>.
- [32] C. Christopoulos, S. Pampanin, and M.J.N. Priestley. Performance-based seismic response of frame structures including residual deformations. part i: Single-degree of freedom systems. *Journal of Earthquake Engineering*, 7(1):97 – 118, 2003. URL <http://www.tandfonline.com/doi/abs/10.1080/13632460309350443>.
- [33] C. Christopoulos, R. Tremblay, H.J. Kim, and M. Lacerte. Self-centering energy dissipative bracing system for the seismic resistance of structures: Development and validation. *Journal of Structural Engineering*, 134(1):96–107, 2008. URL <http://ascelibrary.org/doi/abs/10.1061/%28ASCE%290733-9445%282008%29134%3A1%2896%29>.
- [34] P.W. Clark, I.D. Aiken, K. Kasai, E. Ko, and I. Kimura. Design procedures for buildings incorporating hysteretic damping devices. In *Proceedings of the 69th Annual Convention of SEAOC*, Sacramento, California, 1999.
- [35] P.W. Clark, K. Kasai, I.D. Aiken, and I. Kimura. Evaluation of design methodologies for structures incorporating steel unbonded braces for energy dissipation. In *Proceedings of the 12th World Conference on Earthquake Engineering*, Auckland, New Zealand., 2000.
- [36] P. Clayton, J. Berman, and L. Lowes. Seismic design and performance of self-centering steel plate shear walls. *Journal of Structural Engineering*, 138(1):22–30, 2012. URL <http://ascelibrary.org/doi/abs/10.1061/%28ASCE%29ST.1943-541X.0000421>.
- [37] P.M. Clayton. Self-centering steel plate shear walls: Development of design procedure and evaluation of seismic performance. Master's thesis, University of Washington, 2010.
- [38] P.M. Clayton, J.W. Berman, T. Winkley, and L.N. Lowes. Development of a self-centering steel plate shear wall. In *Proceedings of the 8th International Conference on Urban Earthquake Engineering*, Tokyo Institute of Technology, Tokyo, Japan., March 7th - 8th 2011.

- [39] R.W. Clough and J. Penzien. *Dynamics of Structures*. Computers and Structures, Berkeley, USA, 3rd edition, 2003.
- [40] CSA. Cold-formed steel structural members. Canadian Standard CSA S136-94, Canadian Standards Association, Ontario, Canada, 1994.
- [41] G. Della Corte and F.M. Mazzolani. Theoretical developments and numerical verification of a displacement-based design procedure for steel braced structures. In *Proceedings of 14th World Conference on Earthquake Engineering*, Beijing, China, 12th - 17th October 2008.
- [42] ECCS. Recommended testing procedure for assessing the behaviour of structural steel elements under cyclic loads. European Standard Technical Working Group 1.3 Seismic Design, Technical Committee 1 Structural Safety and Loadings, 1986.
- [43] M. Elchalakani, Y. Zhang, and R. Grzebieta. Tests of cold-formed circular tubular braces under cyclic axial loading. *Journal of Structural Engineering*, 129(4), 2003. URL <http://ascelibrary.org/doi/abs/10.1061/%28ASCE%290733-9445%282003%29129%3A4%28507%29>.
- [44] A.Y. Elghazouli. Seismic design procedures for concentrically braced frames. *Institute of Civil Engineers: Structures and Buildings*, 156(SB4):381 – 394, 2003. URL <http://www.icevirtuallibrary.com/content/article/10.1680/stbu.2003.156.4.381>.
- [45] A.Y. Elghazouli, B.M. Broderick, J. Goggins, H. Mouzakis, P. Carydis, J. Bouwkamp, and A. Plumier. Shake table testing of tubular steel bracing members. *Institute of Civil Engineers: Structures and Buildings*, 158(SB4):229 – 241, 2005. URL <http://www.icevirtuallibrary.com/content/article/10.1680/stbu.2005.158.4.229>.
- [46] J.P. English. *Experimental and Numerical Seismic Analysis of Steel Gusset Plates in Concentrically Braced Frames*. PhD thesis, National University of Ireland, Galway, Ireland, 2013.
- [47] J.P. English and J. Goggins. Nonlinear seismic response of concentrically braced frames using finite element models. In *Proceedings of the 15th World Conference on Earthquake Engineering*, Lisbon, Portugal, 2012.
- [48] J. Erochko, C. Christopoulos, R. Tremblay, and H. Choi. Residual drift response of smrfs and brb frames in steel buildings designed according to asce 7-05. *Journal of Structural Engineering*, 137(5):589–599, 2011. URL <http://ascelibrary.org/doi/abs/10.1061/%28ASCE%29ST.1943-541X.0000296>.
- [49] E. Faccioli, R. Paoluci, and J. Rey. Displacement spectra for long periods. *Earthquake Spectra*, 20(2):347–376, 2004.
- [50] F. C. Filippou, E. P. Popov, and V. V. Bertero. Effects of bond deterioration on hysteretic behavior of reinforced concrete joints. Technical Report UCB/EERC-83/19, Earthquake Engineering Research Center, 1983. URL <http://nisee.berkeley.edu/elibrary/Text/132000474>.
- [51] M.M. Garlock. *Design, Analysis, and Experimental Behavior of Seismic Resistant Post-Tensioned Steel Moment Resisting Frames*. PhD thesis, Lehigh University, Lehigh, PA, USA, 2002.

- [52] M.M. Garlock, J.M. Ricles, R. Sause, C. Zhao, and L.W. Lu. Seismic behavior of post-tensioned steel frames. In *Proceedings of 3rd International Specialty Conference on Behavior of Steel Structures in Seismic Areas*, Montréal, Canada, 2000.
- [53] M.M. Garlock, J.M. Ricles, and R. Sause. Experimental studies of full-scale post-tensioned steel connections. *Journal of Structural Engineering*, 131(3):438–448, 2005. URL [http://ascelibrary.org/doi/abs/10.1061/\(ASCE\)290733-9445\(282005\)29131%3A3%28438%29](http://ascelibrary.org/doi/abs/10.1061/(ASCE)290733-9445(282005)29131%3A3%28438%29).
- [54] S. Gavridou, R. Pinho, H. Crowley, G. M. Calvi, V. Montaldo, C. Meletti, and M. Stucchi. Preliminary study on the impact of the introduction of an updated seismic hazard model for italy. *Journal of Earthquake Engineering*, 11(sup1):89–118, 2007. URL <http://www.tandfonline.com/doi/abs/10.1080/13632460701280195>.
- [55] Y. Ghanaat. Study of x-braced steel frame structures under earthquake simulation. Technical Report UCB/EERC-80/08, Earthquake Engineering Research Center, 1980. URL <http://nisee.berkeley.edu/elibrary/Text/101000953>.
- [56] J. Goggins. *Earthquake Resistant Hollow and Filled Steel Braces*. PhD thesis, University of Dublin, Trinity College, Dublin, Ireland, 2004.
- [57] J. Goggins and T. Sullivan. Displacement-based seismic design of sdof concentrically braced frames. In *Proceedings of 6th International Conference on Behaviour of Steel Structures in Seismic Areas*, Philadelphia, Pennsylvania, USA, 2009.
- [58] J. Goggins, B.M. Broderick, A.Y. Elghazouli, and A.S. Lucas. Behaviour of tubular steel members under cyclic axial loading. *Journal of Constructional Steel Research*, 62 (1-2):121–131, 2005. URL <http://www.sciencedirect.com/science/article/pii/S0143974X05001094>.
- [59] J. Goggins, B.M. Broderick, A.Y. Elghazouli, and A.S. Lucas. Experimental cyclic response of cold-formed hollow steel bracing members. *Engineering Structures*, 27 (7):977–989, 2005. URL <http://www.sciencedirect.com/science/article/pii/S0141029605000064>.
- [60] J. Goggins, B.M. Broderick, and A.Y. Elghazouli. Recommendations for the earthquake resistant design of braced steel frames. In *Proceedings of 1st European Conference on Earthquake Engineering & Seismology*, Geneva, Switzerland., 2006.
- [61] Golden Bay Cement. Press technology seminar gets enthusiastic support in new zealand., 27/05/2011 2011. <http://www.goldenbay.co.nz>.
- [62] H. Gugerli and S.C. Goel. Large scale tests for the hysteresis behavior of inclined members. In *Proceedings of the 7th World Conference on Earthquake Engineering*, Istanbul, Turkey., 1980.
- [63] C.B. Haselton, C.A. Goulet, J. Mitrani-Resier, J.L. Beck, G.G. Deierlein, K.A. Porter, J.P. Stewart, and E. Taciroglu. An assessment to benchmark the seismic performance of a code-conforming reinforced concrete moment frame building. Technical Report 2007/07, Pacific Earthquake Engineering Research Center, 2007. URL http://peer.berkeley.edu/publications/peer_reports/reports_2007/web_PEER712_HASELTONetal.pdf.
- [64] R.S. Henry. *Self-centering precast concrete walls for buildings in regions with low to high seismicity*. PhD thesis, University of Auckland, Auckland, New Zealand, 2011.

- [65] H.M. Hilber, T.J.R. Hughes, and R.L. Taylor. Improved numerical dissipation for time integration algorithms in structural dynamics. *Earthquake Engineering & Structural Dynamics*, 5(3):283–292, 1977. URL <http://onlinelibrary.wiley.com/doi/10.1002/eqe.4290050306/abstract>.
- [66] P.C. Hsiao, D.E. Lehman, and C.W. Roeder. Improved analytical model for special concentrically braced frames. *Journal of Constructional Steel Research*, 73(0):80 – 94, 2012. URL <http://www.sciencedirect.com/science/article/pii/S0143974X12000120>.
- [67] Y. Huang and S.A. Mahin. Simulating the inelastic seismic behavior of steel braced frames including the effects of low cycle fatigue. Technical Report 2010/104, Pacific Earthquake Engineering Research Center, 2010. URL http://peer.berkeley.edu/publications/peer_reports/reports_2010/webPEER_10104_HUANG_Mahin.pdf.
- [68] K. Ikeda and S.A. Mahin. Cyclic response of steel braces. *Journal of Structural Engineering*, 112(2):342–361, 1986. URL [http://ascelibrary.org/doi/abs/10.1061/\(ASCE\)290733-9445\(1986\)112:3A2\(28342\)29](http://ascelibrary.org/doi/abs/10.1061/(ASCE)290733-9445(1986)112:3A2(28342)29).
- [69] J. Iyama, C. Y. Seo, J. M. Ricles, and R. Sause. Self-centering mrf's with bottom flange friction devices under earthquake loading. *Journal of Constructional Steel Research*, 65 (2):314–325, 2009. URL <http://www.sciencedirect.com/science/article/pii/S0143974X08000722>.
- [70] L.S. Jacobsen. Damping in composite structures. In *Proceedings of the 2nd World Conference on Earthquake Engineering*, Tokyo and Kyoto, Japan., 1960.
- [71] A.K. Jain, S.C. Goel, and R.D. Hanson. Static and dynamic hysteresis behavior of steel tubular members with welded gusset plates. Technical Report UMEE 77R3, University of Michigan at Ann Arbor, 1977.
- [72] A.K. Jain, S.C. Goel, and R.D. Hanson. Hysteresis behaviour of bracing members and seismic response of braced frames with different proportions. Technical Report UMEE 78R3, University of Michigan at Ann Arbor, 1978.
- [73] A.K. Jain, R.D. Hanson, and S.C. Goel. Hysteretic cycles of axially loaded steel members. *Journal of the Structural Division*, 106(8):1777–1795, 1980.
- [74] K. Kawashima, G.A. MacRae, J. Hoshikuma, and K. Nagaya. Residual displacement response spectrum. *Journal of Structural Engineering*, 124(5):523–530, 1998.
- [75] I.F. Khatib, S.A. Mahin, and K.S. Pister. Seismic behavior of concentrically braced steel frames. Technical Report UCB/EERC-88/01, Earthquake Engineering Research Center, University of California., 1988. URL <http://nisee.berkeley.edu/elibrary/Text/200362>.
- [76] S. Kiggins and C. Uang. Reducing residual drift of buckling-restrained braced frames as a dual system. *Engineering Structures*, 28(11):1525–1532, 2006. URL <http://www.sciencedirect.com/science/article/pii/S0141029606000757>.
- [77] H. Kim and C. Christopoulos. Seismic design procedure and seismic response of post-tensioned self-centering steel frames. *Earthquake Engineering & Structural Dynamics*, 38 (3):355–376, 2009. URL <http://onlinelibrary.wiley.com/doi/10.1002/eqe.859/abstract>.

- [78] H.J. Kim and C. Christopoulos. Numerical models and ductile ultimate deformation response of post-tensioned self-centering moment connections. *Earthquake Engineering & Structural Dynamics*, 38(1):1–21, 2009. URL <http://onlinelibrary.wiley.com/doi/10.1002/eqe.836/abstract>.
- [79] J.W. Lai. *Experimental and Analytical Studies on the Seismic Behavior of Conventional and Hybrid Braced Frames*. PhD thesis, University of California, Berkeley, CA, USA, 2012.
- [80] K. Lee and M. Bruneau. Energy dissipation of compression members in concentrically braced frames: Review of experimental data. *Journal of Structural Engineering*, 131(4):552–559, 2005. URL [http://ascelibrary.org/doi/abs/10.1061/\(ASCE\)290733-9445\(2005\)131:4/29131](http://ascelibrary.org/doi/abs/10.1061/(ASCE)290733-9445(2005)131:4/29131).
- [81] D. Lehman, C. Roeder, D. Herman, S. Johnson, and B. Kotulka. Improved seismic performance of gusset plate connections. *Journal of Structural Engineering*, 134(6):890–901, 2008. URL [http://ascelibrary.org/doi/abs/10.1061/\(ASCE\)290733-9445\(2008\)134:6/28890](http://ascelibrary.org/doi/abs/10.1061/(ASCE)290733-9445(2008)134:6/28890).
- [82] Y.C. Lin, J.M. Ricles, R. Sause, and C.Y. Seo. Experimental assessment of the seismic performance of a self-centering steel mrf system with beam web friction devices. In *Proceedings of 6th International Conference on Behaviour of Steel Structures in Seismic Areas*, Philadelphia, Pennsylvania, USA, 2009.
- [83] G.A. Macrae and K. Kawashima. Post-earthquake residual displacements of bilinear oscillators. *Earthquake Engineering & Structural Dynamics*, 26(7):701–716, 1997. URL [http://onlinelibrary.wiley.com/doi/10.1002/\(SICI\)1096-9845\(199707\)26:7%3C701::AID-EQE671%3E3.0.CO;2-I/abstract](http://onlinelibrary.wiley.com/doi/10.1002/(SICI)1096-9845(199707)26:7%3C701::AID-EQE671%3E3.0.CO;2-I/abstract).
- [84] T.J. Maley, T.J. Sullivan, and G. Della Corte. Development of a displacement-based design method for steel dual systems with buckling-restrained braces and moment-resisting frames. *Journal of Earthquake Engineering*, 14(sup1):106–140, 2010. URL <http://www.tandfonline.com/doi/abs/10.1080/13632461003651687>.
- [85] J. McCormick, H. Aburano, M. Ikenaga, and M. Nakashima. Permissible residual deformation levels for building structures considering both safety and human elements. In *Proceedings of the 14th World Conference on Earthquake Engineering*, Beijing, China, 2008.
- [86] F. McKenna, G. Fenves, F. Filippou, and S. Mazzoni. Open system for earthquake engineering simulation (OpenSees). http://opensees.berkeley.edu/wiki/index.php/Main_Page, 2000.
- [87] M.S. Medhekar and D.J.L. Kennedy. Seismic evaluation of steel buildings with concentrically braced frames. Technical Report 219, Department of Civil and Environmental Engineering, University of Alberta, 1997.
- [88] M. Nakashima, T. Nishino, B. Tsuji, and Y. Iwasa. Effect of strain hardening on post buckling resistance of steel braces. In *Proceedings of 3rd Pacific Structural Steel Structure Conference*, Tokyo, Japan., 1992.
- [89] NIBS. Performance-based engineering, 09/09/2009 2009. <http://www.nibs.org>.
- [90] K.H. Nip, L. Gardner, and A.Y. Elghazouli. Cyclic testing and numerical modelling of carbon steel and stainless steel tubular bracing members. *Engineering Structures*, 32(2):424–441, 2010. URL <http://www.sciencedirect.com/science/article/pii/S0141029609003228>.

- [91] G.J. Nordenson. Notes on the seismic design of concentrically braced frames. In *Proceedings of the 8th World Conference on Earthquake Engineering*, San Francisco, California, USA, 1984.
- [92] NZCS. Presss design handbook. Technical report, New Zealand Concrete Society Inc, Auckland, New Zealand., 2010.
- [93] G.J. O'Reilly, J. Goggins, and S.A. Mahin. Behaviour and design of a self-centering concentrically braced steel frame system. In *Proceedings of the 15th World Conference on Earthquake Engineering*, Lisbon, Portugal, 2012.
- [94] G.J. O'Reilly, J. Goggins, and S.A. Mahin. Performance-based design of a self-centering concentrically braced frame using the direct displacement-based design procedure. In *Proceedings of the 15th World Conference on Earthquake Engineering*, Lisbon, Portugal, 2012.
- [95] G.J. O'Reilly, J. Goggins, and S.A. Mahin. Development of a novel self-centering concentrically braced frame system for deployment in seismically active regions. In *Proceedings of the Bridge and Concrete Research in Ireland Conference*, Dublin, Ireland, 2012.
- [96] S. Pampanin, C. Christopoulos, and M.J.N. Priestley. Performance-based seismic response of frame structures including residual deformations. part ii: Multi-degree of freedom systems. *Journal of Earthquake Engineering*, 7(1):119 – 147, 2003. URL <http://www.tandfonline.com/doi/abs/10.1080/13632460309350444>.
- [97] D. Pettinga, C. Christopoulos, S. Pampanin, and N. Priestley. Effectiveness of simple approaches in mitigating residual deformations in buildings. *Earthquake Engineering & Structural Dynamics*, 36(12):1763–1783, 2007. URL <http://onlinelibrary.wiley.com/doi/10.1002/eqe.717/abstract>.
- [98] M.J.N. Priestley. Myths and fallacies in earthquake engineering, revisited. Technical Report The Ninth Mallet Milne Lecture, European School for Advanced Studies in Reduction of Seismic Risk, 2003. URL <http://www.paviariskcentre.org/en/7/1/10/>.
- [99] M.J.N. Priestley, G.M. Calvi, and M.J. Kowalsky. *Displacement-Based Seismic Design of Structures*. IUSS Press, Pavia, Italy, 1st edition, 2007. URL <http://www.iusspress.it/pc/viewPrd.asp?idcategory=7&idproduct=41>.
- [100] J.M. Ricles, R. Sause, M.M. Garlock, and C. Zhao. Posttensioned seismic-resistant connections for steel frames. *Journal of Structural Engineering*, 127(2):113–121, 2001. URL <http://ascelibrary.org/doi/abs/10.1061/%28ASCE%290733-9445%282001%29127%3A2%28113%29>.
- [101] J.M. Ricles, R. Sause, S.W. Peng, and L.W. Lu. Experimental evaluation of earthquake resistant post-tensioned steel connections. *Journal of Structural Engineering*, 128(7):850–859, 2002. URL <http://ascelibrary.org/doi/abs/10.1061/%28ASCE%290733-9445%282002%29128%3A7%28850%29>.
- [102] C.W. Roeder, D.E. Lehman, P.C. Hsiao, and K. Palmer. Braced frames for seismic design in urban areas. In *Proceedings of the 8th International Conference on Urban Earthquake Engineering*, Tokyo Institute of Technology, Tokyo, Japan., 2011.
- [103] C.W. Roeder, E.J. Lumpkin, and D.E. Lehman. A balanced design procedure for special concentrically braced frame connections. *Journal of Constructional Steel Research*, 67 (11):1760 – 1772, 2011. URL <http://www.sciencedirect.com/science/article/pii/S0143974X11001416>.

- [104] D. Roke, R. Sause, J.M. Ricles, and N. Gonner. Design concepts for damage-free seismic resistant self-centering steel concentrically-braced frames. In *Proceedings of 14th World Conference on Earthquake Engineering*, Beijing, China., 2008.
- [105] S. Salawdeh. *Seismic Design of Concentrically Braced Steel Frames*. PhD thesis, National University of Ireland, Galway, Ireland, 2012.
- [106] S. Salawdeh and J. Goggins. Numerical simulation for steel brace members incorporating a fatigue model. *Engineering Structures*, 46(0):332 – 349, 2013. URL <http://www.sciencedirect.com/science/article/pii/S0141029612004105>.
- [107] S. Santagati, D. Bolognini, and R. Nascimbene. Strain life analysis at low-cycle fatigue on concentrically braced steel structures with rhs shape braces. *Journal of Earthquake Engineering*, 16:107–137, 2012. URL <http://www.tandfonline.com/doi/abs/10.1080/13632469.2012.675840>.
- [108] R. Sause, J.M. Ricles, M.M. Garlock, E. VanMarcke, L.S. Peh, and J. Liu. Self-centering seismic-resistant steel frame systems: Overview of past and current research. In *U.S.A Taiwan Workshop on Self-Centering Structural Systems, NCREE*, Taiwan., 2005.
- [109] SEOAC. Vision 2000: Performance based seismic engineering of buildings. Technical report, Structural Engineers Association of California, Sacramento, California, USA., 1995.
- [110] B. Shaback and T. Brown. Behaviour of square hollow structural steel braces with end connections under reversed cyclic axial loading. *Canadian Journal of Civil Engineering*, 30(4):745–753, 2003. URL <http://www.nrcresearchpress.com/doi/pdf/10.1139/103-028>.
- [111] C. Shuhaiibar, A. López, and R. Sabelli. Buckling-restrained braced frames. In *Proceedings of Seminar on Response Modification Technologies for Performance-Based Seismic Design*., pages 321–328, ATC and MCEER., 2002.
- [112] C.A. Shutt. Apartment skyscraper shows pre-cast's seismic capabilities. *Ascent Magazine*, Summer 2000, 2000.
- [113] E. Spacone, F. C. Filippou, and F. F. Taucer. Fibre beam-column model for non-linear analysis of r/c frames: Part i. formulation. *Earthquake Engineering & Structural Dynamics*, 25(7):711–725, 1996. URL [http://onlinelibrary.wiley.com/doi/10.1002/\(SICI\)1096-9845\(199607\)25:7%3C711::AID-EQE576%3E3.0.CO;2-9/abstract](http://onlinelibrary.wiley.com/doi/10.1002/(SICI)1096-9845(199607)25:7%3C711::AID-EQE576%3E3.0.CO;2-9/abstract).
- [114] J. Stanton, W. Stone, and G. Cheok. A hybrid reinforced precast frame for seismic regions. *PCI Journal*, -(March-April):20–32, 1997.
- [115] StreetEasy, 2013. URL <http://img.streeteasy.com/nyc/image/39/27675539.jpg>.
- [116] T. Sullivan. The current limitations of displacement-based design. Master's thesis, European School of Advanced Studies in Reduction of Seismic Risk (ROSE SCHOOL), Pavia, Italy, 2002.
- [117] A. Tanaka, K. Morita, and H. Yamanouchi. Damage of braced steel frames due to the 1978 myagiken oki earthquake. In *Proceedings of the 7th World Conference on Earthquake Engineering*, Istanbul, Turkey., 1980.
- [118] X. Tang and S.C. Goel. Brace fractures and analysis of phase i structure. *Journal of Structural Engineering*, 115(8):1960–1976, 1989. URL <http://ascelibrary.org/doi/abs/10.1061/%28ASCE%290733-9445%281989%29115%3A8%281960%29>.

- [119] S.V. Tolis and E. Faccioli. Displacement design spectra. *Journal of Earthquake Engineering*, 3(1):107–125, 1999. URL <http://www.tandfonline.com/doi/abs/10.1080/13632469909350342>.
- [120] R. Tremblay. Inelastic seismic response of steel bracing members. *Journal of Constructional Steel Research*, 58(5-8):665–701, 2002. URL <http://www.sciencedirect.com/science/article/pii/S0143974X01001043>.
- [121] R. Tremblay and M. Lacerte. Influence of the properties of bracing members on the seismic response of concentrically braced steel frames. In *Proceedings of the 12th European Conference on Earthquake Engineering*, London, UK., 2002.
- [122] R. Tremblay, A. Filiatrault, P. Timler, and M. Bruneau. Performance of steel structures during the 1994 northridge earthquake. *Canadian Journal of Civil Engineering*, 22(2):338–360, 1995. URL [http://onlinelibrary.wiley.com/doi/10.1002/\(SICI\)1096-9845\(199612\)25:12%3C1373::AID-EQE615%3E3.0.CO;2-Y/abstract](http://onlinelibrary.wiley.com/doi/10.1002/(SICI)1096-9845(199612)25:12%3C1373::AID-EQE615%3E3.0.CO;2-Y/abstract).
- [123] R. Tremblay, M.H. Archambault, and A. Filiatrault. Seismic response of concentrically braced steel frames made with rectangular hollow bracing members. *Journal of Structural Engineering*, 129(12):1626–1636, 2003. URL <http://ascelibrary.org/doi/abs/10.1061/%28ASCE%290733-9445%282003%29129%3A12%281626%29>.
- [124] R. Tremblay, M. Lacerte, and C. Christopoulos. Seismic response of multistory buildings with self-centering energy dissipative steel braces. *Journal of Structural Engineering*, 134(1):108–120, 2008. URL <http://ascelibrary.org/doi/abs/10.1061/%28ASCE%290733-9445%282008%29134%3A1%28108%29>.
- [125] C.M. Uang and M. Nakashima. Steel buckling-restrained braced frames. In Y. Bozorgnia and V.V. Bertero, editors, *Earthquake Engineering: From Engineering Seismology to Performance Based Engineering*. CRC Press, 2004.
- [126] P. Uriz. *Towards Earthquake Resistant Design of Concentrically Braced Steel Frames*. PhD thesis, University of California, Berkeley, CA, USA, 2005.
- [127] P. Uriz and S.A. Mahin. Towards earthquake resistant design of concentrically braced steel structures. Technical Report 2008/08, Pacific Earthquake Engineering Research Center, 2008. URL http://peer.berkeley.edu/publications/peer_reports/reports_2008/web_PEER808_URIZMahin.pdf.
- [128] USGS. 2008 interactive deaggregations, 2008. <https://geohazards.usgs.gov/deaggint/2008/>.
- [129] M. Wakabayashi, C. Matsui, K. Minami, and I. Mitani. Inelastic behaviour of steel frames subjected to constant vertical and alternating horizontal loads. In *Annual Conference Preprints AIJ.*, 1970.
- [130] W.R. Walpole. Behaviour of cold-formed steel rhs members under cyclic loading. Technical Report 96-4, Dept. of Civil Engineering, University of Canterbury, 1996.
- [131] D.P Welch, T.J. Sullivan, and G.M. Calvi. Developing displacement-based design and assessment procedures for performance-based earthquake engineering. Research Report ROSE 2012/03, Istituto Universitario di Studi Superiori di Pavia, 2012. URL <http://www.iusspress.it/pc/viewPrd.asp?idcategory=25&idproduct=173>.

- [132] R.E. Whitmore. Experimental investigation of stresses in gusset plates. *Engineering Experiment Station Bulletin No.16*, The University of Tennessee, 1952.
- [133] K. Wijesundara, R. Nascimbene, and T. Sullivan. Equivalent viscous damping for steel concentrically braced frame structures. *Bulletin of Earthquake Engineering*, 9:1535–1558, 2011. URL <http://dx.doi.org/10.1007/s10518-011-9272-4>.
- [134] K.K. Wijesundara. *Design of Concentrically Braced Steel Frames with RHS Shape Braces*. PhD thesis, European Centre for Training and Research in Earthquake Engineering (EUCENTRE), Pavia, Italy, 2009.
- [135] E. L. Wilson, I. Farhoomand, and K. J. Bathe. Nonlinear dynamic analysis of complex structures. *Earthquake Engineering & Structural Dynamics*, 1(3):241–252, 1972. ISSN 1096-9845. URL <http://dx.doi.org/10.1002/eqe.4290010305>.
- [136] T.B Winkley. Self-centering steel plate shear walls: Large scale experimental investigation. Master's thesis, University of Washington, 2011.
- [137] T. Wyss. *Beitrag zur Spannungsuntersuchung an Knotenblechen eiserner Fachwerke*. PhD thesis, Swiss Federal Institute of Technology, Zurich, Switzerland, 1923.
- [138] J. Yoo, C. Roeder, and D. Lehman. Analytical performance simulation of special concentrically braced frames. *Journal of Structural Engineering*, 134(6):881–889, 2008. URL <http://ascelibrary.org/doi/abs/10.1061/%28ASCE%290733-9445%282008%29134%3A6%28881%29>.
- [139] V.A. Zayas, E.P. Popov, and S.A. Mahin. Cyclic inelastic buckling of tubular steel braces. Technical Report UCB/EERC-80/16, Earthquake Engineering Research Center, 1980. URL <http://nisee.berkeley.edu/elibrary/Text/101000956>.
- [140] S. Zhu and Y. Zhang. Seismic behaviour of self-centring braced frame buildings with reusable hysteretic damping brace. *Earthquake Engineering & Structural Dynamics*, 36(10):1329–1346, 2007. URL <http://onlinelibrary.wiley.com/doi/10.1002/eqe.683/abstract>.
- [141] S. Zhu and Y. Zhang. Seismic analysis of concentrically braced frame systems with self-centering friction damping braces. *Journal of Structural Engineering*, 134(1):121–131, 2008. URL <http://ascelibrary.org/doi/abs/10.1061/%28ASCE%290733-9445%282008%29134%3A1%28121%29>.

Appendix A

Test Frame Design Calculations

Using the results of the pushover analysis performed on the OpenSees model presented in Chapter 6, the design forces can be found for the test frame. The design drift for which the frame was displaced to was 4% as this is the intended maximum displacement of the test frame. In addition to the displacement to which the frame is pushed, details about the material properties and geometry need to be established.

Material strengths are assumed to be Grade S355 steel for beams and columns and Grade S235 for braces elements. This gives a material yield strength of $355N/mm^2$ and $235N/mm^2$ for the Grades S355 and S235, respectively. The Young's modulus for each of these grades is taken to be $210,000N/mm^2$, as given in Eurocode 3 [20]. However, for the pushover analysis of the structure to determine the maximum force in the beams and columns, the expected yield strength of the braces should be used, which are the yield strengths taking into account over-strength of the steel. This was discussed in Section 2.3.3, and the yield strength of the braces is factored up by 1.1×1.25 .

In addition to the size of the braces to be used, the PT elements need to be sized also. For this experiment, two 12.5mm nominal diameter PT elements are used along each beam and are given an initial force of 80kN over the two strands. The material properties for these strands are given in Table 6 of BSI [14], and the yield strength is taken as $1770N/mm^2$ and its Young's modulus as $195,000N/mm^2$. This initial force and PT elements size is the same for each test.

Using the developed model, the frame can be designed and the beam and column members sized to remain elastic. In addition to the beams and columns, the pinned and roller connections need to be sized, the shear connection at the end of each beam needs to be sized, along with the beam flange reinforcement and panel zone shear reinforcement. The sizing of each of these components is now discussed.

A.1 Beams and Columns

The pushover of the B4 frame is the governing design for the test setup, as this is the largest section size to be tested and hence will induce the largest forces in the test frame. From this, the design forces are established and the members can be designed to the provisions given in Eurocode 3 [20].

The checks that are performed on the members for design are the utilisation ratios η for the

Table A.1: Beam member sizing details for test frame.

		Lower	Upper
Section		203x133x25UB	203x133x25UB
f_y	N/mm^2	355	355
A_b	m^2	0.0032	0.0032
b_h	m	0.2032	0.2032
L_b	m	1.4382	1.4382
N_{RD}	kN	1136	1136
V_{RD}	kN	655.9	655.9
M_{RD}	kNm	91.6	91.6
N_{ED}	kN	407.4	284.6
V_{ED}	kN	192.9	163.1
M_{ED}	kNm	41.6	32.7
η_N		0.36	0.25
η_V		0.29	0.25
η_M		0.45	0.36
$\eta_N + \eta_M$		0.81	0.61

shear force (η_V), axial force (η_N), bending moment (η_M) and the combined axial and moment interaction ($\eta_N + \eta_M$). The resulting design for the beams of the test setup are given in Table A.1, with the beam properties, design forces and member capacities shown also. The labels 'Upper' and 'Lower' refer to the beams above and below the storey being tested.

Similar checks are performed on the columns as with beams. Table A.2 shows the sizing of the columns with the relevant checks. The labels 'Upper' and 'Lower' refer to the columns used in the actual storey. The column marked 'Lower' refers to the section of column from the lower beam to the floor connection. This is necessary as to ensure that the column force in the lower section remain elastic, and as seen from Table A.2, these are the forces that govern the design.

A.2 Pinned/Roller Connections

The connection of the test frame to the reaction frame consists of two different connections. The first consists of a pinned connection that is located at the centre column and will transfer all of the storey shear into the reaction floor. The second is the roller connection, which is the same as the pinned connection with the exception that no shear is transferred as the gap opening at the exterior columns means these connections must provide adequate distance for the column to expand without any resistance. The value that was used to determine how far was sufficient when designing these roller connections was to use the OpenSees model and measure the maximum translation of the roller connection during cyclic pushover of the model. The roller connection is then detailed to provide this spacing to allow expansion of the frame.

For the pinned connection, the design forces are taken as the base shear and axial force measured in the OpenSees model with the B4 test specimen. The design forces that are measured are $V_{ED} = 277.6kN$ and $N_{ED} = 119.8kN$. The connection was then checked for the following using the provisions listed in Eurocode 3 [20]:

- Welds.

Table A.2: Column member sizing details for test frame.

		Lower	Upper
Section		152x152x37UC	152x152x37UC
f_y	N/mm^2	355	355
A_c	m^2	0.00471	0.00471
c_h	m	0.16180	0.16180
N_{RD}	kN	1672.1	1672.1
V_{RD}	kN	965.4	965.4
M_{RD}	kNm	109.7	109.7
N_{ED}	kN	214.4	106.4
V_{ED}	kN	244.3	66.9
M_{ED}	kNm	63.5	38.5
η_N		0.13	0.06
η_V		0.25	0.07
η_M		0.58	0.35
$\eta_N + \eta_M$		0.71	0.41

- Pin Shear.
- Plate Yielding.
- Bolts.

For the final dimensions of the plates and welds being described, refer to the tender drawings provided in Appendix B.

A.2.1 Welds

The longitudinal resistance of a 8mm CFW S355 is taken as 1.35kN/mm run, and 1.01kN/mm for 6mm CFW S355.

For the connection of the column to pin weld, the design resistance is:

$$F_{RD} = 2 \times 160mm \times 1.35kN/mm = 432kN \rightarrow FOS = 1.56$$

For the connection of top plate of pin to middle:

$$F_{RD} = 2 \times 200mm \times 1.01kN/mm = 404kN \rightarrow FOS = 1.46$$

For the connection of bottom of pin connection:

$$F_{RD} = 3 \times 200mm \times 1.01kN/mm = 606kN \rightarrow FOS = 2.18$$

A.2.2 Pin Shear

The area of a 40mm pin is taken as:

$$A_p = \frac{\pi 40^2}{4} = 1256.63mm^2$$

Using the provisions and notation in Eurocode 3 CEN [20] for the shear resistance of a bolt, the resistance is determined to be:

$$F_{RD} = \frac{2\alpha_v f_u A_p}{\gamma_{m2}} = \frac{2 \times 0.6 \times 430 \times 1256.63}{1.25} = 518kN \rightarrow FOS = 1.87$$

A.2.3 Plate Yield

The net section area is checked for yielding of the plate. The design resistance is as follows:

$$F_{RD} = (200mm - 40mm) \times 20mm \times 355N/mm^2 = 1136kN \rightarrow FOS = 4.09$$

A.2.4 Bolts

The shear capacity of 4 no. M24 Gr8.8 bolts is taken as 136kN and the tensile capacity as 203kN. The design resistances are then:

$$F_{RD} = 4 \times 136kN = 544kN \rightarrow FOS = 1.96$$

$$F_{RD} = 4 \times 203kN = 812kN \rightarrow FOS = 6.78$$

Looking at the details in Appendix B, we now have the design of the pinned connection completed. To design the roller connection, we need to simply adjust this pinned connection design for the expansion of the frame. This expansion is taken for OpenSees to be just under 10mm at 4% drift. Hence, a slot length of 30mm is provided to ensure adequate length is provided in both directions.

A.3 Beam Shear Connection

From the OpenSees analysis, the design shear to be transferred is 191.6kN. The design checks that are carried out are:

- Bolts.
- Welds.
- Net section.
- Moment on weld.

A.3.1 Bolts

The shear capacity of two M24 Gr8.8 bolts are:

$$F_{RD} = 2 \times 136kN = 272kN \rightarrow FOS = 1.42$$

A.3.2 Welds

The longitudinal resistance of a 6mm CFW on either side of the 135mm long plate is:

$$F_{RD} = 2 \times 135mm \times 1.01kN/mm = 272.7kN \rightarrow FOS = 1.42$$

A.3.3 Net section

The net section along the plate where the bolt holes are drilled is checked as follows:

$$A_{net} = (135mm - 2(26mm))(15mm) = 996mm^2$$

$$F_{RD} = 996 \times 355N/mm^2 / \sqrt{3} = 255kN \rightarrow FOS = 1.33$$

A.3.4 Moment on weld

Since the shear force is transferred through the bolts, and these bolts are a distance 57.5mm from the weld, the design moment acting on the weld is:

$$M_{ED} = 191.6kN \times 57.5mm = 11kNm$$

This moment is then resisted by the transverse resistance of the weld which is given by:

$$M_{RD} = 2 \times 135mm \times 1.24kN/mm \times 135/2 = 22.6kNm \rightarrow FOS = 2.05$$

A.4 Beam Flange Reinforcement

The area of the beam flange is therefore calculated as:

$$A_{b,fl} = 133.2mm \times 7.8mm = 1038.96mm^2$$

The axial capacity is then:

$$N_{RD} = 1038.96mm^2 \times 355N/mm^2 = 368.8kN$$

The axial capacity that the flange must transfer is taken as 534.7kN. Therefore, there is an additional 165.9kN to be transferred. We try a $85 \times 10mm$ plate.

$$N_{RD} = 85mm \times 10mm \times 355N/mm^2 = 301.75kN \rightarrow FOS = 1.82$$

This plate is adequate as it is sufficiently wide to connect a gusset plate for the braces and also leaves room for the welds to be applied.

A.5 Panel Zone Reinforcement

The OpenSees modelling gives the maximum force that will be acting through the connection as $V_{ED} = 534.7kN$. The panel zone is then checked for its capacity and the amount of required reinforcement.

The depth between the column flanges d_c is taken as 123.6mm, and with an 8mm web, the shear area of the column is $A_v = 123.6mm \times 8mm = 988.8mm^2$. The depth between the panel zone is taken as 204mm. The resistance is given by:

$$M_{RD} = A_v \times d_{pz} \times \tau_y$$

and the design force is given by:

$$M_{ED} = 2 \times V_{ED} \times d_{pz}/2 = P_t d_{pz}$$

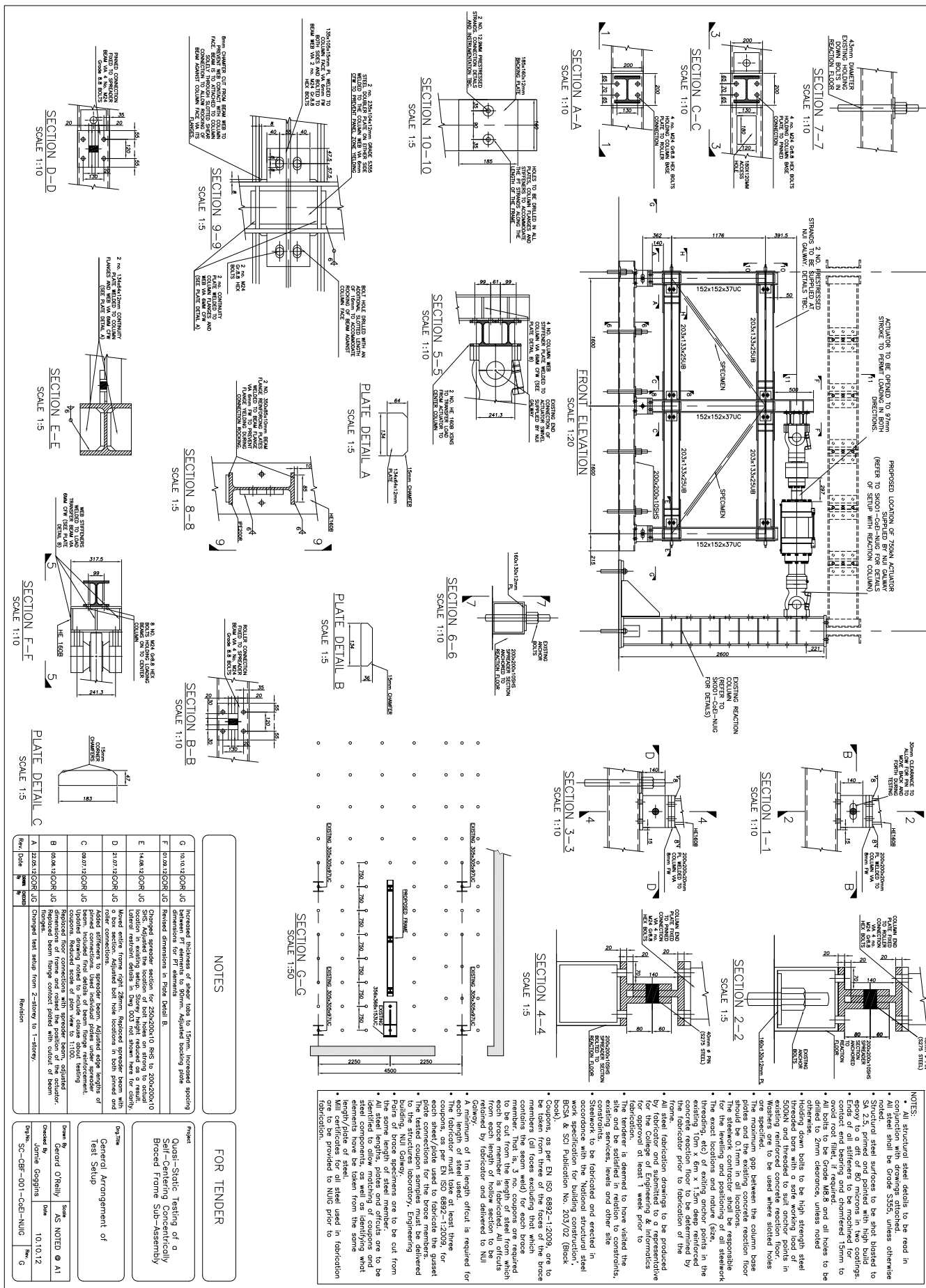
Equating the two we get the following relationship:

$$t_{pz} = \frac{V_{ED}\sqrt{3}}{d_c f_y} = \frac{534.7 \times \sqrt{3}}{123.6 \text{mm} \times 355 \text{N/mm}^2} = 21.1 \text{mm}$$

Since the column web is already contributing 8mm, two 12mm plates are provided to bring the total panel zones thickness up to 32mm.

Appendix B

SC-CBF Test Setup Drawings



ID	SERIAL (S235 STEEL)	LENGTH (mm)	NUMBER
T4	40x40x4 SHS	1395.3	4
T3	30x30x2.5 SHS	1432.6	4
T2	25x25x2.5 SHS	1435.1	4
T1	20x20x2.0 SHS	1437.6	4

NOTES:

- All structural steel details to be read in conjunction with drawings attached.
- All steel shall be Grade S235, unless otherwise noted.
- Stainless steel surfaces to be shot blasted to 200 grit and primed with high build epoxy to a grit of 80 microns in two coatings.
- Flanges to be machined for contact end bearing and chamfered 15mm to 20mm.
- Oil stiffeners to be machined for end bearing.
- Welds to be made with all holes to be drilled to 2.0mm diameter, unless noted.
- Holding down bolts to be high strength steel threaded bars with a sets working load of 30kN and threaded to suit anchor points in concrete or steel. Anchors to be cast in concrete or welded to steel. Anchors to be threaded into 10mm dia. holes.
- Workers are to be used where slotted holes are specified.
- The maximum gap between the column base plates and the existing concrete reaction floor plates is to be 10mm. Column base plates to be cut to 10mm thickness.
- The brace to be positioned in the correct locations on the frame (size, threading, etc) of existing anchor points in concrete reaction floor x 6m x 1.5m deep reinforced by 10mm dia. bars.
- Brace reaction force to be determined by the fabricator prior to fabrication of the frame.
- Brace reaction force to be determined by the fabricator and submitted to a representative for the College of Engineering & Informatics for approval at least 1 week prior to fabrication.
- The tenderer is to have visited the site and be satisfied in relation to constraints, existing services, levels and other site conditions.
- Structures to be fabricated and passed in accordance with the "National Structural Steel Work Specification for Building Construction", BCSA & SCI Publication No. 20/3-02 (Black book).
- Coupons, as per EN ISO 8892-1:2009, are to be taken from three of the faces of the brace members (the seam weld) for each brace to be cut from the length of steel from which each brace member is fabricated. All coupons from each length of hollow section to be retained by fabricator and delivered to NUI Galway.
- A minimum of 1m length offset is required for each length of steel used in fabrication of the brace. The fabricator must take at least three coupons, as per EN ISO 8892-1:2009, for each sheet/plate used to fabricate the gusset plate connections for the brace members.
- Brace specimens are to be cut from the same length of steel member.
- Steel identification plates and/or colour coding elements have to be taken from the same length/plate of steel.
- Min certificates for all steel used in fabrication are to be provided to NUG prior to fabrication.

BRAKE SECTION SIZES – TABLE 1

SECTION S1-S1
SCALE 1:5
DRAWING 1:5

SECTION H1-H1
SCALE 1:5
DRAWING 1:5

SECTION S2-S2
SCALE 1:5
DRAWING 1:5

SECTION H2-H2
SCALE 1:5
DRAWING 1:5

SPECIMEN 1 DETAIL
SCALE 1:10
DRAWING 1:10

SPECIMEN 2 DETAIL
SCALE 1:10
DRAWING 1:10

SPECIMEN 3 DETAIL
SCALE 1:10
DRAWING 1:10

PLATE DETAIL GP1
SCALE 1:5
DRAWING 1:5

PLATE DETAIL GP2
SCALE 1:5
DRAWING 1:5

PLATE DETAIL GP3
SCALE 1:5
DRAWING 1:5

NOTES

FOR TENDER

Project	Quasi-Static Testing of a Self-Centring Concentrically Braced Frame Sub-Assembly
Obj./Ref.	Brace Specimen Details
Drawn By	Gerard O'Reilly
Spec. No.	AS-NOTED @ A1
Checked By	Jerome Grogan
Date	10.10.12
Rev. Date	10.10.12
Comments	Changed test setup from 2-story to 1-story
Revision	G

SECTION S3-S3
SCALE 1:5
DRAWING 1:5

SECTION H3-H3
SCALE 1:5
DRAWING 1:5

SECTION S4-S4
SCALE 1:5
DRAWING 1:5

SECTION H4-H4
SCALE 1:5
DRAWING 1:5

PLATE DETAIL GP4
SCALE 1:5
DRAWING 1:5

Appendix C

Brace and Gusset Plate Details

Table C.1: Brace details.

Specimen		B1	B2	B3	B4
Section		20x20x2.0SHS	25x25x2.5SHS	30x30x2.5SHS	40x40x4.0SHS
f_y	N/mm^2	235	235	235	235
A	mm^2	134	209	259	535
b	mm	20	25	30	40
t	mm	2.0	2.5	2.5	4.0
c	mm	14	17.5	22.5	28.0
ϵ		1	1	1	1
$c/t\epsilon$		7	7	9	7
Class		1	1	1	1
L	mm	1437.6	1435.1	1432.6	1395.3
λ_1		93.9	93.9	93.9	93.9
i	mm	7.2	8.99	11.0	14.4
$\bar{\lambda}$		2.12	1.70	1.39	1.03
B-Curve		c	c	c	c
α		0.49	0.49	0.49	0.49
Φ		3.23	2.31	1.75	1.24
χ		0.176	0.26	0.35	0.52
$N_{t,RD}$	kN	31.49	49.1	60.865	125.7
$N_{b,RD}$	kN	5.55	12.7	21.6	65.6

Table C.2: Gusset plate design checks.

		B1	B2	B3	B4
Brace Info					
$F_{ED,t}$	kN	56.55	72.7	88.86	186.12
$\bar{\lambda}$		2.44	1.95	1.54	1.17
$F_{ED,c}$	kN	7.82	14.9	26.83	83.44
Initial sizing					
L_c	mm	40	50	50	70
t_{gp}	mm	4	4	4	6
W_w	mm	66.1	82.7	87.7	120.8
$t_{gp,min}$	mm	2.18	2.25	2.59	3.94
Whitmore Yielding					
F_{RD}	kN	103.3	129.2	137.0	283.1
Block Shear					
F_{RD}	kN	79.9	99.9	99.9	209.9
Whitmore Fracture					
F_{RD}	kN	110.2	137.8	146.1	301.9
Thornton Buckling					
L_1	mm	44.0	31.61	38.0	44.8
L_2	mm	68.0	65.12	71.0	89.2
L_3	mm	23.0	14.04	11.0	7.0
L_{ave}	mm	45.0	36.92	40.0	47.0
k		1.5	1.5	1.5	1.5
i	mm	1.15	1.15	1.15	1.73
kL/i		58.4	47.9	51.9	40.7
$\bar{\lambda}_{gp}$		0.76	0.62	0.68	0.53
α_{gp}		0.49	0.49	0.49	0.49
Φ_{gp}		0.93	0.80	0.84	0.72
χ_{gp}		0.68	0.76	0.73	0.82
F_{RD}	kN	57.8	81.2	82.6	190.9
Free Edge Length					
L_{fg}	mm	56.0	70.07	72.0	102.0
$L_{fg,max}$	mm	72.9	72.9	72.9	109.4
Net Section Fracture					
F_{RD}	kN	61.6	81.0	101.4	209.3
b_{pl}	mm	12	15	20	20
t_{pl}	mm	2	2	2	4
Weld Lengths					
$F_{ED,V}$	kN	33.2	45.7	52.2	109.3
$F_{ED,H}$	kN	45.7	56.5	71.8	150.5
L_V	mm	106	96.39	106	130
L_H	mm	130	119	130	150
$F_{w,l,RD}$	kN/mm	1.01	1.01	1.01	1.01
$F_{RD,V}$	kN	214.12	194.7	214.12	262.6
$F_{RD,H}$	kN	262.6	240.38	262.6	303
$F_{w,conn}$	kN	108.8	202	136	190.4

Appendix D

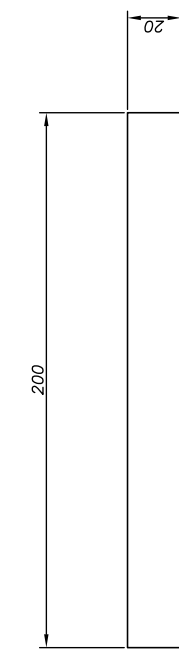
Coupon Specimen Drawings and Mill Certificates

TABLE 1

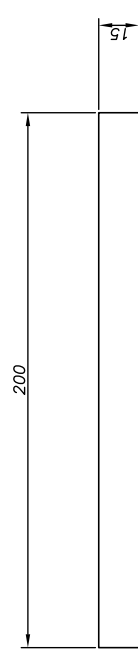
SECTION	SIZE	Number	LENGTH (L) [mm]	WIDTH (B) [mm]	TOLERANCE [mm]
1	20x20x2.0	3	200	12	0.090
2	25x25x2.5	3	200	15	0.090
3	30x30x2.5	3	200	15	0.090
4	40x40x4.0	3	200	20	0.105

COUPONS TO BE LABELLED C-(1)-(2)-(3) WHERE (1) CORRESPONDS TO THE SECTION TYPE (OPTIONS: 40, 30, 25 OR 20). (2) CORRESPONDS TO THE FACE FROM WHICH THE COUPON WAS TAKEN (OPTIONS: A, B, C OR D) AND (3) CORRESPONDS TO THE INDEX OF THAT SECTIONS FACE.

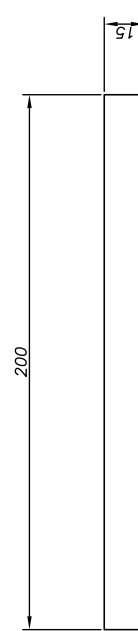
EXAMPLE: THE 2ND COUPON CUT FROM FACE C OF THE 25X25X2.5SHS IS TO BE LABELLED C-25-C-2.



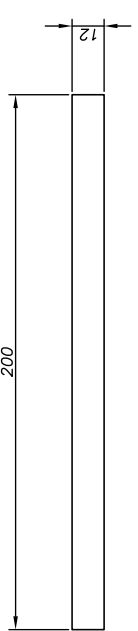
SECTION 1 COUPON
SCALE 1:2



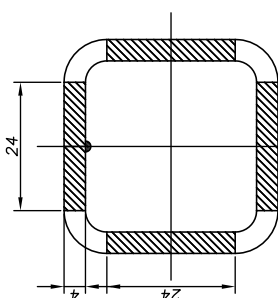
SECTION 2 COUPON
SCALE 1:2



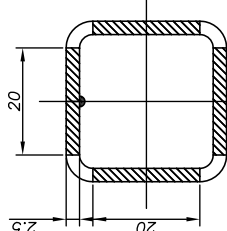
SECTION 3 COUPON
SCALE 1:2



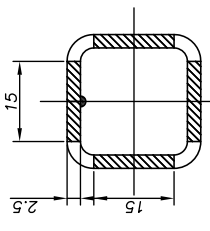
SECTION 4 COUPON
SCALE 1:2



SECTION 1 - 40x40x4.0 SHS
SCALE 1:1



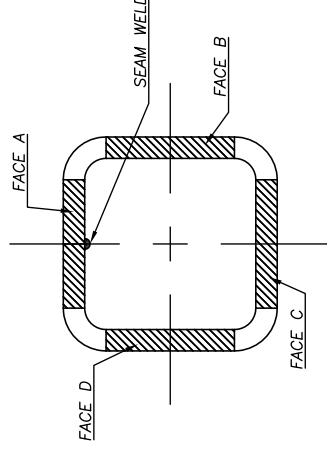
SECTION 2 - 30x30x2.5 SHS
SCALE 1:1



SECTION 3 - 25x25x2.5 SHS
SCALE 1:1

SECTION 2 - 20x20x2.0 SHS
SCALE 1:1

TABLE 1



SECTION NOTATION
SCALE 1:1

NOTES

- Coupons sized in accordance with BS EN 10002-1:2001.
- Require 4 coupons from each of the faces (A through D).
- Tolerances for each Section are as per Tables D2 and D3 of the above EN and are noted in Table 1.

FOR FABRICATION

Project
Quasi-Static Testing of a Self-Centring Concentrically Braced Frame Sub-Assembly

Drawn By
Gerard O'Reilly
Scale
AS NOTED @ A3
Checked By
Jamie Goggins
Date
20.02.2013
Rev
B
Coupon Specimen Details

Drawn By Gerard O'Reilly	Scale AS NOTED @ A3
Checked By Jamie Goggins	Date 20.02.2013
Rev B	
SC-CBF-004-CoEi-NUIG	



TATA STEEL UK LIMITED
P.O. Box 1, Brigg Road,
Scunthorpe,
North Lincolnshire, DN16 1BP.
Telephone: 01244 402040
Fax: 402353 Telex: 52601

A1

INSPECTION CERTIFICATE

A1

Customer
Mr. [Redacted]

Product manufactured under a Management System Approved to ISO 9001

Tata Steel Ref. No. 303679/ 5
Customer Order No. 00399389

AS Work Order No. 241155/ 6
AS

TATA STEEL UK LIMITED
(LISBURN)
STEEL HOUSE , HULLS HILL,
MOIRA ROAD,
LISBURN, COUNTY ANTRIM
NORTHERN IRELAND.

BT28 2SN

Inspection

WORKS INSPECTION

11 BEAM 203 X 133 X 25
As Rolled.

Length 17000mm

Spec. Approval Pending
EN10025-2:SS55J0+R
11 BEAM 203 X 133 X 25
As Rolled.

B1/B2
CE

303610

0036

Quantity	Customer Ref. No.	Piece No.	C	Yield Strength kg/mm ²	Tensile Strength kg/mm ²	Rm kg/mm ²	Elongation %	Impact Energy Joule	Thickness mm	S-Salt Surface	M-Mid-Thick mm	Q-Quarter-thick mm	R-Roll-thick mm	T-Tri-thick mm	C-Cross Section	C-Cross Section	B-Bottom Surface	A-Assym Cross Section	N-Nominal d	S-Steel Specified Condition	S-Steel Specified Condition	C-Heat Stamping Process												
50	62818		C	27	OC	76	75	74	14 Aw/ 10 Ind t	OC	C	Si	Cr	Ni	Al	Cu	Nb	N	Sn	Ti	V													
				424	556	410	545	26																										

Customer Ref. No. 303679/ 5
These details are certified by Tata Steel UK Limited to be correct and complete
with the requirements of the Product Description.

All original Inspection Certificates issued by Tata Steel UK Limited will contain either an embossed stamp or be unprinted with a Tata Steel UK Limited customer's logo, or a combination of both. Any reissue of a copy of a Tata Steel UK Limited Inspection Certificate will be:

A3

R.P. Haas

R.P. Haas, Test House Manager, Tata Steel UK

Customer Ref. No. 303679/ 5
These details are certified by Tata Steel UK Limited to be correct and complete
with the requirements of the Product Description.

A3

195525



STAHLWERK THÜRINGEN
 Grupo Alfonso Gallardo

A01 Stahlwerk Thüringen GmbH
A02 Quality Assurance Department
 Kronacher Straße 6
 07333 Unterwellenborn
 Germany
A03 Our Order No.: 2019525110
A04 Your Order No.: 49096

A05 Certificate No. 2847/2-2011
 Advice No. A110224048

A06 Inspection Certificate 3.1
 according to EN 10204:2004/3.1

SWT

South Park Road MATERIAL AND TEST
 DN17 2BY Bottesford Scunthorpe CERTIFICATE SUPPLIED BY
 UNITED KINGDOM NSD LTD
 TA SOUTH PARK STEELS
 OUR ORDER REF D 16-327 334-754
 ADVISER NOTE NO. 227284
 SIGNED
 FOR AND ON BEHALF OF NSD LTD
 THIS IS A TRUE COPY OF THE ORIGINAL CERTIFICATE

A07 Quality: S355JR+AR
 according to: EN 10025-2/2004

Pos.	Heat No.	Dimension	Length [mm]	Pieces [stck]	Theoretical Weight [kg]
002	87793	UC 152X152X23	10 000 mm	50	11 500 kg
004	87788	UC 152X152X23	12 200 mm	150	42 090 kg
007	87792	UC 152X152X23	15 500 mm	108	38 502 kg
007	87793	UC 152X152X23	15 500 mm	10	3 565 kg
008	87791	UC 152X152X23	16 000 mm	24	8 832 kg
009	87794	UC 152X152X23	16 500 mm	7	2 657 kg
010	87792	UC 152X152X23	17 500 mm	48	19 320 kg
010	87793	UC 152X152X23	17 500 mm	6	2 415 kg
011	87791	UC 152X152X23	18 300 mm	48	20 202 kg
011	87794	UC 152X152X23	18 300 mm	4	1 684 kg
013	87783	UC 152X152X30	11 000 mm	15	4 950 kg
014	87783	UC 152X152X30	12 200 mm	84	30 744 kg
016	87784	UC 152X152X30	14 000 mm	66	27 720 kg
017	87763	UC 152X152X30	15 500 mm	40	18 600 kg
021	87780	UC 152X152X30	18 300 mm	20	10 980 kg
024	87721	UC 152X152X37	12 200 mm	70	31 598 kg
027	87771	UC 152X152X37	15 500 mm	36	20 648 kg
028	87785	UC 152X152X37	16 000 mm	18	10 656 kg
029	87786	UC 152X152X37	16 500 mm	18	10 989 kg
030	87772	UC 152X152X37	17 500 mm	15	9 713 kg
031	87772	UC 152X152X37	18 300 mm	15	10 157 kg

Heat Analysis [%]	C	Si	Mn	P	S	N	Al	Nb	V	Cr
Heat No.	[wt]	[wt]	[wt]	[wt]	[wt]	[wt]	[wt]	[wt]	[wt]	[wt]
max	0.24	0.25	1.08	0.040	0.040					
min	0.14									
87771	0.07	0.18	1.43	0.019	0.023	0.009	0.001	0.040	0.007	0.11
87772	0.07	0.19	1.44	0.021	0.020	0.008	0.001	0.040	0.007	0.09
87780	0.08	0.19	1.41	0.018	0.021	0.011	0.001	0.039	0.006	0.09
87783	0.07	0.19	1.40	0.021	0.020	0.009	0.001	0.038	0.006	0.09
87784	0.07	0.19	1.38	0.019	0.020	0.008	0.001	0.036	0.006	0.08
87786	0.08	0.18	1.39	0.026	0.023	0.008	0.018	0.039	0.006	0.09
87788	0.07	0.17	1.41	0.026	0.018	0.010	0.017	0.039	0.005	0.07
87791	0.06	0.18	1.41	0.021	0.020	0.011	0.016	0.037	0.005	0.11

A08 Works Inspector
 Renate Schmidt

24-Feb-2011

We hereby certify that this is a true copy of an
 original mill test certificate held on Tata Steel files.

Signature N.M.

Customer o/n Mat!

Tata Steel o/n 2272848

TATA STEEL



THYSSENKRUPP MANNESMANN LTD
UNIT 6, WESTMINSTER COURT
HIPLEY ST, OLD WOKING
WOKING, SURREY GU22 9LG

NO : 36717
DATE : 11.02.2011

MILL TEST CERTIFICATE
(ACC TO EN 10204/3.1)

Descript of Goods and / or Services

IRELAND : S2893

PRIME NEWLY PRODUCED COLD FORMED ERW STEEL HOLLOW SECTION TO EN10219 : 2008 PARTS 1 AND 2.
PRODUCED FROM HOT ROLLED COILS TO EN10025 GRADE S235JR (OLD ST 37/2) IN VARIOUS LENGTHS. OILED
(OIL OF PRODUCTION ONLY), SUITABLE FOR GALVANISING. TUBE ENDS TO CUT FLUSH AND MUST BE CLEAN
AND FREE FROM BURRS. MATERIAL TO BE SECURELY BANDED AND EXPORT WRAPPED IN HESSIAN IN 1.5-2.0 MT
BUNDLES. MATERIAL IS CE MARKED

8) S2095

ORDER S2893 SPECIFICATION - GRADE S235JR

STANDARD : EN 10219 ORDER NO : 16598 D

SIZE (MM)	mm	KG/PC	NO OF BUNDLES	NO OF PIECES	DIAMETER	TWS	QUALITY	CHEMICAL ANALYSIS AND MECHANICAL PROPERTIES													
								Tested Strength Nominal	Tested Strength Nominal	Tested Strength Nominal	C-Content	Si Content	Cr Content	N Content	Sulfur and Chlor.	Fusion	Bend	Knot-Tensile	Impact Strength Value	Impact Strength Value	
20x20x2	✓	7.5	144	3	432	3240	3400	S 235 JR	44	37	30	3	3	21	27	18	-	-	-	-	07919
25x25x2		7.6	121	4	484	3630	4940	S 235 JR	37	27	26	4	3	18	12	14	-	-	-	-	00591 02
25x25x3		7.5	121	1	121	907.5	1700	S 235 JR	44	35	29	8	1	50	19	12	-	-	-	-	916523
30x30x2.5	✓	7.5	100	3	300	2250	4490	S 235 JR	45	31	26	17	1	31	15	32	-	-	-	-	034022
40x40x2		7.5	81	4	324	2480	5400	S 235 JR	37	26	30	3	2	22	10	9	-	-	-	-	00658 02
40x40x2.5		7.5	81	12	972	7290	19730	S 235 JR	40	30	31	11	3	51	14	10	-	-	-	-	917683
40x40x3		7.5	81	3	243	1822.5	6760	S 235 JR	41	31	31	8	1	40	12	6	-	-	-	-	917688 01
40x40x4	✓	7.5	49	2	90	735	3080	S 235 JR	47	25	36	4	1	34	17	14	-	-	-	-	020598
50x50x2.5		7.5	56	13	728	5460	18780	S 235 JR	40	30	31	8	2	51	14	10	-	-	-	-	917663
50x50x3		7.5	56	13	728	5460	22130	S 235 JR	37	29	25	4	1	35	17	20	-	-	-	-	140372
50x50x4		7.5	49	3	147	1102.5	8040	S 235 JR	37	27	33	6	1	35	6	16	-	-	-	-	106658
50x50x5		7.5	42	2	84	630	4000	S 235 JR	47	26	31	3	1	34	11	29	-	-	-	-	033941 02
60x60x4		7.5	36	3	100	810	5200	S 235 JR	42	36	30	5	3	20	11	15	-	-	-	-	06418 01
60x80x5		7.5	36	3	100	810	6300	S 235 JR	45	33	26	5	3	25	12	10	-	-	-	-	06625 02
70x70x9		7.5	36	3	100	810	4750	S 235 JR	43	34	28	6	2	23	16	9	-	-	-	-	06608 04
80x80x3		7.5	25	1	200	1500	9860	S 235 JR	42	34	20	4	2	21	11	9	-	-	-	-	07208 03
80x80x4		7.5	25	2	50	375	3320	S 235 JR	37	26	26	4	1	38	15	30	-	-	-	-	065461
80x80x5		7.5	25	12	300	2250	23720	S 235 JR	41	35	29	4	2	24	14	15	-	-	-	-	06457 01
80x80x6		7.5	16	6	96	720	9560	S 235 JR	42	37	25	4	20	30	16	5	-	-	-	-	102282 01
90x90x3		7.5	20	3	60	450	3300	S 235 JR	41	33	30	5	3	22	17	8	-	-	-	-	062321
100x100x3		7.5	16	9	144	1080	8830	S 235 JR	37	27	20	4	1	22	15	32	-	-	-	-	520585
100x100x4		7.5	16	13	208	1560	17130	S 235 JR	42	35	29	5	2	23	22	15	-	-	-	-	06360 03
100x100x5	✓	7.5	16	9	144	1080	14200	S 235 JR	42	35	29	6	2	26	19	19	-	-	-	-	06133 04
100x100x6		7.5	16	6	96	720	12070	S 235 JR	42	36	29	5	3	30	26	11	-	-	-	-	10784 04
100x100x8		7.5	16	2	32	240	5000	S 235 JR	42	36	32	7	2	46	13	17	-	-	-	-	06421
100x100x8		12	9	2	18	216	4810	S 235 JR	42	36	32	7	2	48	13	17	-	-	-	-	06421
120x120x5		12	9	11	99	1180	19100	S 235 JR	44	34	29	8	3	22	20	8	-	-	-	-	06161 02
120x120x6		12	9	3	27	324	6660	S 235 JR	38	32	29	6	3	24	14	15	-	-	-	-	057691
120x120x8		12	9	1	9	108	2820	S 235 JR	43	33	34	7	3	53	16	10	-	-	-	-	06283
150x150x5		12	6	4	24	280	5860	S 235 JR	42	31	32	4	1	30	13	17	-	-	-	-	07163 01
60x25x2,6		7.5	84	3	252	1890	4900	S 235 JR	42	33	37	4	3	22	20	9	-	-	-	-	07225
30x30x3		7.5	70	3	210	1575	4960	S 235 JR	42	34	34	7	18	34	13	25	-	-	-	-	101175
30x40x3		7.5	50	5	250	1876	9110	S 235 JR	44	30	27	4	2	22	16	8	-	-	-	-	06030
30x40x4		7.5	40	4	160	1200	7780	S 235 JR	37	27	29	4	1	38	12	15	-	-	-	-	020602
100x50x3		7.5	40	9	360	2700	16780	S 235 JR	41	34	31	4	2	21	23	10	-	-	-	-	06162
100x50x5		8.1	40	2	80	480	4600	S 235 JR	41	34	35	5	2	23	17	19	-	-	-	-	06453 02
100x50x5		7.5	30	7	210	1575	15350	S 235 JR	40	31	38	4	2	26	15	12	-	-	-	-	06204
100x50x6		7.5	21	3	63	472,5	5740	S 235 JR	38	32	29	6	3	24	14	15	-	-	-	-	105769
100x60x6		7.5	20	3	60	450	5840	S 235 JR	39	32	30	6	3	20	19	17	-	-	-	-	06488 02
120x80x3,6		7.5	20	2	40	300	2740	S 235 JR	42	36	27	7	2	49	20	10	-	-	-	-	937752
120x80x5		7.5	15	2	30	225	2960	S 235 JR	42	34	33	5	2	24	18	16	-	-	-	-	06505 03
120x80x6		7.5	15	3	45	337,5	5670	S 235 JR	41	36	36	5	3	29	18	11	-	-	-	-	107 06491 04
150x100x6		7.5	12	2	24	180	3000	S 235 JR	38	32	31	6	2	20	15	15	-	-	-	-	05624 01
150x100x8		12	9	2	18	216	4650	S 235 JR	38	33	32	4	3	26	13	18	-	-	-	-	128 05951 01
150x100x8		12	8	1	8	108	2940	S 235 JR	41	30	31	11	2	72	28	13	-	-	-	-	122 816230
160x80x5		7.8	12	3	36	270	4300	S 235 JR	44	36	35	8	2	33	13	21	-	-	-	-	55439 02
200x100x5		12	6	2	12	144	3760	S 235 JR	40	33	30	4	1	22	11	9	-	-	-	-	90 08715 01
200x100x8		12	6	2	12	144	4770	S 235 JR	43	33	34	7	3	53	16	10	-	-	-	-	234 06283
200x39,7x5		7.5	10	3	30	225	3300	S 235 JR	42	35	40	4	2	28	18	14	-	-	-	-	07154 01
200x160,3x4		6	10	10	100	600	6810	S 235 JR	37	25	28	3	1	29	18	18	-	-	-	-	04350 2 01

Weight 1600 kg 100% INSPECTED

GP4.F18 / 20.03.2010

TOTAL P.05

TO WHOM IT MAY CONCERN"

COPY

MILL TEST CERTIFICATE

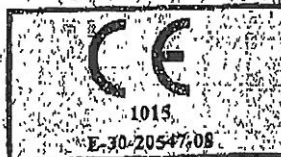
ACC TO 2.2 EN10204

DESCRIPTION OF GOODS

ST 3025 / 15463

STRUCTURAL HOLLOW SECTIONS, ACC TO EN10219 PART 1 & 2
IN GRADE S235JRH SUITABLE FOR HOT DIP GALVANISINGOZDEMIR BORU PROFIL
SAHAYI V TICARET
LIMITED SIKNETI

IMBODU L 001 111 111 621 001 8908



SIZE (MM)	LENGTH (M)	CAST NUMBERS	CHEMICAL COMPOSITION (%)						MECHANICAL PROPERTIES		
			C	Si	Mn	P	S	Cu	Al	Yield P. N/mm ²	Tens St. N/mm ²
S235JRH											
25x25x2.00	7,500	19930	0,036	0,014	0,162	0,017	0,013	0,024	0,026	322,74	403,56
25x25x2.50	7,500	19931	0,044	0,004	0,369	0,012	0,031	0,021	0,004	246,55	361,45
30x30x2.00	7,500	19930	0,036	0,014	0,162	0,017	0,013	0,024	0,026	322,74	403,56
30x30x2.50	7,500	19931	0,044	0,004	0,369	0,012	0,031	0,021	0,004	246,55	361,45
30x30x3.00	7,500	19932	0,079	0,009	0,601	0,010	0,011	0,027	0,054	333,30	421,14
40x40x2.50	7,500	19931	0,044	0,004	0,369	0,012	0,031	0,021	0,004	246,55	361,45
40x40x3.00	7,500	19932	0,079	0,009	0,601	0,010	0,018	0,068	0,023	279,47	408,56
40x40x4.00	7,500	19933	0,120	0,023	0,365	0,021	0,031	0,021	0,004	246,55	361,45
50x50x2.50	7,500	19931	0,044	0,004	0,369	0,012	0,031	0,021	0,004	246,55	361,45
50x50x4.00	7,500	19933	0,120	0,023	0,365	0,021	0,018	0,068	0,023	279,47	408,56
60x60x5.00	7,500	19934	0,030	0,007	0,219	0,010	0,014	0,022	0,037	242,36	363,24
70x70x3.00	7,500	19932	0,079	0,009	0,601	0,010	0,011	0,027	0,054	333,30	421,14
80x80x3.00	7,500	19932	0,079	0,009	0,601	0,010	0,011	0,027	0,054	333,30	421,14
80x80x4.00	7,500	19933	0,120	0,023	0,365	0,021	0,018	0,068	0,023	279,47	408,56
80x80x5.00	7,500	19934	0,030	0,007	0,219	0,010	0,014	0,022	0,037	242,36	363,24
80x80x6.00	7,500	19935	0,091	0,004	0,592	0,008	0,016	0,024	0,046	261,59	392,28
90x90x3.00	7,500	19932	0,079	0,009	0,601	0,010	0,011	0,027	0,054	333,30	421,14
90x90x5.00	7,500	19935	0,091	0,004	0,592	0,008	0,016	0,024	0,046	261,59	392,28
100x100x3.00	7,500	19932	0,079	0,009	0,601	0,010	0,011	0,027	0,054	333,30	421,14
100x100x6.00	7,500	19935	0,091	0,004	0,592	0,008	0,016	0,024	0,046	261,59	392,28
125x50x2.00	7,500	19930	0,036	0,014	0,162	0,017	0,013	0,024	0,026	322,74	408,56
125x50x2.50	7,500	19936	0,083	0,006	0,623	0,012	0,014	0,027	0,043	332,41	427,87
125x50x3.00	7,500	19937	0,135	0,030	0,327	0,031	0,014	0,033	0,026	275,42	456,81
140x60x3.00	7,500	19937	0,135	0,030	0,327	0,031	0,014	0,033	0,026	275,42	456,81
140x80x3.00	7,500	19937	0,135	0,030	0,327	0,031	0,014	0,033	0,026	275,42	456,81
160x90x3.00	7,500	19937	0,135	0,030	0,327	0,031	0,014	0,033	0,026	275,42	456,81
160x100x3.00	7,500	19937	0,135	0,030	0,327	0,031	0,014	0,033	0,026	275,42	456,81
160x100x6.00	12,000	19935	0,091	0,004	0,592	0,008	0,016	0,024	0,046	261,59	392,28
20x9xØx2.50	7,500	19936	0,083	0,006	0,623	0,012	0,014	0,027	0,043	332,41	427,87
26.9xØx3.00	7,500	19937	0,135	0,030	0,327	0,031	0,014	0,033	0,026	275,42	456,81
33.7xØx2.50	7,500	19936	0,083	0,006	0,623	0,012	0,014	0,027	0,043	322,42	427,87
33.7xØx3.00	7,500	19938	0,088	0,009	0,596	0,011	0,009	0,020	0,036	324,32	424,11
42.4xØx2.50	7,500	19936	0,083	0,006	0,623	0,012	0,014	0,027	0,043	322,42	427,87
42.4xØx3.00	7,500	19938	0,088	0,009	0,596	0,011	0,009	0,020	0,036	324,32	424,11
48.3xØx2.50	7,500	19936	0,083	0,006	0,623	0,012	0,014	0,027	0,043	322,42	424,11
48.3xØx3.00	7,500	19938	0,088	0,009	0,596	0,011	0,009	0,020	0,036	324,32	427,87
48.3xØx4.00	7,500	19933	0,120	0,023	0,365	0,021	0,018	0,068	0,023	279,47	408,56
50.3xØx3.00	7,500	19938	0,088	0,009	0,596	0,011	0,009	0,020	0,036	324,32	424,11
50.3xØx4.00	7,500	19933	0,120	0,023	0,365	0,021	0,018	0,068	0,023	279,47	408,56
76.1xØx3.00	7,500	19938	0,088	0,009	0,596	0,011	0,009	0,020	0,036	324,32	424,11
88.9xØx4.00	7,500	19933	0,120	0,023	0,365	0,021	0,018	0,068	0,023	279,47	408,56
88.9xØx5.00	7,500	19934	0,030	0,007	0,219	0,010	0,014	0,022	0,037	242,36	363,24
114.3xØx3.00	7,500	19938	0,088	0,009	0,596	0,011	0,009	0,020	0,036	324,32	424,11
114.3xØx3.50	7,500	19939	0,051	0,004	0,359	0,018	0,022	0,057	0,002	247,89	373,24
114.3xØx5.00	7,500	19934	0,030	0,007	0,219	0,010	0,014	0,022	0,037	242,36	363,24
139.7xØx5.00	7,500	19934	0,030	0,007	0,219	0,010	0,014	0,022	0,037	242,36	363,24
158.3xØx5.00	7,500	19934	0,030	0,007	0,219	0,010	0,014	0,022	0,037	242,36	363,24

MANUFACTURER : OZDEMIR BORU PROFIL SAN.VE TIC.LTD.STI.

CELSA STEEL UK
OFFICES: Build. 58, Castle Works, East Moors Road
CF24 5NN Cardiff (United Kingdom)



CELSA
GROUP

CELSA
MANUFACTURING UK

INSPECTION CERTIFICATE BS-EN 10204-2004, Type 3.1

Standard
BS-EN 10025/04

Customer:
DUGGANS STEEL IRELAND LTD.
TULLAMALINE, CALLAN ROAD
00000 KILKENNY
Ireland

Destination:
DUGGANS STEEL IRELAND LTD.
TULLAMALINE, CALLAN ROAD
00000 KILKENNY
Ireland

MATERIAL
Hot rolled structural steel products

	CAST	C	MN	SI	S	P	Cr	N	Ni	Cu	Mo	V	CE	Reh	Rm	A	T	Res1.	Res2.	Res3.	Res Av
	#	#	#	#	#	#	#	#	#	#	#	#	#	#	MPA	MPA	%	%C	J	J	J
S 275 JR +AR 100X10 6m	CM077012	0.10	0.49	0.15	0.014	0.022	0.123	0.010	0.22	0.46	0.039	0.000	0.257	328	451	39.3					
S 275 JR +AR 100X10 6m	CM077012	0.10	0.49	0.15	0.014	0.022	0.123	0.010	0.22	0.46	0.039	0.000	0.257	331	460	39.2					
S 275 JR +AR 100X10 6m	CM077012	0.10	0.49	0.15	0.014	0.022	0.123	0.010	0.22	0.46	0.039	0.000	0.257	331	464	39.3					
S 275 JR +AR 100X10 6m	CM077012	0.10	0.49	0.15	0.014	0.022	0.123	0.010	0.22	0.46	0.039	0.000	0.257	333	463	39.2					
S 275 JR +AR 150X10 6m	CM077029	0.09	0.50	0.15	0.031	0.022	0.095	0.011	0.21	0.38	0.041	0.000	0.243	327	457	34.8					
S 275 JR +AR 150X10 6m	CM077029	0.09	0.50	0.15	0.031	0.022	0.095	0.011	0.21	0.38	0.041	0.000	0.243	327	489	36.7					
S 275 JR +AR 150X10 6m	CM077029	0.09	0.50	0.15	0.031	0.022	0.095	0.011	0.21	0.38	0.041	0.000	0.243	317	455	36.1					

Certified that the material detailed hereon meets the requirements of the specified standard.
Cardiff, 18.06.2012

Stuart Thomas
Quality Manager



LIVIDA, srl
Certificazione
Qualità e
Sicurezza
EN ISO 9001:2008



The use of the CARES certification marks indicates certification in respect of those products covered by the product certificate number 030801.

Delivery number: 25837173
Order number : 15612379
Your order : 100117095

CELSA STEEL UK
OFFICES: Build. 58, Castle Works, East Moors Road
CF24 5NN Cardiff (United Kingdom)



CE
CERTIFIED
BY THE
MANUFACTURER
EN 10000-4

INSPECTION CERTIFICATE BS-EN 10204-2004, Type 3.1

Standard
BS-EN 10025 / 04

Customer:
DUGGANS STEEL IRELAND LTD.
TULLAMMAINE, CALLAN ROAD
00000 KILKENNY
Ireland

The use of the CARES certification marks indicates
certification in respect of those products covered
by the product certificate number 030801.

Delivery number: 25834646
Order number : 15611619
Your order : 10017058

Destination:
DUGGANS STEEL IRELAND LTD.
TULLAMMAINE, CALLAN ROAD
00000 KILKENNY
Ireland

MATERIAL	CAST	C	MN	SI	S	P	Cr	N	Ni	Cu	Mo	V	CE	Reh	Rm	A 5.65	T	Res1	Res2	Res3	Res Av
Hot rolled structural steel products		%	%	%	%	%	%	%	%	%	%	%	%	MPA	MPA	%	°C	J	J	J	
S 275 JR +AR 150X6 6m	CM076728	0.10	0.49	0.16	0.029	0.026	0.121	0.010	0.19	0.45	0.039	0.000	0.258	350	464	40.1					
S 275 JR +AR 130X12 L. 6.00	CM076827	0.10	0.49	0.16	0.031	0.022	0.083	0.010	0.18	0.41	0.033	0.000	0.247	314	445	37.2					
S 275 JR +AR 130X12 L. 6.00	CM076827	0.10	0.49	0.16	0.031	0.022	0.083	0.010	0.18	0.41	0.033	0.000	0.247	313	447	35.6					
S 275 JR +AR 130X12 L. 6.00	CM076827	0.10	0.49	0.16	0.031	0.022	0.083	0.010	0.18	0.41	0.033	0.000	0.247	312	444	33.4					
S 275 JR +AR 120X12 L. 6.00	CM075994	0.09	0.54	0.15	0.030	0.018	0.073	0.011	0.15	0.36	0.029	0.000	0.232	322	443	39.9					
S 275 JR +AR 120X10 6m	CM076985	0.11	0.48	0.14	0.033	0.025	0.095	0.010	0.20	0.43	0.038	0.000	0.260	340	471	41.2					

Certified that the material detailed hereon meets the
requirements of the specified standard.

Cardiff, 24.05.2012

Stuart Thomas
Quality Manager

Laboratorio de Laminaciones S.A.
D.F. C.P. 10700, Hacienda Las Flores
Calle 156 Col. Lomas de Chapultepec, D.F.
M.F. D.F. 03153611 Subsidiaria International
Telefono: +34 93 773 04 00 Fax: +34 93 773 05 52
Celdas: +34 93 817 66 84 Fax: +34 93 773 05 52



CERTIFICATE OF RESULTS OF ASSAYS ONE IN 10.2000, TYPE 31

Standard: UNE-EN 10025-2:2006
Type: S 275 JR +AR
St. Mea.: UNE-EN 10058-2004
St. Tol.: UNE-EN 10058-2004
Our Ref: 000000000
(B08-31BAL2)

Customer: MCARTHUR GROUP LTD.
M50 BUSINESS PARK, BALLYMOUNT AV.
00000 DUBLIN 12
Ireland

Delivery number: 25672321
Order number : 15559122
Your order : 14548

TO

07196339900

Sample	Heat Number	C	Si	Mn	P	S	N	Cr	Ni	Mo	V	Al	Ca	Si	Cr	Ni	Mo	V	Al	Ca	Si	Cr	Ni	Mo	V	Al	Ca
S 275 JR +AR 60X12 L. 6,00m	CB143861	0.090	0.570	0.170	0.034	0.011	0.090	0.150	0.170	0.029	0.002	0.002	0.0114	0.001	0.251	309	435	37.0									
S 275 JR +AR 60X10 L. 6,00m	CB143864	0.090	0.560	0.180	0.024	0.012	0.090	0.160	0.190	0.034	0.002	0.002	0.0099	0.001	0.242	309	444	38.0									
S 275 JR +AR 65X12 L. 6,00m	MCR143864	0.080	0.560	0.180	0.024	0.012	0.090	0.160	0.190	0.034	0.002	0.002	0.0099	0.001	0.242	305	430	37.0									
S 275 JR 65.00X10.0 6	CB143880	0.090	0.580	0.170	0.019	0.015	0.140	0.150	0.180	0.035	0.002	0.002	0.0106	0.001	0.264	310	445	39.0									
S 275 JR +AR 60X10 L. 6,00m	CB143897	0.090	0.560	0.160	0.031	0.014	0.100	0.120	0.160	0.022	0.002	0.002	0.0093	0.001	0.247	310	446	39.0									

- Product suitable for galvanizing: $0.14 < Si <= 0.25 \& P <= 0.035$.
- Intended use: construction and civil engineering.
- Durability: not determined.

-Regulated substances: not determined

Castellbisbal, 20.06.2008

Sergi Cabrerizo Sanjuan
Jefe de Control de Calidad

CELSA STEEL UK
OFFICES: Build. 58, Castle Works, East Moors Road
CF24 5NN Cardiff (United Kingdom)

CELSA
GROUP



INSPECTION CERTIFICATE BS-EN 10204-2004, Type 3.1

Standard
BS-EN 10025/04

Customer:
DUGGANS STEEL IRELAND LTD.
TULLAMAINÉE, CALLAN ROAD
00000 KILKENNY
Ireland

Destination:
DUGGANS STEEL IRELAND LTD.
TULLAMAINÉE, CALLAN ROAD
00000 KILKENNY
Ireland

The use of the CARES certification marks indicates
certification in respect of those products covered
by the product certificate number 030801.

Delivery number: 25827695
Order number : 15609196
Your order : 10016920

MATERIAL	CAST	C	MN	Si	S	P	Cr	N	Ni	Cu	Mo	V	CE	Reh	Rm	A 5.65	T	Reb1	Reb2	Reb3	Reb AV
Hot rolled structural steel products																					
S 275 JR +AR 150X12 6m	CM075221	0.10	0.51	0.17	0.027	0.019	0.069	0.010	0.17	0.42	0.027	0.000	0.241	314	435	35.2					
S 275 JR +AR 150X12 6m	CM075221	0.10	0.51	0.17	0.027	0.019	0.069	0.010	0.17	0.42	0.027	0.000	0.241	303	433	35.4					
S 275 JR +AR 150X12 6m	CM075221	0.10	0.51	0.17	0.027	0.019	0.069	0.010	0.17	0.42	0.027	0.000	0.241	324	437	35.2					
S 275 JR +AR 150X12 6m	CM075221	0.10	0.51	0.17	0.027	0.019	0.069	0.010	0.17	0.42	0.027	0.000	0.241	315	437	35.2					
S 275 JR +AR 150X6 6m	CM075050	0.09	0.48	0.14	0.027	0.017	0.057	0.010	0.14	0.34	0.028	0.000	0.237	320	451	40.1					
S 275 JR +AR 150X6 6m	CM075050	0.09	0.48	0.14	0.027	0.017	0.057	0.010	0.14	0.34	0.028	0.000	0.237	332	451	40.4					
S 275 JR +AR 150X6 6m	CM075050	0.09	0.48	0.14	0.027	0.017	0.057	0.010	0.14	0.34	0.028	0.000	0.237	340	449	40.6					
S 275 JR +AR 150X6 6m	CM075050	0.09	0.48	0.14	0.027	0.017	0.057	0.010	0.14	0.34	0.028	0.000	0.237	328	450	40.8					
S 275 JR +AR 180X15 L. 6m	CM075549	0.09	0.50	0.15	0.017	0.022	0.058	0.012	0.14	0.46	0.026	0.000	0.234	320	452	38.1					
S 275 JR +AR 180X15 L. 6m	CM075549	0.09	0.50	0.15	0.017	0.022	0.058	0.012	0.14	0.46	0.026	0.000	0.234	316	451	37.7					
S 275 JR +AR 180X15 L. 6m	CM075549	0.09	0.50	0.15	0.017	0.022	0.058	0.012	0.14	0.46	0.026	0.000	0.234	310	450	36.9					
S 275 JR +AR 180X15 L. 6m	CM075549	0.09	0.50	0.15	0.017	0.022	0.058	0.012	0.14	0.46	0.026	0.000	0.234	320	453	38.0					
S 275 JR +AR 180X20 6m	CM076371	0.14	0.55	0.16	0.014	0.024	0.091	0.011	0.19	0.42	0.035	0.000	0.296	303	463	33.5					
S 275 JR +AR 180X20 6m	CM076371	0.14	0.55	0.16	0.014	0.024	0.091	0.011	0.19	0.42	0.035	0.000	0.296	297	470	33.3					
S 275 JR +AR 180X20 6m	CM076371	0.14	0.55	0.16	0.014	0.024	0.091	0.011	0.19	0.42	0.035	0.000	0.296	306	473	34.1					

Certified that the material detailed hereon meets the requirements of the specified standard.
Cardiff, 24.03.2012

Stuart Thomas
Quality Manager

Appendix E

Coupon Specimen Results

Table E.1: Test results for C1 coupons.

Face	Length	b [mm]	t [mm]	S_0 [mm ²]	L_0 [mm]	L_t [mm]	b_f [mm]	t_f [mm]	S_u [mm ²]	$L_u - L_0$ [mm]	Z [%]	A [%]	E [GPa]	f_y [MPa]	f_u [MPa]
A	1	12.36	1.98	24.47	95	200	10.22	1.32	13.49	5.05	44.9	5.3	230.98	462.24	465.40
	2	12.38	1.96	24.26	95	200	10.66	1.28	13.64	5.85	43.8	6.2	232.68	469.04	475.92
	3	12.36	1.86	22.99	95	200	9.52	1.34	12.76	5.24	44.5	5.5	247.05	485.32	488.26
B	1	12.26	2.02	24.77	95	200	9.14	1.22	11.15	6.95	55.0	7.3	223.11	415.55	419.49
	2	12.38	2.04	25.26	95	200	9.76	1.36	13.27	5.96	47.4	6.3	222.93	414.92	418.77
	3	12.36	2.04	25.21	95	200	10.36	1.48	15.33	6.21	39.2	6.5	221.95	410.15	414.12
C	1	12.28	1.96	24.07	95	200	10.44	1.26	13.15	5.34	45.3	5.6	231.44	423.44	424.65
	2	12.24	1.98	24.24	95	200	10.64	1.62	17.24	5.64	28.9	5.9	231.39	418.32	425.28
	3	12.18	1.98	24.12	95	200	10.62	1.32	14.02	6.15	41.9	6.5	221.97	421.94	423.02
D	1	12.14	1.98	24.04	95	200	9.22	1.48	13.65	6.95	43.2	7.3	237.87	422.73	427.18
	2	12.20	1.96	23.91	95	200	10.72	1.32	14.15	6.65	40.8	7.0	235.62	427.55	430.10
	3	12.18	1.96	23.87	95	200	9.58	1.38	13.22	7.15	44.6	7.5	236.28	428.93	432.41
Mean		12.28	1.98	24.27		10.07	1.37	13.76	43.3	6.4	231.11	433.34	437.05		
COV		0.007	0.024	0.025		0.059	0.082	0.106	0.139	0.117	0.033	0.057	0.06		

Table E.2: Test results for C2 coupons.

Face	Length	b [mm]	t [mm]	S_0 [mm 2]	L_0 [mm]	L_t [mm]	b_f [mm]	t_f [mm]	S_u [mm 2]	$L_u - L_0$ [mm]	Z [%]	A [%]	E [GPa]	f_y [MPa]	f_u [MPa]
A	1	15.16	2.56	38.81	95	200	12.38	1.42	17.58	6.65	54.7	7.0	213.20	490.70	508.38
	2	15.14	2.58	39.06	95	200	12.68	1.58	20.03	8.52	48.7	9.0	212.10	489.17	511.27
	3	15.14	2.42	36.64	95	200	13.44	1.76	23.65	6.71	35.4	7.1	220.46	494.53	514.02
B	1	15.04	2.52	37.90	95	200	12.76	1.58	20.16	9.49	46.8	10.0	220.22	479.31	507.47
	2	15.02	2.54	38.15	95	200	12.6	1.82	22.93	10.62	39.9	11.2	215.05	468.47	497.30
	3	15.04	2.52	37.90	95	200	12.78	1.78	22.75	9.11	40.0	9.6	220.27	465.82	489.57
C	1	15.00	2.52	37.80	95	200	13.24	1.84	24.36	8.38	35.6	8.8	218.77	470.88	497.97
	2	15.18	2.5	37.95	95	200	12.76	1.78	22.71	9.85	40.2	10.4	209.15	453.39	479.60
	3	15.16	2.58	39.11	95	200	12.48	1.42	17.72	10.68	54.7	11.2	219.22	464.55	488.96
D	1	15.02	2.58	38.75	95	200	13.06	1.74	22.72	10.15	41.4	10.7	225.24	456.56	483.65
	2	15.10	2.64	39.86	95	200	12.58	1.64	20.63	11.05	48.2	11.6	212.75	446.67	472.38
	3	15.06	2.6	39.16	95	200	12.66	1.66	21.02	10.86	46.3	11.4	215.54	450.53	476.43
Mean		15.09	2.55	38.42		12.79	1.67	21.36		44.3	9.8	216.83	469.22	493.92	
COV		0.004	0.022	0.022		0.024	0.087	0.103		0.149	0.163	0.021	0.035	0.029	

Table E.3: Test results for C3 coupons.

Face	Length	b [mm]	t [mm]	S_0 [mm ²]	L_0 [mm]	L_t [mm]	b_f [mm]	t_f [mm]	S_u [mm ²]	$L_u - L_0$ [mm]	Z [%]	A [%]	E [GPa]	f_y [MPa]	f_u [MPa]
A	1	15.16	2.4	36.38	95	200	12.68	1.64	20.80	8.69	42.8	9.1	218.71	492.89	505.11
	2	15.04	2.38	35.80	95	200	12.68	1.56	19.78	7.61	44.7	8.0	206.57	470.12	486.89
	3	15.18	2.48	37.65	95	200	12.46	1.48	18.44	7.86	51.0	8.3	226.39	490.86	504.93
B	1	15.12	2.48	37.50	95	200	11.36	1.66	18.86	10.05	49.7	10.6	216.51	463.67	482.04
	2	15.16	2.68	40.63	95	200	12.08	1.42	17.15	8.12	57.8	8.5	186.85	400.34	422.05
	3	15.18	2.56	38.86	95	200	12.02	1.54	18.51	10.98	52.4	11.6	218.84	444.87	468.05
C	1	15.02	2.48	37.25	95	200	13.02	1.58	20.57	8.79	44.8	9.3	221.46	442.13	466.96
	2	15.02	2.46	36.95	95	200	12.86	1.74	22.38	8.57	39.4	9.0	212.66	440.64	463.86
	3	15.02	2.48	37.25	95	200	12.64	1.66	20.98	9.94	43.7	10.5	227.66	447.12	471.64
D	1	15.20	2.52	38.30	95	200	11.58	1.62	18.76	10.36	51.0	10.9	210.15	442.45	465.38
	2	15.08	2.54	38.30	95	200	12.06	1.60	19.30	7.94	49.6	8.4	214.27	422.96	442.39
	3	15.04	2.56	38.50	95	200	11.74	1.36	15.97	10.04	58.5	10.6	217.76	434.38	455.48
Mean		15.10	2.50	37.78			12.27	1.57	19.29		48.8	9.6	214.82	449.37	469.57
COV		0.005	0.032	0.033			0.044	0.069	0.091		0.121	0.125	0.050	0.059	0.051

Table E.4: Test results for C4 coupons.

Face	Length	b [mm]	t [mm]	S_0 [mm 2]	L_0 [mm]	L_t [mm]	b_f [mm]	t_f [mm]	S_u [mm 2]	$L_u - L_0$ [mm]	Z [%]	A [%]	E [GPa]	f_y [MPa]	f_u [MPa]
A	1	20.12	3.88	78.07	95	200	14.82	2.24	33.20	13.60	57.5	14.3	173.95	443.03	462.06
	2	20.18	3.82	77.09	95	200	14.64	2.36	34.55	22.54	55.2	23.7	168.21	433.19	457.36
	3	20.12	3.98	80.08	95	200	14.72	1.76	25.91	10.85	67.6	11.4	157.35	413.50	425.29
B	1	25.12	3.94	98.97	95	200	18.96	1.58	29.96	14.20	69.7	14.9	153.01	404.94	423.51
	2	24.98	3.72	92.93	95	200	17.56	1.98	34.77	12.40	62.6	13.1	161.87	424.95	444.49
	3	24.98	3.94	98.42	95	200	17.18	1.96	33.67	14.25	65.8	15.0	156.77	411.22	427.81
C	1	20.02	3.92	78.48	95	200	14.04	2.20	30.89	14.35	60.6	15.1	163.84	400.36	418.39
	2	20.02	3.86	77.28	95	200	14.22	2.22	31.57	12.65	59.1	13.3	160.75	401.73	419.09
	3	20.00	3.94	78.80	95	200	14.48	1.84	26.64	13.15	66.2	13.8	160.72	408.94	427.04
D	1	20.14	3.86	77.74	95	200	14.18	1.64	23.26	12.32	70.1	13.0	169.90	401.99	417.73
	2	20.18	3.96	79.91	95	200	13.96	1.98	27.64	12.58	65.4	13.2	166.35	393.34	405.03
	3	20.20	3.98	80.40	95	200	13.34	2.12	28.28	19.42	64.8	20.4	163.97	397.36	416.11
Mean		21.34	3.90	83.18		15.18	1.99	30.03		63.7	15.1	163.06	411.21	428.66	
COV		0.104	0.020	0.101		0.114	0.125	0.124		0.075	0.231	0.036	0.037	0.040	

Appendix F

Strain Gauge Test Data

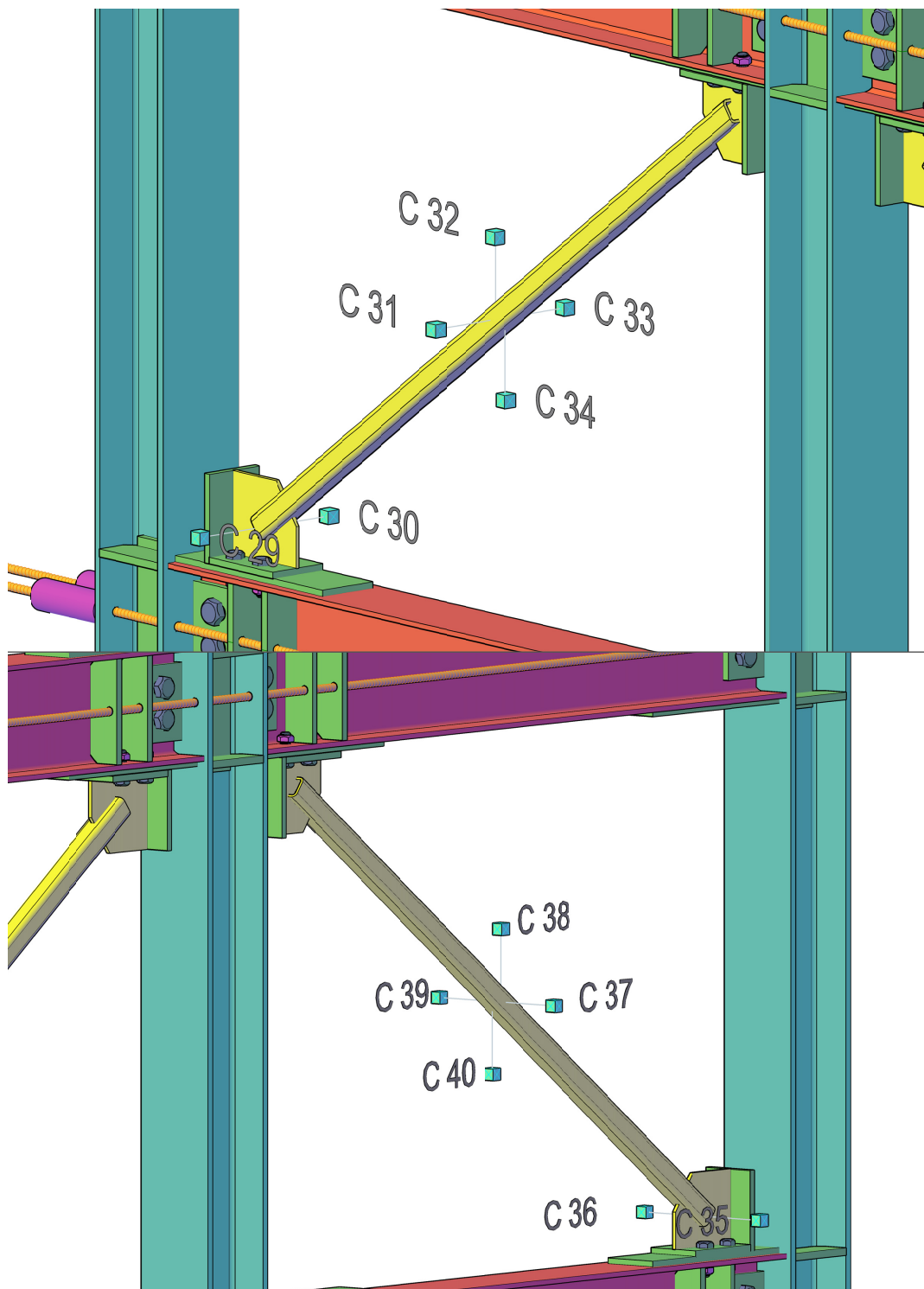


Figure F.1: Brace strain gauge locations.

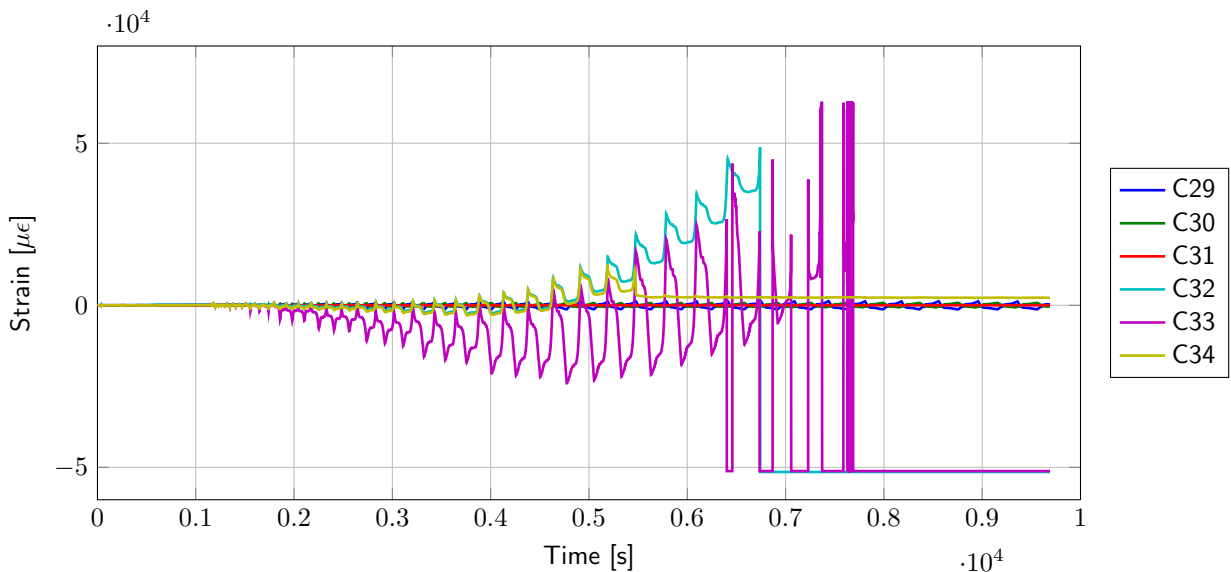


Figure F.2: B1A LHS Brace Strains v Time.

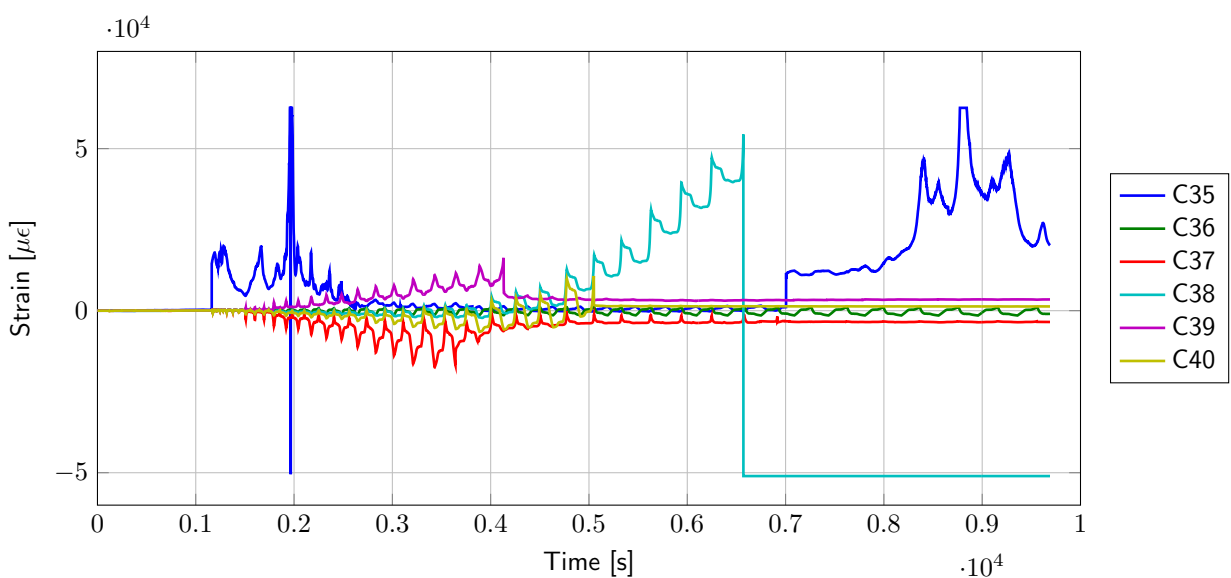


Figure F.3: B1A RHS Brace Strains v Time.

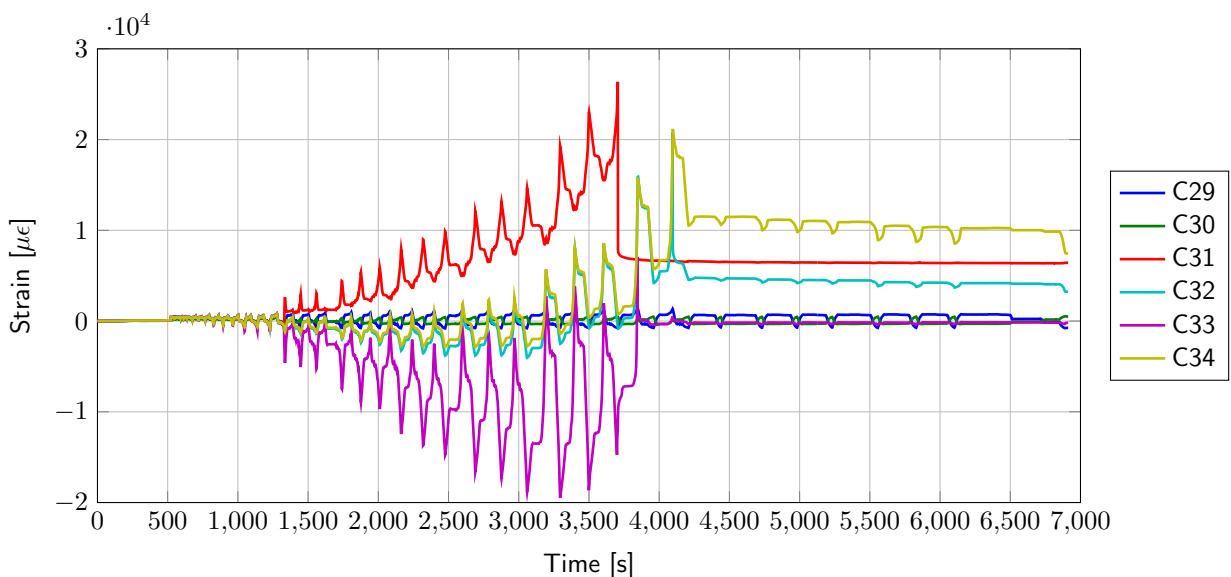


Figure F.4: B2A LHS Brace Strains v Time.

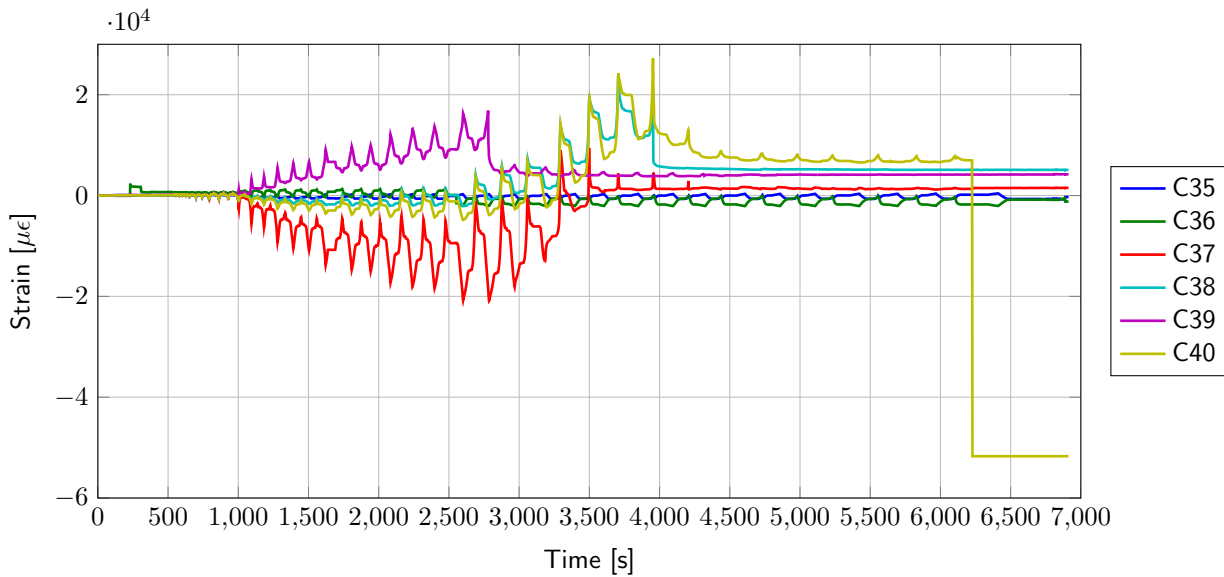


Figure F.5: B2A RHS Brace Strains v Time.

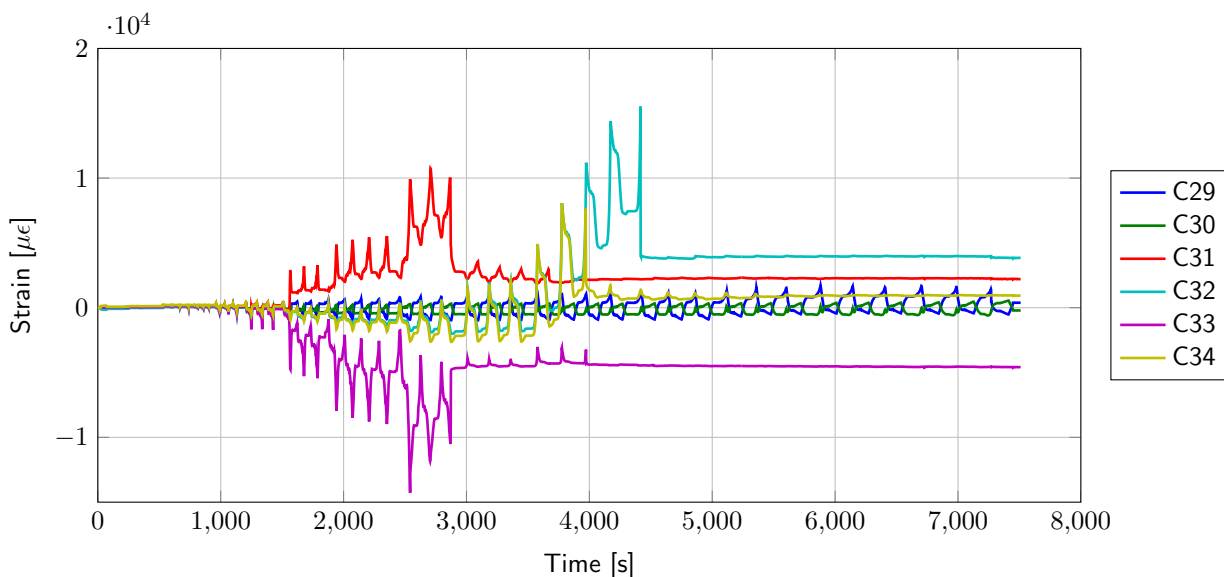


Figure F.6: B2B LHS Brace Strains v Time.

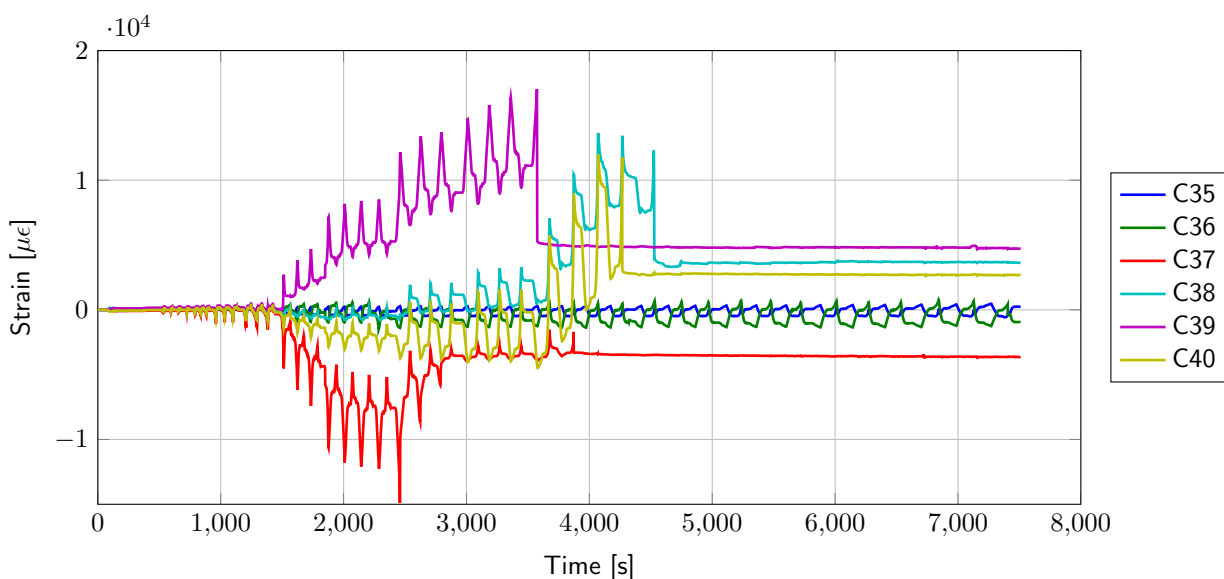


Figure F.7: B2B RHS Brace Strains v Time.

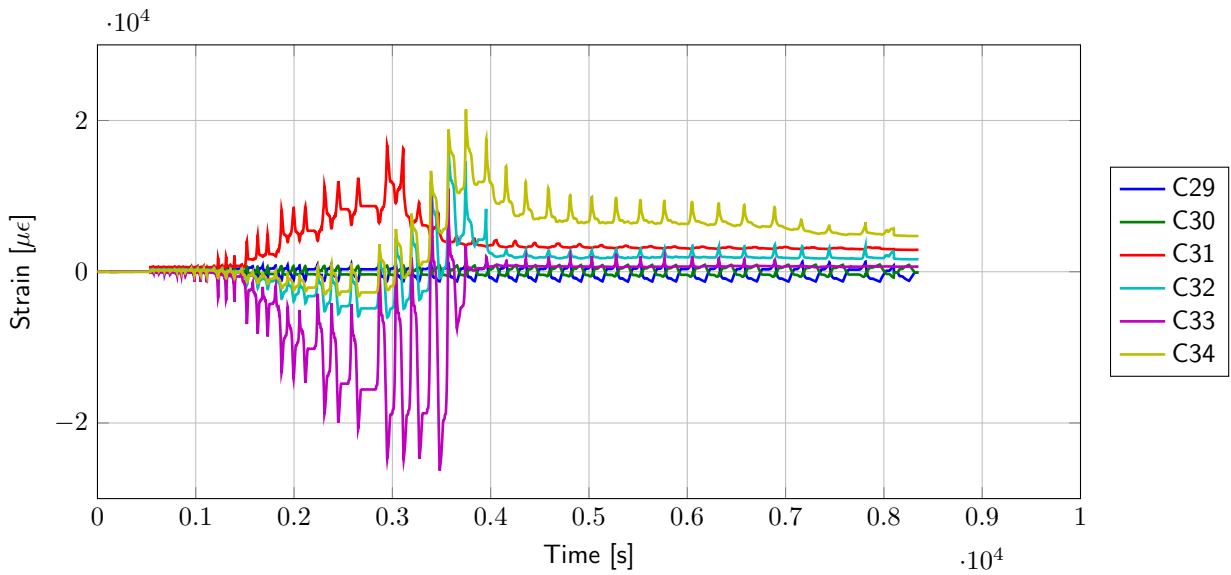


Figure F.8: B1B LHS Brace Strains v Time.

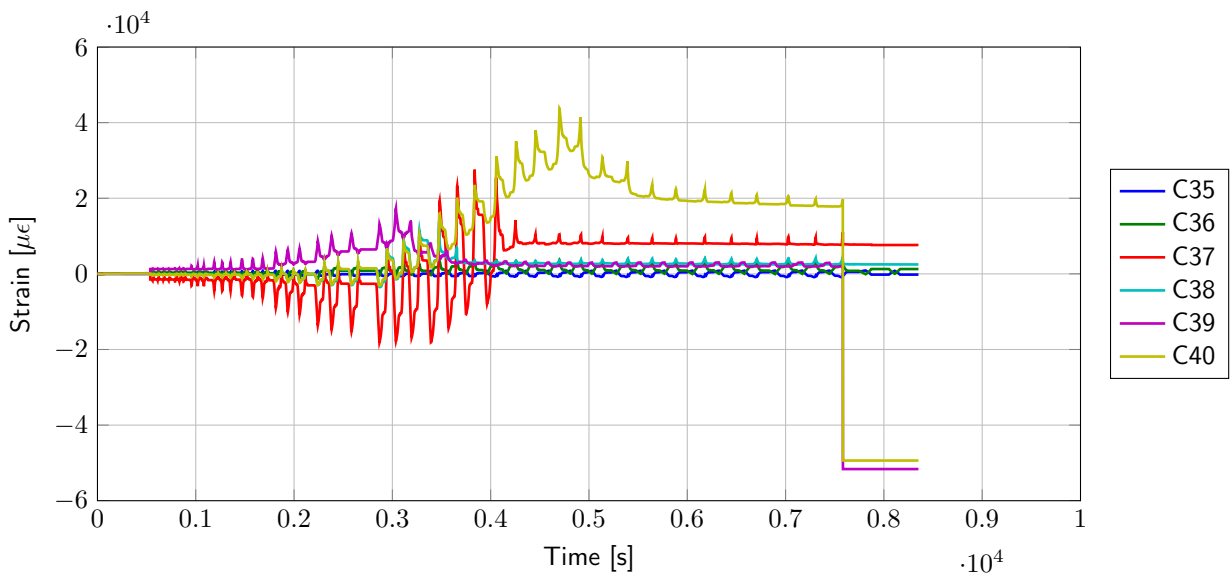


Figure F.9: B1B RHS Brace Strains v Time.

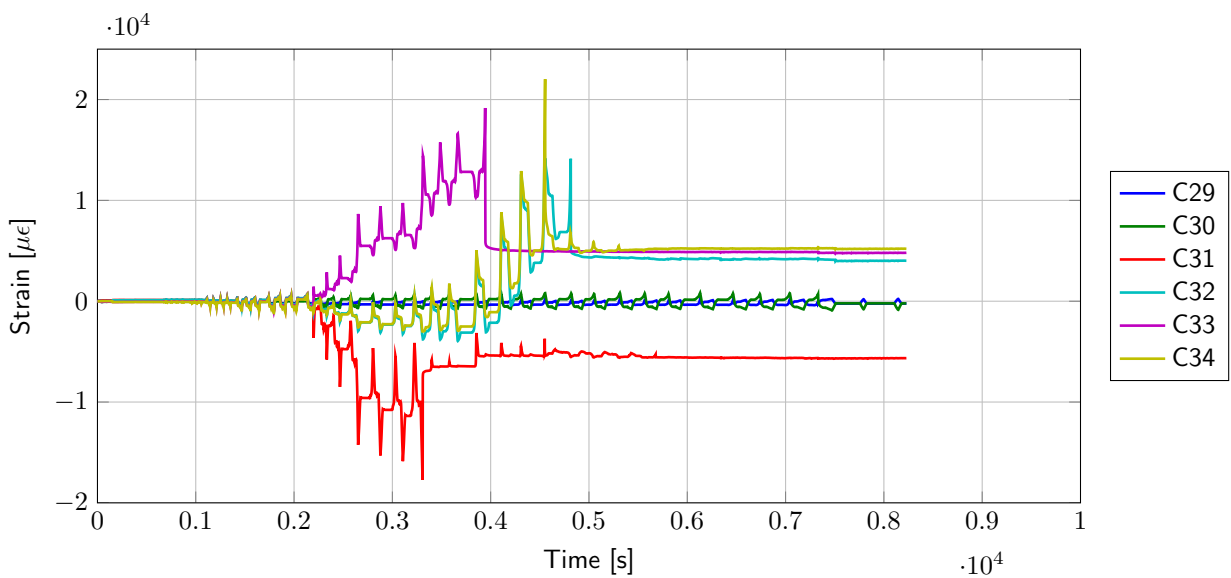


Figure F.10: B3A LHS Brace Strains v Time.

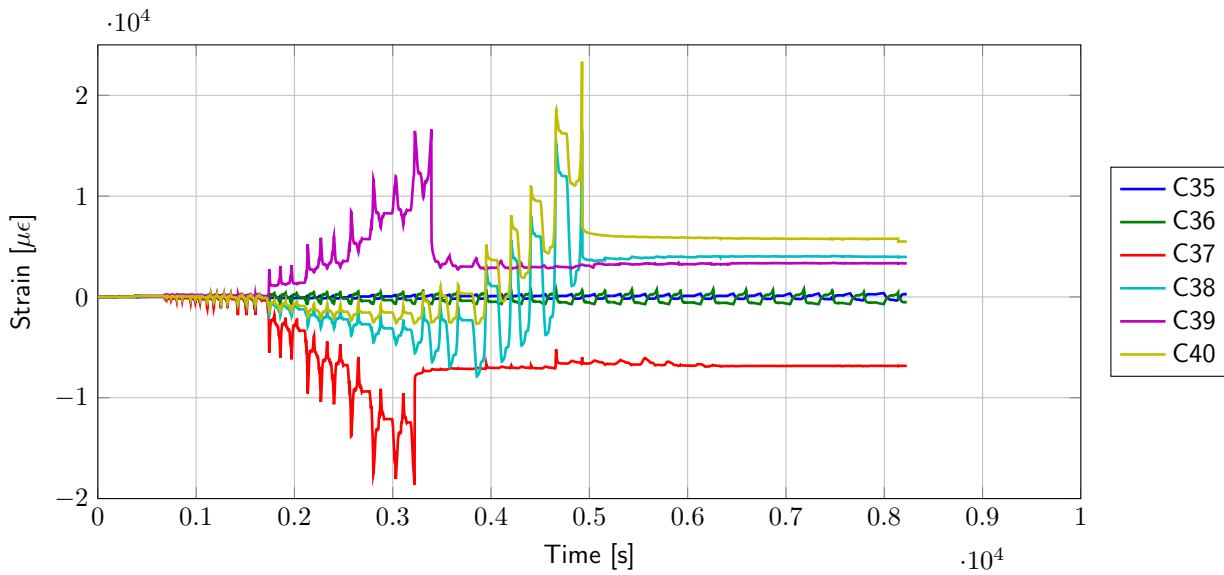


Figure F.11: B3A RHS Brace Strains v Time.

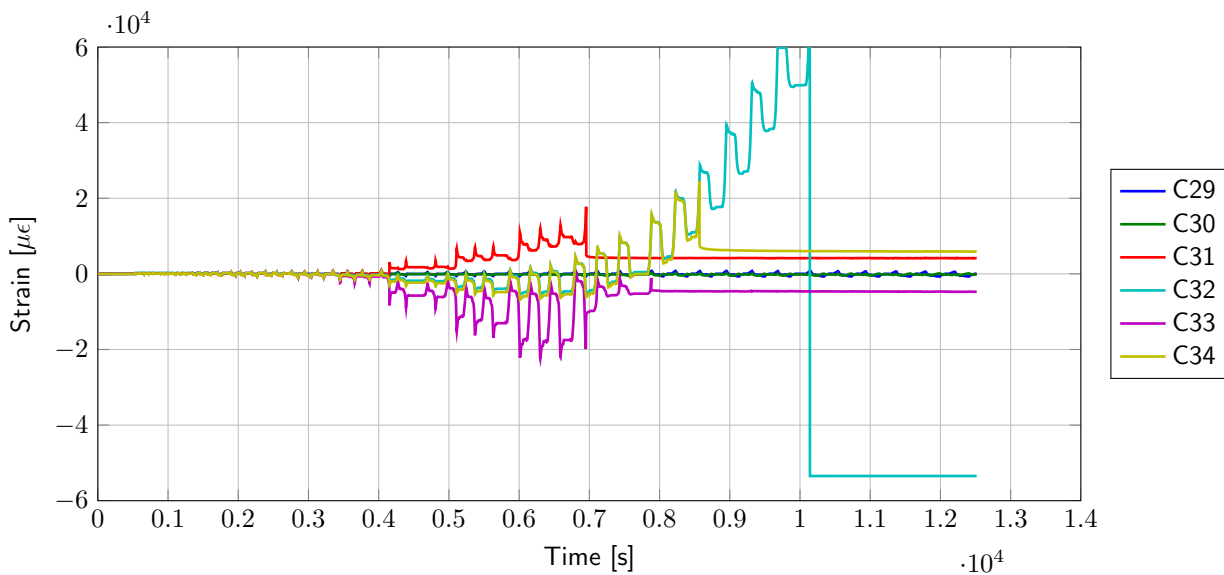


Figure F.12: B4A LHS Brace Strains v Time.

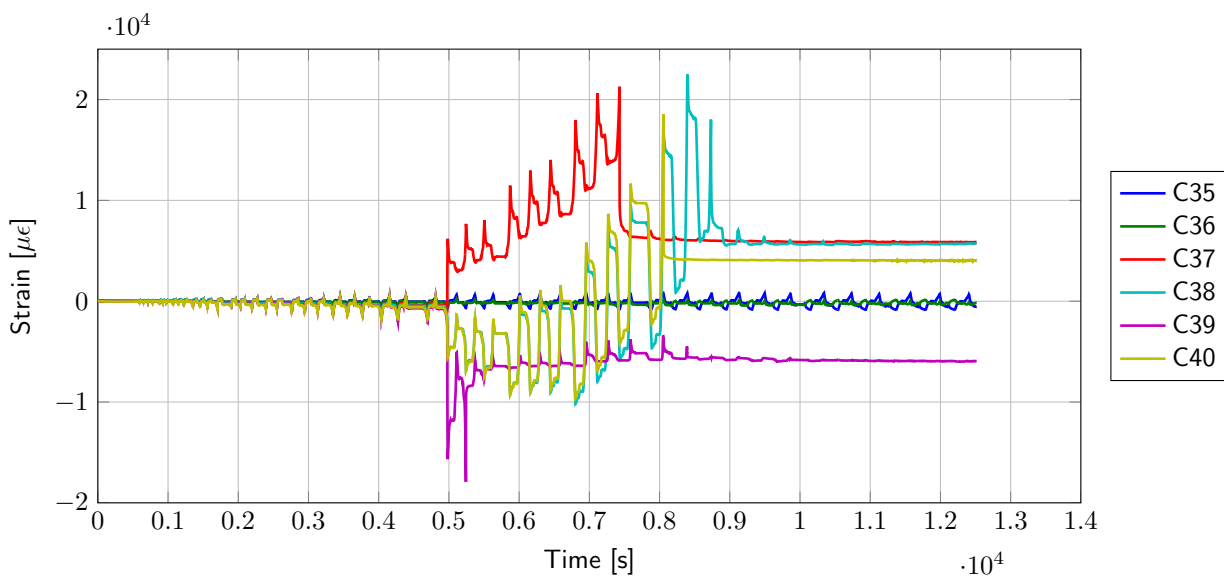


Figure F.13: B4A RHS Brace Strains v Time.

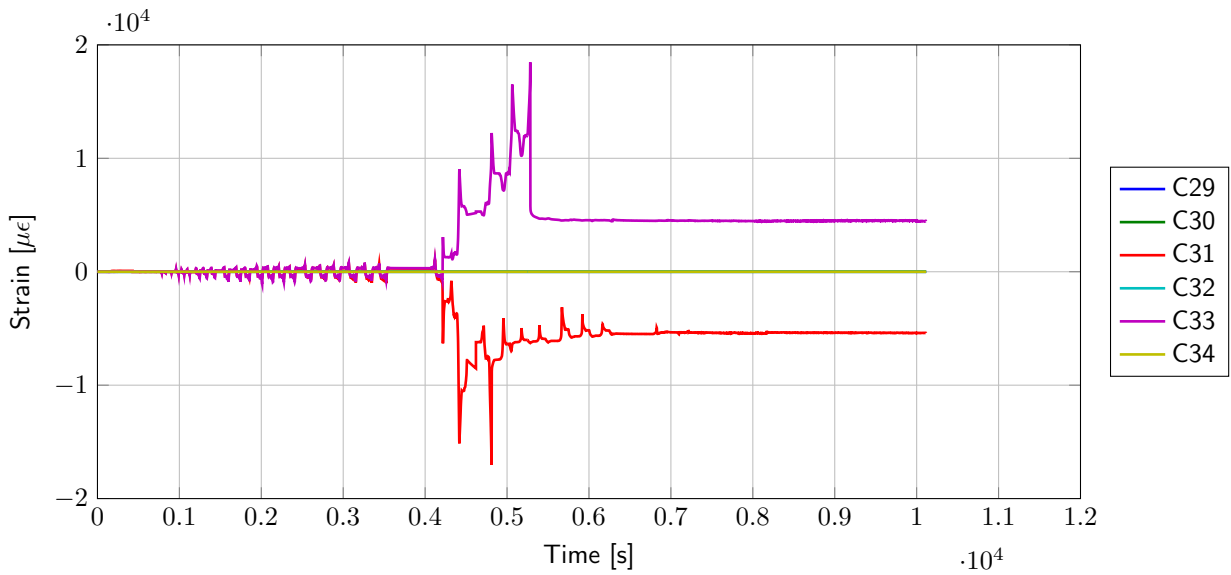


Figure F.14: B3B LHS Brace Strains v Time.

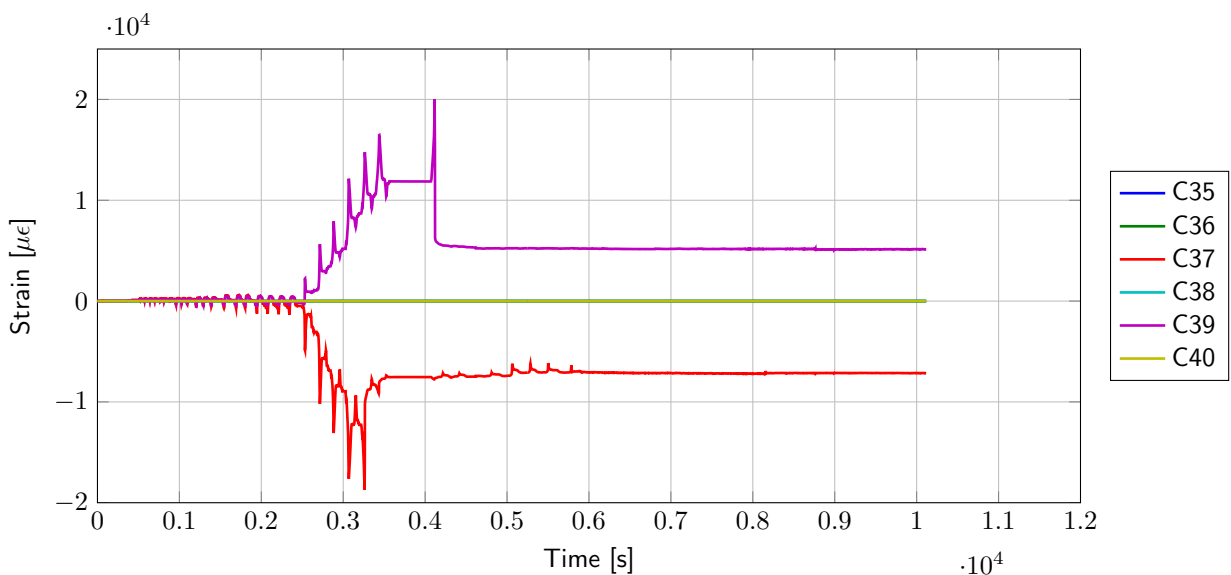


Figure F.15: B3B RHS Brace Strains v Time.

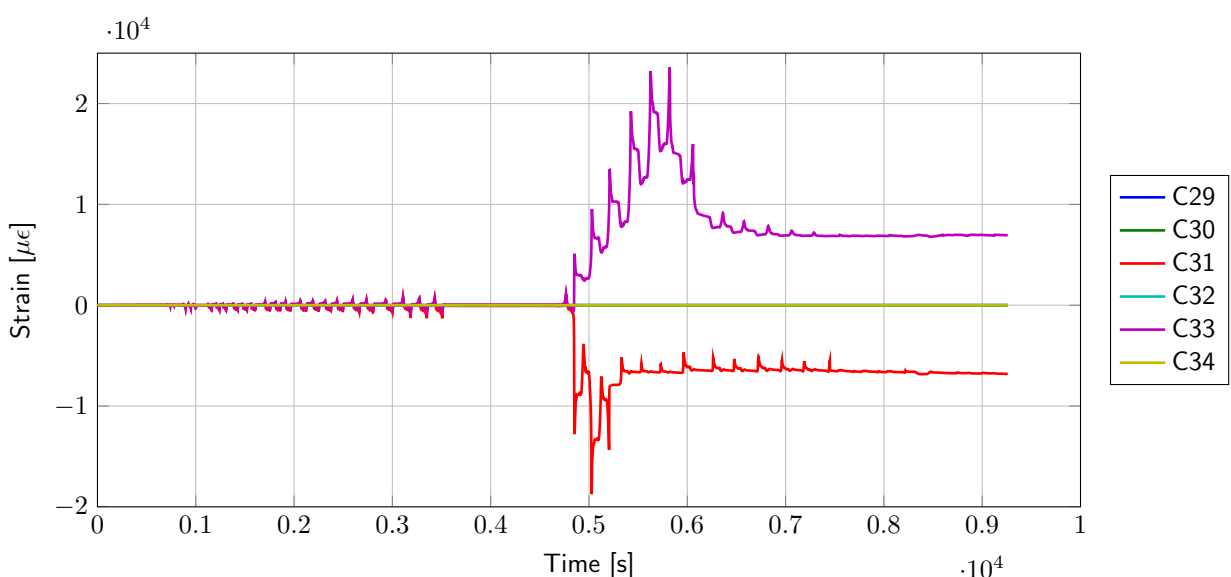


Figure F.16: B4B LHS Brace Strains v Time.

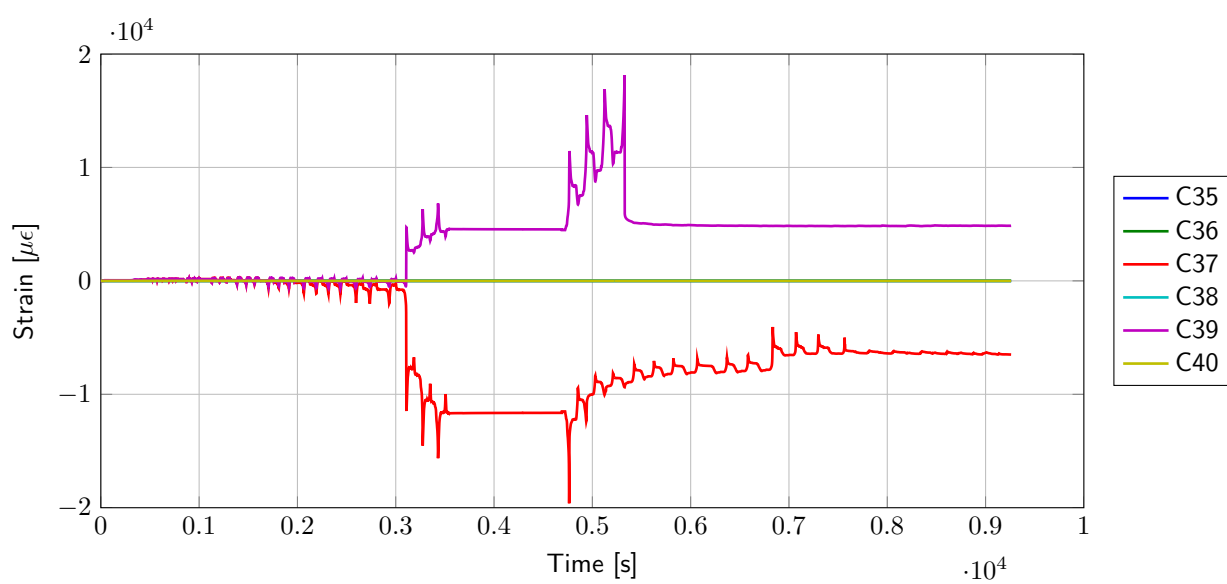


Figure F.17: B4B RHS Brace Strains v Time.

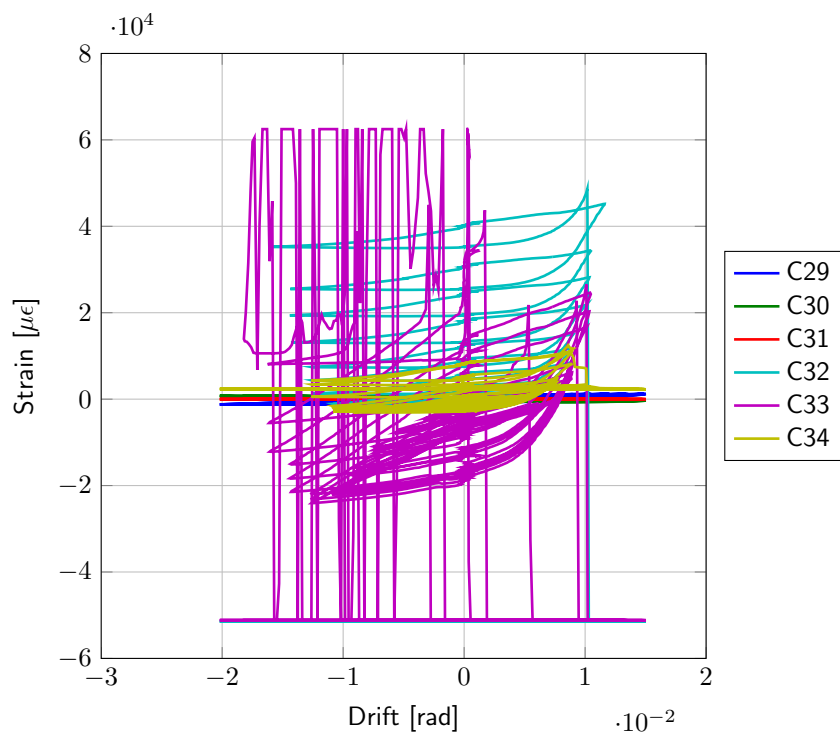


Figure F.18: B1A LHS Brace Strains v Drift.

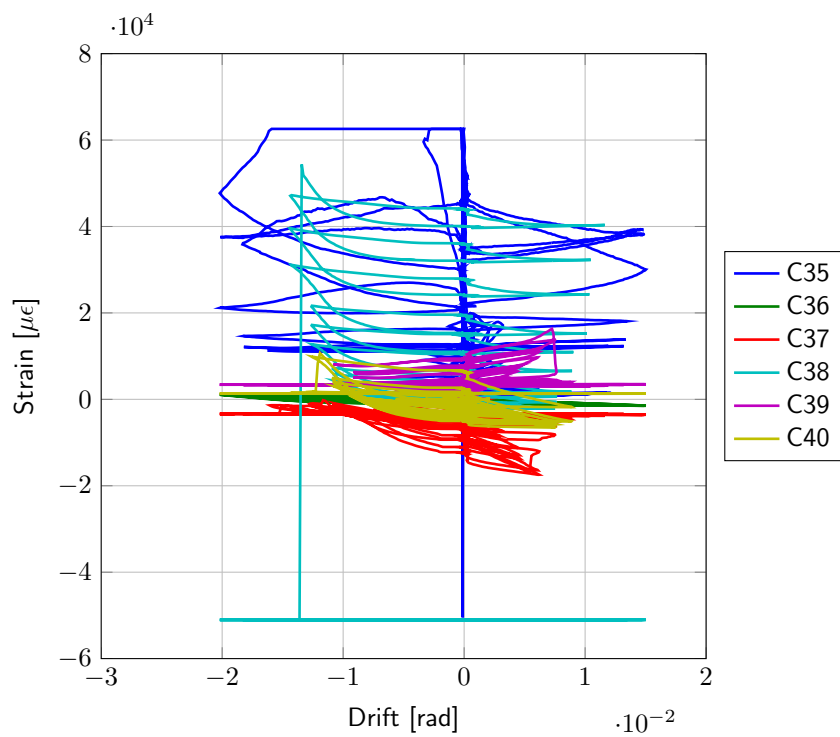


Figure F.19: B1A RHS Brace Strains v Drift.

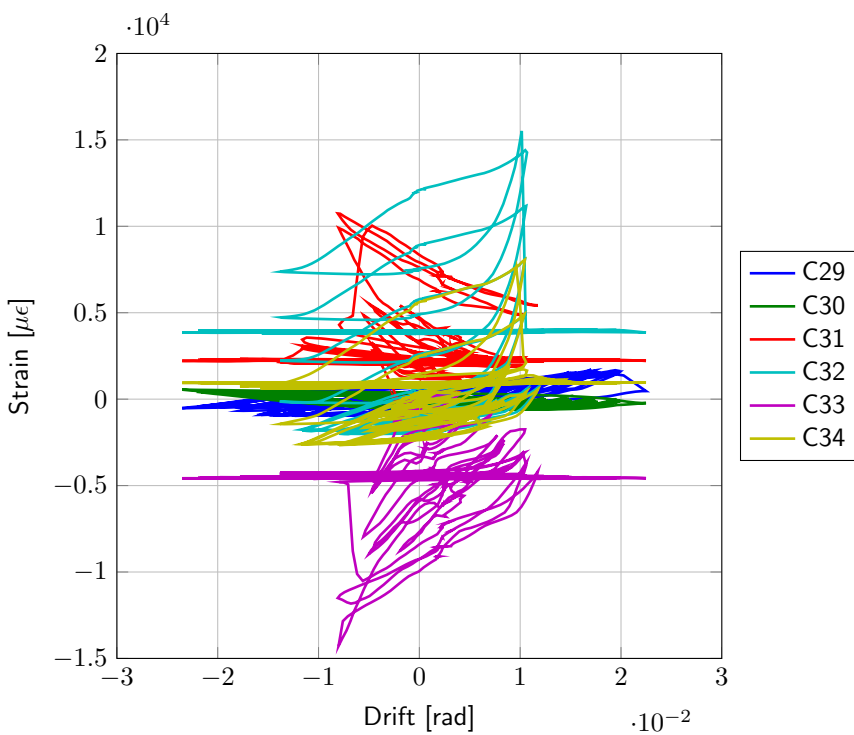


Figure F.20: B2B LHS Brace Strains v Drift.

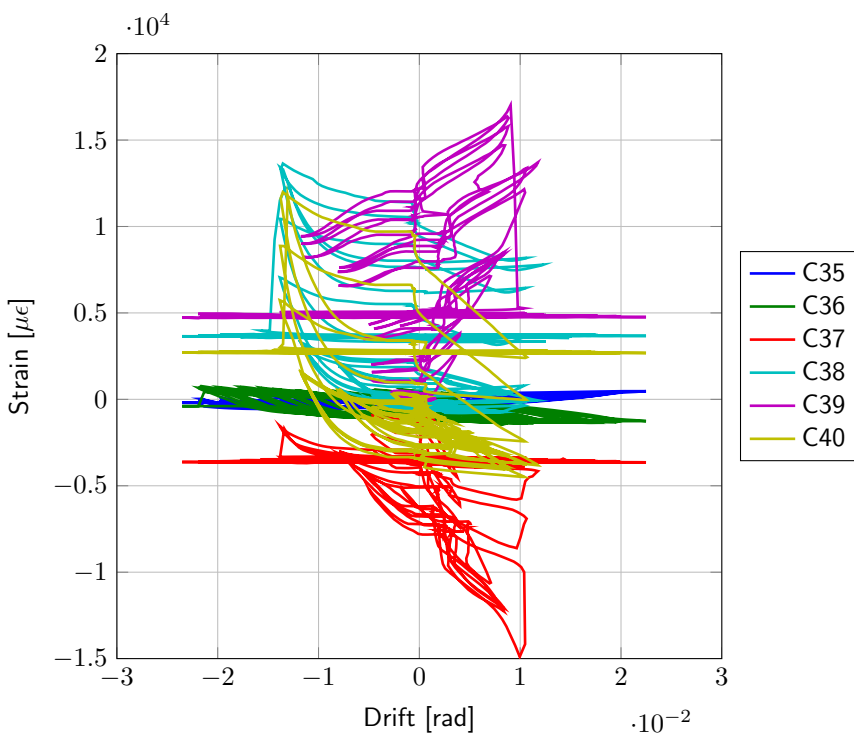


Figure F.21: B2B RHS Brace Strains v Drift.

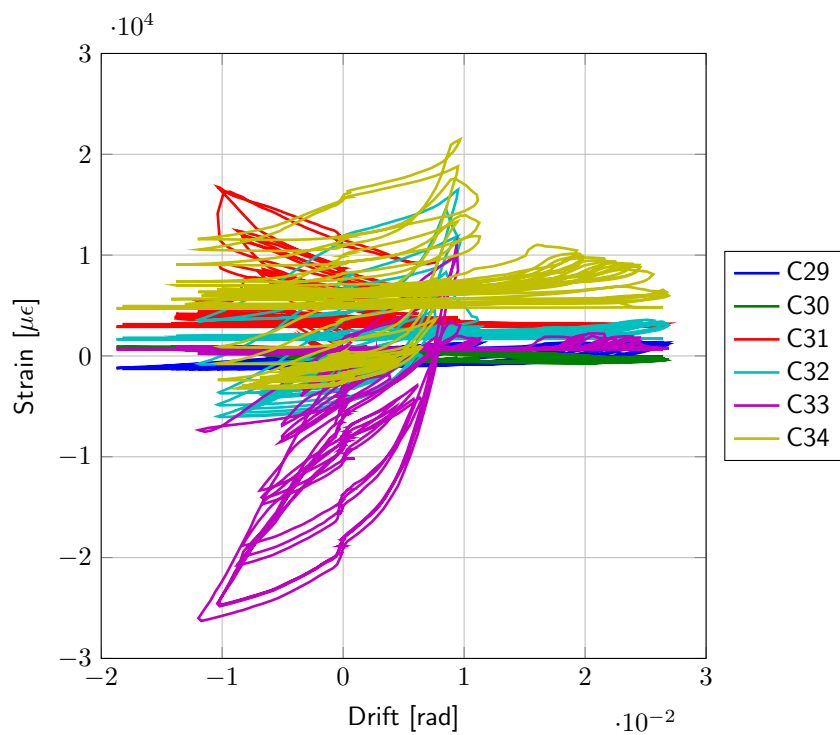


Figure F.22: B1B LHS Brace Strains v Drift.

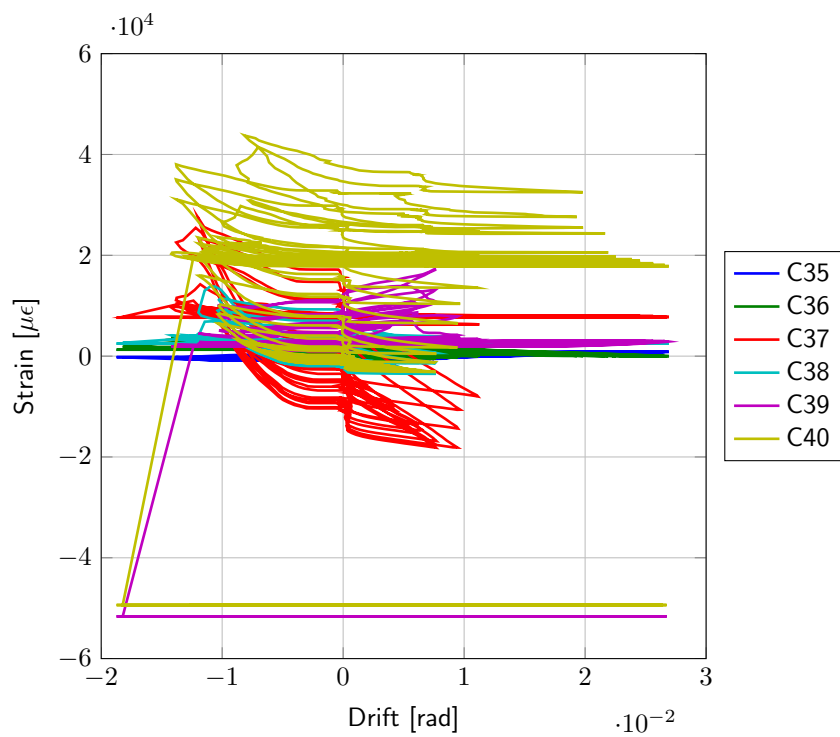


Figure F.23: B1B RHS Brace Strains v Drift.

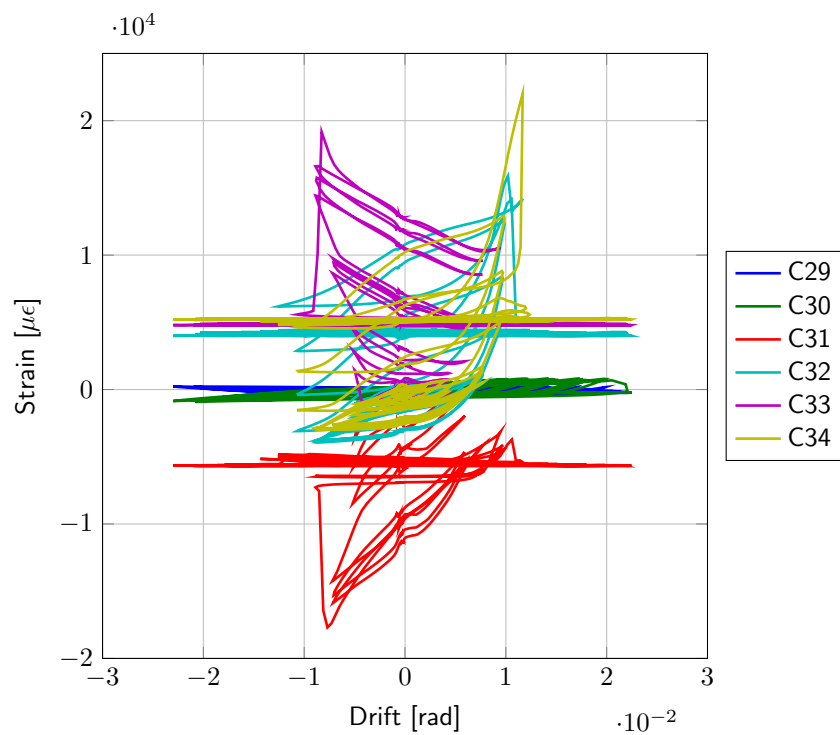


Figure F.24: B3A LHS Brace Strains v Drift.

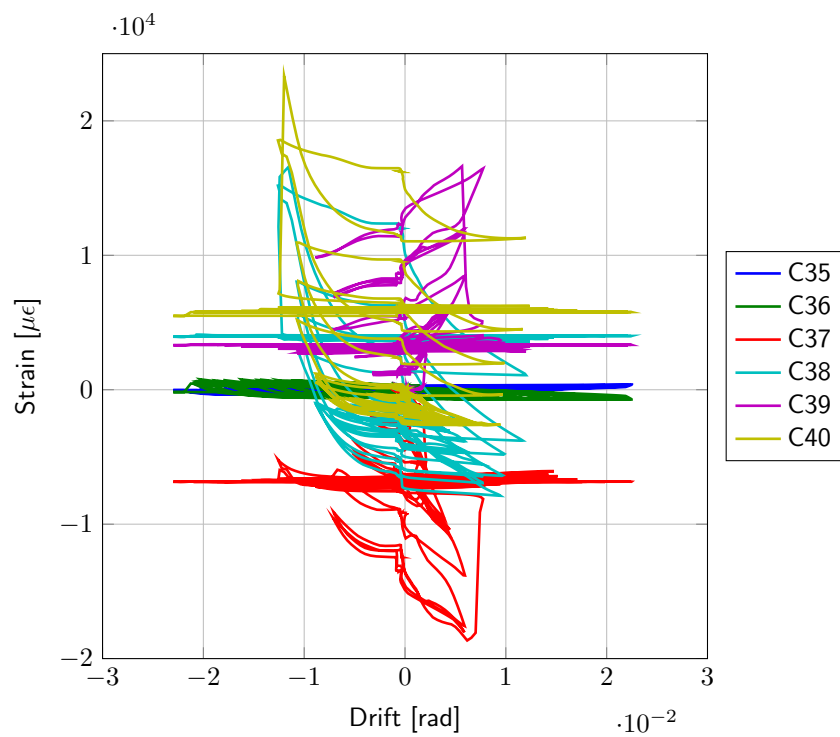


Figure F.25: B3A RHS Brace Strains v Drift.

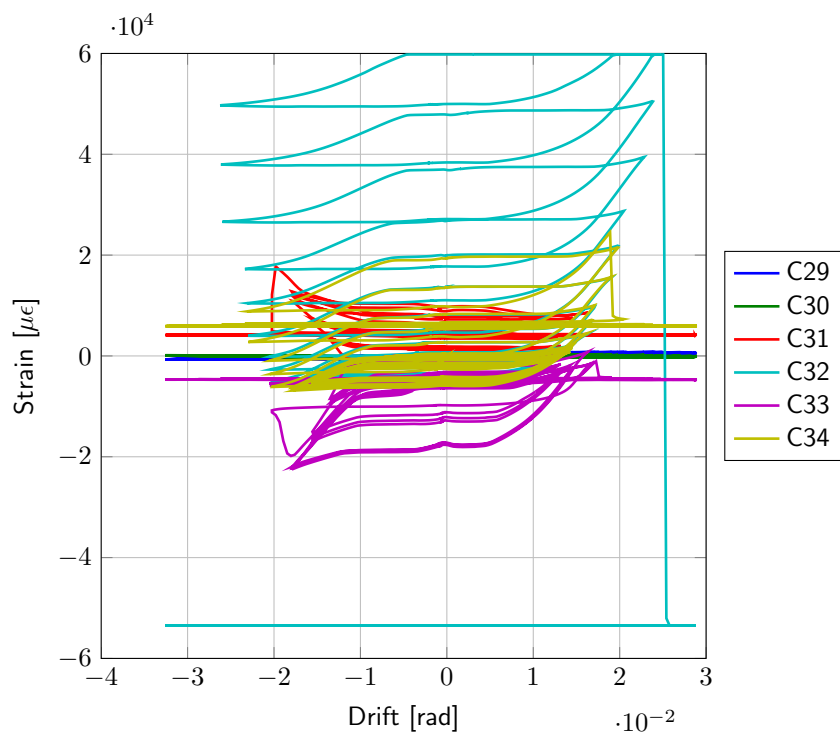


Figure F.26: B4A LHS Brace Strains v Drift.

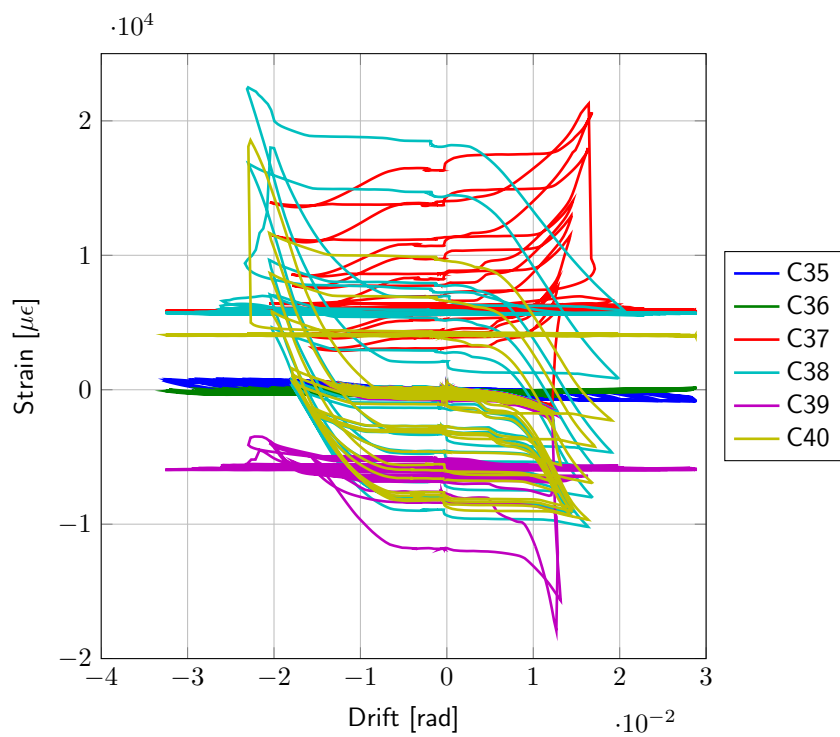


Figure F.27: B4A RHS Brace Strains v Drift.

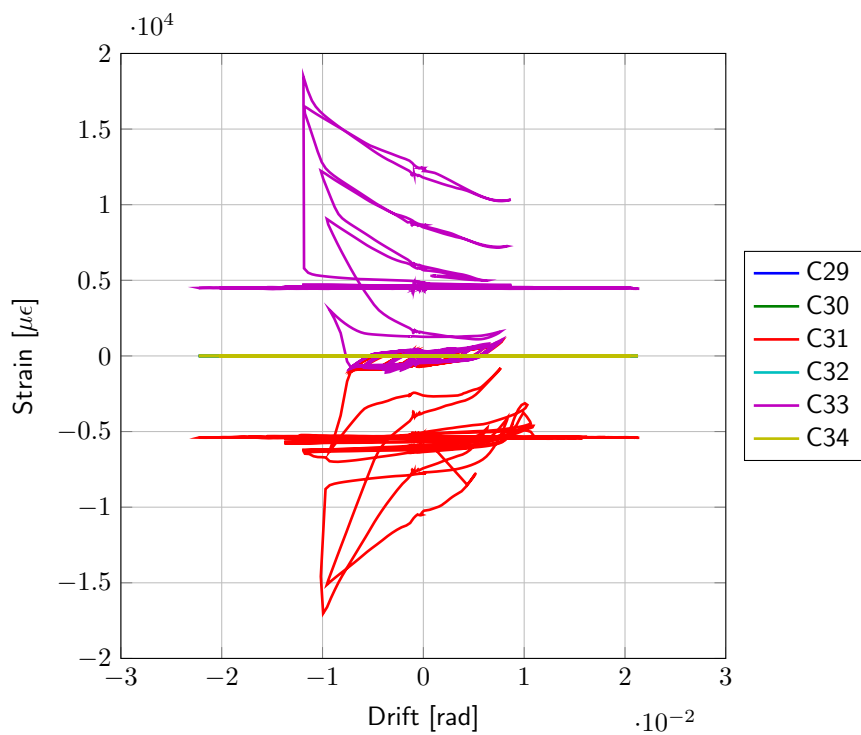


Figure F.28: B3B LHS Brace Strains v Drift.

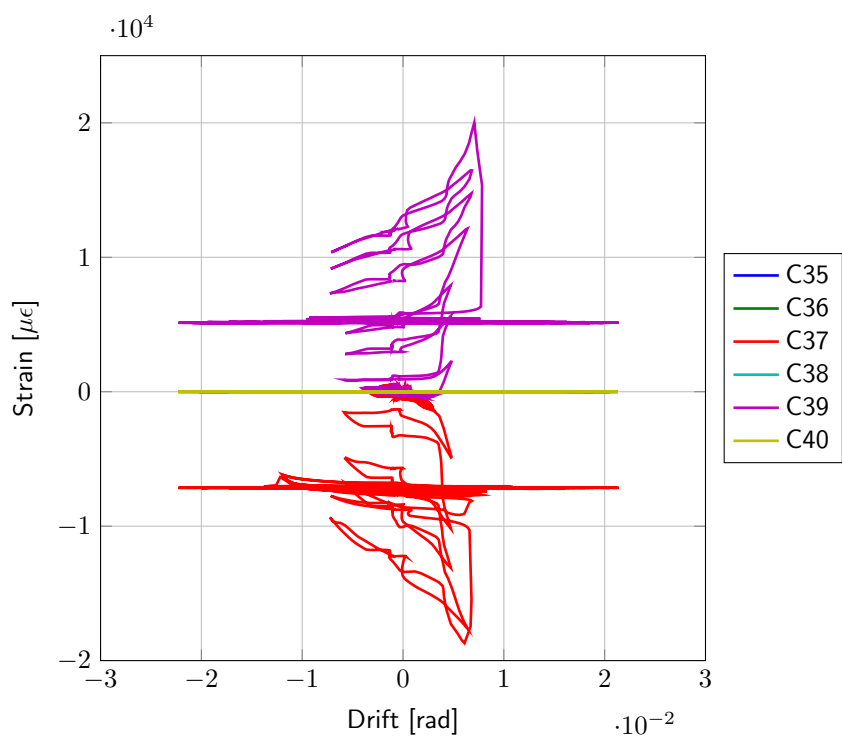


Figure F.29: B3B RHS Brace Strains v Drift.

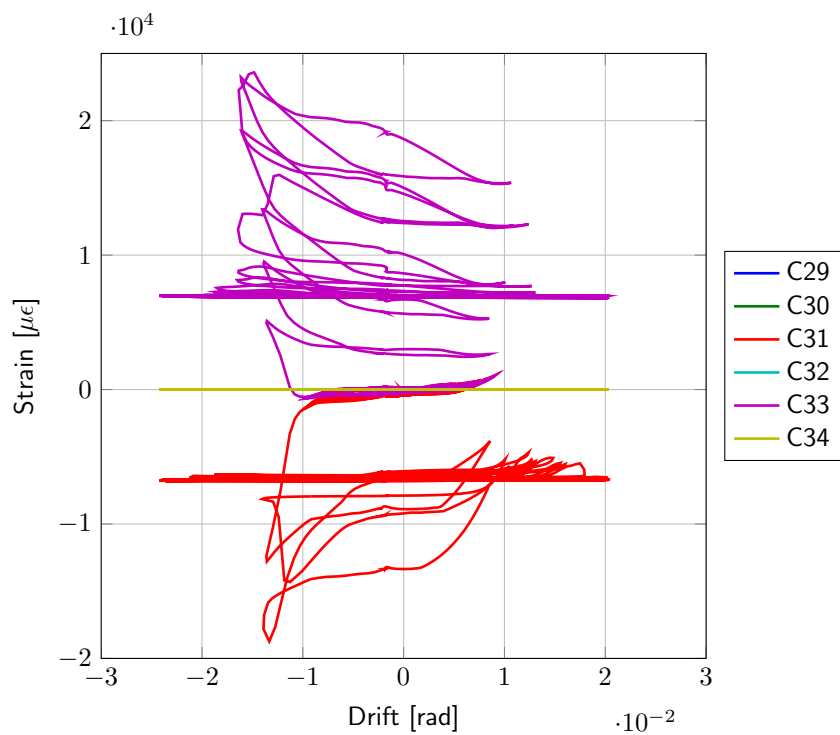


Figure F.30: B4B LHS Brace Strains v Drift.

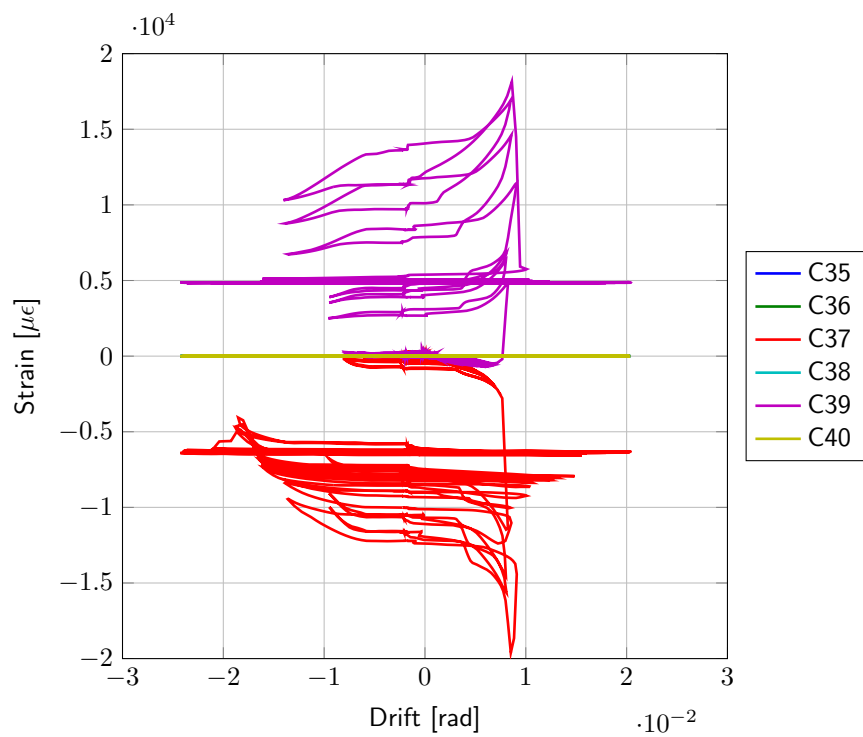


Figure F.31: B4B RHS Brace Strains v Drift.